Alias Abdul Rahman
Pawel Boguslawski
François Anton
Mohamad Nor Said
Kamaludin Mohd Omar   *Editors*

Geoinformation for Informed Decisions

Springer

Lecture Notes in Geoinformation and Cartography

Alias Abdul Rahman · Pawel Boguslawski
François Anton · Mohamad Nor Said
Kamaludin Mohd Omar
Editors

Geoinformation for Informed Decisions

Editors
Alias Abdul Rahman
Pawel Boguslawski
Mohamad Nor Said
Kamaludin Mohd Omar
Faculty of Geoinformation
    and Real Estate
Universiti Teknologi Malaysia
Skudai
Malaysia

François Anton
National Space Institute
Technical University of Denmark
Copenhagen
Denmark

Printed on acid-free paper

Preface

This book is a compilation of the best papers among the papers presented at the International Symposium and Exhibition on Geoinformation 2013 (ISG 2013), which was held at the Universiti Teknologi Malaysia, Kuala Lumpur campus on 24–25 September 2013. The papers have been reviewed by experts (at least two blind-reviews for each paper) in the field of Geoinformation, including Geomatic Engineering, GPS, Photogrammetry, Cartography, Remote Sensing, LiDAR, GIS, etc., and they formed major discussions in the conference. The conference received around 80 full papers and only 20 % were accepted for this book.

We would like to thank all the reviewers from Australia, Canada, China, Denmark, France, Germany, Greece, Italy, Malaysia, The Netherlands, Poland, Trinidad and Tobago, Turkey, and the United Kingdom. Their great effort in the paper reviewing process is greatly acknowledged.

Last but not least, many thanks go to all local organizing committee members who have contributed significantly to the success of this conference.

We hope this book triggers more advanced ideas for the near future research within Geoinformation.

Enjoy!

<div align="right">

Alias Abdul Rahman
Pawel Boguslawski
François Anton
Mohamad Nor Said
Kamaludin Mohd Omar

</div>

Organization

Program Committee

Alias Abdul Rahman—Universiti Teknologi Malaysia
Pawel Boguslawski—Universiti Teknologi Malaysia
François Anton—Technical University of Denmark
Mohamad Nor Said—Universiti Teknologi Malaysia
Kamaludin Mohd Omar—Universiti Teknologi Malaysia

Reviewers

Adam Lyszkowicz—University of Warmia and Mazury in Olsztyn, Poland
Albert Chong—The University of Southern Queensland, Australia
Alias Abdul Rahman—Universiti Teknologi Malaysia, Malaysia
Behnam Alizadehashrafi—Universiti Teknologi Malaysia, Malaysia
Bheshem Ramlal—University of West Indies, Trinidad and Tobago
Christopher Gold—University of Glamorgan, UK
Claire Ellul—University College London, UK
Clive Fraser—University of Melbourne, Australia
Darka Mioc—Technical University of Denmark, Denmark
Derek Lichti—The University of Calgary, Canada
Efi Dimopoulou—National Technical University of Athens, Greece
Eliseo Clementini—University of L'Aquila, Italy
Fabio Remondino—Bruno Kessler Foundation, Italy
François Anton—Technical University of Denmark, Denmark
Gerhard Groeger—Universität Bonn, Germany
Gurcan Buyuksalih—Bimtas, Istanbul, Turkey
Halim Setan—Universiti Teknologi Malaysia, Malaysia
Halmi Kamaruddin—Universiti Teknologi MARA, Malaysia
Hugo Ledoux—Delft University of Technology, The Netherlands
Ismail Rakip Karas—Karabuk University, Turkey
Jane Drummond—University of Glasgow, UK

Jantien Stoter—Delft University of Technology, The Netherlands
Jaroslaw Bosy—Wroclaw University of Environmental and Life Sciences, Poland
Kamaludin Mohd Omar—Universiti Teknologi Malaysia, Malaysia
Kazimierz Becek—Wroclaw University of Environmental and Life Sciences,
                 Poland
Lars Bodum—Aalborg Universitet, Denmark
Marco Scaioni—Tongji University, China
Martijn Meijers—Delft University of Technology, The Netherlands
Martin Kada—University of Osnabrueck, Germany
Michael Hahn—HFT Stuttgart University, Germany
Mike Jackson—The University of Nottingham, UK
Mohamad Nor Said—Universiti Teknologi Malaysia, Malaysia
Mohd Nadzri Md Reba—Universiti Teknologi Malaysia, Malaysia
M. Zulkarnain Abd Rahman—Universiti Teknologi Malaysia, Malaysia
Pawel Boguslawski—Universiti Teknologi Malaysia, Malaysia
PC Lai—The University of Hong Kong, China
Peter van Oosterom—Delft University of Technology, The Netherlands
Robert Laurini—INSA Lyon, France
Rod Thompson—Queensland Government, Australia
Shuanggen Jin—Chinese Academy of Sciences, China
Sisi Zlatanova—Delft University of Technology, The Netherlands
Stephan Winter—The University of Melbourne, Australia
Tajul Arifin Musa—Universiti Teknologi Malaysia, Malaysia
Tuong Thuy Vu—University of Nottingham Malaysia Campus, Malaysia
Umit Isikdag—Beykent University, Turkey
William Cartwright—RMIT University, Australia
Xiaoli Ding—The Hong Kong Polytechnic University, China
Zulkepli Majid—Universiti Teknologi Malaysia, Malaysia

Additional Reviewers

Ibrahim Sufiyan—Universiti Teknologi Malaysia, Malaysia
Jacky Chow—The University of Calgary, Canada

Local Organizing Committee (Universiti Teknologi Malaysia)

Abdullah Othman
Azman Ariffin
Behnam Alizadehashrafi
Ivin Amri Musliman
Khamarrul Aazahari Razak

Latifah Ibrahim
Mohamad Ghazali Hashim
Muhammad Imzan Hassan
Muhammad Zulkarnain bin Abdul Rahman
Norazalina A. Samad
Nurul Hawani Idris
Rozaimi Che Hasan
Shuib Rambat
Tajul Ariffin Musa
Wan Muhd Hairi Wan Ab. Karim
Zulkepli Majid

Contents

The Interoperable Building Model
of the European Union

Gerhard Gröger and Lutz Plümer

Abstract The INSPIRE initiative of the European Union (EU) aims at developing a huge spatial data infrastructure (SDI) for authoritative spatial data in Europe. The member states are obligated to provide a large amount of their spatial data in this SDI. The building model is an important aspect among the 34 themes which are covered by INSPIRE. To cope with the heterogeneity of use cases and of data availability in the EU, the model consists of two normative profiles: a 2D and 3D profile. In addition, two non-normative extended profiles are provided. The chapter describes the use cases for buildings and the normative part of the building model in detail, as well as the relation to the standard CityGML for 3D city models, which has influenced the INSPIRE building model significantly. Although the regional scope of INSPIRE is the EU, it presumably will function as a role model also for other regions in the world.

1 Introduction

Currently, a new huge, widespread and multi-faceted spatial data infrastructure (SDI) is developed and build-up in the European Union. This initiative is called *INSPIRE* (Infrastructure for Spatial Information in the European Community)[1] and

---

[1] See http://inspire.jrc.ec.europa.eu/

G. Gröger (✉) · L. Plümer
Institute for Geodesy and Geoinformation, University of Bonn,
Meckenheimer Allee 172, 53115 Bonn, Germany
e-mail: groeger@igg.uni-bonn.de

L. Plümer
e-mail: pluemer@igg.uni-bonn.de

was initiated by the European Parliament and the Council.[2] INSPIRE addresses 34 spatial data themes which are needed for various applications of spatial data. However, the focus is set on environmental applications. The aim of INSPIRE is to provide metadata and spatial data in an interoperable way across country and system boundaries. In particular Geo-Web-Services such as Web Feature Services (WFS) (Vretanos 2010) will be employed.

An essential prerequisite for interoperable access are unified, harmonized data models. To cover the applications targeted by INSPIRE, manifold data models are needed. For 34 themes, corresponding data models have been developed. In a first phase (called Annex I) which was completed in 2010, unified models for the following basic themes have been designed: Administrative Units, Cadastral Parcels, Geographical Names, Hydrography, Protected Sites, Transport Networks, Addresses, Coordinate Reference Systems, and Geographical Grid Systems. Based on these models, a second phase (Annex II & III) is conducted which covers themes such as Agricultural/Aquaculture and Production/Industrial Facilities, Buildings, Elevation, Energy Resources, Environmental monitoring Facilities, Geology, Human health and safety, Land cover and use, Natural risk zones, Oceanographic geographical features, Orthoimagery, Population distribution, Soil, Statistical units, and Utility and Government Services. The specifications of the second phase have been completed in 2013.

The theme *Buildings* plays a crucial role for a large number of relevant spatial applications from many fields such as simulation of noise, of water flood or of air circulation, for the computation of population for statistical units, for communication and construction purposes, risk assessment and management, to mention only a few applications. Hence, the model for buildings is one important part of the INSPIRE specifications. The model has been developed since 2010 by the *Thematic Working Group on Buildings (TWG BU)*, in which 15 experts from cadastral, mapping and other agencies as well as from universities cooperate.[3] In a first step of the modeling process, the group analyzed various use cases for buildings in the European Union and collected the corresponding requirements for the model. Afterwards, existing models for buildings—either national models such as the German cadastral model (AAA) (AdV 2009) or international standards such as CityGML (Gröger et al. 2012; Gröger and Plümer 2012), Industry Foundation Classes (IFC) (buildingSMART 2007), Land Administration Domain Model (LADM) (ISO TC 211 2012), ISO 6707 (Building and Civil Engineering) (ISO/TC 59/SC 2 2004) and DGIWG Feature Data Dictionary (DFDD) (DGIWG 2010) were analyzed in order to check whether the models or particular concepts are suitable for the INSPIRE building model.

The INSPIRE building model consists of a normative part (profiles *Core 2D* and *Core 3D*) which are included in the Implementing Rules and will be legally

---

[2] INSPIRE was initiated by the Directive 2007/2/EC of the European Parliament and of the Council of 14 March 2007.

[3] The first author of this chapter is member of the TWG BU.

binding for the member states. The extended profiles (*Extended 2D* and *Extended 3D*) are in contrast optional. It should be noted that INSPIRE covers only spatial data which is already available in the member states or which can be derived from existing data at reasonable costs. The gathering of new data is not required by INSPIRE.

This chapter provides a detailed description of the normative part of the building model (profiles *Core 2D* and *Core 3D*) and of the intended use cases of the model. Furthermore, an overview on the extended profiles is given. Current version of the building model is v. 3, release candidate 3, see INSPIRE TWG BU (2013).

The rest of this chapter is organized as follows: In Sect. 2, the results of the analysis of use cases for buildings are presented, as well as the resulting requirements for the building model. Section 3 is devoted to the description of the building model. The normative profiles are presented in Sects. 3.1–3.3 and the non-normative, extended profiles in Sect. 3.4. The chapter ends with concluding remarks, an outlook on the further development of SDIs in Europe and a discussion of the relation to the international standard CityGML for 3D city models.

2 Use Cases

A detailed and widespread analysis of use cases of building data in the member states of the European Union was conducted by the TWG BU. Aim of the analysis was to explore what building data is used for the use cases and what the requirements for the building model with regard to geometry and attributes are. The results of the use case analysis are as follows (for a detailed description of the use cases see INSPIRE TWG BU 2013):

- **Modeling of buildings as physical phenomena**, which influences air circulation, air pollution, wind, water flood, noise, etc. Building data is used as input for corresponding simulation and propagation models. Mostly, a 3D model of buildings is required, the shape of the roof, information about architecture, and the material of the roof and of the façade.
- **Computation of population for statistical units**, to estimate the number of inhabitants of a building. Required are the footprint area of a building, the current usage (residential, office, etc.), the number of floors or alternatively, the height of the building to estimate this number.
- **Large scale 2D mapping for city maps (tourism, business, …) and medium scale mapping for topographic and land use/cover maps.** The 2D geometry of buildings (often in addition the geometry of building parts), the building nature, and the name of the building are required. Constructions which are not considered as buildings are important for this use case as well.
- **3D models for communication and construction purposes**. For this use case, the three-dimensional geometry of the building has to be provided, as well as the

positions of walls, roofs surfaces, and openings. In addition, the material of the roof, of the façade and of the building's structure and textures for walls and roofs are required.

- **Safety: Buildings as obstacles for air navigation and as landmarks to support marine navigation**. The geometry and height/elevation of buildings and other constructions (chimneys, antennas, wind turbines, …) and their qualification as landmark are needed for this use case.
- **Risk assessment/management: Assessment of risks in order to take protection and rescue measures**. Risks may be caused by floods, earthquake, landslides, and fire. Required is information on the current usage of buildings, in particular the service type (schools, hospitals, rescue services, …) or the qualification as residential building. Furthermore, the material of the structure and of the façade, the number of floors, the description of floors, openings, and the height above ground are needed. The dates of construction and of last renovation help to assess the vulnerability of the building, and the external reference to corresponding representations of the building/construction in other data sets is useful to obtain further information on the building/construction. For risk management, constructions such as tunnels and bridges, open air pools, buildings with flat roofs (helicopter landing), addresses, the 3D representation of openings, internal and external installations (stairs, lifts), rooms and building units are needed in addition.
- **Urban Expansion/Urban Atlas:** For this use case, the classification of buildings or constructions as industrial site, sewage plant, farming industries, public service (school, university, church, …), dam, bunker, acoustic fence, leisure facility is needed.
- **Urban monitoring (demography, energy, water, …) and urban planning:** For buildings, the detailed 2D geometry, the height above ground, the material of roof/façade, the official area are required.
- **Environment (noise, soil, air quality, energy/sustainability, …):** For noise simulation, the 2D geometry, the height above ground (alternatively the coarse 3D geometry), the roof type, the material of roof/facade, the service type (school, hospital, …), and the number of dwellings are required. For estimating the energy performance of buildings[4], the 2D geometry, the official area, the usage, the number of floors, the date of construction and the external reference are needed. The result of the estimation should be represented as attribute of the building (energy performance). In order to promote the reduction of CO_2 emissions, the indoor model of a building (LoD4 in CityGML)—geometrical descriptions of rooms and building units—along with information on the material of the roof and of the façade, the heating source, the heating system, installations such as air conditioning units, solar panels or wind turbines) have to be provided.

---

[4] Energy Performance of Building Directive 2010/31/EU of the European Parliament and of the Council of 19 May 2010.

- **Infrastructure planning (planning the location of a new service,** …**):** For example, for planning a new wind farm, the current use and the 2D geometry of buildings are needed (to exclude, for example, locations in a 500 m buffer around residential buildings), as well as the locations of constructions such as castles, churches or other protected sites which might generate constraints for wind farms.

The result of the use case analysis was the starting point for the design of the building model. In the following section the building model is introduced which was designed to meet these requirements.

3 The INSPIRE Building Model

The scope of the building model is given by the following definition, which is more or less used in all member states: 'A Building is an enclosed construction above and/or underground, used or intended for the shelter of humans, animals or things or for the production of economic goods. A building refers to any structure permanently constructed or erected on its site.' (INSPIRE TWG BU 2013). Civil engineering constructive works which are not enclosed such as self-standing antennas are not considered as buildings, but as *OtherConstructions*. Those objects are covered by the extended profiles (see Sect. 3.4).

Due to the heterogeneous data availability in the EU member states and due to heterogeneous requirements of the use cases for buildings, one single model would not be appropriate. Instead, four profiles are provided:

- *Core 2D* profile: feature types for buildings and building parts, basic attributes such as year of construction, external reference, and usage. The geometrical representation is 2D or 2.5D.
- *Core 3D* profile: same semantics as *Core 2D*, but 3D representation from CityGML (Gröger et al. 2012; Gröger and Plümer 2012) in four Levels-of-Detail (in addition to 2D/2.5D geometry).
- *Extended 2D* profile: based on *Core 2D*, feature types for building units and constructions which are not considered as buildings have been added, as well as a rich set of attributes and relations.
- *Extended 3D* profile: the geometry of *Core 3D* is combined with the semantics of *Extended 2D* and with 3D feature types (CityGML version 2.0) for boundary surfaces, building installations, rooms and textures.

The normative core profiles are based on the data which is widely used, widely available and whose harmonization is required at European level (for reporting on Environmental Directives, for example). The non-normative extended profiles are based on data that is widely required but whose harmonization in the EU is not easily achievable at short term. The relations between the four profiles and the application schemas of the INSPIRE building model are illustrated in Fig. 1.

Fig. 1 Structure of the building model. It consist of six application schemas (*grey boxes*) which define four profiles (depicted *black*). An *arrow* denotes a dependency between application schemas: the schema on the *backside* of the *arrow* uses and extends the schema the *arrow* points to (INSPIRE TWG BU 2013)
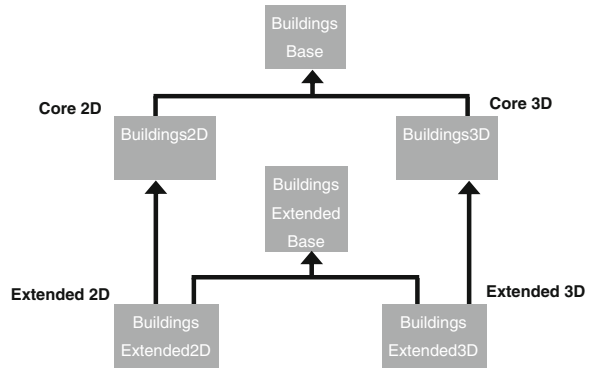
3.1 The BuildingsBase Schema

The *BuildingsBase* schema collects all types, attributes and relations which are common to all profiles. It defines two feature types: *Building* and *BuildingPart*. The scope of *Building* has already been defined in the preceding paragraph. A Building can be partitioned in different *BuildingParts*. This concept has been taken from CityGML and accommodates the fact that components of a building may differ with regard to geometry (different heights, for example) or thematic properties (different years of construction, different usages, …). However, a *BuildingPart* potentially might be considered itself as a building. In particular, it must rest on the ground. This excludes dormers or towers on *Buildings* from being *BuildingParts*. The UML diagram for the *BuildingsBase* application schema is given in Fig. 2 and the (complex) data types used in the schema are provided in Fig. 3.

Buildings and BuildingParts potentially have the same spatial and non-spatial attributes. The attribute values of a part apply only to that part, whereas attribute values of a building refer to all parts. Care should be taken that no contradictions are introduced (for details, see Stadler and Kolbe 2007). If parts are present, the building geometry should be represented for the parts only. The attributes of *Building* and *BuildingPart* are provided by two super classes *AbstractBuilding* and *AbstractConstruction* (the differentiation into two classes is due to the usage in the extended profiles, where constructions inherit from *AbstractConstruction* only). The *inspire id* (the type of this attribute is complex, see INSPIRE Drafting Team Data Specifications 2010) is the unique object identifier published by the responsible body, which may be used by external applications to reference the spatial object. Date and time a spatial object was inserted or changed in the data set, and date and time is was removed are defined by the attributes *beginLifespanVersion* and *endLifespanVersion*: Both attributes are common for all INSPIRE objects (for details see INSPIRE Drafting Team Data Specifications 2010). The *conditionOfConstruction* of a building can take one of the values 'declined', 'demolished', 'functional', 'projected', 'ruin', or 'under construction'. The dates
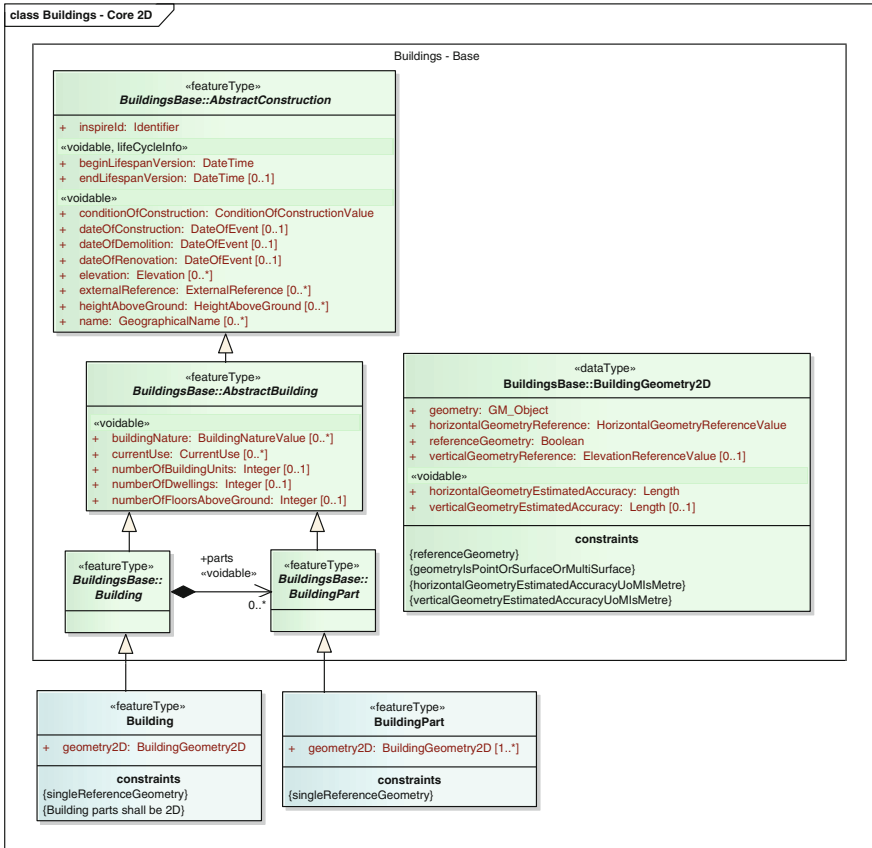
Fig. 2 UML diagram of the *Core 2D* profile. This profile mainly consists of the *BuildingsBase* package (classes enclosed by the *box*). The stereotype ≪voidable≫ for attributes and associations means that a reason for a missing value must (multiplicity at least 1) or can (multiplicity at least 0) be given. For specifying the reason, the following options are provided: 'Unpopulated' (value not part of the dataset maintained by the data provider), 'Unknown' (value is not known to data provider or not computable by the data provider), and 'Withheld' (value is confidential), see INSPIRE Drafting Team Data Specifications (2010)

of construction, of demolition and of renovation can be provided in addition. The *elevation* of a building is defined as the (absolute) z-coordinate of a specific point of the building. The height level of this point is defined by a value of an enumeration data type *ElevationReferenceValue* (see Fig. 3). Some values are *topOfConstruction*, *lowestGroundPoint*, *bottomOfConstruction*, see Fig. 4 for an illustration of all values.

In contrast to the absolute elevation, the *heightAboveGround* denotes the relative height of a building. This concept is often used in 2D and 3D data models (CityGML, for example), but mostly this relative height is not defined precisely
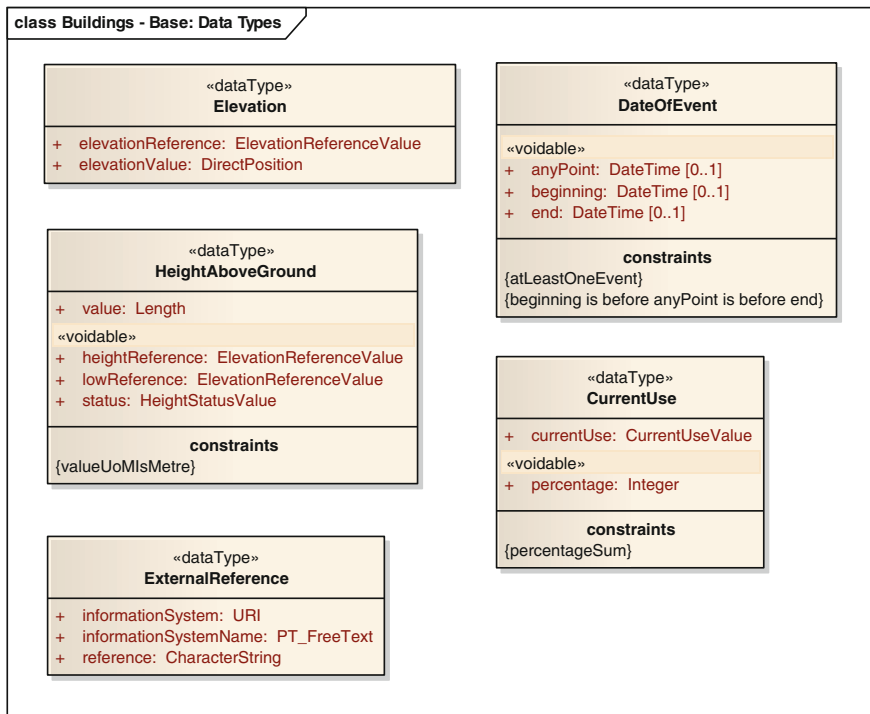
Fig. 3 UML diagram of the data types used in the building base package

and sufficiently: Is the relative height the difference between the topmost point of a building and the lowest point where the building touches the terrain? Or is it the difference between the topmost point and the bottom of construction, including cellars? The INSPIRE building model defines this concept very precisely, by providing the height reference as well as the low reference the relative height refers to. The values of both attributes again are defined by the data type *ElevationReferenceValue* (see Fig. 4).

The *externalReference* can be used to obtain further information on the building from external data stores by storing the id of the building in the data store. This concept has been borrowed from CityGML.

For representing the name of a building, the complex data type *Geographial Names* defined in INSPIRE Annex I (INSPIRE TWG GN 2010) is used.

If a building is a landmark or is significant from a topographical point of view, this is denoted by the attribute *buildingNature*. The usage of the building is represented by the *currentUse* attribute. The values are listed in a 'hierarchical code list' (in such a list, also values on a higher level can be provided):

Fig. 4 Illustrations for the values of type *ElevationReferenceValue* (INSPIRE TWG BU 2013)
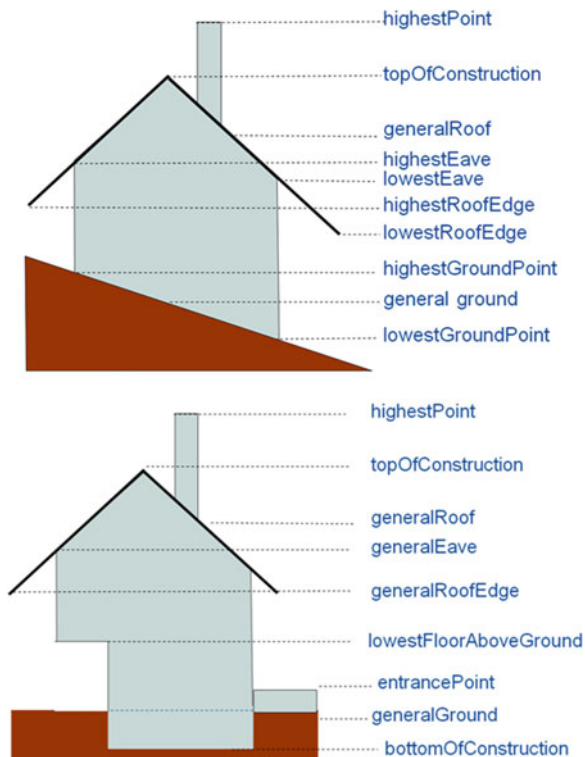
1. residential

    1.1 individualResidence
    1.2 collectiveResidence

        1.2.1 twoDwellings
        1.2.2 moreThanTwoDwellings

    1.3 residenceFor Communities

2. agriculture
3. industrial
4. commerceAndServices

    4.1 office
    4.2 trade
    4.3 publicServices

5. ancillary

The resolution of the values (besides 'residential') is very coarse. The intention is that more detailed values are provided by the specifications in other INSPIRE themes such as *Agricultural/Aquaculture Facilities* (INSPIRE TWG AF 2013) (for
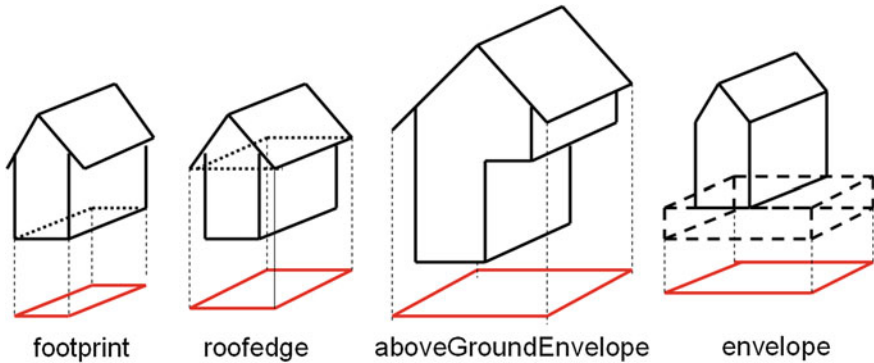
Fig. 5 Illustrations for values of *HorizontalGeometryReferenceValue* (height level where 2D geometry is measured) (INSPIRE TWG BU 2013)

value 'agriculture'), *Production/Industrial Facilities* (INSPIRE TWG PF 2013) (for value 'industrial'), and *Utility and Government Services* (INSPIRE TWG US 2013) (for value 'commerceAndServices'). Since there is no theme for residential buildings in INSPIRE, only this part of the list is relatively detailed. A building can be characterized by multiple usage values; the percentage of a value can be represented explicitly (c.f. Fig. 3).

In addition, the numbers of dwellings, of *BuildingUnits* (see Sect. 3.4) and of floors above ground can be represented. The data type *BuildingGeometry2D* will be described in the next section.

3.2 The Core 2D Profile

The *Core 2D* profile adds a geometrical description to *Building* and *BuildingPart* (see Fig. 2). The geometry is represented by the data type *BuildingGeometry2D*. Note that the multiplicity of the geometry in a *Building/BuildingPart* is 0..*. Hence, a *Building/BuildingPart* may be represented by multiple geometries simultaneously.

Each of the geometries may be 2D or 2.5D. In 2D, a *Building/BuildingPart* may be represented either by a point or by a polygon (optionally with holes, to accommodate for atrium buildings, for example). For the representation of geometry, the standard ISO 19125 'Simple Features' version 1.1 (ISO TC 211 2004) is used.

A crucial point in 2D representations of objects which are 3D in reality is the vertical reference where the 2D geometry is measured. This reference is explicitly stored in an attribute of type *HorizontalGeometryReference*. Values are 'above ground envelope', 'combined', 'entrance point', 'envelope', 'footprint', 'lower
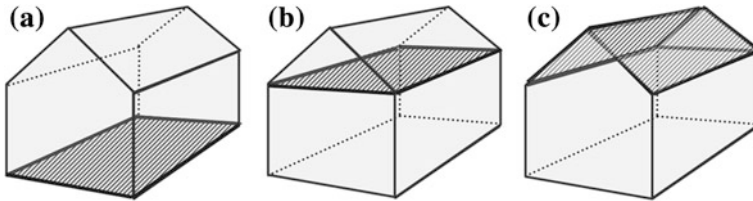
Fig. 6 Examples for 2.5D representations (*hatched*) of buildings and the corresponding *ElevationReferenceValues*. **a** general ground, **b** general eave, **c** general roof

floor above ground', 'point inside building', 'point inside cadastral parcel', and 'roof edge'. Figure 5 illustrates the most important values by giving examples.

The 2.5D representation is defined as usual: for each x/y-coordinate, there is at most one z-value. Hence, vertical walls and overhangs are excluded. Examples for 2.5D representations are given in Fig. 6: the roof can be represented at eaves level by a horizontal polygon, or the roof polygon (one polygon in case of a shed roof (a), two in case of a gabled roof) can be represented by its actual coordinates (a). Information on the height level the geometry refers to is given again by the values of the type *ElevationReferenceValue*, see Fig. 4. In analogy to the 2D case, the *HorizontalGeometryReferenceValue* can be represented. In addition, metadata on the accuracy of the (horizontal and vertical) geometries can be stored. The 2.5D geometry is represented by the OGC standard 'Simple Features' version 1.2 (Herring 2006), since the 'Simple Features' ISO standard (version 1.1) (ISO TC 211 2004) is restricted to 2D.

3.3 The Core 3D Profile

One crucial outcome of the analysis of use cases for buildings was that three-dimensional representations are required. Corresponding applications are noise simulation and mapping, identifications of obstacles for air traffic, to mention only a few examples. Hence, a mandatory 3D profile *Core 3D* is provided by the INSPIRE building model. This model extends the *Core 2D* profile by adding three-dimensional geometrical representations (see Fig. 7 for the UML diagram of the *Core 3D* profile). The well-known *Boundary Representation* (Foley et al. 1995) which represents a solid by its bounding surfaces is employed. Buildings can be provided in different *Levels-of-Detail* (LoD), which correspond to specific data collection methods as well as to a specific group of applications. The LoD and the geometry concepts from CityGML are used, see Fig. 8 for illustrations of LoD1 to LoD4. The geometrical representation as well as the semantic resolution becomes more detailed with increasing LoD. Note that a building can be represented in more than one LoD simultaneously; an application can choose the level which is most appropriate.
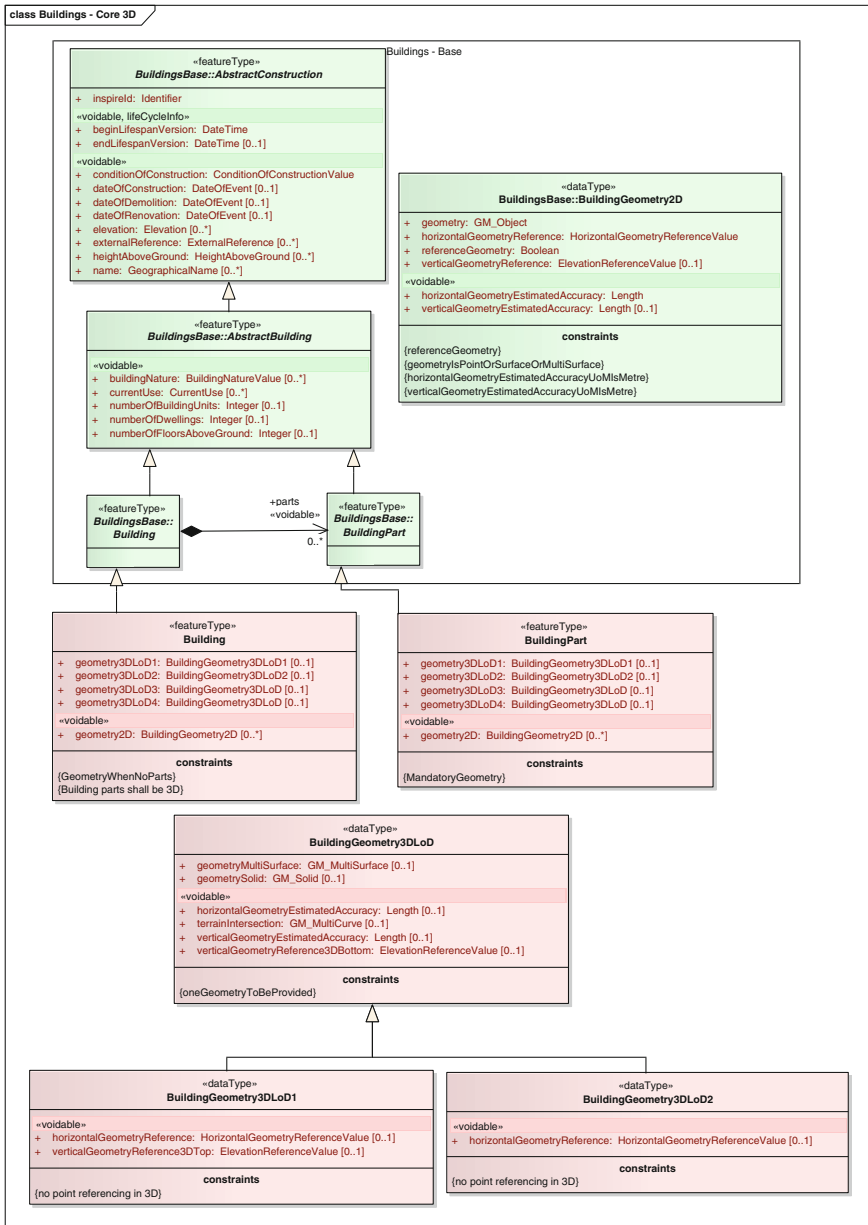
Fig. 7 UML diagram of the *Core 3D* profile

The different LoDs are represented by different (complex) attributes *geometry3DLoD1*, … *geometry3DLoD4* with types *BuildingGeometryLoD1*, *Building-GeometryLoD2* and *BuildingGeometryLoD* (for LoD3 and 4). Each geometry
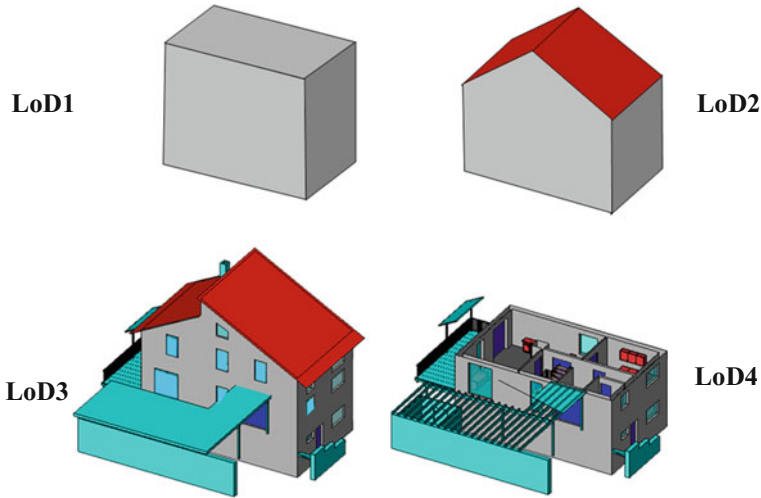
Fig. 8 Four Levels-of-Detail (LoD) provided by CityGML (*images* KIT Karlsruhe, K.-H. Häfele or Gröger and Plümer 2012). In CityGML, there is also a LoD0. Since LoD0 is more or less equivalent to the 2/2.5D INSPIRE geometry (LoD0 is restricted to horizontal surfaces, whereas INSPIRE 2.5D allows for non-vertical surfaces), it is omitted in the figure
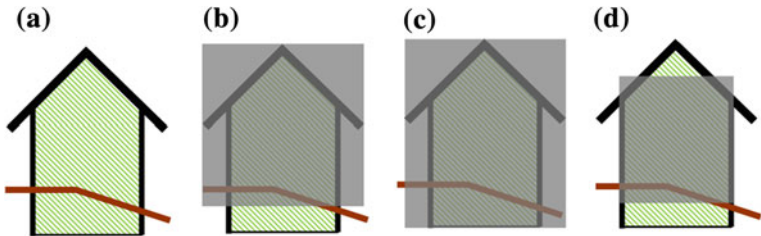
Fig. 9 Enrichment of a *box* representation (LoD1, *grey*) of a gabled roof building (*hatched*)— the terrain profile is depicted *brown*, **a** by adding information on the low/high and the horizontal reference. **b** *Top* topOfConstruction, *low* lowestGroundPoint, *horizontal* roofEdge. **c** *top* topOfConstruction, *low* bottomOfConstruction, *horizontal* roofEdge. **d** *top* generalRoof, *low* lowestGroundPoint, *horizontal* footprint

provides a (topologically clean) solid representation and a multi surface representation (which might not be topologically clean, e.g. the ground surface may be missing). See for the UML diagram of the *Core 3D* profile.

The generalized representation in LoD1 by prismatic block models with vertical walls and horizontal 'roofs' is enhanced by metadata which denote the reference for the lower and for the upper side of the block. The values of type *ElevationReferenceValue* are used (see Sect. 3.1, in particular Fig. 4). For LoD2 to LoD4 only the lower reference is needed, since the (generalized) actual roof shape is represented geometrically. In LoD1 and LoD2, the horizontal extension of the building's shape is represented in a generalized way. To enrich the expressiveness

of this representation, the horizontal reference is represented explicitly by the attribute *horizontalGeometryReference* of type *HorizontalGeometryReference* (see Sect. 3.2, in particular Fig. 5). Some combinations of values for lower and upper vertical geometry reference and horizontal geometry reference for a LoD1 representation are illustrated in Fig. 9.

3.4 The Extended Profiles

Two extended profiles (*Extended 2D* and *Extended 3D*) are specified in addition to the two base profiles, in order to accommodate for applications requiring a richer set of attributes and more 3D feature types for components of buildings. Both are not mandatory and hence, data has not to be provided by the member states.

The *Extended 2D* profile adds new feature types and attributes and relations to *Building* and *BuildingPart*. A new feature type is *BuildingUnit* for decomposing a *Building* (or *BuildingPart*) further into units which may be defined legally, for example with regard to ownership. Civil engineering constructive works which are not enclosed such as self-standing antennas are represented by the feature type *OtherConstruction*.

Building and *BuildingPart* are enriched by further attributes giving more detailed information on the topography (*heightBelowGround*, *numberOfFloors-BelowGround*, *floorDistribution*, *floorDescription*, *roofType*), on materials of the façade, of the roof, and of the structure, and energy-related attributes (connection to electricity, to gas, to sewage, to water, energy performance, heating source, heating system).

Official information such as the official area, the official value as well as the address and the reference to the cadastral parcel of the building are represented in addition.

The *Extended 3D* profile enriches the *Extended 2D* profile. It is very similar to the building module of CityGML: boundary surfaces (*Wall-*, *Roof-*, *Ground-*, *Closure-*, *OuterCeiling-*, and *OuterFloorSurfaces*) are represented semantically as well as geometrically. Openings (doors and windows) also are also represented as features. Furthermore, installations (dormers, balconies, …) and rooms are provided. The *Extended 3D* profile also offers textures, which are defined as simplified version of CityGML textures. See Gröger et al. (2012) and Gröger and Plümer (2012) for more details on CityGML.

4 Conclusions and Outlook

The INSPIRE initiative of the EU will significantly accelerate the process of providing spatial data via Geo Web Services in the next years. Currently, the only type of Geo Web Services which is commonly available is the Web Map Service

(La Beaujardiere 2006). Operable Web Feature Services are extremely rarely found in practice. This presumable will drastically change in future. Even if INSPIRE is restricted to the European Union, this development hopefully will function as a role model also for other regions.

The focus of this chapter was set on the INSPIRE building model. It is the result of a detailed and extensive analysis of all use cases for buildings. Four profiles of the building model accommodate for the heterogeneous uses cases and the heterogeneous data availability in the member states of the EU. The INSPIRE building model has largely been influenced by the building model of CityGML: modeling patterns such as the *Building—BuildingPart* hierarchy and many attributes such as the *YearOfConstruction* and the *RoofType* have been borrowed from CityGML. The geometry representation of the *Core 3D* profile has completely been adopted from CityGML, as well as the geometry and 3D feature types such as *BoundarySurfaces* (*WallSurfaces*, *RoofSurfaces*, …), *BuildingInstallations* and *Rooms* of the extended 3D profile.

In the groups which develop CityGML, particularly in the 'Special Interest Group (SIG) 3D'[5] of the initiative 'Spatial Infrastructure Germany' (GDI-DE) and in the OGC CityGML Standards Working Group, currently there is a discussion to adapt INSPIRE concepts back to CityGML. Examples are the feature types *OtherConstruction* and *BuildingUnit* as well as metadata which enrich the coarse LoD1 and LoD2 representations (low and high *ElevationReferenceValues*, *HorizonalGeometryReferenceValues*, accuracies). In addition to the move from GML 3.1 to GML 3.2, these extensions of CityGML will contribute significantly to the harmonization between CityGML and INSPIRE.

Although the INSPIRE and the CityGML building models are similar, their standard encodings are different: The INSPIRE encoding is derived automatically by rules from the UML diagrams and maps to GML 3.2 (Portele 2007), whereas the GML 3.1 schemas (Cox et al. 2003) of CityGML have been derived manually. Due to the different encodings, CityGML tools and software can not immediately be used for INSPIRE buildings data. However, there are a lot of tools with CityGML support: tools for storing CityGML data such as the open source database *3DCityDB*, *Bentley Map 3D*, ESRI *ArcGIS*, to mention only a few. Conversion tools such as the *FME* (Feature Manipulating Engine) have CityGML interfaces, and Web Feature Services such as *XtraServer/WFS* from Interactive Instruments, Snowflake *GoPublisher*, or *deegree 3* from lat/lon provide CityGML data. In order to enable the usage of these tools for INSPIRE building data and to facilitate the harmonization between CityGML and INSPIRE, an alternative encoding for this model based on CityGML was developed (Gröger et al. 2013). It uses the CityGML concept of *Application Domain Extensions* (ADE), which adds the INSPIRE-specific attributes and relations to CityGML buildings and building parts. These ADEs for the *Core 3D* and *Extended 3D* profiles currently are developed by the Chair of Geoinformation at the Institute for Geodesy and

---

[5] See www.sig3d.org

Geoinformation at Bonn University and the Chair of Geoinformatics at Technische Universität München in cooperation with the TWG Buildings. These ADEs will be the topic of a subsequent publication.

References

AdV (ed) (2009) Documentation on the modelling of geoinformation of official surveying and mapping, version 6.0.1. Working committee of the surveying authorities of the states of the Federal Republic of Germany (AdV). http://www.adv-online.de/icc/extdeu/broker.jsp?uMen= 4b370024-769d-8801-e1f3-351ec0023010. Accessed 30 Jun 2013

buildingSMART (ed) (2007) Industry foundation classes IFC2x3 TC1 release. http:// buildingsmart-tech.org/specifications/ifc-releases/ifc2x3-tc1-release/summary

Cox S, Lake R, Portele C, Whiteside A (eds) (2003) Geography markup language GML 3.1. OGC Doc. No. 03-105r1

DGIWG (ed) (2010) DGIWG-500 implementation guide to the DGIWG feature data dictionary (DFDD). https://portal.dgiwg.org/files/?artifact_id=7148&format=pdf

Foley JD, van Dam A, Feiner SK, Hughes JF (1995) Computer graphics: principles and practice. Addison-Wesley systems programming series, 2nd edn. Addison-Wesley, Boston

Gröger G, Plümer L (2012) CityGML-interoperable semantic 3D city models. ISPRS J Photogramm Remote Sens 71:12–33

Gröger G, Kolbe TH, Nagel C, Häfele K (eds) (2012) OGC city geography markup language (CityGML) encoding standard, version 2.0.0. Open geospatial consortium. OGC Doc. No. 12-019. https://portal.opengeospatial.org/files/?artifact_id=47842. Accessed 20 Aug 2013

Gröger G, Kutzner T, Kolbe TH (2013) A CityGML based encoding for the INSPIRE data specification on buildings (Abstract). In: INSPIRE conference 2013. Florence, Italy, June 2013

Herring JR (2006) OpenGIS® implementation specification for geographic information-simple feature access-part 1: common architecture. Open geospatial consortium, version: 1.2.0, OGC Doc. No. 06-103r3

INSPIRE drafting team data specifications (ed) (2010) Generic conceptual model, version 3.3, identifier D2.5_v3.3. http://inspire.jrc.ec.europa.eu/documents/Data_Specifications/D2.5_v3_3.pdf. Accessed 30 Jun 2013

INSPIRE TWG GN (ed) (2010) INSPIRE data specification on geographical names-guidelines v 3.0.1. INSPIRE thematic working group geographical names. http://inspire.jrc.ec.europa.eu/documents/Data_Specifications/INSPIRE_DataSpecification_GN_v3.0.1.pdf. Accessed 10 Aug 2013

INSPIRE TWG BU (ed) (2013) INSPIRE data specification on buildings version 3, release candidate 3–draft technical guidelines, identifier D2.8.III.2_v3.0rc3, INSPIRE thematic working group buildings. http://inspire.jrc.ec.europa.eu/documents/Data_Specifications/INSPIRE_DataSpecification_BU_v3.0rc3.pdf. Accessed 30 Jun 2013

INSPIRE TWG PF (ed) (2013) Data specification on production and industrial facilities-draft guidelines, version 3 release candidate 3, identifier: D2.8.III.8_v3.0rc3, INSPIRE thematic working group production and industrial facilities. http://inspire.jrc.ec.europa.eu/documents/Data_Specifications/INSPIRE_DataSpecification_PF_v3.0rc3.pdf. Accessed 30 Jun 2013

INSPIRE TWG US (ed) (2013) Data specification on utility and governmental services–draft technical guidelines, version 3 release candidate 3, Identifier: D2.8.III.6_v3.0rc3, INSPIRE thematic working group utility and governmental services. http://inspire.jrc.ec.europa.eu/documents/Data_Specifications/INSPIRE_DataSpecification_US_v3.0rc3.pdf. Accessed 30 Jun 2013

INSPIRE TWG AF (ed) (2013) INSPIRE data specification for the spatial data theme agricultural and aquaculture facilities, identifier D2.8.III.9_v3.0rc3, INSPIRE thematic working group agricultural and aquaculture facilities. http://inspire.jrc.ec.europa.eu/documents/Data_Specifications/INSPIRE_DataSpecification_AF_v3.0rc3.pdf. Accessed 30 Jun 2013

ISO TC 211 (ed) (2004) 19125-1 geographic information-simple feature access-part 1: common architecture. Version 1.1

ISO TC 211 (ed) (2012) ISO 19152:2012 geographic information-land administration domain model (LADM)

ISO/TC 59/SC 2 (ed) (2004) ISO 6707-1:2004 building and civil engineering-vocabulary-part 1: general terms

La Beaujardiere JD (ed) (2006) OpenGIS web map server implementation specification, version 1.3.0. Open geospatial consortium, Doc. No. 06-042. http://www.opengeospatial.org/standards/wms. Accessed 10 Feb 2008

Portele C (ed) (2007) OpenGIS geography markup language (GML) encoding standard, version 3.2.1. Open geospatial consortium, OGC Doc. No. 07-036. http://portal.opengeospatial.org/files/?artifact_id=20509. Accessed 20 Aug 2013

Stadler A, Kolbe TH (2007) Spatio-semantic coherence in the integration of 3d city models. In: 5th international ISPRS symposium on spatial data quality. ITC, Enschede, 13–15 June 2007

Vretanos PA (ed) (2010) OpenGIS web feature service 2.0 interface standard (ISO/DIS 942). OpenGIS[®] implementation standard. OGC 09-025r1. http://portal.opengeospatial.org/files/?artifact_id=39967. Accessed 20 Aug 2013

Reverse RTK Data Streaming for Low-Cost Landslide Monitoring

Etim E. Eyo, Tajul A. Musa, Khairulnizam M. Idris and Yusuf D. Opaluwa

Abstract This chapter describes the preliminary study of real-time data streaming in support of the proposed low-cost landslide monitoring system using the Reverse Real-Time Kinematic (RRTK) technique. The RRTK algorithm was implemented by streaming raw Global Positioning System (GPS) data of both the reference and roving station(s) to the control centre for processing, and transmission of the position solution to the roving station. The main purpose of the data streaming was to investigate the quality of the measurements, for utilization in landslide modelling and analysis in near real-time. A novel methodology using a high pass filtering technique was implemented, to detect outliers in the observations. Also, the autocorrelation of GPS time series was investigated.

Keywords Data streaming · Landslide · Monitoring · Low-cost · GPS · High pass filter · Autocorrelation

1 Introduction

Landslide is defined as "the movement of a mass of rock, debris, or earth down a slope" (Cruden 1991). Globally, there is an upsurge in landslide occurrence, which could be attributed to the increasing human activities on the environment (Glade 2003; Sidle et al. 2004) and the impact of climate change (Geertsema et al. 2006). The consequences of landslides are enormous. Recent landslide disasters in Brazil, Philippines, China, Indonesia, Pakistan, etc. have destroyed infrastructure, killed thousands of people, and resulted in heavy economic losses (USGS 2013). The

E. E. Eyo (✉) · T. A. Musa · K. M. Idris · Y. D. Opaluwa
Department of Geomatic Engineering, Faculty of Geoinformation and Real Estate,
Universiti Teknologi Malaysia, Johor Bahru, Malaysia
e-mail: etim_eyo@yahoo.com

continuous occurrence of disastrous landslide events has increased the demand for new and improved techniques for landslide monitoring and analysis.

The Global Navigation Satellite Systems (GNSS), namely—GPS, GLONASS, Galileo, Compass, QZSS and IRNSS are now being utilized as global infrastructure for a wide range of applications. The Global Positioning System (GPS), in particular, has been widely used in monitoring the dynamics of landslide. GPS has been employed in landslide monitoring based on the type of monitoring campaigns, namely, periodic (Rawat et al. 2011; Wang 2012; Yalçinkaya and Bayrak 2002) and continuous (Wang and Soler 2012; Xiao et al. 2012). These studies highlight the critical factors in the choice of a particular monitoring campaign, which include accuracy, cost, and safety of equipment. Some studies in landslide monitoring have used GPS to compare results from conventional surveying or geotechnical methods, such as theodolite, Electronic Distance Measurement, levels, total station, inclinometers, and wire extensometers (Bertachini et al. 2009; Calcaterra et al. 2012; Coe et al. 2003; Gili et al. 2000; Malet et al. 2002; Moss 2000; Rizzo 2002; Tagliavini et al. 2007).

Other studies have integrated GPS and other surveying techniques, namely, terrestrial laser scanning, SAR interferometry, and photogrammetry, to investigate the landslide phenomenon (Mora et al. 2003; Peyret et al. 2008; Rott and Nagler 2006; Wang et al. 2011). This combination provides valuable information on the magnitude and direction of the displacements, total volume of the moving mass, and the evolution of the landslide process. Some studies have investigated the accuracy of low-cost single-frequency GPS receivers for landslide monitoring (Janssen and Rizos 2003; Squarzoni et al. 2005). Finally, GPS has been employed in landslide monitoring based on different GPS techniques, namely, static (Brunner et al. 2007), rapid-static (Hastaoglu and Sanli 2011), real-time kinematic, RTK (Wang 2011), and based on the comparisons of these techniques (Othman et al. 2011a, b).

The main goal of our ongoing research is to design a low-cost monitoring system for landslide investigation using the RRTK technique. Some of the advantages of RTK GPS which can be utilized for landslide monitoring application include (Mekik and Arslanoglu 2009): (1) post-processing is not required, (2) acquired coordinates of points can be easily transformed to local coordinate system in real-time, and (3) it is a reliable tool for monitoring multiple number of points—increasing productivity and saving cost. For a standard RTK-GPS operation, dual-frequency geodetic-grade receivers with the supporting firmware are usually required. However, the high cost of these receivers and the supporting software is one of the reasons limiting the use of RTK GPS for several monitoring applications (Takasu and Yasuda 2009). Due to the harsh operational environment frequently faced during landslide monitoring, coupled with security concern and the prospect of losing the equipment during landslide event, the needs for low-cost monitoring equipment are imperative.

The big challenge, therefore, in GNSS monitoring is how to reduce the cost of the monitoring scheme. The cost of monitoring includes the costs of RTK GPS receivers, power supply, communication, logistics, and personnel. Several authors

have proposed the use of low cost GPS L1-only monitoring receivers (Chen 2001; Roberts 2002). The shortcoming of this approach is the fact that, unlike the dual-frequency data, the single-frequency GNSS receivers' data cannot be corrected for ionospheric delay (Rizos et al. 2010). Research on the development of low-cost RTK GPS deformation monitoring systems for landslide monitoring application are ongoing (e.g. Aguado et al. 2006; Brown et al. 2006; Glabsch et al. 2009; Verhagen et al. 2010; Yu 2011).

In this chapter, a new landslide deformation monitoring concept that uses RRTK principle is being proposed. The unique advantage of the RRTK approach is that low-cost receiver hardware can be deployed for field data streaming since the responsibility of complex computations is shifted from the roving receivers to the control centre.

This chapter is organized as follows. In Sect. 2, the server-based processing technique is discussed. In Sect. 3, an overview of GPS/GNSS Continuously Operating Reference Stations (CORS) is presented. In Sect. 4, the real-time GPS data streaming using Networked Transport of RTCM via Internet Protocol (Ntrip) is described. Section 5 presents the experimental data collection and processing. The results and analyses are presented in Sect. 6. Finally, the summary, outlook and field challenges are presented in Sect. 7.

2 The Server-Based Processing Technique

The conceptual framework of this study is based on the server-based RTK processing concept. According to Feng et al. (2009), the server-based RTK processing concept can be used in various RTK techniques (see Fig. 1)—precise point positioning (PPP), standard single-baseline RTK, network-RTK (NRTK), reverse single-baseline RTK (RRTK), and reverse network RTK (RNRTK).

The last two techniques (RRTK and RNRTK) combine the server-based processing concept and two-way communication for the computation and transmission of the user's accurate position. The reverse technique, which technically alters the one-way communication flow in the conventional RTK technique, involves a two-way communication (see Fig. 2) which requires the field users to transmit their raw observations to a control centre for the computation of the position solution, after which the computed solution along with the quality control indicators are transmitted back to the field users.

The reverse approach based on combining the server-based processing concept and two-way communication has evolved for over 5 years now. But research opportunities offered by this approach is still not adequately exploited. The first practical implementation of RNRTK was made by Nippon GPS Solution in Japan (Kanzaki 2006). Rizos (2007) proposed the development of new business model using the RNRTK approach, with the main goals of placing the control of the products with the service providers and enhancement of commercial value on the service. A new framework for RNRTK using distributed-computing technique was
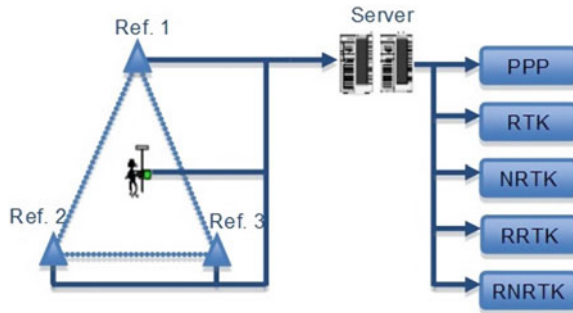
Fig. 1 Server-based RTK concept (Feng et al. 2009)

Fig. 2 Two-way communication channel

proposed by Lim and Rizos (2008). The main goal of the framework was to integrate information and communication technologies, database and web technologies, and GPS CORS network infrastructure, to upgrade the capability of the server to real-time data processing. These augmentations enable the servers to carry out data management and spatial analysis, and at the same time creating a platform for the users to efficiently utilize the results. Zinas et al. (2012) present an enhanced processing strategy by combining a single-baseline and a multiple rover network solution in a centralized (server-based) GNSS architecture. The main goal of this study was to use the shorter inter-receiver baselines to improve the results of single-epoch ambiguity resolution.

Some of the advantages of combining the server-based processing concept and two-way communication in the reverse approach include (Rizos 2007; Zinas et al. 2012):

- Control of the products is vested with the service providers.
- Quality of service is guaranteed.
- Increased value on product, and enhancement of commercial value on the service.
- The user is relieved from the burden of complex computations.
- Low-cost receiver hardware can be deployed for field data streaming.
- Multiple users can be supported simultaneously.

- The streaming of raw observations data from both the reference and roving stations to the control centre implies that all available information can be effectively utilized.

   The main advantages that the server-based processing technique can provide for landslide monitoring application are that the costs and tasks of the monitoring scheme will be drastically reduced, as low-cost receiver hardware will be utilized for real-time streaming of raw GPS measurements and complex algorithms and computations at the user end will be eliminated.

3 Continuously Operating Reference Stations (CORS)

Networks of GNSS are being established in many regions of the world to provide valuable infrastructure for real-time kinematic positioning and applications in areas such as surveying, mapping, navigation and environmental monitoring. The server-based processing technique usually utilizes existing GPS/GNSS CORS infrastructure. The CORS facilities utilized for this study is the ISKANDARnet. The control centre of ISKANDARnet is located in the Faculty of Geoinformation and Real Estate, Universiti Teknologi Malaysia (Shariff et al. 2009). ISKAN-DARnet was developed to provide infrastructure for strategic research in areas such as atmosphere, meteorology, and precise positioning in the Iskandar region of Johor, Southern Malaysia. At the time of writing this chapter, ISKANDARnet consists of four reference stations (ISK1, ISK2, ISK3, and ISK4), while more reference stations are being planned for the future. The distribution of the current ISKANDARnet reference stations is given in Fig. 3.

   The conventional RTK method employs radio links to transmit reference receiver data (or observation corrections) to the rover receiver. The rover unit utilizes this data together with its own raw measurements to resolve the ambiguity of the differenced carrier phase data and to estimate the rover's position. The main problem of the single-base RTK technique is the restriction of the baseline length to 10–20 km, due to distance-related errors (e.g. orbit errors, and atmospheric signal refraction) (Rizos et al. 2010). The network RTK technique, on the other hand, uses a network of CORS to acquire a large amount of data, over a wide geographical scale, for the determination of the position solutions. The NRTK allows the separation between the reference stations at significantly longer baseline lengths, and has been able to address the baseline length restriction of the single-base RTK technique. In this study, the reverse approach is being implemented based on the standard single-base RTK technique (i.e. RRTK).

Fig. 3 Distribution of ISKANDARnet reference stations (as modified in Google Maps)

4 Real-Time GPS Data Streaming Using NTRIP Protocol

Ntrip protocol is used for the real-time GPS data streaming in this study. Ntrip (see Fig. 4) basically consists of the following components (Weber et al. 2006):

(a) *NtripSources* generate continuous raw GPS data streams. Each GPS data sources are recognized by a unique identifier called mount-point.
(b) *NtripServers* transfer raw GPS data stream of an NtripSource to the Ntrip-Caster or control centre.
(c) *NtripCaster* provides security for the service providers and facilitates the accessibility of data to multiple users. The administrator of the NtripCaster organizes all available NtripSources and defines all source identifiers (mountpoints), port number, and user passwords. Source-table containing information on stations and data streams is also managed by NtripCaster. The control centre and NtripCaster used for this study are located at GNSS and Geodynamics Laboratory, Universiti Teknologi Malaysia.
(d) *NtripClient* receives final position solution from the NtripCaster or control centre.

In this study, the Ntrip protocol was utilized to test the RRTK algorithm (see Fig. 5) by streaming raw GPS data from both the reference and roving stations to the control centre for processing, and transmission of the position solution to the
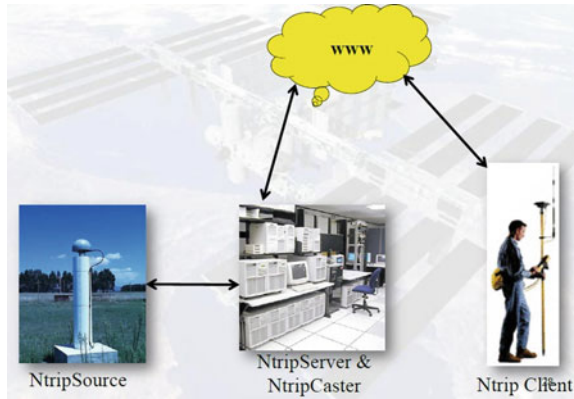
Fig. 4 Ntrip system components
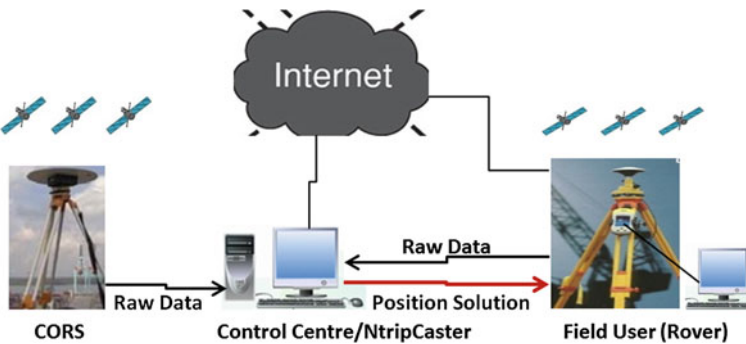
Fig. 5 The architecture of RRTK technique

roving station (user). The transmission of both data and results were performed over the Internet. The real time GPS measurement stream provided a new measurement every second for each GPS data sources. The emphasis of this preliminary study was to investigate the quality of the measurements.

5 Experimental Data Collection and Processing

The proposed landslide deformation monitoring technique using RRTK principle and the server-based processing methodology was tested using data from test sites located at the Universiti Teknologi Malaysia. A 388-s dataset acquired at 1 s interval on March 18, 2013, was processed to test the performance of the developed methodology. The reference station and rover configuration is shown in Fig. 6.
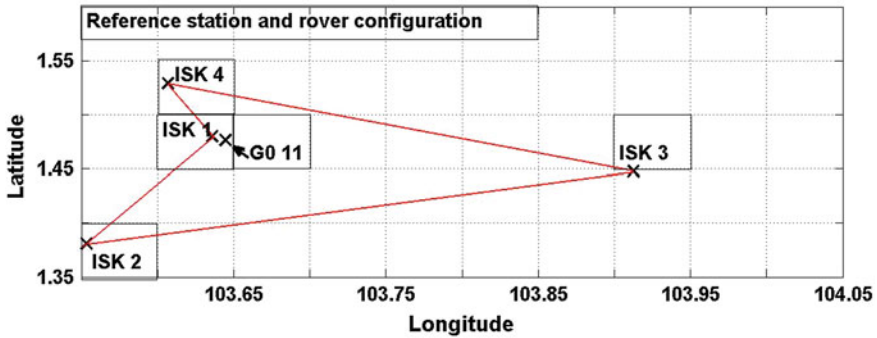
Fig. 6 Test network consisting of four reference stations (ISK1, ISK2, ISK3 and ISK4) and one rover (GO11)

The processing of the real-time GPS data was performed using the modified RTKLIB software package, based on server-based processing methodology. In this approach, the rover station was processed using the single-base RTK technique from the closest reference station. The reference station used for the data streaming at G011 was ISK 3, a distance of about 23 km apart. In the next test campaign, all the reference stations will be utilized in processing the rover position. The results of the baselines solutions are presented in the local cartesian coordinates.

The baseline of about 23 km may have introduced distance-related errors into the observations. Also, the high latency rate caused by fluctuations in Internet service in the streaming of data to the control centre, may have contributed to delay in ambiguity resolution for the determination of the position solution. In order to detect outliers in the observations, a high pass filter was implemented. In this study, a weighted mean value is calculated from the coordinates and sigma according to Eq. (1) (Sundström 2009):

$$X_f = X - \hat{X}, \tag{1}$$

where X_f is the filtered position, X is the observed value and $\hat{X}$ is the weighted mean value obtained from:

$$\hat{X} = \sum_{i=1}^{N} X_i . w_i, \tag{2}$$

where N is the total number of observations for the filter and w is the weight obtained from Eq. (3):

$$w_i = \frac{\frac{1}{\sigma^3}}{\sum_{j=1}^{N} \frac{1}{\sigma^3}}, \tag{3}$$

where σ is sigma (the standard deviation values of Easting, Northing and Height).

The autocorrelation of GPS time series was also investigated. The observation time series is described as $(Y_1, Y_2, Y_3, \ldots, Y_k, \ldots Y_n)$, which are made at equidistant

time intervals Δt. N is the total number of the observations. The mean value of all observations is computed as $\bar{Y}$; then the autocorrelation coefficient (R_h) of the observation series is computed as follows:

$$R_h = {C_h}\big/{C_o}, \tag{4}$$

where C_h is the autocovariance function:

$$C_h = \sum_{t=1}^{N-h} (Y_t - \bar{Y})(Y_{t+h} - \bar{Y})/N, \tag{5}$$

and C_o is the variance function:

$$C_o = \sum_{t=1}^{N} (Y_t - \bar{Y})^2 \big/ N, \tag{6}$$

h is time lag ($h = 1, 2, 3, \ldots$).

The plot of R_h for varying h is called the correlogram for the random process Y_k. The correlogram is used to check for serial dependency in an observed time series.

6 Results and Analysis

The plots of both filtered and unfiltered observations for the first 25 s are given in Figs. 7, 8, 9. It is shown that the implementation of the high pass filter has been able to detect outliers in the observations. The observations of first 5 and 16 s are outliers. The noises were due to the fact that the position solutions of first 5 s were in float solution as the system was still in the initialization stage. The fixed solution commenced from the sixth second observation.

The plot of the standard deviation values for the first 25 s is given in Fig. 10. The standard deviation values for the three components were generally high in observations of first 5 and 16 s; Northing and Easting having the highest values of about 1 m, and height more than 3 m. The standard deviation values for the subsequent observations were about 1 mm for Northing and Easting and about 3 mm for Height.

The plot of the displacement vectors for Northing, Easting and Height components, for the first 25 s is given in Fig. 11. It is shown that the displacements are affected by high standard deviation values. That is, large displacements have high standard deviation values.

The autocorrelation functions of the GPS time series for Northing, Easting, and Height, respectively are shown in Figs. 12, 13, 14.

In the correlogram of Northing (Fig. 12), the autocorrelation functions take the value Ro = 0.003 and decrease exponentially until at time lag 300 s when the autocorrelation of the observations is not so obvious. In the correlogram of Easting

Fig. 7 Filtered and
unfiltered observations for
Northing components
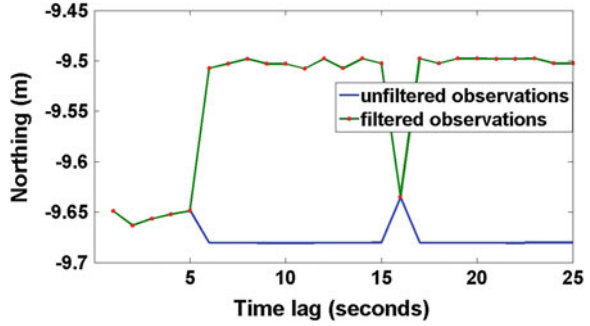
Fig. 8 Filtered and
unfiltered observations for
Easting components
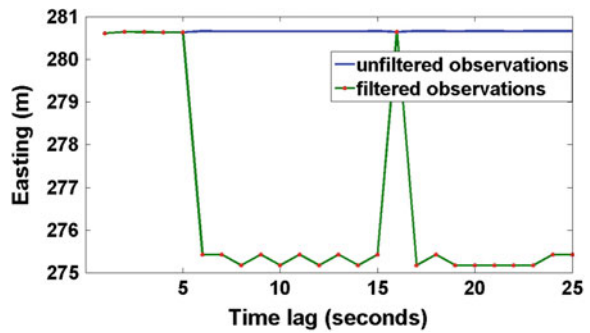
Fig. 9 Filtered and
unfiltered observations for
Height components
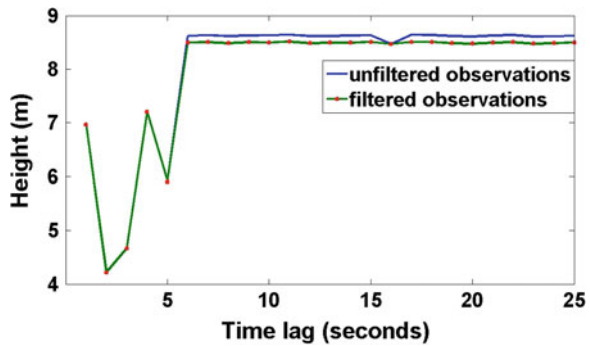
(Fig. 13), the autocorrelation functions take the value Ro = 0.003 and decrease exponentially until at time lag 300 s when the autocorrelation of the observations is not so obvious. In the correlogram of Height (Fig. 14), the autocorrelation functions take the value Ro = 0.003 and decrease exponentially until at time lag 200 s when the autocorrelation of the observations is not so obvious. These deviations show that the GPS measurements contain white and coloured noises. The coloured noises in the GPS measurements follow the exponential distribution. When the time lag is larger, for example 200 s, the autocorrelation of the
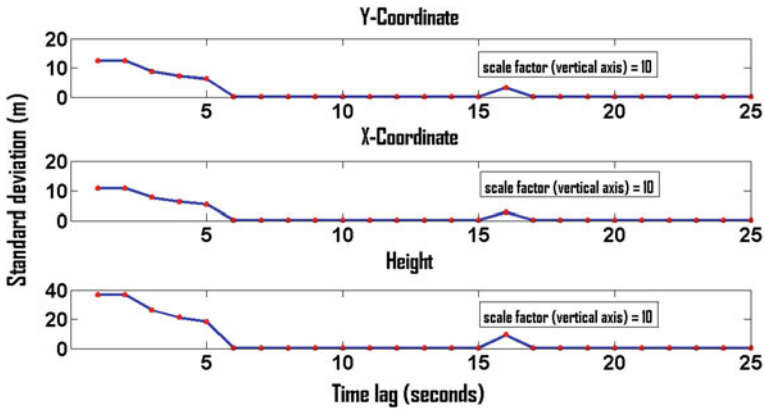
Fig. 10 Standard deviation values for Northing, Easting, and Height components
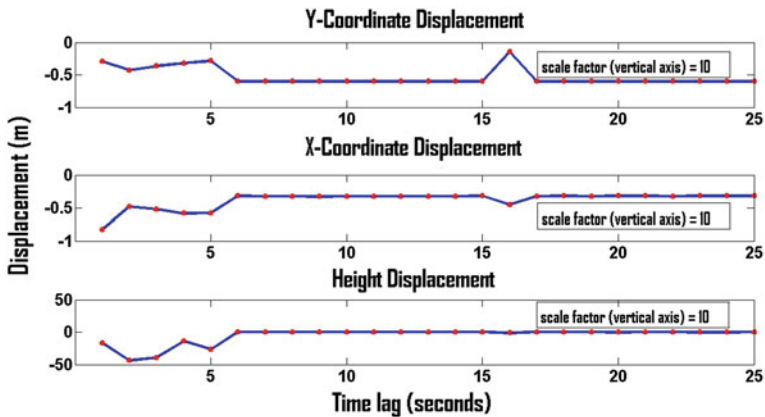
Fig. 11 Displacement vectors for Northing, Easting, and Height components

observations is not so obvious. But when the time lag is smaller, for example 1 s, the autocorrelation coefficient between two observations becomes larger.

7 Summary and Outlook

We have discussed the concept, principles and advantages of a proposed low-cost landslide monitoring system using RRTK technique. In order to implement the RRTK algorithm, a real-time data streaming of raw GPS data of both the reference and roving stations was carried out by utilizing the Ntrip protocol. The main purpose of the data streaming was to investigate the quality of the measurements.
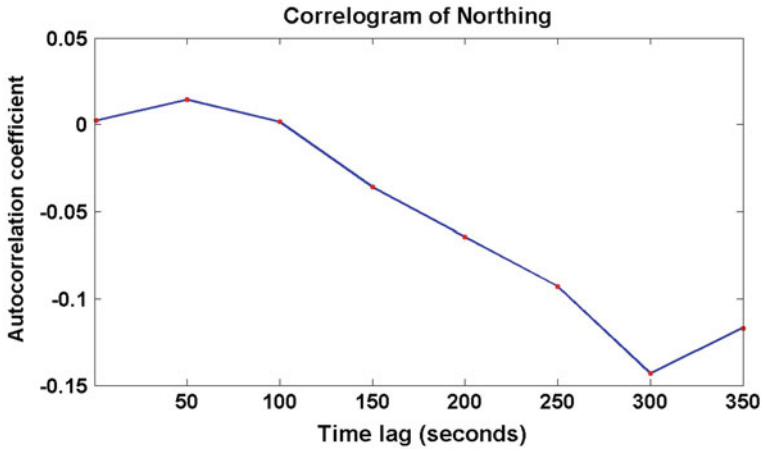
Fig. 12 Correlogram of Northing components for time lag 0–350 s
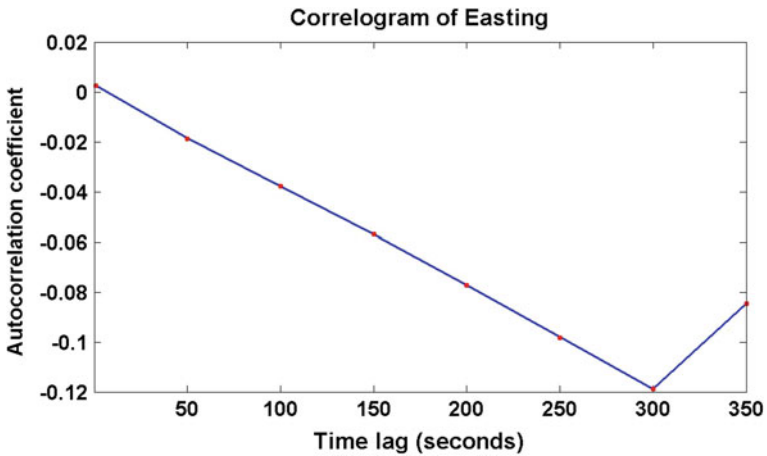
Fig. 13 Correlogram of Easting components for time lag 0–350 s

In order to detect outliers in the measurements, a high pass filter was implemented. Autocorrelation analysis of GPS time series was also performed to validate the presence of white and coloured noises in the GPS measurements.

The main problems encountered during field work include: power supply problems and fluctuation in Internet services. There is a great concern for power supply because a typical landslide site may be located in remote areas where access to the electric network is not readily available. The fluctuation in Internet services was a big concern as this may have contributed to a high latency rate in the streaming of the data.
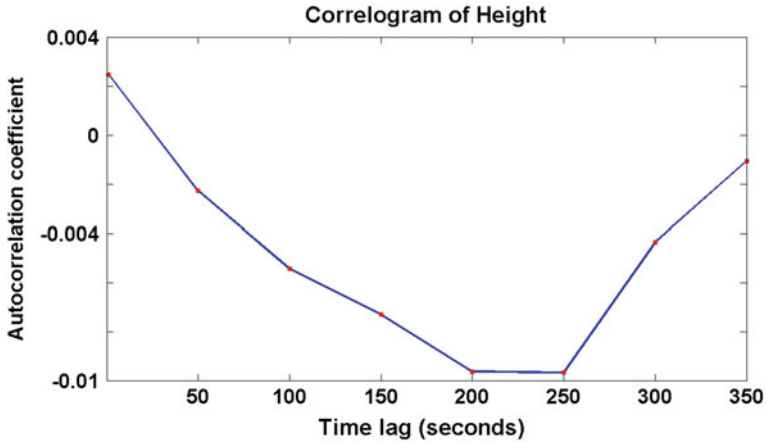
Fig. 14 Correlogram of Height components for time lag 0–350 s

The next phase of the study will involve the implementation of RRTK GPS technique on real-world landslide sites.

References

Aguado LE, O'Driscoll C, Xia P, Nurutdinov K, Hill C, O'Beirne P (2006) A low-cost, low-power Galileo/GPS positioning system for monitoring landslides. In: Proceedings of the 2006 Navitec Oct 2006. http://www.ggphi.eu/monitoring_landslides.pdf

Bertachini E, Capitani A, Capra A, Castagnetti C, Corsini A, Dubbini M, Ronchetti F (2009) Integrated surveying system for landslide monitoring, Valoria landslide (Appennines of Modena, Italy). In: FIG working week 2009, Eilat, Israel

Brown N, Troyer L, Zelzer O, van Cranenbroek J (2006) Advances in RTK and post processed monitoring with single frequency GPS. J Global Position Syst 5(1–2):145–151

Brunner FK, Macheiner K, Woschitz H (2007) Monitoring of deep-seated mass movements. In: Proceedings of the 3rd international conference on structural health monitoring of intelligent infrastructure. British Columbia, Canada

Calcaterra S, Cesi C, Di Maio C, Gambino P, Merli K, Vallario M, Vassallo R (2012) Surface displacements of two landslides evaluated by GPS and inclinometer systems: a case study in Southern Apennines, Italy. Nat Hazards 61(1):257–266

Chen HY (2001) A study on real-time medium-range carrier phase-based GPS multiple reference stations. UNISURV S-64, The University of New South Wales, Sydney, Australia, p 182, ISBN 0 7334 1872 2

Coe JA, Ellis WL, Godt JW, Savage WZ, Savage JE, Michael JA, Kibler JD, Powers PS, Lidke DJ, Debray S (2003) Seasonal movement of the Slumgullion landslide determined from global positioning system surveys and field instrumentation, July 1998–March 2002. Eng Geol 68:67–101

Cruden DM (1991) A simple definition of a landslide. Bulletin of the international association of engineering geology-Bulletin de l'Association Internationale de Géologie de l'Ingénieur 43(1):27–29

Feng Y, Rizos C, Higgins M, Lim S, Tang M (2009) Developing regional precise positioning services using the legacy and future GNSS receivers. J Global Position Syst 8(1):17–25

Geertsema M, Clague JJ, Schwab JW, Evans SG (2006) An overview of recent large catastrophic landslides in northern British Columbia, Canada. Eng Geol 83(1–3):120–143

Gili JA, Corominas J, Rius J (2000) Using global positioning system techniques in landslide monitoring. Eng Geol 55(3):167–192

Glabsch J, Heunecke O, Schuhbäck S (2009) Monitoring the Hornbergl landslide using a recently developed low cost GNSS sensor network. J Appl Geodesy 3:179–192

Glade T (2003) Landslide occurrence as a response to land use change: a review of evidence from New Zealand. CATENA 51(3–4):297–314

Hastaoglu K, Sanli D (2011) Monitoring Koyulhisar landslide using rapid static GPS: a strategy to remove biases from vertical velocities. Nat Hazards 58(3):1275–1294

Janssen V, Rizos C (2003) A mixed-mode GPS network processing approach for deformation monitoring applications. Surv Rev 37(287):2–19

Kanzaki M (2006) Inverted RTK system and its applications in Japan. In: Proceedings of the 2006 12th IAIN congress and 2006 international symposium on GPS/GNSS, Jeju, Korea, 18–20 Oct, pp 455–458

Lim S, Rizos C (2008) A conceptual framework for server-based GNSS operations. J Global Position Syst 7(2):125–132

Malet J-P, Maquaire O, Calais E (2002) The use of global positioning system techniques for the continuous monitoring of landslides: application to the super-sauze earth flow (Alpes-de-Haute-Province, France). Geomorphology 43:33–54

Mekik C, Arslanoglu M (2009) Investigation on accuracies of real time kinematic GPS for GIS applications. Remote Sens 1(1):22–35

Mora P, Baldi P, Casula G, Fabris M, Ghirotti M, Mazzini E, Pesci A (2003) Global positioning systems and digital photogrammetry for the monitoring of mass movements: application to the Ca' di Malta landslide (northern Apennines, Italy). Eng Geol 68(1–2):103–121

Moss JL (2000) Using the global positioning system to monitor dynamic ground deformation networks on potentially active landslides. Int J Appl Earth Obs Geoinf 2(1):24–32

Othman Z, Wan Aziz WA, Anuar A (2011a) Evaluating the performance of GPS survey methods for landslide monitoring at hillside residential area: static vs rapid static. In: IEEE 7th international colloquium on signal processing and its applications, George Town, Penang

Othman Z, Wan Aziz WA, Anuar A (2011b) Landslide monitoring at hillside residential area using GPS technique: static vs. RTK network. In: Joint international symposium & exhibition on geoinformation (ISG) 2011 and ISPRS 2011, Shah Alam convention centre, Selangor

Peyret M, Djamour Y, Rizza M, Ritz JF, Hurtrez JE, Goudarzi MA, Nankali H, Chéry J, Le Dortz K, Uri F (2008) Monitoring of the large slow Kahrod landslide in Alborz mountain range (Iran) by GPS and SAR interferometry. Eng Geol 100(3–4):131–141

Rawat MS, Joshi V, Rawat BS, Kumar K (2011) Landslide movement monitoring using GPS technology: a case study of Bakthang landslide, Gangtok, East Sikkim, India. J Dev Agric Econ 3(5):194–200

Rizos C (2007) Alternatives to current GPS-RTK services and some implications for CORS infrastructure and operations. GPS Solut 11(3):151–158

Rizos C, van Cranenbroeck J, Lui V (2010) Advances in GNSS-RTK for structural deformation monitoring in regions of high ionospheric activity. In: Proceedings of the FIG congress 2010, Sydney, Australia, 11–16 April

Rizzo V (2002) GPS monitoring and new data on slope movements in the Maratea Valley (Potenza, Basilicata). Phys Chem Earth, Parts A/B/C 27(36):1535–1544

Roberts CA (2002) A continuous low-cost GPS-based volcano deformation monitoring system in Indonesia. UNISURV S-73, School of Surveying & Spatial Information Systems, The University of New South Wales, Sydney, Australia, p 271, ISBN 0 7334 1976 3

Rott H, Nagler T (2006) The contribution of radar interferometry to the assessment of landslide hazards. Adv Space Res 37(4):710–719

Shariff NS, Musa TA, Ses S, Omar K, Rizos C, Lim S (2009) ISKANDARnet: a network-based real-time kinematic positioning system in ISKANDAR Malaysia for research platform. South East Asian survey congress, Bali international convention center, Nusa Dua, Bali, Indonesia, 4–7 Aug

Sidle RC, Taylor D, Lu XX, Adger WN, Lowe DJ, de Lange WP, Newnham RM, Dodson JR (2004) Interactions of natural hazards and society in Austral-Asia: evidence in past and recent records. Quat Int 118–119:181–203

Squarzoni C, Delacourt C, Allemand P (2005) Differential single-frequency GPS monitoring of the La Valette landslide (French Alps). Eng Geol 79(3–4):215–229

Sundström J (2009) Evaluation of high rate real time GPS based tsunami warning system. M.Sc. Thesis, Space geodesy and geodynamics research group, Chalmers University of Technology, Göteborg, Sweden, p 36

Tagliavini F, Mantovani M, Marcato G, Pasuto A, Silvano S (2007) Validation of landslide hazard assessment by means of GPS monitoring technique–a case study in the dolomites (Eastern Alps, Italy). Nat Hazards Earth Syst Sci 7:185–193

Takasu T, Yasuda A (2009) Development of the low-cost RTK GPS receiver with the open source program package RTKLIB. In: International symposium on GPS/GNSS, International convention centre, Jeju, Korea

USGS (2013) Landslide events in 2013. http://landslides.usgs.gov/recent/index.php?year=2013&month. Accessed on May 27, 2013

Verhagen S, Odijk D, Teunissen PJG, Huisman L (2010) Performance improvement with low-cost multi-GNSS receivers. In: 5th ESA workshop on satellite navigation technologies and European workshop on GNSS signals and signal processing (NAVITEC), Noordwijk, 8–10 Dec

Wang G (2011) GPS landslide monitoring: single base vs. network solutions—a case study based on the Puerto Rico and Virgin Islands permanent GPS network. J Geodetic Sci 1(3):191–203

Wang G-Q (2012) Kinematics of the Cerca del Cielo, Puerto Rico landslide derived from GPS observations. Landslides 9(1):117–130

Wang G, Soler T (2012) OPUS for horizontal sub-centimeter accuracy landslide monitoring: case study in Puerto Rico and Virgin Islands region. J Surv Eng 138(3):11

Wang G, Philips D, Joyce J, Rivera F (2011) The integration of TLS and continuous GPS to study landslide deformation: a case study in Puerto Rico. J Geodetic Sci 1(1):25–34

Weber G, Dettmering D, Gebhard H (2006) Networked transport of RTCM via internet protocol (NTRIP). In: International association of geodesy symposia: a window on the future of geodesy, vol 128

Xiao R, He X, Li L (2012) Continuous monitoring of landslide and atmospheric water vapour using GPS: applications in Pubugou hydropower resettlement zone. In: Proceedings of the 2012 China satellite navigation conference (CSNC) 2012, Lecture Notes in Electrical Engineering, pp 305–313

Yalçinkaya M, Bayrak T (2002) GPS in landslides monitoring: a case study from North Eastern Turkey. In: International symposium on GIS, Istanbul, Turkey

Yu F (2011) The feasibility of applying single-frequency receivers to slope monitoring. Geotechnical special publication, ASCE library, No 216, pp 13–141

Zinas N, Parkins A, Ziebart M (2012) Improved network-based single-epoch ambiguity resolution using centralized GNSS network processing. GPS Solut (23 Feb 2012):1–11. doi:10.1007/s10291-012-0256-x

An Alternative Technique for Landslide Inventory Modeling Based on Spatial Pattern Characterization

Omar F. Althuwaynee and Biswajeet Pradhan

Abstract The present study analyses the spatial patterns of historical/present landslide inventory in the Kuala Lumpur and vicinity areas. The main objective is to statistically test the spatial nature pattern of landslide inventory, i.e. to determine whether it rejects the independency of spatial pattern or not (i.e. random or cluster distribution). For that purpose, the nearest neighbor index (NNI) was applied to measure and test the randomness. First, we tested the spatial patterns of 153 landslides. The results showed a percentage of clustered to dispersed was 85 % (130 events) to 15 % (23 events), indicating landslides have a cluster pattern tendency. Then, the spatial relationship between the cluster landslides and conditioning factors were analyzed using evidential belief function (EBF) model. Additionally, the susceptible map produced by an earlier study was used to compare the results of the inventory selection. Finally, two landslide susceptible maps (LSMs) were validated by using prediction rate curve techniques. Prediction accuracy of the cluster data LSM2 was 0.80 (80 %), whereas the random data produced LSM1 showed 0.75 (75 %) prediction accuracy. From the results obtained in this study, one can infer that the spatial nature pattern of landslide inventory follows a cluster patterns. Secondly, clustered data can be used as training data instead of random selection technique. As a conclusion, the same technique can be replicated elsewhere.

Keywords Landslide · Spatial pattern analysis · Cluster · Nearest neighbor index · GIS · Malaysia

O. F. Althuwaynee · B. Pradhan (✉)
Department of Civil Engineering, Faculty of Engineering, University Putra Malaysia,
43400 Serdang, Selangor Darul Ehsan, Malaysia
e-mail: biswajeet24@gmail.com; biswajeet@lycos.com

1 Introduction

Over the last 30 years, landslides had caused thousands of fatalities and damages, costing of almost 10 billion USD in Asia (Chu et al. 2009). This statistics shows that landslide modeling as one of the most highly sought topics among the researchers. Landslides in Malaysia mostly occur during the heavy monsoon rainfall season. Also, anthropogenic factors such as deforestation and unplanned developmental works play important roles in initiation of landslides.

According to Varnes (1984), "past is a key for the future" thus, landslide inventory play the main role in spatial and temporal prediction of landslides. Therefore, in recent years many statistical approaches have been developed to measure the spatial correlation between landslide location as a dependent factor and its conditioning factors (Akgun et al. 2011, 2012; Devkota et al. 2013; Pourghasemi et al. 2012a, b, 2013a, b, c; Pradhan 2013; Pradhan et al. 2010a, b, 2011, 2012; Tien Bui et al. 2012a, b, c, d, 2013; Zare et al. 2013).

Spatial pattern in landslide inventory plays a vital role in predictive analysis. Generally, landslides are frequently distributed in cluster pattern groups both in space and time than a disperse pattern (Jarman 2006). Cluster pattern can be described as, high density of events occurring in specific location than other locations. Moreover, the random simulation test of data distribution should reject the hypothesis of independency among the events. In an earlier chapter, Keeper (1984) concluded that landslides triggered by earthquakes, have more tendencies to occur at well-defined location around the epicenter. Some chapters mentioned that, the intensity of geological events in some areas, are not constant along the area, then their cluster pattern cannot be considered as an evident (Bai et al. 2011; Oh and Lee 2011).

Many statistical approaches have been used for spatial pattern analysis, Ripley's K-function K(r) (Ripley 1976), Poisson model (Zuo et al. 2009). In this chapter, a second-order statistics Nearest Neighbor Index (NNI) (Clark and Evans 1954), was used to test the spatial nature pattern of landslides events in Kuala Lumpur and surrounding areas. NNI method uses a ratio between two distances i.e. nearest neighbor distance and mean random nearest neighbor distance that is expected basis by chance. It is worth to mention that, in this article we used point features representation, because it is widely used in landslide modeling and it ease the analysis process simpler in a stochastic way (Stoyan 2006).

2 Study Area

Kuala Lumpur and vicinity areas, plays a major role in economic and social development in Malaysia. During the monsoon, the area receive high amount of precipitation that weakness the slopes stability (Pradhan 2011; Pradhan and Lee 2007). The study area is enclosed geographically between 2°1560 and 3°1200N

latitude and 101°1290 to 101°1440E longitude, with approximate area of 1975 km^2.

The major types of landcover in the study area comprises of settlement, peat swamp forest, and abandoned mining, grassland and few shrub areas. The overall temperature of the area ranges between 29 and 32 °C. The average precipitation varies from 58 to 240 (mm/month), which trap large amount of water leading to a high pore-water pressure that decreases the shear stress stability (Malaysian Meteorological Services Department). Also, the deforestation activity play some role in destabilizing the slopes (Evett et al. 2006). More about geological and geomorphological characteristics of the study area can be seen in Althuwaynee et al. (2012a, b).

3 Data

Since this is a follow-up article to (Althuwaynee et al. 2012a, b), therefore the basic data and other characteristics of the study area can be referred to those aforementioned articles. The landslide inventory consists of 219 landslides, was collected over the past 25 years mainly by using remote sensing sources:

- An archived 1:5000–1:50,000 aerial photos, SPOT 5 panchromatic satellite image and archived landslide location map and previous reports.
- A 1:25,000 scale topographic map used to model a digital elevation model,
- The geological map at scale 1:63,000 was used to produce the lithological map and distance from the faults.
- The Soil map at the scale 1:100,000 was used to extract the soil properties.
- The precipitation map was prepared using the past 29 years (1981–2010) of rainfall data. Enhanced Thematic Mapper (ETM +) satellite data was used to extract the land cover and NDVI (Normalize difference vegetation index) maps.

4 Methodology

Bothe landslide inventory map and conditioning factors were constructed and converted to a common pixel unit size. The NNI method will test the spatial pattern of landslides, then the output will be used as a training dataset for EBF modeling to produce landslide susceptible map LSM2.

LMS2 should be validated by comparing it with previous LMS1 produced by using random inventory selection technique (Althuwaynee et al. 2012a). Finally, the results were evaluated by using the landslides location which was not used during the model building process (Fig. 1).
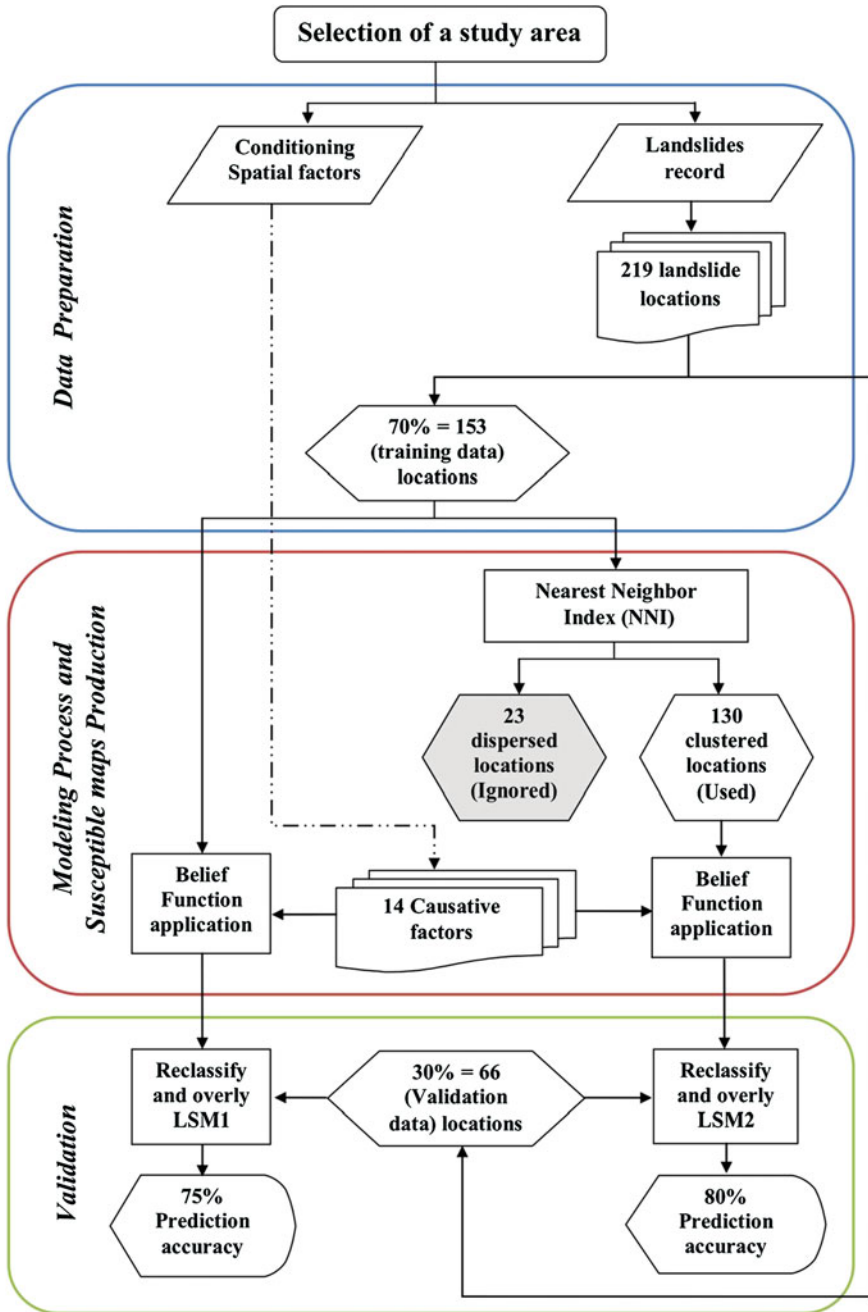
Fig. 1 Flow chart of the proposed methodology

4.1 Nearest Neighbour Index (NNI) Model

Spatial patterns of landslide events can be described in two statistical orders; 1st order (global test), which describes the pattern distribution of: center locations; extend of distribution, and ordination or dispersion direction. The 2nd order (local test), mostly describes the overall neighborhood or sub-region patterns. In this article a 2nd order NNI was used to test the landslide pattern in the study area.

Theoretically, NNI is calculated by taking the ratio of two measures components (Eq. 3). First component is the nearest neighbor distance between all points (Eq. 1), which measures the distance from a specific landslide location (ex., location no.1) to all other locations, then, register only the shortest distance. Subsequently, it measure the distance from location no.2 to the other locations, and register only the shortest distance and add it to the shortest distance value of location no.1. This process will be repeated till all the locations have their shortest distances. Then, all the shortest distances values will be summed and divided by N (total locations amount), to produce the average nearest distance.

$$\text{Nearest Neighbor Distance} = d(NN) = \sum_{i=1}^{N} \left[\frac{\text{Min}(d_{ij})}{N} \right] \qquad (1)$$

where:

Min (dij): distance between each point and its nearest neighbor (m).
N: number of points.

Second component is the mean random distance, which measures the expected nearest neighbor distances (i.e. if the spatially random distributed points) (Eq. 2). The unit of study area is measured in meter square, and distances between landslides are measured in meter length, thus, Eq. 2 will also give a random distance measure in meter length.

$$\text{Mean Random Distance} = d(ran) = 0.5 \ \text{SQRT} \left[\frac{A}{N} \right] \qquad (2)$$

where:

A: area of study (m^2)

Note that, if the result of Eq. 3 is less than 1, then it will confirm the landslides nature tendency toward the cluster distribution patterns (i.e. a group density higher than other location in study area). On the contrary, if the result is more than 1, then the distribution is dispersed in nature.

$$\text{Nearest Neightbor Index} = NNI = \frac{d(NN)}{d(ran)} \qquad (3)$$

Equation 4 shows the Z-test which is defined as an indicator to check if the result of Eq. 1 is significantly different from the Eq. 2 results or not. Negative result of Z-test confirms the cluster nature, and vice versa (Clark and Evans 1954). Moreover, Z-test result value has a direct proportion with the significant *p* value,

i.e. higher significant p-value is achieved where the z-value is far enough by the bell peak of statistical normal distribution shape.

$$Z = \frac{d(NN) - d(ran)}{SE_{d(ran)}} \tag{4}$$

The standard error of the mean random distance is calculated using Eq. 5.

$$SE_{d(ran)} \approx SQRT\left[\frac{(4 - \pi)A}{4\pi N^2}\right] \approx \frac{0.26136}{SQRT[N^2/A]} \tag{5}$$

More theoretical discussion about the NNI equations can be found in (Clark and Evans 1954). In this study, "Average Nearest Neighbor" function under Spatial Statistics tools of ArcGIS software was used. The result file provided all the above mentioned values such as; observed mean distance, expected mean distance, nearest neighbor ratio, z-score, and p-value.

4.2 Evidential Belief Function (EBF) model

The Dempster–Shafer theory of evidence (belief) (Dempster 1968; Shafer 1976), is a mathematical based model with a bivariate statistically methodology, used to find the spatial integration based on the rule of combination. Generally, it is applied successfully as knowledge based approach in mineral potential mapping (Carranza 2009).

Theory of belief is built up from direct mass function (Eq. 6) to present 4 maps:

- Bel (degree of belief) as stated in Eqs. 7 and 8,
- Dis (degree of disbelief) based on Eqs. 9 and 10,
- Unc (degree of uncertainty) based on Eq. 11, and;
- Pls (degree of plausibility) based on Eq. 12. Which can handle the analysis even with incomplete data coverage information (Carranza 2009).

According to Dempster 1968, the main parts of the theory is represented by Bel (lower probability), and Pls (upper probability).

$$M : 2 = \{\varnothing, Tp, Tp^-, \} = \{Tp, Tp^-\} \tag{6}$$

where:

Tp = class pixels affected by landslide

Tp$^-$ = class pixels not affected landslide

Equation 7 shows the ratio of Bel in each individual class of conditioning factor and landslide ratio.

$$\beth(Tp)Eij = [N(L \cap Eij)/N(L)]/[N(Eij) - N(L \cap Eij))/(N(A) - N(L)] = N/D \tag{7}$$

where:

$N(L \cap Eij)$:   number of landslide pixels in domain

$N(L)$:   total number of landslides, or $\sum N\left(L \cap E_{ij}\right)$

$N(Eij)$:   number of pixels in domain

$N(A)$:   total number of pixels in domain, or $\sum N(E_{ij})$

N: proportion of landslide area

D: proportion of non-landslide area

Equation 8 shows the final result of Bel ratio in each class.

$$Bel = \beth(Tp)Eij / \sum \beth(Tp)Eij \tag{8}$$

Similarly, Eqs. 9 and 10, were used to find the Dis ratio in each class. Finally, Eq. 11 was used to calculate the Unc and Eq. 12 gave the Pls result.

$$\beth(Tp^-)Eij = [(N(L) - N(L \cap Eij))/N(L)]/[(N(A) - N(L) - N(Eij) + N(L \cap Eij))/(N(A) - N(L))] = K/H \tag{9}$$

where:

K: proportion of landslides that do not occur.

H: proportion of non-landslide areas in other attributes outside class

$$Dis = \beth(Tp^-)Eij / \sum \beth(Tp^-)Eij \tag{10}$$

$$Unc = 1 - Dis - Bel \tag{11}$$

$$Pls = 1 - Dis \tag{12}$$

The EBF model gave the spatial distribution of landslide prediction map through different zones showing the degree of uncertainty of the same zone (Park 2010). Therefore, some conclusion can be drawn in terms of model capability:

(a) Degrees of belief: showed the susceptible areas.
(b) Degrees of disbelief: showed the non-susceptible areas.
(c) Degrees of uncertainty: showed where the evidences are insufficient to provide the proofs for landslide information, or guide for further field assessment.
(d) Degrees of plausibility: represented all the integrated maps evidence except the disbelief map. Generally it shows where spatial evidences are sufficient. Or evidences are inefficient to prove where the landslide triggered factor will effect.

Moreover, data-driven EBF model could compromise the results if spurious evidence arises from insignificant spatial associations between landslides and conditioning factors such as the case of geology. Additionally, the model can produce acceptable evidences even with large number of input dataset. Finally, two LSMs were produced, one using the cluster selection technique and the other

by using the random selection technique. Subsequently, the validation of prediction performances was compared by using prediction rate curve and the unused landslide points.

5 Results and Discussion

A total of 219 landslide locations were randomly divided into 30 % (66) validation data, and 70 % (153) training data (Althuwaynee et al. 2012b) to build LSM1. In this chapter, the same amounts of training data (153) points were tested by NN index ratio to identify the spatial nature pattern (Fig. 2).

The NNI test showed a ratio of 0.53, which proved the cluster nature of landslides pattern. Also, the expected mean distance was about 1457 m. Since the expected mean distance represents the limit distance which separates between the non-random and random distribution in the current study area. For that reason, all the points' distances with less than the expected mean distance range will be used for model training, and others will be ignored.

A total 132 or 86 % out of 153 points, have an expected mean distance less than or equal to 1457 m, and will be used to train the EBF model. Additionally, the remaining 21 or 14 % out of 153 points were tested with NNI, and the results confirmed its dispersed pattern as shown in Fig. 3.

The EBF model was applied with 132 clustered training landslides to produce LMS2 (Fig. 4). The prediction rate curve with unknown spatial pattern data of 67 landslide points were used to evaluate the prediction performance of LMS1 and LMS2. The prediction rate curve showed higher percentage in LMS2 (0.8) than LMS1 (0.75) as shown in Fig. 5.

Here two major points can be highlighted: first, the current technique used only 132 cluster points, showed better prediction than 153 random selected points. Also it confirms the clustering pattern of landslides recorded in the past 25 years in Kuala Lumpur and vicinity areas. Second, LSM2 showed high contrast and sharp identified zones edges, with less diffused and uncertain susceptible areas than LMS1.
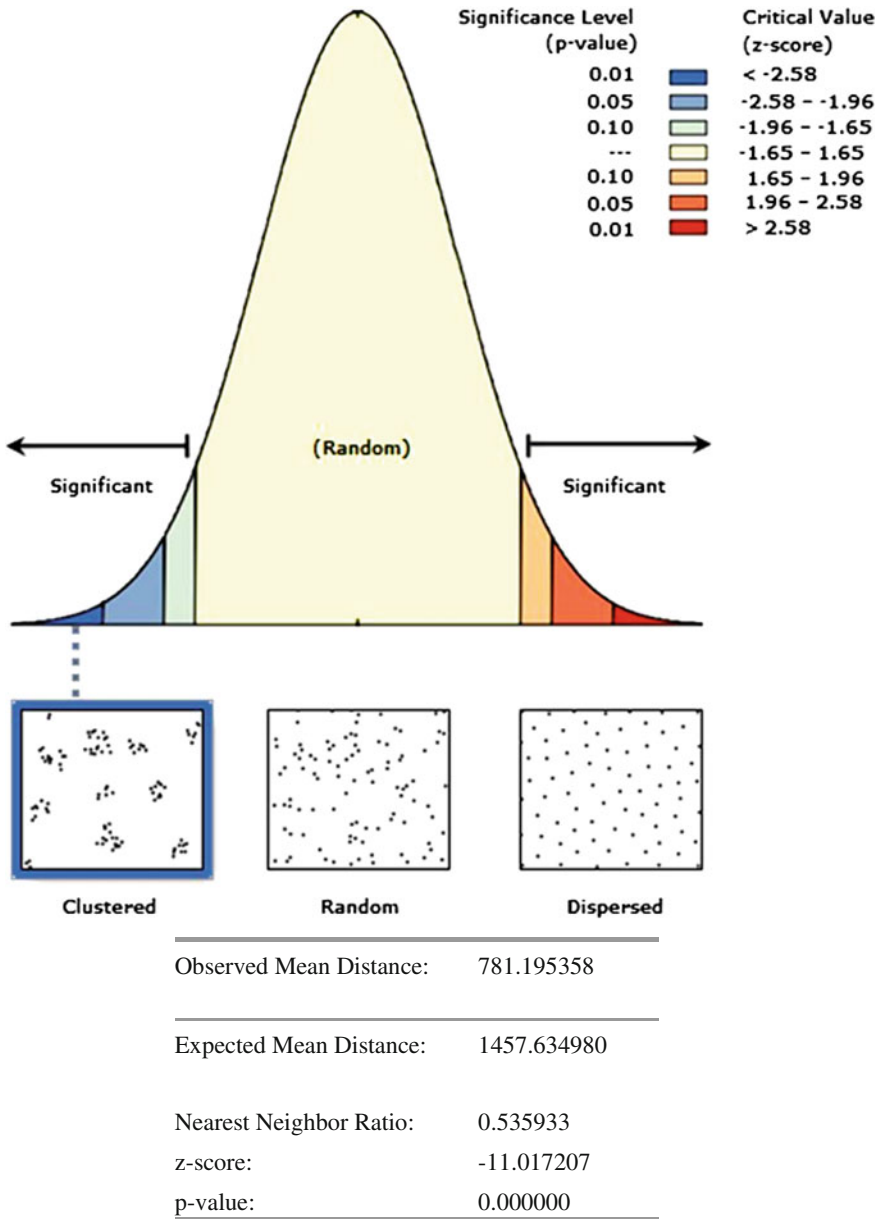
Fig. 2 Nearest neighbour result of 132 points events
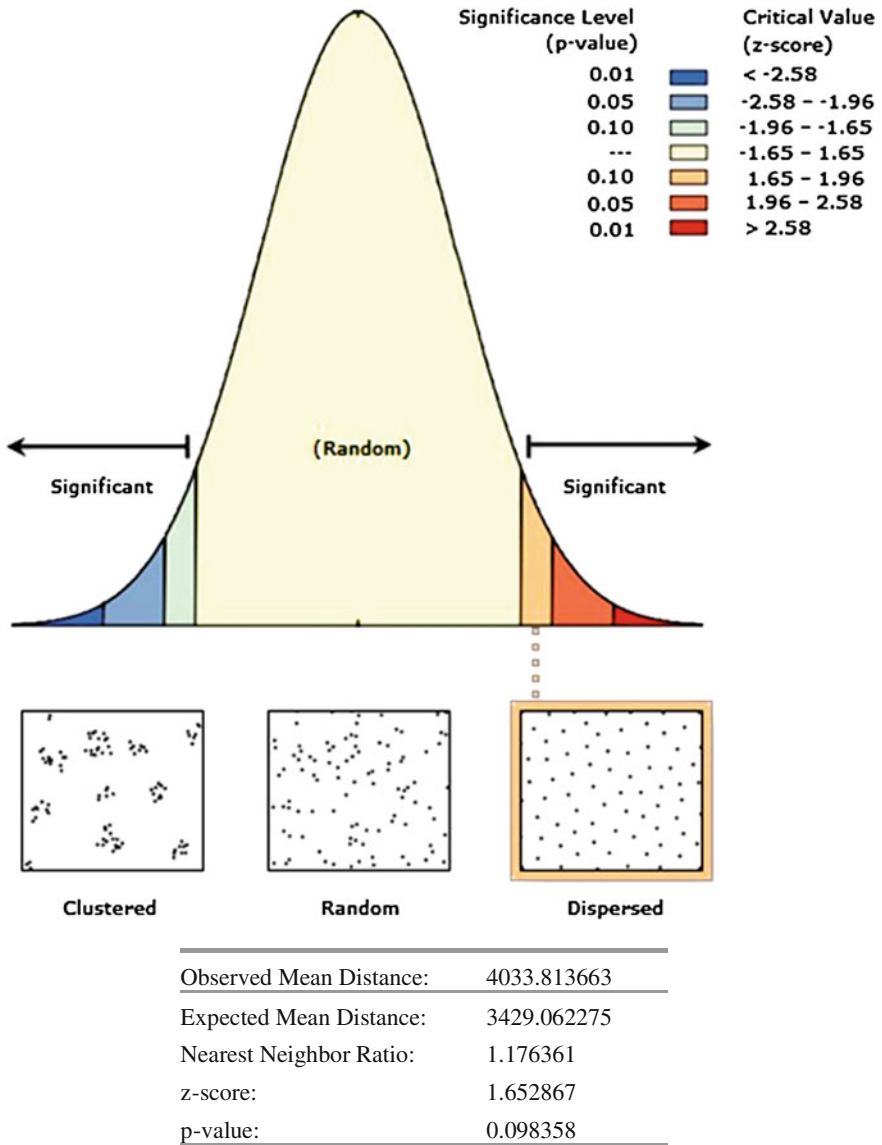
Fig. 3 Nearest neighbour result of 21 points events
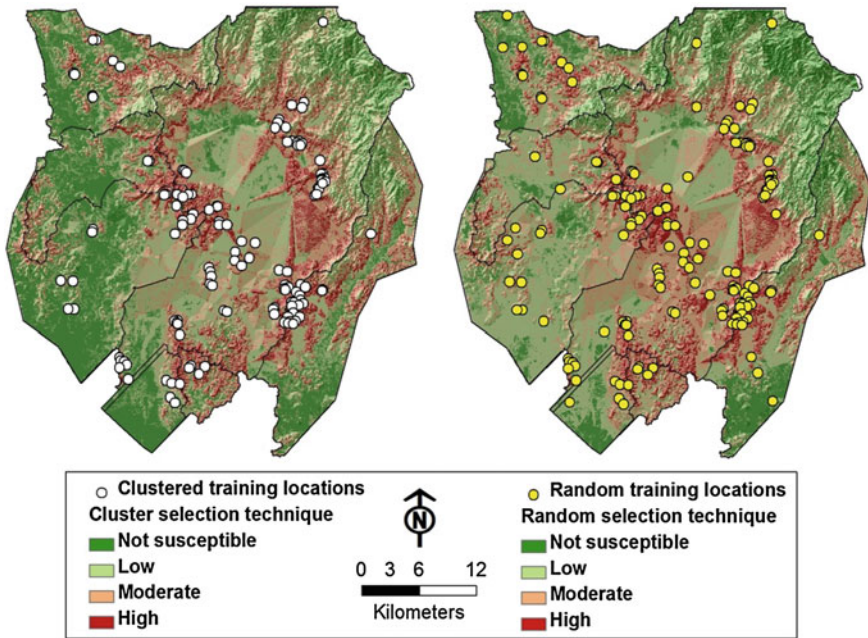
Fig. 4 Final landslide susceptible maps

Fig. 5 Prediction rate curve
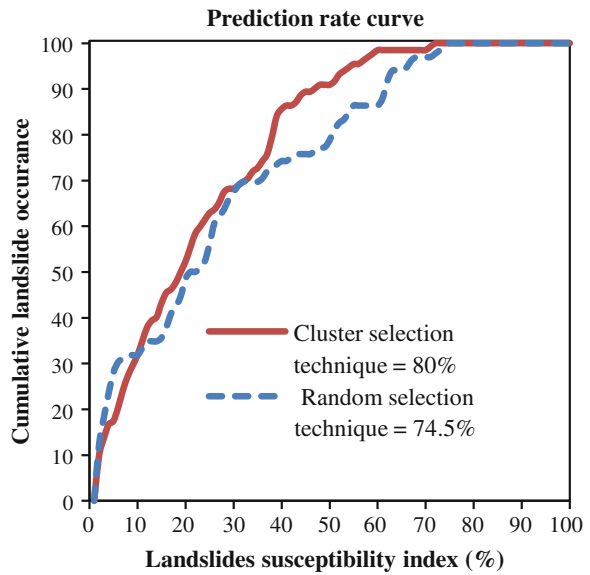
6 Conclusion

In this chapter, a cluster spatial pattern of shallow landslide events were tested and confirmed in a landslide prone area in Malaysia. Generally, different spatial patterns are tested to determine whether landslides pattern rejects the independency of spatial pattern or not (i.e. random or cluster distribution). In the present study, a 2nd order statistical test of nearest neighbor index was applied and found that landslides registered over 25 years in Kuala Lumpur and vicinity areas have a cluster nature pattern. In order to validate our findings, 15 causative factors were prepared by using EBF model with the 132 cluster landslides only, and then the layers were combined and produced LSM2. The current map was compared with the previous work, which prepared LMS1 using EBF model with 153 random landslides selection. LMS2 showed higher prediction rate of area under the curve (AUC) than the previous technique of LMS1, with 0.8 and 0.75 rates respectively.

The results showed the tendency of the landslide to cluster in high density locations with 88 % of the data rather than random pattern of other 12 % locations in surrounding areas. The current research recommended to pre-processing the inventory to find a common space or time distribution relationship. The future research will focus on categorization and classification of the cluster groups by taking into consideration of; failure types, volume, shape, and time of occurrence. The additional data will enhance the model prediction accuracy result from general assessment to local details and more specific slope failure zoning. Also, it will reduce the uncertainty in particularly in the zones of high to moderate hazardous landslide prone areas.

References

Akgun A, Kıncal C, Pradhan B (2011) Application of remote sensing data and GIS for landslide risk assessment as an environmental threat to Izmir city (west Turkey). Environ Monit Assess 184(9):5453–5470

Akgun A, Sezer EA, Nefeslioglu HA, Gokceoglu C, Pradhan B (2012) An easy-to-use MATLAB program (MamLand) for the assessment of landslide susceptibility using a Mamdani fuzzy algorithm. Comput Geosci 38(1):23–34

Althuwaynee OF, Pradhan B, Lee S (2012a) Application of an evidential belief function model in landslide susceptibility mapping. Comput Geosci 44:120–135

Althuwaynee OF, Pradhan B, Mahmud AR, Yusoff, ZM, (2012b) Prediction of slope failures using bivariate statistical based index of entropy model. In: IEEE colloquium on humanities, science and engineering (CHUSER), 2012, IEEE, pp 362–367

Bai S, Lü G, Wang J, Zhou P, Ding L (2011) GIS-based rare events logistic regression for landslide-susceptibility mapping of Lianyungang, China. Environ Earth Sci 62:139–149

Carranza EJM (2009) Controls on mineral deposit occurrence inferred from analysis of their spatial pattern and spatial association with geological features. Ore Geol Rev 35:383–400

Chu C-M, Tsai B-W, Chang K-T (2009) Integrating decision tree and spatial cluster analysis for landslide susceptibility zonation. World Acad Sci Eng Technol 59:479–483

Clark PJ, Evans FC (1954) Distance to nearest neighbor as a measure of spatial relationships in populations. Ecology 35:445–453

Dempster AP (1968) Upper and lower probabilities generated by a random closed interval. Ann Math Stat 39:957–966

Devkota K et al (2013) Landslide susceptibility mapping using certainty factor, index of entropy and logistic regression models in GIS and their comparison at Mugling-Narayanghat road section in Nepal Himalaya. Nat Hazards 65:135–165

Evett SR, Tolk JA, Howell TA (2006) Soil profile water content determination: sensor accuracy, axial response, calibration, temperature dependence, and precision. Vadose Zone J 5:894

Jarman D (2006) Large rock slope failures in the Highlands of Scotland: characterisation, causes and spatial distribution. Eng Geol 83:161–182

Keeper DK (1984) Landslides caused by earthquakes. Geol Soc Am Bull 95:406–421

Oh H-J, Lee S (2011) Landslide susceptibility mapping on Panaon island, Philippines using a geographic information system. Environ Earth Sci 62:935–951

Park N-W (2010) Application of Dempster-Shafer theory of evidence to GIS-based landslide susceptibility analysis. Environ Earth Sci 62:367–376

Pourghasemi HR, Pradhan B, Gokceoglu C (2012a) Application of fuzzy logic and analytical hierarchy process (AHP) to landslide susceptibility mapping at Haraz watershed, Iran. Nat Hazards 63:965–996

Pourghasemi HR, Mohammadi M, Pradhan B (2012b) Landslide susceptibility mapping using index of entropy and conditional probability models at Safarood Basin, Iran. Catena 97:71–84. http://dx.doi.org/10.1016/j.catena.2012.05.005

Pourghasemi HR, Jirandeh AG, Pradhan B, Xu C, Gokceoglu C (2013a) Landslide susceptibility mapping using support vector machine and GIS at the Golestan Province. Iran. J Earth Syst Sci 122:1–21

Pourghasemi HR, Moradi HR, Fatemi Aghda SM, Gokceoglu C, Pradhan B (2013b) GIS-based landslide susceptibility mapping with probabilistic likelihood ratio and spatial multi criteria evaluation models (North of Tehran, Iran). Arab J Geosci. http://dx.doi.org/10.1007/s12517-012-0825-x (Article online first available)

Pourghasemi HR, Pradhan B, Gokceoglu C, Moezzi KD (2013c) A comparative assessment of prediction capabilities of Dempster–Shafer and weights of evidence models in landslide susceptibility mapping using GIS. Geomatics Nat Hazards Risk 4(2): 93–118. http://dx.doi.org/10.1080/19475705.2012.662915

Pradhan B, Oh HJ, Buchroithner M (2010a) Weights-of-evidence model applied to landslide susceptibility mapping in a tropical hilly area. Geomat Nat Hazards Risk 1(3):199–223

Pradhan B, Youssef AM, Varathrajoo R (2010b) Approaches for delineating landslide hazard areas using different training sites in an advanced artificial neural network model. Geosp Inf Sci 13(2):93–102

Pradhan B (2011) Manifestation of an advanced fuzzy logic model coupled with Geo-information techniques to landslide susceptibility mapping and their comparison with logistic regression modelling. Environ Ecol Stat 18:471–493

Pradhan B, Mansor S, Pirasteh S, Buchroithner MF (2011) Landslide hazard and risk analyses at a landslide prone catchment area using statistical based geospatial model. Int J Remote Sens 32(14):4075–4087

Pradhan B (2013) A comparative study on the predictive ability of the decision tree, support vector machine and neuro-fuzzy models in landslide susceptibility mapping using GIS. Comput Geosci 51:350–365

Pradhan B, Chaudhari A, Adinarayana J, Buchroithner MF (2012) Soil erosion assessment and its correlation with landslide events using remote sensing data and GIS: a case study at Penang Island, Malaysia. Environ Monit Assess 184:715–727

Pradhan B, Lee S (2007) Utilization of optical remote sensing data and GIS tools for regional landslide hazard analysis using an artificial neural network model. Earth Sci Front 14:143–151

Ripley BD (1976) The second-order analysis of stationary point processes. J appl probab 13:255–266

Shafer G (1976) A mathematical theory of evidence. Princeton university press, Princeton

Stoyan D (2006) Fundamentals of point process statistics, case studies in spatial point process modeling. Springer, New York, pp 3–22

Tien Bui D, Pradhan B, Lofman O, Revhaug I, Dick OB (2012a) Landslide susceptibility assessment in the Hoa Binh province of Vietnam: a comparison of the Levenberg-Marquardt and Bayesian regularized neural networks. Geomorphology 171:12–29

Tien Bui D, Pradhan B, Lofman O, Revhaug I, Dick OB (2012b) Spatial prediction of landslide hazards in Hoa Binh province (Vietnam): a comparative assessment of the efficacy of evidential belief functions and fuzzy logic models. Catena 96:28–40

Tien Bui D, Pradhan B, Lofman O, Revhaug I (2012c) Landslide susceptibility assessment in Vietnam using support vector machines, decision tree and Naïve Bayes models. Math Probl Eng 2012:1–26

Tien Bui D, Pradhan B, Lofman O, Revhaug I, Dick OB (2012d) Landslide susceptibility mapping at Hoa Binh province (Vietnam) using an adaptive neuro-fuzzy inference system and GIS. Comput Geosci 45:199–211

Tien Bui D, Pradhan B, Lofman O, Revhaug I, Dick O (2013) Regional prediction of landslide hazard using probability analysis of intense rainfall in the Hoa Binh province, Vietnam. Nat Hazards 66:707–730

Varnes DJ (1984) Landslide hazard zonation: a review of principles and practice. Nat Hazards 3:63

Zare M, Pourghasemi HR, Vafakhah M, Pradhan B (2013) Landslide susceptibility mapping at Vaz Watershed (Iran) using an artificial neural network model: a comparison between multilayer perceptron (MLP) and radial basic function (RBF) algorithms. Arab J Geosci 6(8):2873–2888

Zuo R, Agterberg FP, Cheng Q, Yao L (2009) Fractal characterization of the spatial distribution of geological point processes. Int J Appl Earth Obs Geoinf 11:394–402

Development of a New D16 Algorithm for Single Flow Direction Model

Wan Muhd Hairi Wan Ab Karim and Mohamad Ghazali Hashim

Abstract Currently, D8 algorithm is widely used on raster-based dataset to illustrate the correlation and relationship between a particular pixel with its neighbouring pixels in water flow direction model. Unfortunately, D8 algorithm has some limitations, for instance, it is not being suitable to model flow divergence in ridge area, sub-catchment identification, among others. Several applications on drainage network, agricultural and some construction planning need accurate information of flow direction. Thus, this study tries to develop a new algorithm, which has the capability to improve the efficiency, accuracy, and reliability of the current D8 algorithm on surface Single Flow Direction (SFD) modelling. The proposed algorithm is called D16 algorithm. This D16 algorithm, not only adds eight new flow direction options, but also introduces some rules and equations to overcome the limitations of the current SFD as well as the D8 algorithm. This paper highlights the process of deriving the D16 model, logical structures, equations, comparison results between D8 and D16 algorithm on topographic map, Shuttle Radar Topography Mission (SRTM) and Advance Spaceborne Thermal Emission and Reflection (ASTER) data.

Keywords D8 algorithm · Raster-based dataset · Water flow direction · Single flow direction model · New D16 algorithm

W. M. H. W. A. Karim (✉) · M. G. Hashim
Department of Geoinformation, Faculty of Geoinformation and Real Estate, Universiti Teknologi Malaysia (UTM), Johor Bahru, Johor, Malaysia
e-mail: wmhairigis@gmail.com

M. G. Hashim
e-mail: ghazalihashim@utm.my

1 Introduction

Basically, Geographic Information System (GIS) can be defined as a designed system to capture, manipulate, analyse, manage and present all kinds of geographical or spatial data in various mediums such as map and model to help the decision making process. People from various professions mostly consider GIS as a tool to help them in providing reliable spatial information to support their work, such as in planning and managing environment, urban, engineering, hydrology, geology, etc (Hengxing et al. 2008; Bernard et al. 2010).

The spatial information provided by GIS is not limited only for the ground entity or object, but it can extend up to above the ground (atmosphere or space) and as well as beneath ground surface. For example, water flow direction information can be either on surface flow direction (which came from rain or flood) model or underground water movement for underground water modelling. Whereas, this study is only concerned with surface water flow direction modelling in order to assist and provide more accurate spatial information to hydrology field.

Water flow directions are commonly used in digital elevation models (DEMs) for hydrology applications to estimate and model the paths of water toward the streams, sedimentations and contaminant movement (Tarboton 1997). DEM is a preferred medium because it consists of an efficient, readily available and completely matrix data structure (Miller 2010; Moore et al. 1991).

Many algorithms available today define the processes of water flow in different approaches to fit their targeted applications. Examples of applications that require crucial decisions are drainage network planning, flood prediction, monitoring and precaution, dam planning and construction, water catchment and others. In short, flow direction algorithms can be divided into two main categories: Single Flow Direction (SFD) and Multiple Flow Direction (MFD). The famous SFD is the simplest D8 algorithm while D-infinity (D∞) represents the most popular algorithm in MFD.

1.1 Problem Statement

The term water flow direction is actually a basic technique in watershed analysis especially used in GIS and other professional fields related to surface water flow direction modelling. In order to provide the most accurate information on water flow direction and watershed model, many new data acquisition techniques have been introduced and the older systems had evolved dramatically (new hardware, software and procedures) to increase the efficiency and accuracy of the output result.

For example, Airborne Light Detection and Ranging (LiDAR) is used as a new data acquisition technique (compared to traditional surveying and mapping methods) especially in GIS and other construction fields for sub-meter accuracy of
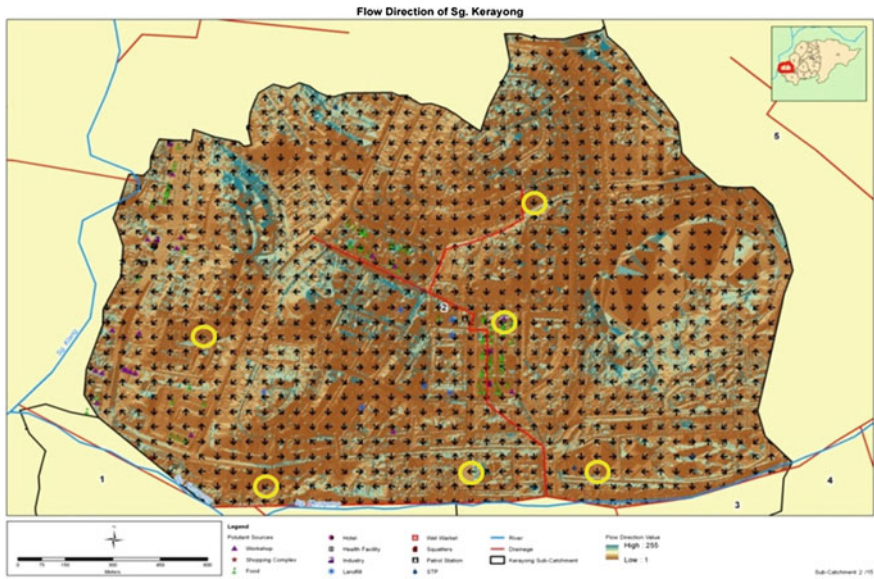
Fig. 1 A flow direction map of discharge waste materials and chemicals from pollutant sources into the river. *Yellow circles* indicate there is a conflict and wrong flow direction produced by D8 algorithm

a large area within a short period. Currently, more than 200 LiDAR systems are available all over the world and can achieve up to 250,000 pulses per second and with different type of sensors that fit variety of purposes (Schuckman and Renslow 2009). In terms of accuracy, LiDAR systems, such as aero-space service, are able to reach up to 15 cm RMSE ground surface (Hodgson and Bresnahan 2004).

Even though a very high data accuracy such as LiDAR or high resolution remote sensing satellite imagery are used, the information on surface water flow directions are still in the same range of accuracy. It is the nature of hardware development must coincide with software, while data development (accuracy of new data acquiring methods) with the processing algorithm development.

At this moment, the overall SFD output of flow direction information could not be provided at the best level of accuracy to the specific application due to the unenhanced algorithms. Thus, there is a need to upgrade and improve SFD algorithms such as D8 to simultaneously catch up with the development of data acquisition techniques in order to provide the most accurate information related to the surface water flow direction.

The study focuses on SFD model especially for D8 algorithm. So, basically this paper tries to dig the limitations of D8 algorithm, how a new D16 algorithm can be designed to overcome those weaknesses and some comparison results from various comparison methods. As summary, this study is mainly conducted to develop and test a new designed algorithm for surface water flow direction called "D16 Water
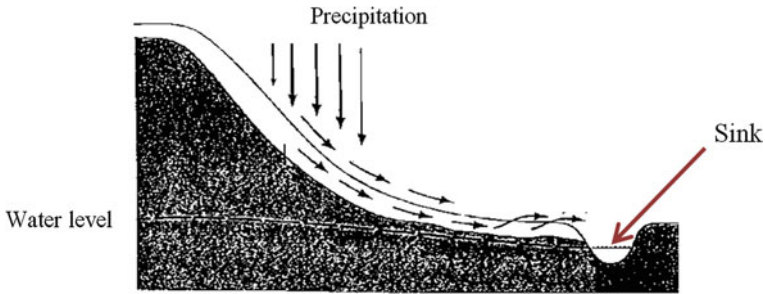
Fig. 2 General concept of flow direction

Flow Direction" to increase the efficiency, accuracy and reliability of current D8 algorithm, used in many GIS and hydrology software which are related to SFD models.

Apart from the requests of several related field applications for high accuracy flow direction information, the demand for developing a new SFD algorithm is encouraged by:

1. Some limitations of D8 algorithms stated by several researchers.
2. The need to increase the dispersion options of current SFD model.
3. The need for other state of water other such as a stagnant and a sink.
4. The reliability on accuracy by the D8 algorithm (Fig. 1).

Apart from limitations of SFD as well as D8 algorithm, there is a main factor of deriving the new SFD algorithm. According to the 1st Law of Geography, "Everything is related to everything else, but near things are more related than distant things" (Tobler 1970). The eight neighbour pixels used in this neighbourhood analysis is definitely true and agree by this law, but we cannot ignore the other parameter of this law on the distant thing.

The main difference highlighted between eight directions of existing SFD with this new SFD algorithm is by adding eight additional directions for D8 algorithm that fully obey the first law of geography as the name given "D16" algorithm. In addition, some rules and equations are also introduced in this algorithm in order to minimize the weaknesses of D8 algorithm.

1.2 Water Flow Direction Concept

Water flow direction is work based on the elevation difference and gravity attraction to the lower height area. At any point (X, Y, Z) in all spatial referenced system, a certain volume or drop of water (example from the rain) will have from 0–360° of horizontal direction to flow from one point to other point or place which is lower than the current surface elevation. That is the nature of the world
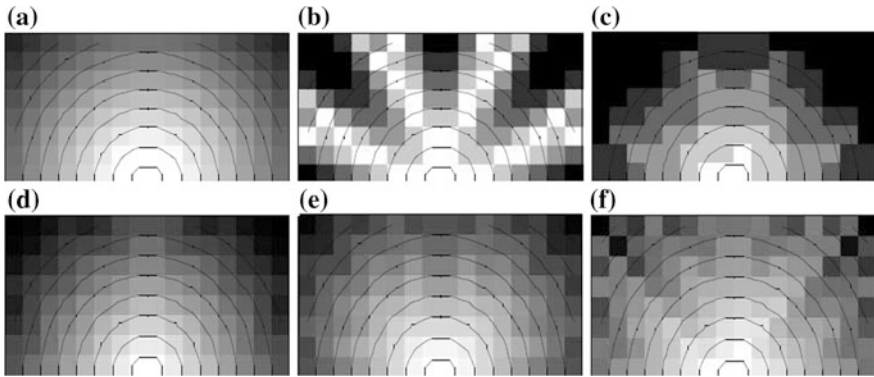
Fig. 3 Comparison of each flow direction concepts (Tarboton 1997). **a** Theoretical flow direction. **b** and **c** Example of SFD model results. **d** Theory of MFD. **e** and **f** Example of MFD model results

phenomenon upon real water flow concept. Apart from that, even if there is stagnant water on the earth surface, it will attempt to flow to the lower places due to the earth gravitational force except surrounded by the higher solid object or material such as in Fig. 2. For instance, the water at upstream river will flow naturally toward the downstream river and then go to the sea as it final destination.

To describe this natural phenomenon, most of the researchers in related fields of study agreed that the best method or model to describe water flow direction concept is represented by eight directions such as D8, Rho8, FD8, and FRho8 algorithms in SFD model. Eight directions are the result of the only eight surrounded pixel that directly touch the pixel except the outer pixel (row and column) of any input raster dataset. The concepts of flow direction and model, examples of expected output results from several algorithms in SFD and MFD are shown in the Fig. 3a–f. The black pixels show the potential flow direction of that particular point.

2 Current SFD and MFD Algorithms

2.1 Single Flow Direction

Single Flow Direction (SFD) is the simplest and very essential model to describe the flow direction either in GIS field or others based on height difference such as in Fig. 4. The formula is based on difference in height (steepest slope) between a certain point to its neighbours.

The D8 algorithm is proposed by O'Callaghan and Mark (1984) and now is widely used in SFD model in various open source and commercial software. This

3	2	4
7	5	8
7	1	9

algorithm is able to approximate the flow directions on a topographic surface, the process of tracking "flow" from each pixel to one of its eight neighbour pixels (Rivix 2008). D8 algorithm uses eight nearest neighbours of a particular pixel to determine which direction the water will flow from its current location or pixel to its neighbour pixel until it reaches the final destination such as a river.

Another popular algorithm in SFD model is Rho8 which was introduced by Fairfield and Leymarie (1991) and work only with DEM surface model (Lindsay 2012). The approach is quite similar to D8 algorithm, but it will correct the removed pixel caused by all flat areas (a stagnant state) and spurious depressions (Lindsay 2012). While, the grid cells that have no lower neighbours (a sink state) are assigned a flow direction of zero.

2.2 Multiple Flow Direction

On the other hand, the Multiple Flow Direction (MFD) model allows the algorithm result to have multiple flow directions for a certain cell, most commonly to all downslope neighbours (Laura 2001). The simplest MFD concept and model is illustrated in Fig. 5. There is a disadvantage of MFD model which is the flow from a cell will be dispersed to all neighbours of lower elevation, resulting more diffuse flow of water (Laura 2001).

One of the famous algorithms of MFD is D-infinity (D∞) that is widely used in advance water flow analysis with slope element as the main factor of study or working field. D∞ uses a range of 45° from each neighbour's pixel origin to the next direction using 4×4 pixel window as illustrated in Fig. 6. D-Infinity algorithm is also capable handling all of the ambiguous situations that can occur in real topography (sometimes resorting to the D8 method) while many other MFD methods cannot provide this solution. Examples of such an application are the landslide accident and other slope applications and models.

2.3 SFD: D8 Algorithm

The D8 algorithm uses 3×3 pixel windows as illustrated in Fig. 7. The angle of each direction to the next direction is 45 degree (45°) and thus the flow direction is limited to only eight options. Although theoretically the water can flow in 360°,

Fig. 5 MFD flow to all
downslope neighbours (Laura
2001)
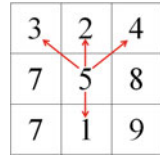
Fig. 6 D∞ algorithm model
(Smith et al. 2009)
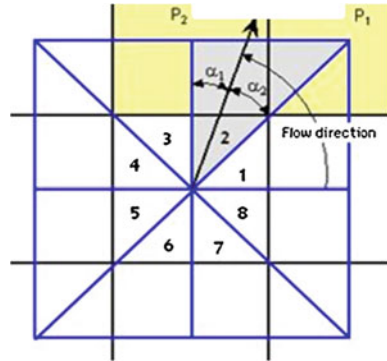
Fig. 7 D8 water flow
direction (Smith et al. 2009)
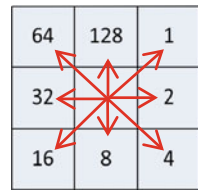
that is in all directions, from high to the lower area pulled by the gravitational
force but this model only allow for eight flow direction due to the limitation of
raster based contacted-neighbour pixels.

2.3.1 Limitations of D8 Algorithm

The D8 algorithm is a well-known flow direction algorithm for SFD and able to fit
many application requirement as well as water modelling in hydrology. There are
many advantages of D8 algorithm, for example, it is a very important model at the
valley by producing many parallel flow lines and yet solved many problems within
the boundaries of the catchment area (Wilson 2002) Nevertheless, some questions
have arisen on the accuracy of this only eight direction options in SFD, especially
for the D8 algorithm.

There are several limitations of D8 algorithm, which was identified by water
related researchers such as:
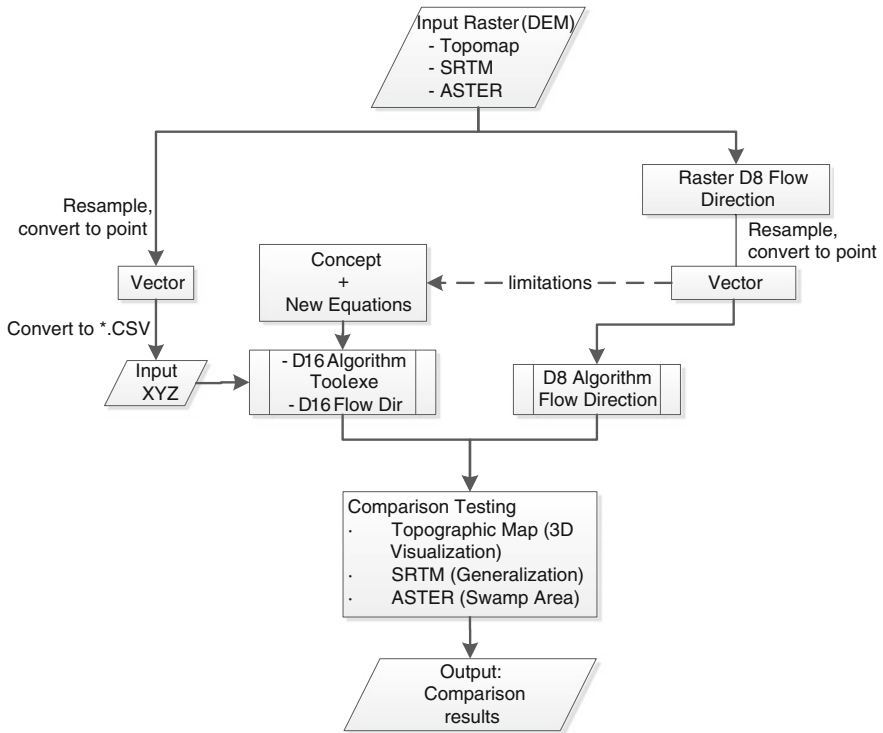
Fig. 8 A framework for developing and comparing D16 algorithm with D8

- Wilson (2002)—"D8 cannot be used to model the water flow direction divergence in ridge area".
- Miller (2010)—D8 is not a suitable method for sub-catchment identification.
- Tarboton (1997):

  – Less options available with a huge separated range angle (Discretization of D8 flow into only one of eight possible directions, separated by 45°).
  – D8 introduces no dispersion, but at the expense of grid bias.

Furthermore, D8 algorithm was also not able to detect other state of water which is with no direction (swamp or stagnant areas) that lead to produce false flow direction information for a certain area. Thus, D8 will produce flow direction result in which may be trapped toward the other pointed neighbouring flow arrows as illustrated in Fig. 1.
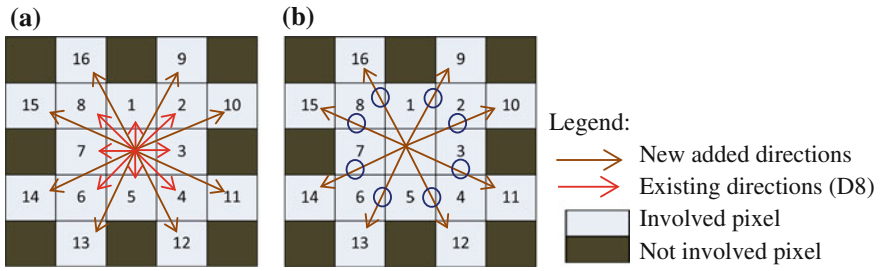
Fig. 9 D16 algorithm approach

3 Developing New D16 Algorithm Framework

The basic structure of the new D16 algorithm is the phase of designing a conceptual model and introduction of new equations, which are derived purposely to overcome the limitations of the current SFD or D8 algorithm. Figure 8 shows the overall framework on how the new D16 is being tested with D8 algorithm from three sources of raster data up to the output phase of accuracy level. Then, any necessary enhancement will be implemented through the concept and new equation of D16 algorithm based on the limitation of D8 results.

The input raster data should be in a two dimensional planar surface and for this study, Rectified Skew Orthomorphic (RSO) Kertau (a local projection system for west peninsular Malaysia) is used to project the data into a spatial referenced system. After resampling the raster-based data into a required pixel resolution, it will then undergo a conversion process to produce a vector-based data in point form features.

The vector-based data representation is used in this study because users can easily visualize and detect the flow direction movement as represented by the arrow, but not in raster-based presentation. The point layer of D8 result is represented as arrow symbol with different angles based on the D8 concept illustrated in Fig. 4. These point features will undergo the process of resampling pixel and convert to point using ArcGIS software.

On the other hand, D16 algorithm should be converted from point features into Comma Separated Value (CSV) format with ID, coordinate (X, Y), and height as the attributes. This CSV file will be the input data for D16 algorithm because this compiler tool is prepared in Ruby programming language which is not supported by ArcGIS software.

The study involved a comparison of several approaches by using different sources of raster data so that the output result of D16 algorithm is valid for almost all GIS raster data. The concept and formulae of D16, D16 coding for external tool and method for comparing the algorithms will be discussed in this section.

3.1 Concept of D16

The designed D16 algorithm uses almost 5×5 pixel neighbour resolutions that will provide 22.5 degree (22.5°) for each neighbour direction as in Fig. 9a, which is half of the angle range for D8 method. This will produce 50 % increment in the available flow direction options compared to the D8 method. However, due to the restriction introduced, it might have less than 40 % chances on flow direction to select these new additional eight directions.

The additional rules and equations are introduced to enhance the result of D8 algorithm. The new features or sub-algorithms embedded in D16 are:

1. Additional of eight new directions option from D8 algorithm.
2. Using D8 method for the first 3×3 pixel resolution for second outer pixels
3. Introduction of Intermediate Factor (IF) to restrict and filter the flow direction to the eight new added directions, illustrated in Fig. 9b.
4. Implementation of Sink and Stagnant formula.

3.1.1 Deriving D16 Algorithm Formulae

Since it is raster based, the array format in programing is the most suitable method to illustrate the derived formulae. The main formulae involved in the computation are:

$$\text{Distance} \quad : \sqrt{\left[(X_1 - X_2)^2 + (Y_1 - Y_2)^2\right]} \tag{1}$$

$$\text{: derived from Distance Weighted, } w(d) = 1/d^p$$

(NCGIA 1988–2013)

$$\text{Height difference} \quad : Z_\alpha = Z_n - Z_{D16} \tag{2}$$

$$\text{Intermediate Factor} \quad : \text{Height intermediate, } Z_{IF} = (Z_a + Z_b)/2 \tag{3}$$

$$\text{: if } Z_{IF} < Z_n, \text{ the test is pass.}$$

$$\text{Stagnant} \quad : Z_{\alpha(max1)} > -0.001 \textbf{ and } Z_{\alpha(max2)} < 0.001 \\ \textbf{and } Z_{\alpha(max3)} > 0.0001 \textbf{ and } Z_\alpha < 0.3 \tag{4}$$

$$\text{Sink} \quad : Z_\alpha = \text{nil } \textbf{or } Z_\alpha > \textbf{Stagnant}(0.3) \tag{5}$$

The values for stagnant formulae (4) are not a constant numbers, it can be varied depend on users or applications requirement of expected result. However, the values of the stagnant formulae were fixed at certain constants in this study for the purpose of general comparison testing on the swamp area aspect.

3.1.2 D16 Algorithm Program Coding

In order to automatically generate the result from D16 algorithm formula, the Ruby programming language is used to write a compact and simple D16 algorithm structure as shown in Fig. 8 into an execution file. Ruby is a dynamic programming language; reflective, general-purpose specialized in object-oriented concept that combines syntax inspired by Perl with Smalltalk-like programming language (Wikipedia 2010).

3.2 Comparison of D8 and D16 Algorithm Result

There are many methods and approaches used to compare the results between D16 algorithm and the existing D8 algorithm. Small resample size pixels, large scale area comparison, 3D modelling technique (3D view) and etc. were used to verify the accuracy increment of the D16 algorithm from the D8 algorithm. In general, these comparison methods can be classified based on the data type itself:

• Topographic map	: 3D Visualization
• SRTM	: Comparison using visual interpretation
	: Generalization technique
	: Edge reliability comparison
• ASTER	: Swamp area detection

Comparison of small pixel size with larger pixel size is a necessary method because small pixel resolution provides more accurate results in situation where the data is stored for each smaller pixel size in details as in a large-scale map. As compared to a bigger resample pixel size, the information or data had been generalised and the output information is less accurate which contains fewer details as stored in large small-scale map. A smaller pixel resolution is used and acts as a schema to a bigger pixel resolution in comparing the accuracy of the final result for both algorithms.

Wilson (2002) highlights D8 algorithm as good at valley area but cannot model the flow divergence at ridge areas. Thus, a test on SRTM data will be used to generate a general visual interpretation for both in valley and hilly areas. STRM data also will be used in generalisation comparison for both algorithms, which use a resampled pixel of 30 m resolution toward 120 m resolution.

A 3D model will be created from ArcScene module (ArcGIS software) for visualisation purposes for both results. This testing technique is organized to determine which algorithm can provide a better reliability result in the real modelling scheme according to the nature of water flow direction (able to flow

freely in 360° in the steepest slope). While, the data used in this testing method is the contour and river tributary data, which had been digitised from topographic map. A Triangulated Irregular Network (TIN) will then be created from the contour data using ArcGIS software. The TIN surface model is the best raster surface to model the terrain slope and aspect of the study area that combined with the river tributary and to create a model the water flow direction.

4 Implementation and Result

The result of this comparison method can be categorised into two. These are based on the implementation categorised by the data sources, which are SRTM and Topographic map (secondary data) and ASTER data.

4.1 SRTM Result (Overlay with TIN Surface)

There are three main comparison aspects used to be observed in this SRTM data. All of them show that D16 algorithm produces much better results than D8 algorithm result. The aspects are:

i. Accuracy (divergence in ridge area and smoother flow direction model and less conflict occur)
ii. Generalisation result
iii. Edge reliability

4.1.1 Accuracy

Figure 10a and b clearly shows that D16 can produce more accurate result (sink and stagnant) based on the TIN surface, higher divergence in hilly area (purple colour indicated eight additional flow direction options) and able to produce a smooth water flow direction model compared to D8 algorithm.

4.1.2 Generalization

Besides that, D16 algorithm is capable of generating a better generalisation result when dealing with bigger pixel size. There are two set of resolution used in this testing method, a resampled of 30 m resolution and 120 m resolution SRTM data samples in order to verify which algorithm will produce better generalisation result. Figures 11 and 12 are the result of D16 algorithm before and after
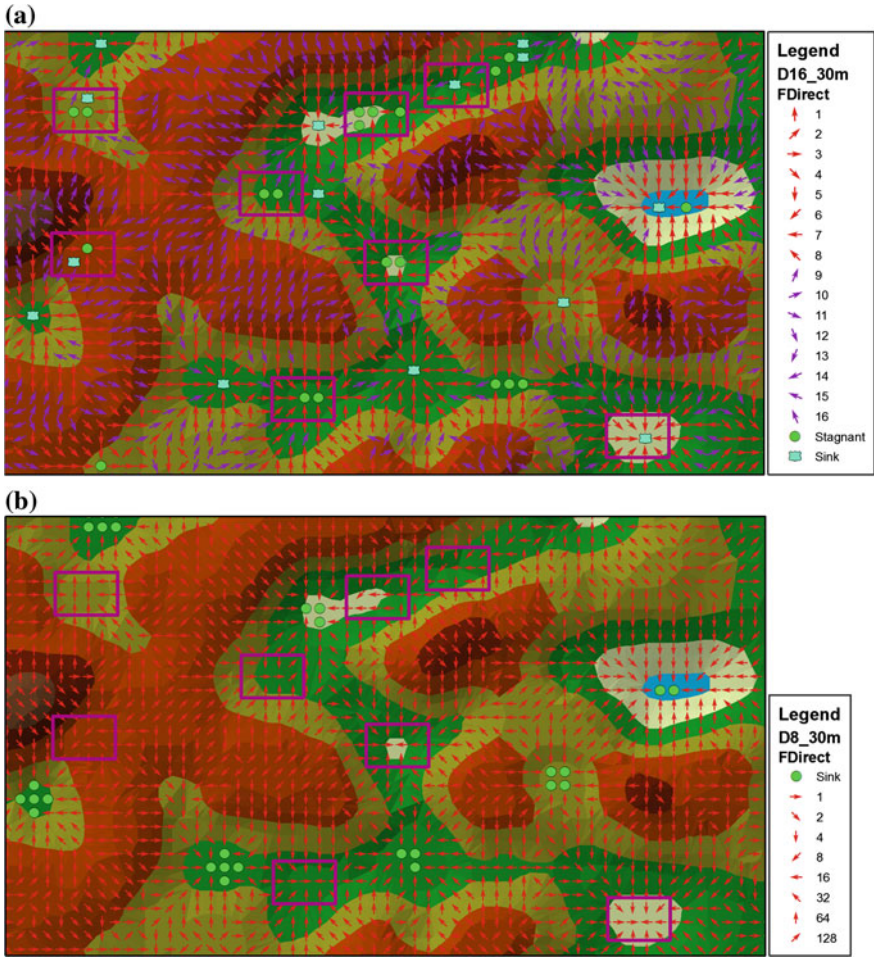
Fig. 10 Accuracy comparison between D16 (**a**) and D8 (**b**) algorithms result

generalisation process respectively. The generalisation technique in D16 will reduce the number of stagnant areas while increasing the number of sink areas.

On the other side, D8 algorithm will reduce the number of sink area when undergo the process of generalisation. As a result, D8 only produces several sink areas as shown in Figs. 13 and 14, after four (4) times scale generalisation from actual resolution. The percentage difference of D8 generalisation process that still maintains the sink area is about 15.38 % compare to D16 result around 125.0 %. Thus, D16 algorithm is capable of producing 8.13 times greater accuracy details in the generalisation process compared to D8 algorithm using the constant values in stagnant and sink formulae as discussed in Sect. 3.1.1.

Number of sink = 16
Number of swamp area (single + clustered) > 67
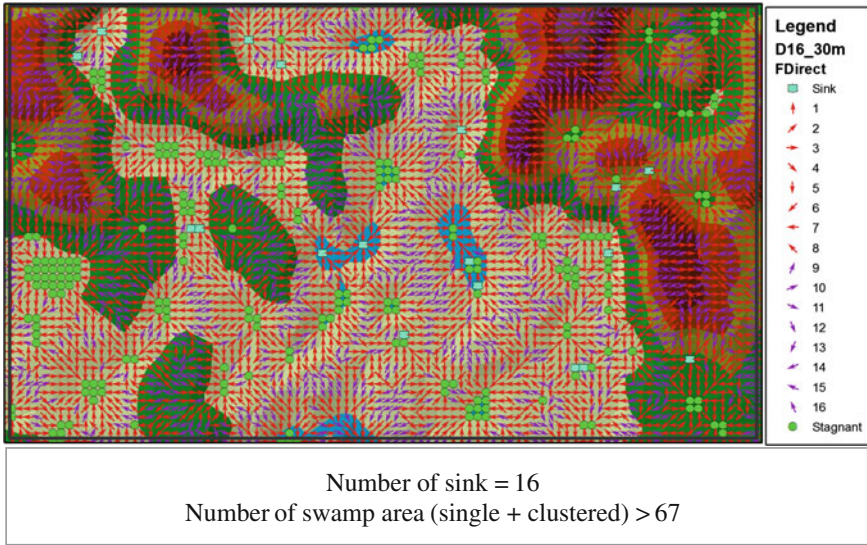
Fig. 11 A 30 m resolution D16 result

Number of sink = 20
Number of swamp area (single + clustered) = 4
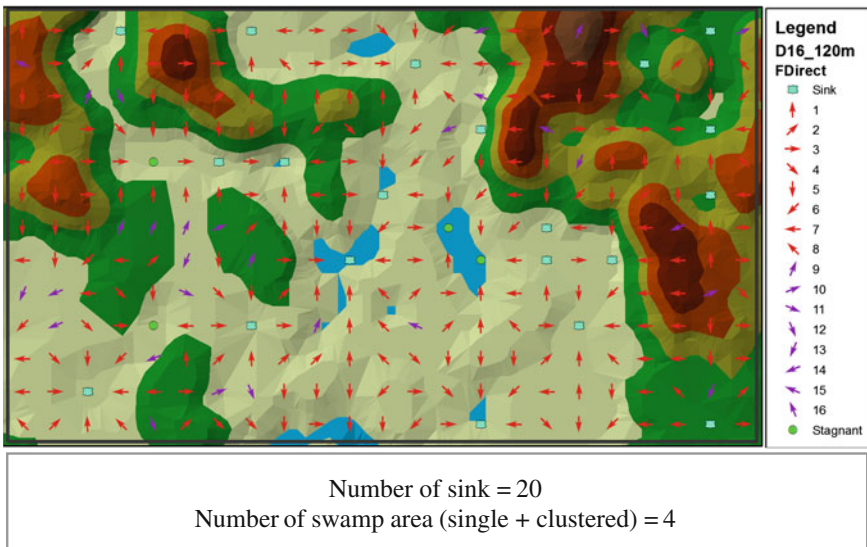
Fig. 12 A 120 m resolution D16 result

Number of sink/no direction location (single + clustered) =26
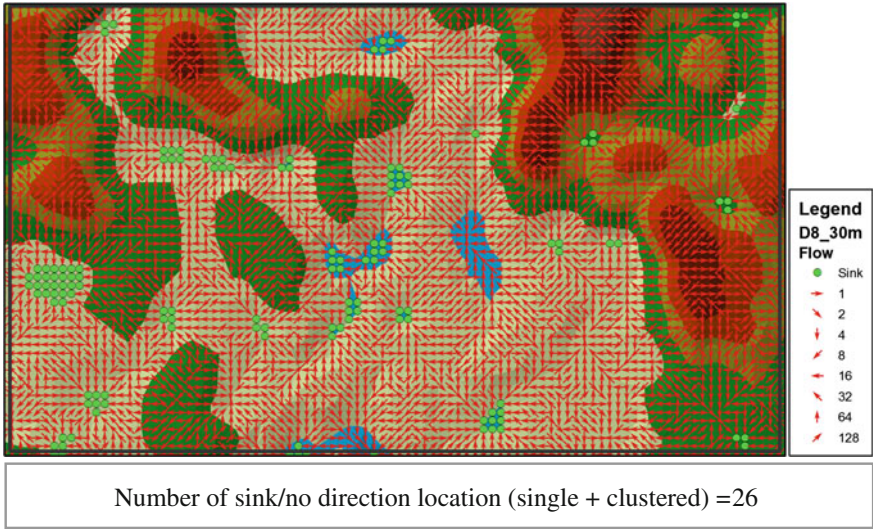
Fig. 13 A 30 m resolution D8 result

Number of sink/no direction location (single + clustered) = 4
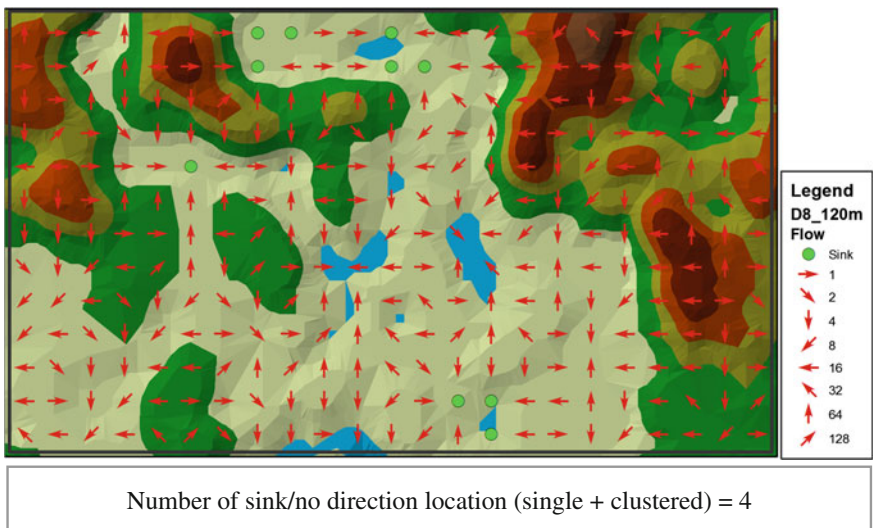
Fig. 14 A 120 m resolution D8 result

4.1.3 Edge Reliability

On the edge reliability aspect, D16 has shown a better result than D8 because it used D8 algorithm to calculate the edge flow direction for 3×3 pixel resolutions and leave the 2×2 outer pixels as shown in Fig. 15a. Figure 15b represents the
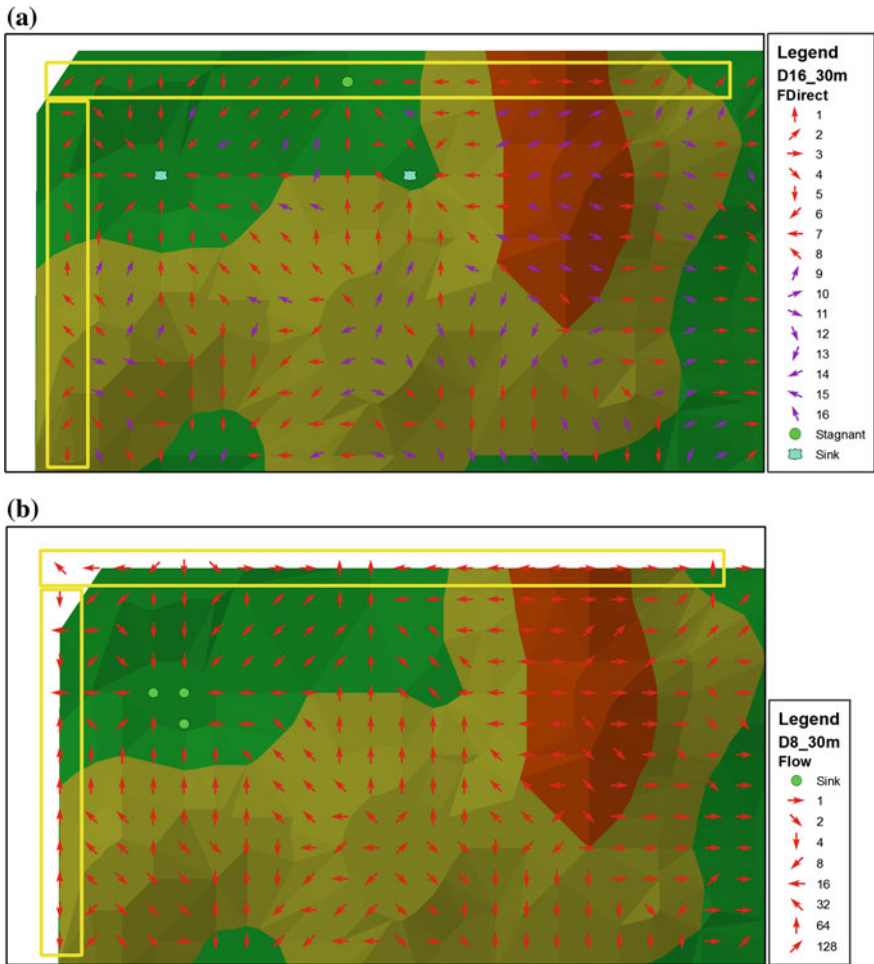
Fig. 15 Comparison of D16 (**a**) and D8 (**b**) in term of edge reliability aspect

edge result produced by D8 algorithm where it clearly shows that some of them point blindly toward no data provided by raster or pixel.

4.2 Topographic Map Result (3D View)

Figure 16 shows that D16 has more capability to model flow divergence and produce reliable result compared to D8 result in Fig. 17. When visualising and inspecting each corner of the 3D model for both results, it clearly showed that D16 produce better reliability of flow divergence either in ridge area or at stream
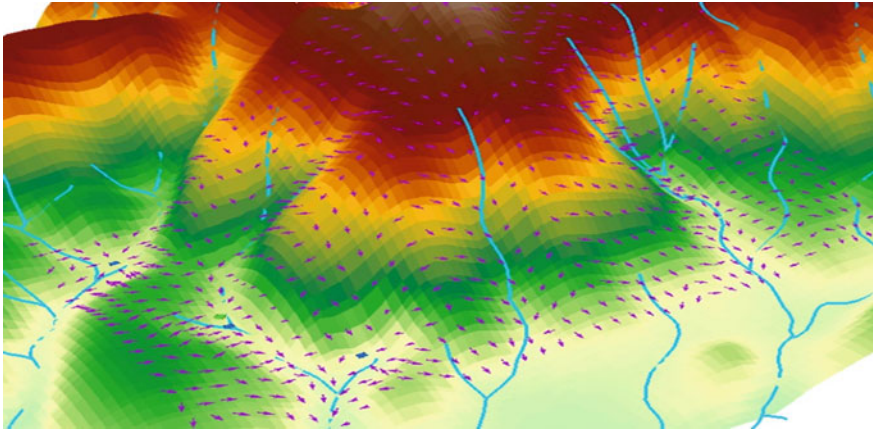
Fig. 16 D16 result with TIN generated from contour and river tributary layer
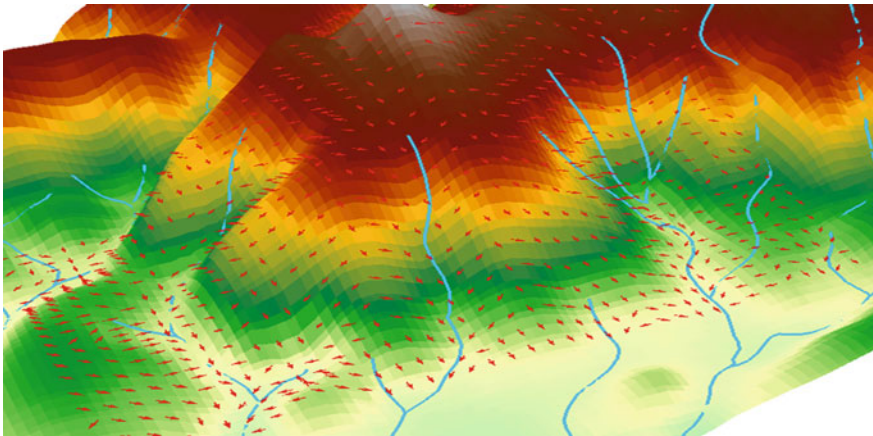
Fig. 17 D8 result with TIN layer and river tributary

network. D16 is able to produce a better reliability upon the nature of surface water flow direction compared to D8.

4.3 ASTER Data for Swamp Area Detection

By introducing another state of water movement such as stagnant and sink, a new application can easily be created through D16 algorithm in which D8 cannot produce. It is the automatic detection of swamp area that was really needed, for example, large-scale agriculture activity and estate plantation companies for their
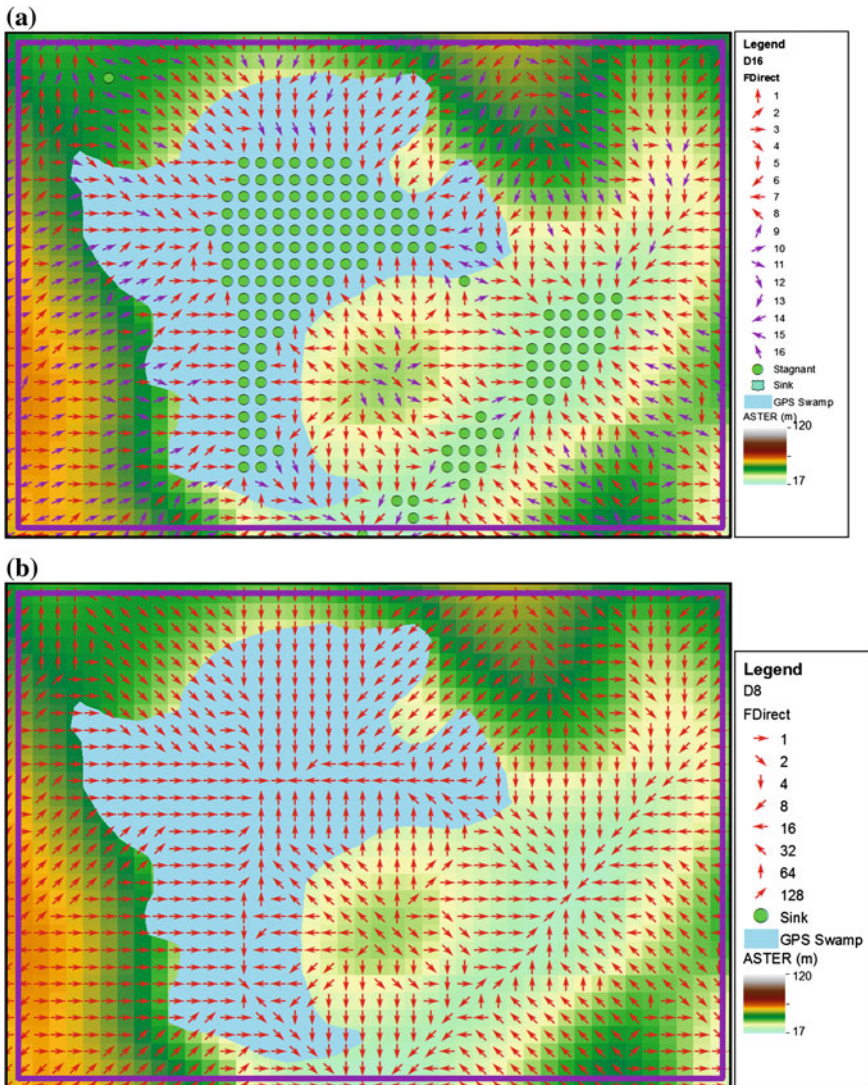
Fig. 18 Comparison of D16 (**a**) and D8 (**b**) result on swamp area detection

water supplement management and other application. An automatic detection of swamp area in the plantation estates can be easily done without embarking on field collection such as using GPS as presented in blue polygon of Fig. 18a and b.

Furthermore, D16 is also capable to produce the stream alignment and stream width using the swamp phase for a larger area. Figures 19 and 20 illustrate the overall shape of stream network that both algorithms produced in a small-scale map. The yellow polygon layer is the GPS data on field collection.
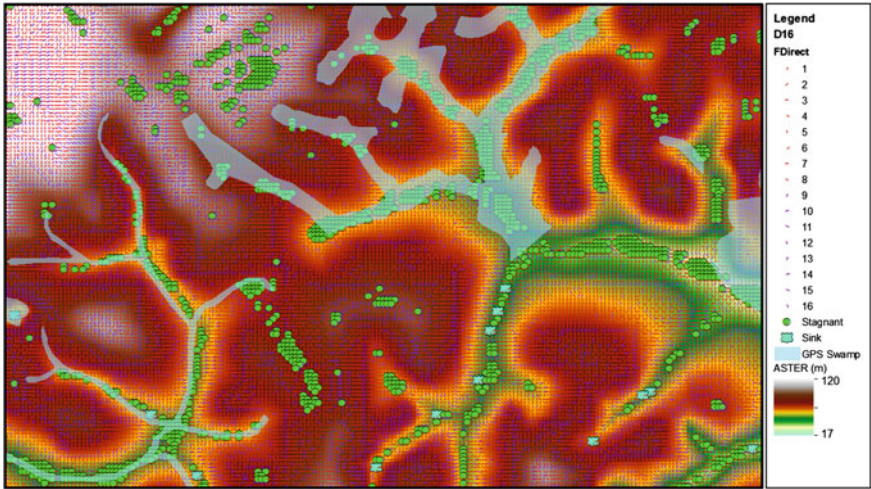
Fig. 19 D16 stream network detection result
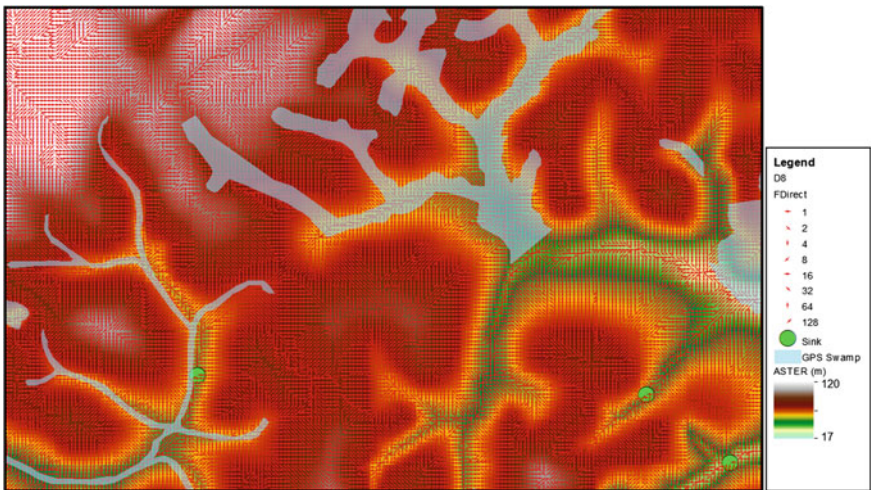
Fig. 20 D8 stream network detection result

5 Concluding Remarks

As a brief introduction of the water flow direction model, this paper discusses the existing algorithms used in SFD and MFD model. The discussion continued further to the concept of several existing flow direction models, especially on D8 algorithm. The limitations of the D8 algorithm stated by some water-related

researchers are highlighted in this paper as the problem statement to introduce the D16 algorithm.

D16 was initially derived to overcome the weakness of the SFD model especially in D8 algorithm, yet when introducing some rules and new equations on the model, the results show a surprising positive enhancement toward the current accuracy of D8 algorithm. D16 algorithm had shown enhancement in accuracy, reliability and consistency of the flow direction results compared to D8 algorithm. The problem related to flow divergence in a ridge area also being enhanced by D16 via the additional eight flow direction options from D8 algorithm.

Based on three sources of raster data used with various testing methods, D16 algorithm had shown that it is capable to produce better accuracy, flow divergence, smoothness, edge reliability, and better result of generalisation and produce a stagnant state of rain water compared to D8. Although the construction of D16 seems to be a bit complicated with many new equations introduced compared to D8 algorithm, a new automated approach can be derived easily with D16 algorithm as discussed in Figs. 18, 19 and 20.

In the nutshell, all the testing methods used in this study have shown a positive enhancement compared to D8 algorithm. Thus, this algorithm, hopefully, fulfils the accuracy demand from other field professions, which are somehow related to the water flow modelling. However, because of the complexity of equations applied in D16 as well as an external program in ArcGIS software, this study cannot afford to measure and compare in terms of processing time for both algorithms. However, the authors believe that the upturn of machine or computer technology today is capable to perform D16 algorithm much faster compared to the D8 algorithm when it was introduced and implemented over 28 years ago.

References

Bernard P, Dee T, Richard H, and Paul B (2010) Geology and the Environment, Cengage Learning. Inc., p 18. ISBN-10:0-538-73755-70

Boonklong O, Jaroensutasinee M, Jaroensutasinee K (2007) Computation of D8 flow line at Ron Phibun area, Nakhon Si Thammarat, Thailand. World Acad Sci Eng Technol 33:2007

Fairfield J, Leymarie P (1991) Drainage networks from grid digital elevation models. Water Resour Res 27(5):709–717

Hengxing LAN, Martin CD, Froese CR, Chao D, & Chowdhury (2008) S. A Web-Based GIS Tool for Managing Urban Geological Hazard Data

Hodgson ME, Bresnahan P (2004) Accuracy of Airborne Lidar-Derived elevation: empirical assessment and error budget, Photogrammetric Engineering & Remote Sensing 70(3):331–339

Laura (2001) Terraflow background. Duke University (Computer Science), Durham

Lindsay J (2012) Rho8 flow pointer (direction), whitebox geospatial analysis tools. University of Guelph, Guelph

Miller B (2010) Comparison of surface hydrologic algorithms in GIS. Michigan State University, USA

Moore ID, Grayson RB, Ladson AR (1991) Digital terrain modeling: a review of hydrological, geomorphological and biological applications. Hydrol Process 5:3–30

NCGIA (1988–2013) Interpolation: inverse distance weighting. The Regents of the University of California, National Center for Geographic Information and Analysis, California

O'Callaghan JF, Mark DM (1984) The extraction of drainage networks from digital elevation data. Comput Vision Graph Image Process 28:328–344

Rivix LLC (2008) RiverTools 3.0 User's Guide. Rivix Limited Liability Company, Broomfield, CO

Schuckman K, Renslow M (2009) Lidar technology and applications. The Pennsylvania State University, USA

Smith MJD, Goodchild MF, Longley PA (2009) Geospatial analysis—a comprehensive guide to principles, techniques and software Tools. Matador, The Winchelsea Press, Winchelsea, UK, p 560

Tarboton DG (1997) A new method for the determination ff flow directions and upslope areas in grid digital elevation models. Water Resour Res Am Geophys Union 33(2):309–319

Tobler WR (1970) A computer movie simulating urban growth in the Detroit region. Econ Geogr 46(2):234–240

Wikipedia (2010) Ruby, Ruby (programming language)

Wilson JP (2002) Terrain analysis tools for routing flow and calculating upslope contributing areas. In: Terrain analysis for water resources applications symposium 2002

The Geocentric Datum of Malaysia: Preliminary Assessment and Implications

Noor Suryati Mohd Shariff, Tajul Ariffin Musa, Kamaludin Omar and Rusli Othman

Abstract The reliability of the national geocentric datum must be assessed regularly to maintain high geospatial accuracy in terms of consistency with respect to the global datum, i.e. International Terrestrial Reference Frame (ITRF). This can be accomplished by considering the spatial and temporal variations caused by plate tectonic movements. This study aims to assess the reliability of Geocentric Datum of Malaysia (GDM2000) by analysing the datum shifts via the displacements of the Malaysian Real Time Kinematic Network (MyRTKnet) stations caused by tectonic movements as well as the displacements induced by reference frame effects. A significant land displacement up to 17 and 30 cm in north and east components were found respectively, due to local active fault and the cumulative plate tectonic motion. The implications of a non-geocentric datum are also discussed.

Keywords Geocentric datum · Reference frame · Plate tectonic

1 Introduction

The geocentric datum represents a best-fit ellipsoid where its origin and orientation is with respect to the Earth-centred Earth-fixed (ECEF) coordinate system. Therefore, the geocentric datum has the following descriptions; (1) its origin coincides with the Earth's centre of mass, (2) the orientation of the X-axis is pointing towards the mean Greenwich meridian, (3) the Z-axis is parallel to the rotation axis of the earth, (4) the Y-axis completes the right-handed system, and

N. S. M. Shariff (✉) · T. A. Musa · K. Omar · R. Othman
GNSS and Geodynamics Research Group, Faculty of Geoinformation and Real Estate,
Universiti Teknologi Malaysia (UTM), Johor, Malaysia
e-mail: suryatishariff@gmail.com

(5) the ellipsoidal axes (a, b) coincides with the X and Z axis, respectively (Leick 2004, Hofmann-Wellenhof et al. 2008).

The realization of a geocentric datum can be classified into three hierarchical levels: global, regional and national. The global realization of a geocentric datum is represented as the foremost datum, followed by the regional and national geocentric datum whereby each realization of the geocentric datum is essentially consistent with the International Terrestrial Reference System (ITRS). The ITRS is realized through the International Terrestrial Reference Frame (ITRF), which represents the best available global geocentric datum. There are several improvements that have been continuously made in the data analysis strategy to achieve the optimal solution for the generation of ITRF (Altamimi et al. 2005). The ITRF takes into account the spatial and temporal variations of its network coordinates and their velocities due to the effects of tectonic plate motion, earth orientation and polar motion (Altamimi et al. 2008, Janssen 2009, Johnston and Morgan 2010). This is achieved by updating and refining its frame regularly. Presently, the version of the ITRF is ITRF2008. Additionally, the ITRF is an indispensable reference that is required to ensure the integrity and inter-operability of Global Satellite Navigation System (GNSS) (Altamimi et al. 2008).

The Geocentric Datum of Malaysia (GDM2000) was adopted by the Department of Survey and Mapping Malaysia (DSMM) to establish a global and homogeneous coordinate system across the country. The realization of the GDM2000 was based on the ITRF2000 at epoch 1st January 2000. However, the GDM2000 remains as a static datum where all site coordinates are fixed or assumed unchanged with time. In fact, the Earth is actually dynamic and experiences numerous deformation events such as plate tectonic motions and earthquakes. The tectonic plates move gradually with the velocity typically varying in many places, up to a few centimetres annually (Anderson 2012). Moreover, a strong earthquake will cause a significant land displacement ranging from decimetre to meters, depending on the site distance from the epicentre.

Malaysia is situated within the Sundaland block. Previously, the Sundaland represents a stable tectonic block, moving approximately east with respect to Eurasia plate at a velocity of 12 ± 3 mm per year (Michel et al. 2001) as shown in Fig. 1. However, since the mega earthquakes in Aceh (2004), Nias (2005) and Bengkulu (2007) the country has experienced significant land displacements (Simons et al. 2007, Chlieh et al. 2007, Socquet et al. 2006, Banerjee et al. 2007). According to Vigny et al. (2005), the 2004 Aceh earthquake had significantly resulted in land displacements up to 10 cm in magnitude for a radius of 400 km away from the earthquake epicentre. Figure 2 shows the post-seismic and co-seismic motions in Peninsular Malaysia from 2004 until 2008 which is the combination of the aforementioned earthquakes and plate tectonic motion (Omar and Mohamed 2010). These studies have indicated that Malaysia is no longer in a stable region.

These earthquakes and plate tectonic motions dislocate the GPS reference stations, thus affecting the geocentric datum causing it to be no longer geocentric (non-geocentric) and does not represent the "true" position of the points. The
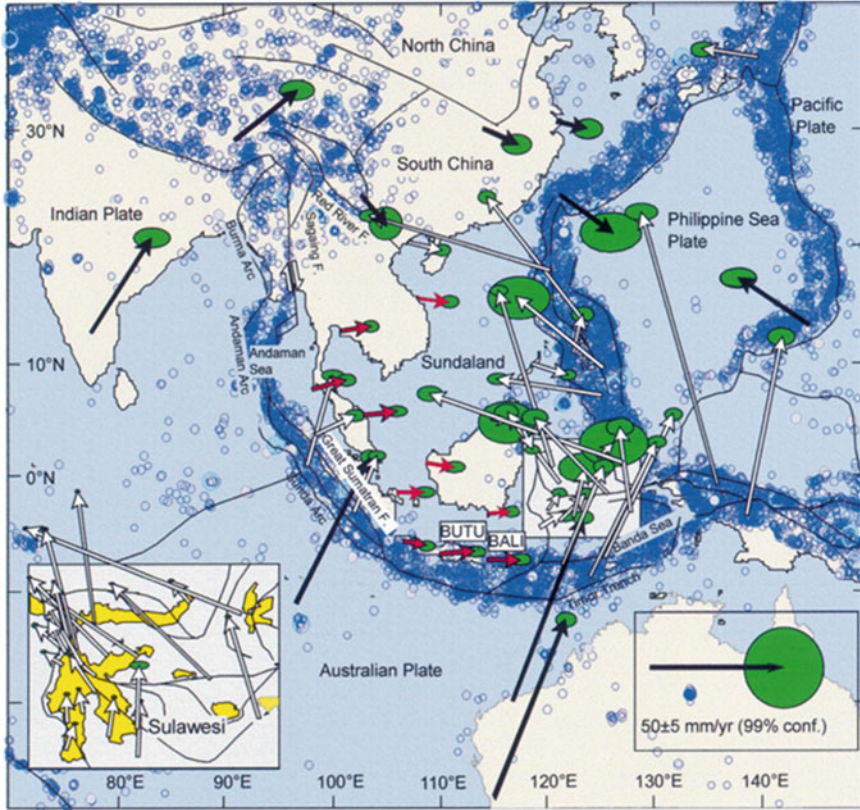
Fig. 1 Map of global positioning system (GPS) velocity vectors from the study by (Michel et al. 2001). *Black arrows* represent GPS velocity vectors of the permanent stations from IGS and AUSLIG; *red* and *white arrows* shows velocities derived in the study where the *red arrows* represent 'stable' Sundaland velocities. *Blue dots* denote epicentres of crustal earthquakes from the U.S. Geological Survey (USGS) catalogue (1973–2001)

consequence is not only seen to affect the activities of survey and mapping, but will also have a big impact on the socio-economic and environment in general. Therefore, a geocentric datum must consider the earth's geodynamic processes (Kelly 2012).

This study firstly addresses the establishment and the current status of the GDM2000. Secondly, tests were conducted to assess the reliability of the MyR-TKnet stations' coordinates in GDM2000 by analysing the datum shifts via (1) the displacement of MyRTKnet stations between epoch 2000 and epoch 2011 in ITRF2000, (2) displacement of MyRTKnet stations between epoch 2000 in ITRF2000 and epoch 2011 in ITRF2008. Finally, the implications of a non-geocentric datum are discussed.
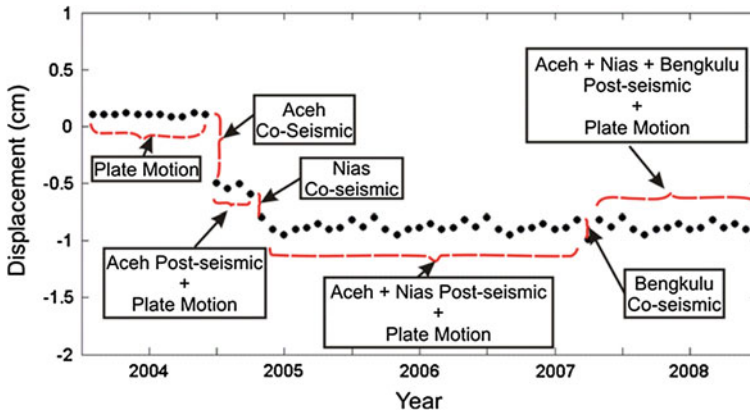
Fig. 2 Post-seismic and co-seismic motions in Peninsular Malaysia (Omar and Mohamed 2010)

2 Status of Geocentric Datum of Malaysia (GDM2000)

Traditionally, there were two existing local geodetic reference systems in Malaysia, namely the Malayan Revised Triangulation 1948 (MRT48) for Peninsular Malaysia and Borneo Triangulation System 1968 (BT68) for Sabah and Sarawak. The reference ellipsoid for the MRT48 and BT68 are Modified Everest (Kertau) and Modified Everest (Timbalai), respectively (Department Survey and Mapping (DSMM) 2009). However, their origins are not explicitly defined and in practice could be many hundreds of metres away from the geocentre (Kadir et al. 2003). On 26 August 2003, the GDM2000 was officially launched nationwide as a national geocentric datum to replace the MRT48 and BT68. It was realized through a set of GPS observations at seventeen (17) Malaysia Active GPS System (MASS) stations and eleven (11) IGS stations, from 1999 to 2002. All the MASS coordinates were defined on the most precise available reference frame at that time i.e. the ITRF2000, based on the Geodetic Reference System (GRS80) ellipsoid.

In 2002, DSMM established a new Continuously Operating Reference Station (CORS) network known as the Malaysian Real-Time Kinematic GNSS Network (MyRTKnet) with 78 reference stations nationwide, to improve the MASS stations and support the generation of network-based positioning solutions. However, on 26 December 2004, these stations underwent land displacements in the range of 1.5–17 cm and orientation predominantly in the south-west direction due to the co-seismic motion from the Aceh earthquake (Department Survey and Mapping (DSMM) 2009). Similarly, the results from Nias and Bengkulu earthquakes indicated land displacements of between 1–6.5 cm and 1–3 cm respectively, also in the south-west direction (Department Survey and Mapping (DSMM) 2009). Therefore, a revision of the GDM2000 was carried out.

Thus far, the revision of GDM2000 had been conducted in epoch 2006 and 2009 which were labelled as GDM2000 (2006) and GDM2000 (2009),

respectively. Both of the versions were revised using a similar procedure where the set of new coordinate data were brought to the ITRF2000 at epoch 2000.0, which is the original of GDM2000. In the case of GDM2000 (2009), the reference stations, i.e. the IGS stations, in ITRF2005 at epoch 2007.67 were brought to ITRF2000 at epoch 2000.0 using published velocity models. Based on the Helmert Transformation, root mean square (RMS) fitting for the coordinates of four reference stations (KUCH, BINT, KINA and MIRI) were less than 1 cm in the north, east and height components, respectively (Department Survey and Mapping (DSMM) 2009). Therefore, the coordinates of these four reference stations were fixed, in the final local combined adjustment, with respect to the original GDM2000 (Department Survey and Mapping (DSMM) 2009). However, the set of coordinates of MyRTKnet in GDM2000 (2006) are still being adopted at present. It is due to the discrepancy involved between the new set of coordinates GDM2000 (2009) and the existing database in GDM2000.

3 The Shift of GDM2000

As aforementioned, the GDM2000 has been revised to take into account the co-seismic motions. However, there are no further actions to revise and update the GDM2000, especially with the consideration of post-seismic motion as well at every MyRTKnet station. In order to test the compatibility of GDM2000 with the current position, GPS observation data on Day of Year (DoY) 001 until 023 in year 2011 have been processed by using Bernese GPS processing software. The processing stage involved 63 MyRTKnet stations and 22 IGS stations using the double-difference with Quasi Ionosphere Free (QIF) strategy. The data was processed in ITRF2008 as well as in ITRF2000. The idea was to compare the two set of coordinates in ITRF2000 and ITRF2008 for DoY 001 until 023 with the available set of GDM2000 (2006) coordinates in ITRF2000 epoch 2000.

3.1 Test I: Comparison Between Epoch 2000 and 2011 in the Same Reference Frame ITRF2000

In this test, the set of coordinates at epoch 1st January 2011 was compared to the published set of coordinates of GDM2000 (2006), where both were in ITRF2000. Figure 3 shows the differences of these two set of coordinates in terms of vector displacements. It can be deduced that the position of the sites moved with an average magnitude of 25.5 cm and orientation of 118.8° from epoch 2000 to epoch 2011.
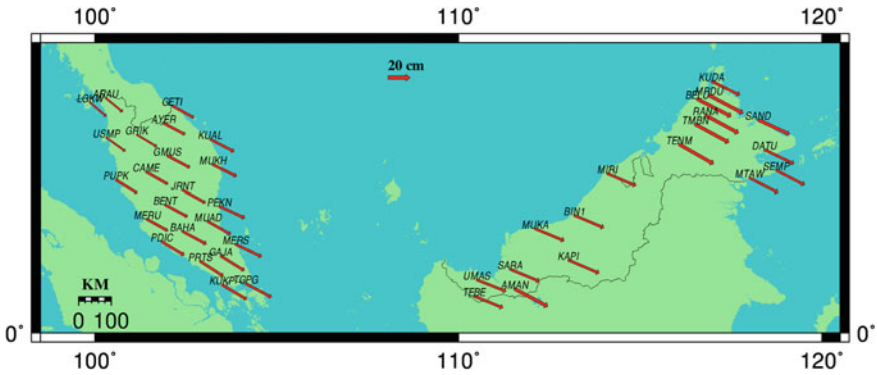
Fig. 3 Comparison between Epoch 2000 and Epoch 2011 in ITRF2000
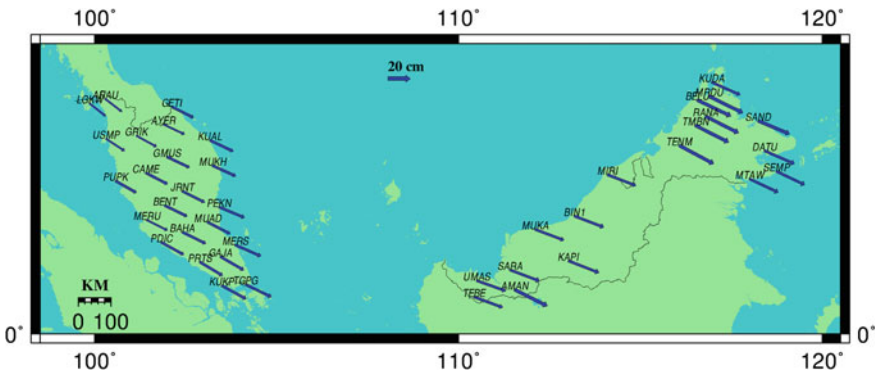
Fig. 4 Comparison between Epoch 2000 in ITRF2000 and Epoch 2011 in ITRF2008

3.2 Test II: Comparison Between Epoch 2000 and 2011 in Different Reference Frames: ITRF2000 and ITRF2008, Respectively

Similar to Test I, one set of coordinates at epoch 1st January 2011 was compared to the published set of coordinates of GDM2000 (2006), but in different reference frames: ITRF2000 and ITRF2008, respectively. Figure 4 illustrates the differences in terms of vector displacements between the two set of coordinates. It can be shown that the position of the sites moved with an average magnitude of 24.7 cm and orientation of 116.7° from epoch 2000, in ITRF2000 to epoch 2011 in ITRF2008.
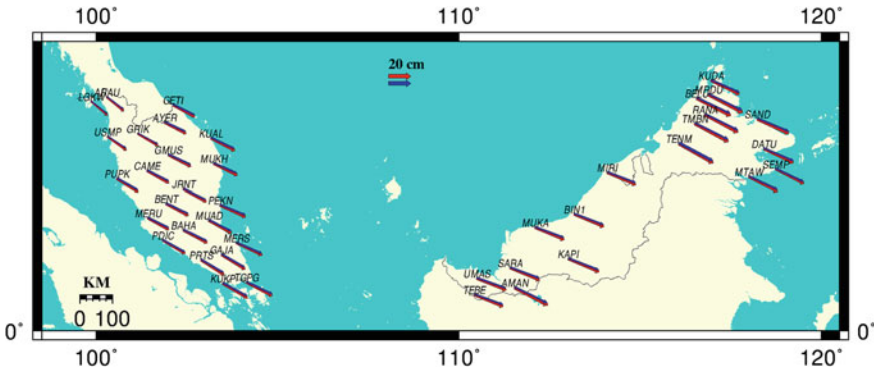
Fig. 5 Comparison between ITRF2000 and ITRF2008 at epoch 2011

3.3 Test III: Comparison Between ITRF2000 and ITRF2008 Reference Frames at Same Epoch 2011

The objective is to show the effect of the set of coordinates in different reference frames, ITRF2000 and ITRF2008, at a single epoch 2011. Figure 5 shows that the vector displacements of epoch 2011 in ITRF2000 (denoted as red arrow) and vector displacements of epoch 2011 in ITRF2008 (denoted as blue arrow). The displacements are almost identical in terms of magnitude and orientation, the difference being about 2 cm in magnitude and about 2° in orientation from the GDM2000 (2006).

3.4 Test IV: Time Series Analysis for Coordinates Difference Between Epoch 2011 in ITRF2000 and the GDM2000 (2006)

The time series of displacements at selected areas is shown in Fig. 6. The selected areas are classified as north (ARAU), south (KUKP) and east (MUKH) of Peninsular Malaysia, as well as Sabah (RANA) and Sarawak (SARA). It was found that the largest horizontal displacement occurred at RANA station up to 17 and 30 cm in the north and east components, respectively. It is due to the fact that the RANA station is located near active fault zone; hence prone to its influences. A study by (Mohamed 2012) shows that the stations coordinates of the Ranau GPS Campaign 2010 underwent displacements of a few mm to 5 cm at stations located in the Mendasan and Lobou-Lobou fault zones. Meanwhile, the smallest displacement occurred at ARAU for the north component and at MUKH for the east component. This is due to the effect of post-seismic motion at the stations.
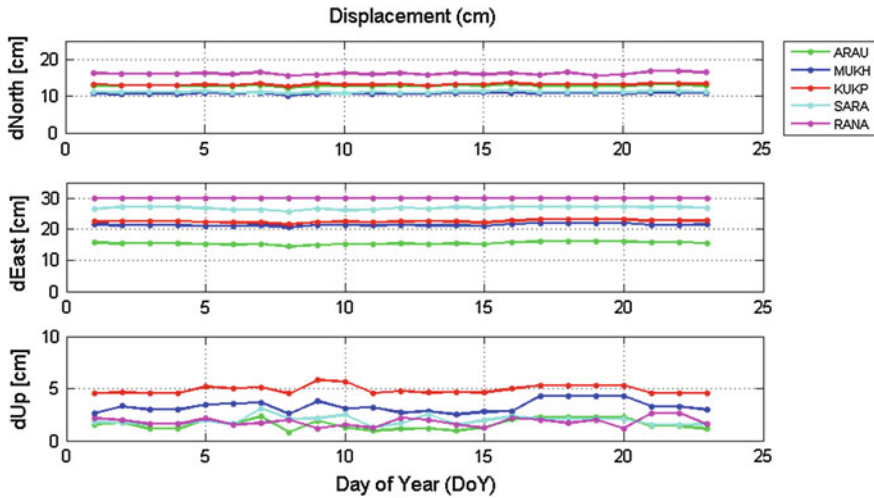
Fig. 6 Time series of displacement at ARAU, KUKP, MUKH, RANA and SARA stations

4 Implication of the Geocentric Datum Shift

The consequences of not updating the geocentric datum to the latest epoch (e.g. 2013), and the present reference frame (ITRF2008) have resulted in a number of implications, which are discussed in the following sub-sections.

4.1 Inconsistent Satellite Orbit and Coordinate Bias

The GNSS reference system for instance, the WGS84 (G1674) for GPS, Parametrop Zemp 1990 (PZ-90) for Globalnaya Navigatsionnaya Sputnikovaya Sistema (GLONASS), China Geodetic Coordinate System 2000 (CGCS2000) for BeiDou, Galileo Terrestrial Reference Frame (GTRF) for Galileo and Japan satellite navigation Geodetic System (JGS) for Quasi-Zenith Satellite System (QZSS) have been designed to be compatible with the global datum, i.e. ITRF. The GNSS reference system is mainly used for satellite orbit determination. Hence, the position of a satellite (ephemeris and especially precise orbit) is corresponding to the ITRF. Therefore, if the national network is contaminated with displacement, the national geocentric datum will no longer be compatible with the ITRF. This can lead to inconsistency in the satellite orbit interpretation. Furthermore, it would introduce coordinate bias, especially in relative positioning, that can be considered in a similar manner as the satellite orbit bias. Figure 7 illustrates the coordinate bias at a reference station; this gives a wrong estimated rover's position in relative positioning.

Fig. 7 Coordinate bias in the relative positioning
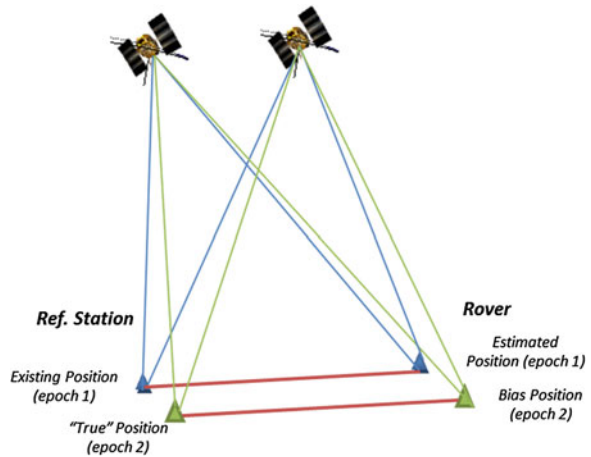
4.2 Confusion and Mismatch with Base Map

It is recognized that many social and economic activities such as navigation, civil engineering, oil and mineral exploration, agriculture and disaster management, are relying on accurate geocentric datum. Therefore, if the national geocentric datum is not accurate and updated, it will lead to misinterpretation and wrong decision making on land, property and other related matters. For instance, there could be a risk in the cadastral matters that involve dispute in the boundaries, size and shape of land parcels due to land displacement. Furthermore, any coordinate disparity between the "true" and existing geocentric datum will lead to confusion and misinterpretation of the actual position, especially when compared to absolute positioning, e.g. Precise Point Positioning (PPP), results with the existing base map. On the contrary, when using maps in the same reference system with the data, the mismatch can be avoided. However, there are users who do not take notice of the different reference system used in the data and maps or the existence of local deformation, but usually attribute such problems to data processing and positioning technology.

4.3 Decreased Accuracy of Reference Stations Coordinates

The reference stations should be maintained in the order of mm-level accuracy in terms of correspondence with the latest realization of ITRF. Furthermore, the reference station should be compatible with the ITRF because it is essential to avoid transition problems in boundary zones of countries (Pinto 2009). Inaccurate coordinates of the reference stations may also limit scientific research and applications that normally require a reliable coordinate system at the reference stations.

4.4 Managing the Geospatial Database

It is realised that significant earth deformation has occurred with evidences as shown in Sect. 3. The static datum option is not appropriate because it would not effectively consider the significant land displacements. Therefore, one of the options is to regularly update the geocentric datum in order to update the cadastral and mapping database. However, this option raises significant issues especially to a major group of cadastral surveyors and stakeholders due to the assumption of complexity in managing the updated geospatial database. At this stage, it is essential to propose the best mechanism to simplify the management of digital spatial data. With the present computing capability, cartography and Geographical Information System (GIS) technology, it is possible to transform spatial data from one epoch and reference frame to the other seamlessly (Pinto 2009). The important input to allow this transformation is either the velocity or transformation parameters.

5 Concluding Remarks and Future Work

The above review on the status of GDM2000 and several tests about the land displacements have justified that the existing datum is static and does not accommodate the land displacements. This implies that the GDM20000 is non-geocentric, which is only useful for local surveys. In Ranau, for instance, a significant land displacement up to 17 and 30 cm in north and east components respectively occurred mainly due to local active faults and the cumulative plate tectonic motion from 2006 to 2011. The consequences include the following—inconsistent satellite orbit and coordinate bias, confusion and mismatch with the base map, decreased accuracy of reference stations coordinates, and problems in managing cadastral and mapping database.

This study will continue to investigate the variations of land displacement over a longer period of time. It is essential to understand the tectonic setting and local land displacement due to either active faults or the influence from nearby earthquakes. Thus, the trend of the site velocities can be drawn to formulate the deformation model for Malaysia. This is an essential step in order to modernize the existing static datum to a semi-dynamic datum or dynamic datum. These two options further require the best mechanism to handle spatial data, especially for the cadastral and mapping applications to meet user requirements over time.

Appendix A

Comparison between Reference Frame of ITRF2000 and ITRF2008.

Station	ITRF2000		ITRF2008		Difference	
	Orientation (degree)	Displacement (cm)	Orientation (degree)	Displacement (cm)	Difference (deg)	Difference (cm)
ARAU	129.678	20.126	127.666	19.123	2.012	1.003
AYER	117.725	21.878	115.315	21.062	2.410	0.816
BABH	123.134	20.993	120.835	20.085	2.299	0.908
BAHA	118.319	24.395	116.194	23.571	2.125	0.823
BANT	117.911	24.457	115.803	23.640	2.107	0.817
BENT	118.388	23.028	116.022	22.289	2.367	0.739
CAME	119.819	22.651	117.476	21.890	2.343	0.761
GAJA	121.985	24.897	120.054	24.030	1.931	0.868
GETI	119.067	22.400	116.759	21.562	2.308	0.838
GMUS	117.709	23.063	115.352	22.318	2.358	0.745
GRIK	121.115	21.475	118.801	20.604	2.314	0.871
JHJY	118.400	25.936	116.437	25.126	1.964	0.810
JRNT	118.879	23.573	116.684	22.739	2.195	0.834
JUML	118.040	25.471	116.028	24.657	2.012	0.815
KLAW	115.560	24.953	113.416	24.176	2.144	0.777
KRAI	111.073	24.795	108.751	24.090	2.322	0.705
KUAL	117.723	24.289	115.579	23.456	2.144	0.833
KUKP	120.700	25.981	118.819	25.134	1.881	0.847
LASA	120.986	22.068	118.759	21.182	2.227	0.887
LGKW	131.051	19.391	128.824	18.443	2.227	0.947
MERS	115.873	25.965	113.822	25.192	2.051	0.773
MERU	119.125	21.705	116.642	20.954	2.483	0.751
MUAD	119.512	23.756	117.385	22.922	2.127	0.834
MUKH	116.571	23.909	114.356	23.096	2.215	0.813
PASP	118.857	22.507	116.531	21.669	2.326	0.838
PDIC	121.218	23.806	119.172	22.941	2.046	0.865
PEKN	114.987	25.360	112.763	24.688	2.223	0.672
PRTS	123.194	24.653	121.293	23.765	1.901	0.887
PUPK	121.988	22.578	119.843	21.693	2.145	0.885
PUSI	121.338	22.391	119.143	21.517	2.195	0.874
SEG1	118.084	24.154	115.932	23.337	2.153	0.817
SETI	117.965	22.846	115.608	22.102	2.356	0.744
SGPT	124.503	20.390	122.191	19.461	2.313	0.928
SIK1	122.426	21.484	120.193	20.574	2.233	0.909
SPGR	122.326	24.937	120.415	24.065	1.911	0.872
SRIJ	120.438	25.959	118.503	25.103	1.935	0.857
TERI	118.846	23.363	116.680	22.517	2.166	0.846
TGPG	118.109	26.382	116.171	25.578	1.938	0.804

(continued)

Station	ITRF2000		ITRF2008		Difference	
	Orientation (degree)	Displacement (cm)	Orientation (degree)	Displacement (cm)	Difference (deg)	Difference (cm)
TGRH	120.590	24.771	118.467	24.008	2.123	0.763
TLKI	122.765	23.171	120.708	22.277	2.057	0.894
TLOH	115.106	24.376	112.799	23.698	2.307	0.678
TOKA	124.661	20.309	122.396	19.367	2.264	0.941
UPMS	117.243	24.038	115.073	23.233	2.171	0.805
USMP	125.818	20.936	123.483	20.072	2.335	0.864
UUMK	126.185	20.012	123.899	19.058	2.286	0.954
AMAN	118.069	33.744	116.513	32.981	1.556	0.763
BELU	117.318	34.483	115.711	33.687	1.607	0.796
BIN1	112.910	28.865	110.894	28.187	2.017	0.678
DATU	115.681	29.575	113.643	28.956	2.038	0.619
KAPI	113.153	30.034	111.276	29.364	1.877	0.670
KUDA	116.318	28.609	114.206	27.954	2.112	0.655
MIRI	113.111	28.091	111.036	27.413	2.074	0.678
MRDU	117.999	34.732	116.365	33.961	1.634	0.771
MTAW	117.230	29.283	115.290	28.556	1.940	0.727
MUKA	112.625	28.467	110.608	27.793	2.017	0.674
RANA	118.489	33.916	116.834	33.193	1.656	0.723
SAND	114.893	31.131	112.938	30.519	1.955	0.612
SARA	112.650	28.855	110.618	28.269	2.032	0.586
SEMP	117.651	28.811	115.603	28.162	2.048	0.648
TEBE	112.374	28.038	110.360	27.367	2.014	0.672
TENM	119.715	35.596	118.195	34.807	1.520	0.789
TMBN	118.464	34.394	116.884	33.584	1.579	0.810
UMAS	111.726	28.432	109.719	27.770	2.007	0.662
AVERAGE	118.815	25.470	116.726	24.676	2.089	0.794

References

Leick A (2004) GPS satellite surveying. John Wiley and Sons Inc, USA

Hofmann-Wellenhof B, Lichtenegger H, Wasle E (2008) GNSS global navigation satellite systems GPS, GLONASS, Galileo and more. Springer, New York

Altamimi Z, Boucher C, Willis P (2005) Terrestrial reference frame requirements within GGOS perspective. J Geodyn 40:363–374. doi: 10.1016/j.jog.2005.06.002

Altamimi Z, Collilieux X, Boucher C (2008) Accuracy assessment of the ITRF datum definition. In: VI hotine-marussi symposium on theoretical and computational geodesy IAG symposium, Wuhan, China, 29 May–2 June 2006, International association of geodesy symposia, vol 132. Springer, IAG. pp 101–110. doi: 10.1007/978-3-540-74584-6_16

Janssen V (2009). Understanding coordinate systems, datums and transformations in Australia. In: Proceedings of the Surveying and Spatial Sciences Institute Biennial International Conference, Adelaide, Australia, 28 September–2 October 2009, pp 697–715

Johnston G and Morgan L (2010). The status of the national geospatial reference system and its contribution to global geodetic initiatives. In: FIG Congress, Sydney, Australia, 11–16 April 2010

Anderson M (2012) Investigating plate tectonics, earthquakes and volcanoes. Britannica Educational Publishing, New York

Michel GW, Yua YQ, Zhua SY, Reigber C, Becker M, Reinhart E, Simons W, Ambrosius B, Vigny C, Chamot-Rooke N, Pichond X, Morgane P, Matheussene S (2001) Crustal motion and block behaviour in SE-Asia from GPS measurements. Earth Planet Sci Lett 187:239–244

Simons W, Socquet A, Vigny C Ambrosius C Abu S, Promthong C, Subarya C, Sarsito DA, Matheussen S, Morgan P, Spakman W (2007) A decade of GPS in Southeast Asia: resolving sundaland motion and boundaries. J Geophys Res 112(B06420). doi: 10.1029/2005JB003868

Chlieh M, Avouac J, Hjorleifsdottir V, Song TA, Ji C, Sieh K, Sladen A, Hebert H, Prawirodirdjo L, Bock Y, Galetzka J (2007). Coseismic slip and afterslip of the great Mw9.15 Sumatra-Andaman earthquake of 2004. Bull Seismol Soc Am 97:152–173. doi: 10.1785/0120050631

Socquet A, Vigny C, Chamot-Rooke N, Simons W, Rangin C, Ambrosius B (2006). India and Sunda plates motion and deformation along their boundary in Myanmar determined by GPS. J Geophys Res 111(B05406). doi: 10.1029/2005JB003877

Banerjee P, Pollitz F, Nagarajan B, Bürgmann R (2007). Coseismic slip distributions of the 26 December 2004 Sumatra-Andaman and 28 March 2005 Nias earthquakes from GPS static offsets. Bull Seismol Soc Am 97:86–102. doi: 10.1785/0120050609

Vigny C, Simons WJF, Abu SH, Ronnachai B, Satirapod C, Chhoosakul M, Subarya C, Omar K, Abidin HZ, Socquet A, Ambrosius BAC (2005) Insight into the 2004 Sumatra-Andaman earthquake from GPS measurements in Southeast Asia. Nature 436:201–206

Omar K, Jhonny and Mohamed A (2010). Post seismic deformation monitoring in peninsular Malaysia using global positioning system. In: Proceedings of the 2010 international symposium on GPS/GNSS, Taipei, Taiwan, 26–28 October 2010

Kelly KM (2012) Implementing dynamic datum data management in GIS. In: Proceeding in FIG working week 2012, Rome, Italy, 6–10 May 2012

Department Survey and Mapping (DSMM) (2009). Technical guide to the coordinate reference systems. Pekeliling Ketua Pengarah Ukur Dan Pemetaan Bilangan 1/2009. Kuala Lumpur

Kadir M, Ses S, Omar K, Desa G, Omar AH, Taib K, Nordin S (2003). Geocentric datum GDM2000 for Malaysia: Implementation and implications. In: Seminar on GDM2000, Department of Survey and Mapping Malaysia, Kuala Lumpur, Malaysia, 28 August 2003

Mohamed A (2012). Monitoring active faults in Ranau, Sabah Using GPS. In: 19th United Nations regional cartographic conference for Asia and the Pacific Bangkok, Thailand, 29 October–1 November 2012

Pinto JT (2009). Questioning the need of regional reference frames. In Drewes H (ed) Proceedings of the geodetic reference frame, International association of geodesy symposia vol 134. Springer, Berlin, Heidelberg, pp 225–230. doi: 10.1007/978-3-642-00860-3_35

Spatial-Based Sustainability Assessment of Urban Neighbourhoods: A Case Study of Johor Bahru City Council, Malaysia

Azman Ariffin, Haziq Kamal Mukhelas, Abd. Hamid Mar Iman, Ghazali Desa and Izran Sarrazin Mohammad

Abstract Rapid population growth has caused expansion of many major cities. Cities begin to expand into new areas as the demand for housing increases, thus, contributing to demand for a variety of natural and man-made resources for urban communities. However, it is our responsibility to sustain these resources so that their usage can be prolonged to the next generation. With sustainability as a goal, the use of indicators for urban monitoring and regulation is becoming more in demand. There are many non-spatial indicators in the form of words and statistics developed by local authorities for assessing urban development sustainability. This chapter proposes the use of spatial indicators for the same purpose. The indicators are derived from the Malaysian Urban Indicators Network (MurniNet) and are then developed using Analytical Hierarchy Process (AHP) comprising spatial elements

A. Ariffin (✉)
TropicalMap Research Group, Faculty of Geoinformation and Real Estate,
Universiti Teknologi Malaysia, Johor Bahru, Malaysia
e-mail: azmanariffin@utm.my

H. K. Mukhelas · G. Desa
Department of Geoinformation, Faculty of Geoinformation and Real Estate,
Universiti Teknologi Malaysia, Johor Bahru, Malaysia
e-mail: haziqmukhelas@gmail.com

G. Desa
e-mail: ghazalidesa@utm.my

Abd. Hamid Mar Iman
Environmental Sustainability and Conservation Cluster, Faculty of Earth Sciences,
Universiti Malaysia Kelantan, Jeli, Malaysia
e-mail: hamid.m@umk.edu.my

I. S. Mohammad
Faculty of Geoinformation and Real Estate, Centre for Real Estate Studies,
Universiti Teknologi Malaysia, Johor Bahru, Malaysia
e-mail: izran@utm.my

of points, lines, and polygons. The AHP is used to determine the ranking of sustainability of urban areas. This study selects Johor Bahru City Council (JBCC) administrative area as a case. The result shows that spatial indicators can contribute to a better visualisation of sustainability via the production of sustainability map.

1 Introduction

Urban development can be defined as the expansion of urban areas into natural and rural areas such as deserts, swamps, and forests (Black et al. 2002). As population grows, socioeconomic needs arise. In particular, population growth in major cities requires city boundary's expansion while developers look into the neighbouring areas to build more housing, recreational, and other facilities. Consequently, demand for a variety of natural and man-made resources for urban communities increases.

The process of urban expansion requires that planners work closely with other parties to ensure environmental protection. In this context, sustainable development seeks to establish a balance between human needs and environmental preservation. Therefore, urban planners need to consider maintaining sustainable development while expanding and renovating urban areas. Especially important, much care needs to be taken to integrate the wilderness with the developing city when an urban area expands into wildlife regions (Litman 2007). Besides, sustainable urban development should function to curtail city pollution, to increase the availability of recycling facilities, and to encourage efficient use of alternative sources of energy.

Urban sustainability needs to be considered from ecological viewpoint and, thus, it needs to adopt the concepts of footprint, emissions, and energy (Broekhof and van Marwijk 2012). Further, to achieve a sustainable city, there are several elements to be considered (Fig. 1).

Figure 1 shows that urban sustainability should be considered from environmental, economic, and social dimensions. Since they are very complex and have different degrees of importance, an approach is needed to rank them accordingly before they can be used as indicators for urban development sustainability assessment (Fig. 1).

In 2004, the Malaysian government has taken an initiative, based on the Eight Malaysia Plan, to develop a set of indicators that can be used to measure sustainable urban development, called Malaysian Urban Indicators Network (Murni-iNet) (Marzukhi et al. 2011). However, these indicators, extracted from several planning sectors, are non-spatial indicators although they can be used for evaluating urban development. We propose the use of spatial indicators for the same purpose. Spatial indicators with sufficient spatial information and geographic visualisation can be useful for local sustainable planning, supporting decision-making in the planning process, and helping policy makers to identify

Fig. 1 The classic dimensions of sustainable development (*source* Tanguay et al. 2010)
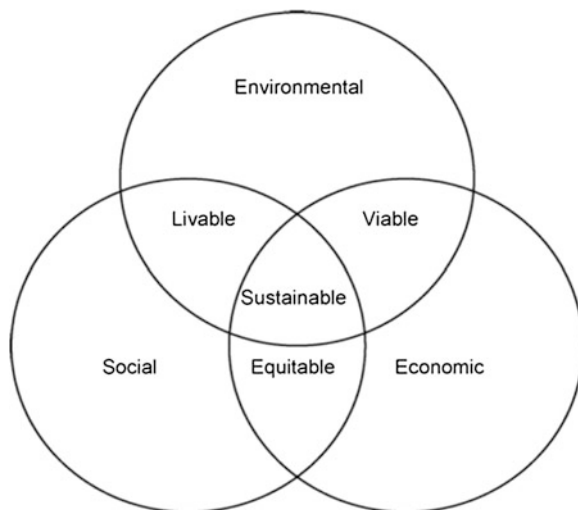
'unsustainable' actions in the planning areas (Broekhof and van Marwijk 2012). As a result, areas of urban development can be mapped as sustainable, semi-sustainable, or non-sustainable.

Geographic visualization plays an important role in any spatial rating to ensure reliable and consistent outcome. Rating using non-spatial indicators usually results in statistics that can only be viewed as words and numbers; its usefulness in the spatial context is quite limited. On the other hand, spatial indicators can be a more meaningful way of generating spatial information thus assisting users on decision making and enhancing policy by perfect viewing of sustainable urban development with multi-layered information included at one time. Broekhof and van Marwijk (2012) have argued that maps can give valuable information to develop sustainable policies at the local scale.

This study attempts to improve the approach to assessing sustainable urban development adopted by MurniNet. In particular, this study attempts to demonstrate how spatial information can be generated to assess urban development sustainability. In all, this study proposes the incorporation of spatial indicators to help the local authority and policy makers to assess urban development sustainability in a more visualized manner.

2 Assessment of Sustainable Urban Development Sustainability

The literature on through-time urban sustainability assessment techniques conducted using built-environment quality evaluation framework (BEQUEST) reveals several methods available for sustainability assessment of urban activities (Deakin

et al. 2001; Ugwu and Haupt 2005). Three of them are Environmental in General (EIG), Life Cycle Assessment (LCA), and Sustainability Indicator Assessment (SIA) methods. Out of these three, the SIA method is most widely used by local authorities around the world. This is because the SIA method seeks to achieve integration of all issues of sustainability compared to the other two which focus solely on environment and socioeconomic aspects, respectively. In general, SIA method employs a wide range of indicators to characterize the different dimensions or aspects of urban development. Therefore, the assessment of sustainability is actually considered as an assessment of indicators by which people can track their progress towards sustainability.

2.1 The Study Area

The study area, Johor Bahru City Council (JBCC), covers an administrative region of 220 km^2 with a total population of 552,026 people. JBCC is divided into 16 planning blocks according to the Johor Bahru Local Plan for 2020 as shown in Fig. 2. These are Daerah Sentral, Tasek Utara/Teluk Danga, Pelangi, Pasir Pelangi, Tampoi, Larkin, Majidee, Teluk Tebrau, Permas Jaya, Rinting, Kempas, Kangkar Tebrau, Pandan/Taman Molek, Bandar Dato' Onn/Setia Tropika, Mount Austin/Taman Daya and Tebrau.

2.2 Sustainability Indicator Assessment Method

An indicator is a measurement to be met, an effect obtained via a gauge of quality or a context variable (European Commission 2008). An indicator produces measured information with a purpose to help researchers concerned with public interventions to communicate, negotiate, or make decisions. In the process of urban sustainability assessment, there is a need for measureable indicators and several approaches of assessment based on these indicators have been developed (Shen et al. 2011).

However, assembling information for all-embracing indicators is not what urban sustainability assessment is all about. Rather, a selective analysis of indicators which are more fundamental in essence and more likely to produce the most accurate information about the status of practice should be focused (Shen et al. 2011). The United Nations Statistical Institute for Asia and Pacific (2007) stated that an indicator must be SMART (i.e. Specific, Measureable, Achievable, Relevant, and Time-related). This can help in effective data management and avoiding data exaggeration of irrelevant selected indicators and, thus, contribute to cost-effective assessment of urban development sustainability.

Sustainability indicators are essential in the overall assessment of progress towards sustainable development. They are useful for measuring and monitoring

Fig. 2 16 Zones in MBJB

the state of the environment by considering a manageable number of variables or characteristics (McLaren and Simonovic 1999). Several studies at the urban, regional, and national levels have compiled extensive lists of sustainability indicators (Foxon et al. 2002; Hellström et al. 2000; Alberti 1996; Maclaren 1996). Based on these indicators, a number of assessment methods have been developed which attempt to simplify the holistic assessment of urban sustainability. These methods rely on key interactions and feedback mechanisms between infrastructure and the surrounding environmental, economic, and social systems and use sustainability criteria and indicators to understand and quantify the resulting interacting effects. From a methodological standpoint, SIA method is recognised as a useful integrative approach to evaluating a multi-dimensional situation and assessment outcome.

2.3 Sustainable Urban Development Indicators

In Malaysia, the Department of Town and Country Planning, Ministry of Housing and Local Government Malaysia has developed a system for assessing the sustainability of a city and region called MurniNet. The goal of this system is to assess

the sustainability of Malaysian cities according to Malaysian Urban Indicators. There are eight dimensions with 21 themes that are further subdivided into 36 urban indicators and are used as overall sustainability indicators of a city. These indicators can be re-grouped into three categories, namely non-spatial, spatial, and mixed indicators.

3 Determination of Spatial Indicators

The selection of spatial indicators is based on several criteria including their reliability and effectiveness in providing sufficient information. These criteria must include three pillars of sustainability, namely economy, environment, and social (see Fig. 1). As mentioned earlier, the indicators must be "SMART". However, in this study, these indicators are filtered by selecting only those that contain spatial elements and mapable data.

There were nine spatial indicators selected to be used in this study. The first three indicators are selected from the economic sustainability dimension. The first indicator represents public transportation terminals and stations. The second indicator represents attraction areas and recreational centres and the last indicator from this dimension represents grade 'A' business. All the indicators are represented as points.

Environmental sustainability is the next dimension in assessing urban development sustainability and it is made up of three indicators. All of these indicators are represented in polygons where the first indicator represents flood prone areas. The second indicator represents provision of public open spaces and the last indicator represents residential areas getting centralized sewerage services.

The last dimension is social sustainability whose first indicator is accessibility to community facilities represented in points and polygons. The next indicator is happiness index that indicates population's satisfaction about their daily life and surroundings. The last indicator is related to demography, in particular, the total population of each zone.

3.1 The Scoring System

The urban sustainability assessment scoring system is extracted the MurniNet system itself. The system uses various weightage scores for each dimension and theme according to the predetermined specification. The spatial indicators scoring system shown in Table 1 is adopted in this study to determine the sustainability of the JBCC's planning blocks.

Table 1 Spatial indicators formula

	Standards	Score
Terminals and stations for public transportation (*TS*)		
A = Numbers of integrated public transportation terminals	>3	3
	2–3	2
	<1	1
Tourism attraction area and recreation centres (*TR*)		
A = Numbers of attraction area and recreational centres	>5	3
	2–5	2
	<2	1
Area prone to flooding (*FA*)		
Score = (A/B) × 100	<10 %	3
A = Total population live in the area prone to flooding	10–20 %	2
B = Total population of the research area	>20 %	1
Grade A business premises (*GA*)		
Score = (A/B) × 100	>70 %	3
A = Numbers of grade A food business premises in research area	30–70 %	2
B = Numbers of food business premises assessed in research area	<30 %	1
Provision to public open space (*OS*)		
Score = (1,000/B) × A	>1.5 ha	3
A = Total area of open space (hectares) in research area	1–1.5 ha	2
B = Total population in research area	<1 ha	1
Centralized sewerage (*CS*)		
Score = (A/B) × 100	>80 %	3
A = Numbers of residential area getting centralized sewerage service	60–80 %	2
B = numbers of residential area	<60 %	1
Accessibility of community to public facilities (*AF*)		
Score = (A/B) × 100	>80 %	3
A = Total area of research zone	50–80 %	2
B = Total area of residential within 400 meter radius of public facilities	<50 %	1
Happiness Index (*HI*)		
Score = (A/B) × 100	>80 %	3
A = Total number of respondents satisfied with daily live and surrounding	40–80 %	2
B = Total number of respondents in study area	<40	1

3.2 Analytical Hierarchy Process for Sustainability Assessment

Analytical hierarchy process (AHP) is a multi-criteria decision-making (MCDM) technique. Underlying MCDM principle is that a decision has to be made by means of analyzing a set of criteria. Saaty (1980) has developed AHP which models a hierarchical decision problem framework consisting of multi-level criteria having unidirectional relationships. AHP works with such a hierarchy that can combine both subjective (intangible) and objective (tangible) criteria.

After finalizing the selected spatial indicators, the hierarchical decision model is then developed. The decision model of this study is broken up into three major levels, namely goal, objective, and design criteria. Goal is the topmost level which describes the decision problem. This study attempts to work out the most sustainable urban development and therefore, the topmost level is to "select the most sustainable area". The objectives of sustainability assessment comprise three aspects: economic, environmental, and social. In order to identify the priorities of three sustainable development objectives in the second level, and the relative importance of different design criteria in the third level, a series of pairwise comparisons have to be performed. The elements in both levels are then weighted.

By using pairwise comparisons, the relative importance of one criterion over another can be expressed by ranking them using AHP's nine-point scale of importance as shown in Tables 2, 3, 4, 5, 6, 7, 8, and 9.

The fractions are converted into decimals to acquire pairwise matrix. A short computational way to obtain the ranking is to raise the pairwise matrix to powers that are successively squared each time. The row sums are then calculated and normalized.

$$[AB]_{i,j} = A_{i,1}B_{1,j} + A_{i,2}B_{2,j} + \cdots + A_{i,n}B_{n,j} = \sum_{r=1}^{n} A_{i,r}B_{r,j} \qquad (1)$$

From the computed eigenvector, the relative criteria are ranked as follows:

EcS	0.3761	The most important criterion
EnS	0.3341	The second most important criterion
ScS	0.2898	The least important criterion

The steps were then implemented for the next level which is design criteria level where it includes all the spatial indicators from environment, economic and social dimensions. Then, the criteria are ranked in a descending order from most important to least important.

Economic sustainability indicators are represented by the numbers of integrated terminals and stations for public transportations (TS), numbers of attraction areas and recreational centres (TR) and percentage of grade 'A' business premises (GA).

TS	0.2380	The second most important criterion
TR	0.6254	The most important criterion
GA	0.1366	The least important criterion

Environmental sustainability indicators are represented by the percentage of population living in areas prone to flooding (FA), provision of public open space ratio compared to 1,000 population (OS) and percentage of centralized sewerage (CS) (Tables 10, 11).

Table 2 Scale of importance

AHP scale of importance for pairwise comparison	Numeric rating
Extreme importance	9
Very strong to extremely	8
Very strong importance	7
Strongly to very strong	6
Strong importance	5
Moderately to strong	4
Moderate importance	3
Equally to moderately	2
Equal importance	1

Table 3 Pairwise comparison

	EcS	EnS	ScS
EcS	1/1	3/1	1/2
EnS	1/3	1/2	3/1
ScS	2/1	1/3	1/1

Table 4 Pairwise matrix

	EcS	EnS	ScS
EcS	1	3	0.5
EnS	0.3	1	3
ScS	2	0.3	1

Social sustainability indicators are represented by the percentage of residential areas within 400 meters from community facilities (AF), happiness index (HI), and demography (DM) (Tables 12, 13).

AF	0.6149	The most important criterion
HI	0.1171	The least important criterion
DM	0.2680	The second most important criterion

The finalised AHP decision model is as shown in Fig. 3.

3.3 Sustainability Map

Sustainability maps are produced for each indicator based on the formula prescribed in MurniNet. These maps represent the sustainability of each planning block according to spatial indicators. There are three sustainability scores:

Table 5 The first eigenvector

	EcS	EnS	ScS	Normalized	Eigenvector
EcS	2.9999	6.16665	10	19.16655	0.3929
EnS	6.6666	2.9998	6.16665	15.83305	0.3246
ScS	4.111089	6.6666	2.9999	13.77759	0.2825
Total				48.77719	1

Table 6 Pairwise comparison of objectives level

	EcS	EnS	ScS	Normalized	Eigenvector
EcS	91.2155	103.6585	98.0166	292.8906	0.3761
EnS	65.3433	91.2200	103.6641	260.2273	0.3341
ScS	69.1056	65.3493	91.2209	225.6757	0.2898
Total				778.7935	1

Table 7 Eigenvector of the objectives level

Objectives	Eigenvector
Economic sustainability (EcS)	0.3761
Environmental sustainability (EnS)	0.3341
Social sustainability (ScS)	0.2898

Table 8 Pairwise comparison of economic sustainability

	TS	TR	GA
TS	1	1/3	2
TR	3	1	4
GA	1/2	1/4	1

1 = 'not-sustainable'; 2 = 'semi-sustainable'; and 3 = 'sustainable'. The production of the maps is important to assist users in interpreting the information correctly. The maps are used in the analysis while graphs and tables created are shown alongside the attributes. With the use of ArcToolbox in ArcGIS 10.0, proximity analysis is performed for the measurement of various data.

4 Results and Discussion

This section discusses the results from the data analysis. The purpose is to spatially visualize the assessed sustainability of each JBCC's planning block. Besides spatial indicators, the usage of non-spatial indicators is also shown in this section.

Table 9 Iterated eigenvector solution

	TS	TR	GA	Normalized	Eigen vector
TS	27.5301	10.4746	48.1068	86.1115	0.2380
TR	72.34	27.5301	126.42	226.2901	0.6254
GA	15.8025	6.0134	27.62	49.4359	0.1366
Total				361.8375	1

Table 10 Pairwise comparison of environmental sustainability

	FA	OS	CS
FA	1	4	3
OS	0.25	1	3
CS	1/3	1/3	1

Table 11 Iterated eigenvector solution

	FA	OS	CS	Normalized	Eigen vector
FA	35.7488	89.4002	168.1425	293.2915	0.6218
OS	13.9403	35.7002	67.1175	116.758	0.2476
CS	7.399	18.52	35.659	61.578	0.1306
Total				471.6275	1

Table 12 Pairwise comparison of social sustainability

	AF	HI	DM
AF	1	4	3
HI	1/4	1	1/3
DM	1/3	3	1

Table 13 Iterated eigenvector solution

	AF	HI	DM	Normalized	Eigen vector
AF	29.6126	155.2424	67.6704	252.5254	0.6149
HI	5.6293	29.6126	12.8749	48.1168	0.1171
DM	12.8748	67.6704	29.5228	110.0680	0.2680
Total				410.7102	1

4.1 Sustainability Based on Economic Indicators

Map 1 shows that out of 16 planning blocks only four are classified as sustainable according to MurniNet standard. These are Teluk Danga, Daerah Sentral, Pelangi and Larkin. Two planning blocks—Tampoi and Pasir Pelangi—have the score of '2' which means semi-sustainable while the rest of the planning blocks are
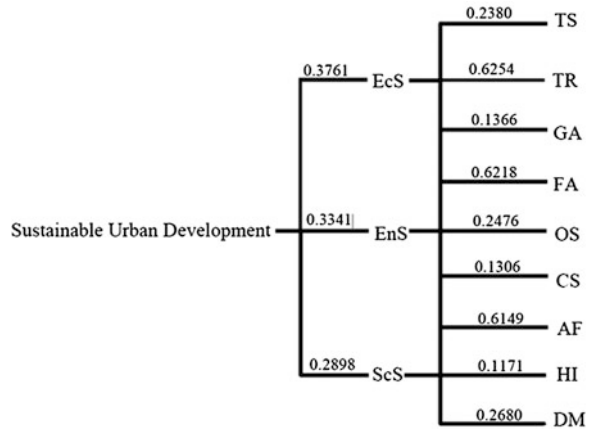
considered not sustainable. Map 2 shows that only Daerah Sentral is considered sustainable. Larkin and Permas Jaya are categorized as semi-sustainable. Overall, the results show that the southern region of the study area is economically sustainable (Fig. 4).

4.2 Sustainability Based on Environmental Indicators

Figure 5 shows that all the planning blocks are sustainable. Map 3 shows that the highest percentage of flood-prone area—Kangkar Tebrau—is only five percent, followed by Teluk Danga (0.28 %) and Teluk Tebrau (0.07 %). Map 4 shows the planning blocks that achieve sustainability on the public open space ratio, namely Tebrau, Bandar Dato' Onn/Setia Tropika, Mount Austin/Taman Daya, Pandan/ Taman Molek, Tampoi and Tasek Utara/Teluk Danga. Each of them has more than 1.5 ha of public open space. Rinting, Pasir Pelangi, Permas Jaya and Kempas are categorized as semi-sustainable planning blocks while the rest of the planning blocks are not sustainable. Six areas are classified as environmentally sustainable by achieving the highest score on both indicators. These are Bandar Dato' Onn/ Setia Tropika, Mount Austin/Taman Daya, Pandan/Taman Molek, Tampoi and Tasek Utara/Teluk Danga.

4.3 Sustainability Based on Social Indicators

In Fig. 6, Map 5 shows the population of JBCC with a total of 555,026 people. The most populated area with a total of 70,141 people is Tebrau followed by Bandar Dato' Onn and Setia Tropika with a total of 60,279 people. Pasir Pelangi is
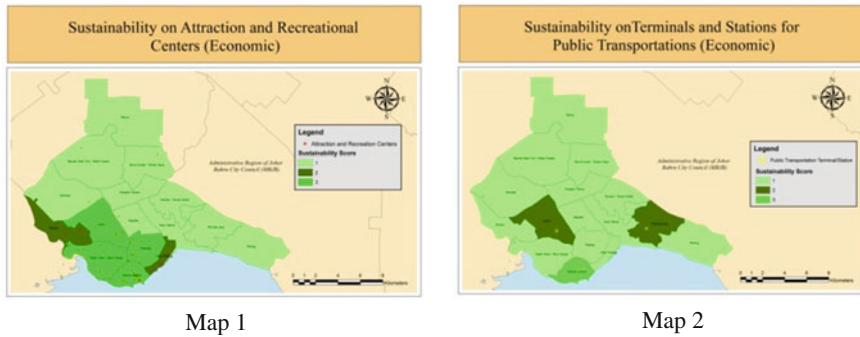
Fig. 4 Attraction and recreational centres (Map 1) and Terminals and stations for public transportations sustainability (Map 2)
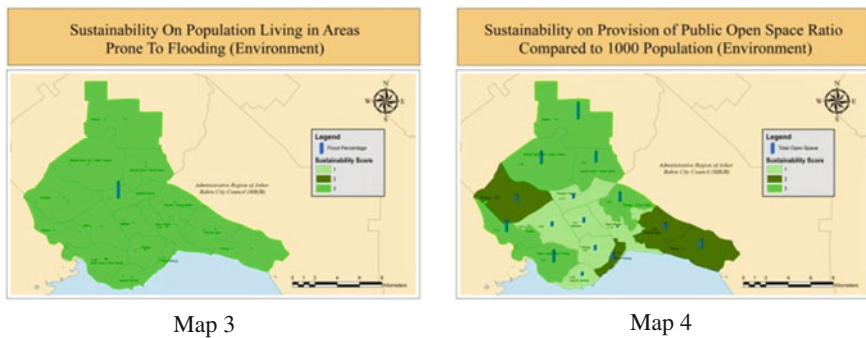
Fig. 5 Population living in areas prone to flooding sustainability (Map 3) and Provision of public open space ratio compared to 1,000 population sustainability (Map 4)

the least populated area with only 7,852 people. The map also shows that Tebrau is the largest area with a total size 27.24 km^2.

The accessibility from residential areas to community facilities is determined by proximity analysis. Map 6 shows that Majidee is the only sustainable planning block with 81 % accessibility. Kempas, Tampoi, Larkin, Daerah Sentral, Pelangi, and Mount Austin/Taman Daya are categorized as semi-sustainable planning blocks with 50–80 % accessibility to community facilities. Other planning blocks are classified as not sustainable. Map 7 shows that the majority of respondents are satisfied with their daily life and the surroundings. Respondents in Teluk Tebrau, Mount Austin/Taman Daya, and Tebrau feel that they are partially satisfied with the surroundings. Both maps show that the most socially sustainable area is Majidee which achieves the highest score for both indicators. Kempas, Tampoi, Larkin, Pelangi, and Daerah Sentral are classified as semi-sustainable with the highest and second highest scores for both indicators.

Map 5

Map 6

Map 7
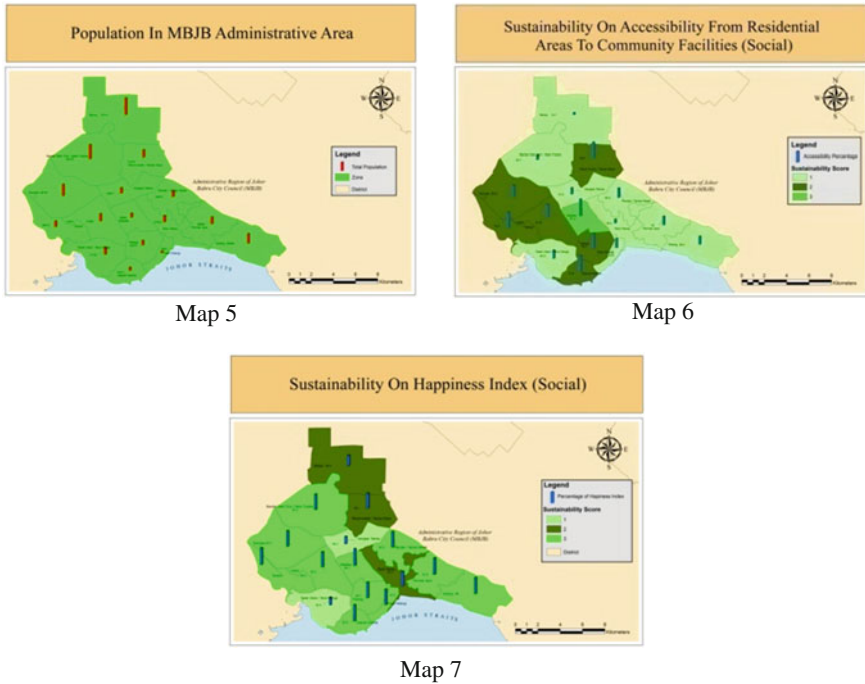
Fig. 6 Population in MBJB, Accessibility from residential areas to community facilities, and Happiness index sustainability map

4.4 Sustainability Map Using AHP

The eigenvector is calculated to decide on the importance ranking of sustainability indicators as explained earlier. Each planning block has its own score of sustainability from each indicator through the index prescribed in the MurniNet. Importance ranking is then used to assess the sustainability of urban development of the planning blocks within the JBCC. Based on the indicators' eigenvalues, economic sustainability is the most important dimension to determine sustainability of an area followed by environmental sustainability and social sustainability (Fig. 7).

Figures 8 and 9 show that Daerah Sentral, Tasek Utara/Teluk Danga, Pelangi and Rinting have the highest score on the most important indicators. For the second most important indicator, all planning blocks achieved the highest score. Majidee is the only area that has the highest score for the third highest ranked indicator. For the fourth indicator, all planning blocks obtained the highest score while for the next highest ranked indicator shows that Tasek Utara/Teluk Danga, Tampoi, Pandan/Taman Molek, Bandar Dato' Onn/Setia Tropika, Mount Austin/ Taman Daya and Tebrau are sustainable planning blocks. The indicator of

Indicators	Ranking
TR	1st
FA	2nd
AF	3rd
DM	4th
OS	5th
TS	6th
GA	7th
CS	8th
HI	9th

Fig. 7 Finalised AHP decision model

Fig. 8 Graph of overall sustainability score

Fig. 9 Sustainable urban development map

integrated terminals and stations for public transportation is ranked sixth with Daerah Sentral having the highest sustainability score. The next indicator is the premises that are awarded grade 'A' status. This indicator shows that only Daerah Sentra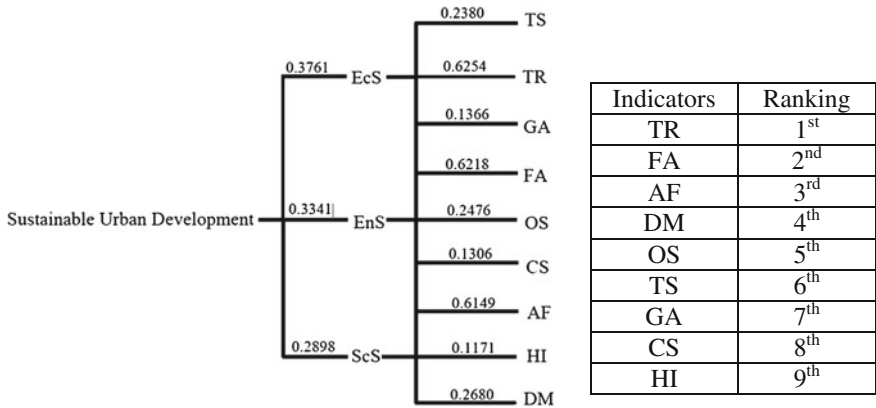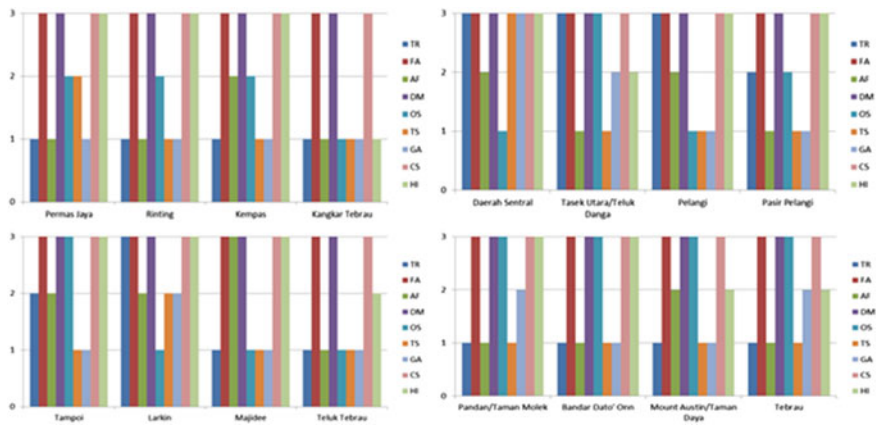l is sustainable compared to other planning blocks. It also indicates that business premises in JBCC, especially the restaurants, do not achieve the standards specified by the Department of Health JBCC. Figure 8 also shows that all the planning blocks are sustainable on the basis of existence of centralized sewerage services. This indicator shows that 82.05 % of the residential areas in JBCC are enjoying sufficient level of centralized sewerage services. The last ranked indicator is the happiness index whereby all planning blocks, except for Kangkar Tebrau, are categorized as sustainable. [Happiness index stipulates that majority of the respondents must be satisfied with their daily life and surroundings.] Kangkar Tebrau, in particular, is found to be not sustainable.

5 Conclusion

Sustainability is a broad concept that encompasses many aspects of the social, economic and environment. The study demonstrates how suitable indicators can be used for the assessment of sustainable urban development. Proper selections of SMART indicators are very important. The use of spatial indicators, with sufficient spatial content provided, can contribute to a better implementation of assessment of areal sustainability. It can also give more understanding and interpretation of spatial information by producing to-be-seen map.

From the overall assessment, we can see that the majority of planning blocks located near city centres such as Daerah Sentral, Pelangi, Teluk Danga, Larkin, Majidee and Tampoi are sustainable because these planning blocks are areas of people's attraction. This study also shows how placement of business premises, recreational areas, community facilities and roads are important to maintain urban sustainability.

References

Black JA, Paez A, Suthanaya PA (2002) Sustainable urban transportation: performance indicators and some analytical approaches. J Urban Plan Dev 128:184–209

Broekhof S, Van Marwijk R (2012) The role of spatial information for planning sustainable cities. In: Paper presented at the proceedings of FIG working week 2012 on knowing to manage the territory, protect the environment, evaluate the cultural heritage. Rome, Italy, 6–10 May 2012

Deakin M, Curwell S, Lombardi P (2001) BEQUEST: sustainability assessment, the framework and directory of methods. Int J Life Cycle Assess 6(6):373–390

Department of Town and Country Planning Peninsular Malaysia and Ministry of Housing and European Commission (2008) The resource for the evaluation of socio-economic development (EVALSED). European Commission

Foxon TJ, McIlkenny G, Gilmour D, Oltean-Dumbrava C, Souter N, Ashley R, Butler D, Pearson P, Jowitt P, Moir J (2002) Sustainability criteria for decision support in the UK water industry. J Environ Planning Manage 45(2):285–301

Hellström D, Jeppsson U, Kärrman E (2000) A framework for systems analysis of sustainable urban water management. Environ Impact Assess Rev 20:311–321

Litman T (2007) Developing indicators for comprehensive and sustainable transport planning. J Transp Res Board 2017:10–15

Marzukhi AM, Omar D, Leh OLH, Hamir MS, Barghchi M (2011) Malaysian urban indicators network: a sustainable development initiative in Malaysia. Eur J Soc Sci 25(1):77–84

McLaren RA, Simonovic SP (1999) Data needs for sustainable decision making. Int J Sustain Dev World Ecol 6:103–113

Shen LY, Ochoa JJ, Shah MN, Zhang X (2011) The application of urban sustainability indicators—a comparison between various practices. Habitat Int 35(2):17–29

Tanguay GA, Rajaonson J, Lefebvre J, Lanoie P (2010) Measuring the sustainability of cities: an analysis of the use of local indicators. Ecol Ind 10:407–418

Ugwu OO, Haupt TC (2005) Key Performance indicators and assessment methods for infrastructure sustainability—A South African construction industry perspective. Build Environ 42(2007):666–680

The Dual Half-Arc Data Structure: Towards the Universal B-rep Data Structure

François Anton, Pawel Boguslawski and Darka Mioc

Abstract In GIS, the use of efficient spatial data structures is becoming increasingly important, especially when dealing with multidimensional data. The existing solutions are not always efficient when dealing with big datasets, and therefore, research on new data structures is needed. In this chapter, we propose a very general data structure for storing any real or abstract cell complex in a minimal way in the sense of memory space utilization. The originality and quality of this novel data structure is to be the most compact data structure for storing the geometric topology of any geometric object, or more generally, the topology of any topological space. For this purpose, we generalize an existing data structure from 2D to 3D and design a new 3D data structure that realizes the synthesis between an existing 3D data structure (the Dual Half-Edge (See Footonote 1) data structure) and the generalized 3D Quad-Arc data structure, (See Footnote 2) and at the same time, improves the Dual Half-Edge towards a simpler and more effective representation of cell complexes through B-rep structures. We generalize the idea of the Quad-Arc data structure from 2D to 3D, but instead of transforming a simple edge of the Quad-Edge data structure to an arc with multiple points along it, we group together primal edges of the Dual Half-Edge that have the same dual Half-Edge vertex tags (volume tags) into one Dual Half-Arc whose dual is the common Dual Half-Edge and primal faces corresponding to dual. This corresponds to grouping together straight line segment edges into arcs. This allows us to transform the Dual Half-Edge data structure into a 3D data structure for cell complexes

F. Anton (✉) · D. Mioc
Department of Geodesy, DTU Space—National Space Institute,
Technical University of Denmark, 2800 Kgs, Lyngby, Denmark
e-mail: fa@space.dtu.dk

D. Mioc
e-mail: mioc@space.dtu.dk

F. Anton · P. Boguslawski
3D GIS Research Group, Department of Geoinformation,
Universiti Teknologi Malaysia, Johor Bahru, Malaysia
e-mail: pawel@utm.my

with fewer Dual Half-Edges. Since the input/output operations are the most costly on any computer (even with solid state disks), this will result in a much more efficient data structure, where computation of topological relationships is much easier and efficient, like cell complex homologies (See Footonote 3) are easier to compute than their simplicial counterparts. This new data structure, thanks to its efficiency, could have a positive impact on applications that need near real time response, like mapping for natural disasters, emergency planning, evacuation, etc.

1 Introduction

In GIS, multi-dimensional representations are still not completely functional.[1] In spite of the new developments in spatial databases, where systems like Oracle and Post GIS allow for storage,[2] maintenance and query of 3D Information, GIS systems are still not capable of spatial analysis on 3D objects Ellul and Haklay (2009). For this purpose,[3] the main issue seems to be the representation of the topological relationships for 3D objects within commercial GIS systems.

There are several ways to represent topological relationships among spatial objects (i.e., all binary relationships among spatial objects that are invariant by continuous transformations, i.e., incidence, containment, adjacency) in a computer. One of them is concerned with boundaries of objects, and is known as the family of boundary representations (B-rep, see Stroud 2006; Ellul and Haklay 2009 and Sect. 2). Another one is concerned with the tessellation of the space into cells of different dimensions (cell complexes, see Webster (2003) for a gentle introduction on cell complexes and Sect. 2).

In two dimensions, a primal subdivision can store the geometry of spatial objects, while its dual subdivision stores the spatial relationships between adjacent objects: as shown in Fig. 1, Gold (1991) uses two connected data structures to store simultaneously a polygonal map (where each polygon has certain attributes) and its dual (the boundaries between two map objects having certain attributes, e.g. the boundary type or the flow direction). The data structure used was the *quad-edge* structure of Guibas and Stolfi (1985). He argues that the boundaries do not characterise *per se* any of the objects, but rather the adjacency relationships that exist between them.

---

[1] An half-edge is an edge with an oriented edge in the primal or dual subdivision.

[2] The Quad-Arc data structure groups quad-edges (which are composed of one pair of oriented edges of the primal subdivision and the corresponding pair of dual edges), whose dual edge extremities have the same pair of polygon tags.

[3] All boundaries are cycles, but not all cycles are boundaries; homologies are equivalence classes of cycles modulo boundaries, i.e., cycles that are not boudaries, i.e., topological spaces formed by cycles, where all boundaries have been removed.
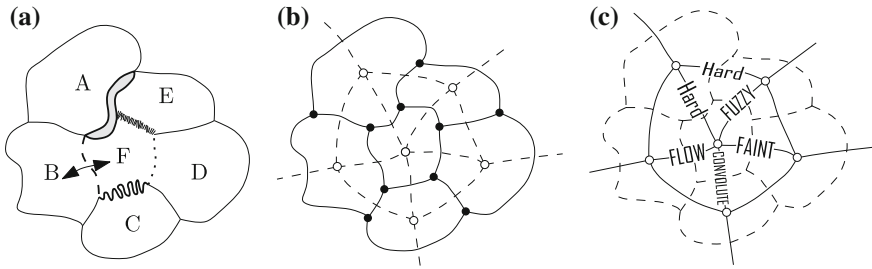
Fig. 1 **a** Six map objects and their boundaries. **b** The same map stored as a graph and its dual (*dotted lines*). **c** The dual graph is used to describe the relationships between adjacent *polygons*. (Figure after Gold (1991))

However, in his paper Gold (1998), in the context of automating the maps production for the forest industry, Gold acknowledges that there are far too many points in a discretization of forest polygons (in the sense that not so many points are required to retain the shape and topology of these forest polygons), and that the only arcs that should be retained are those that are critical to respect the polygonal structure. This approach can be generalized to 3D, or more generally to nD.

In this chapter, we propose a very general data structure for storing any real or abstract cell complex in a minimal way in the sense of memory space utilization. The originality and quality of this novel data structure is to be the most compact data structure for storing the geometric topology of any geometric object, or more generally, the topology of any topological space. We achieved this purpose by providing a data structure that generalizes the Quad-Arc data structure to 3D and realizes the synthesis between that 3D Quad-Arc data structure and the Dual Half-Edge (DHE) data structure, in order to get a more efficient data structure that stores the geometry of 3D objects (and particularly their ramification) and their topological relationships in a pair of dual subdivisions with much fewer elements than the original DHE. One might think that this is only of theoretical interest, but in fact, it is very important practically for any 3D GIS, because the efficiency of 3D GIS systems is currently very limited by the amount of necessary input/output operations, which take much longer than any operation in the Central Processing Unit or in between the Random Access Memory and the Central Processing Unit. Therefore, this most compact geometric topology storing data structure is central to the development of efficient 3D GIS systems that can process quickly large spatial data sets (for example a 3D city model or any local or regional development model).

We first review the key data structures related to our research including the Dual Half-Edge in Sect. 2 and the concepts of geometric topology (ramification) in Sect. 3. In Sect. 4, we generalize the 2D Quad-Arc data structure to 3D. We present our new synthesis of these two data structures (the Dual Half-Arc data structure) in Sect. 5. Finally, in Sect. 6, we analyze potential applications of this data structure.

2 Background

2.1 Boundary Representation

Boundary representation (abbreviated as "B-rep") is a method in solid modeling for representing solids and shapes using their boundaries (which separate the interior of the solid from the exterior of the solid). These solid boundaries are obtained by ''sewing" together connected surface elements (or patches), whose boundaries are composed of vertices and edges. Typically, the surface elements are B-splines (which are linear combinations of the parametric polynomial Bézier curves) or their generalizations (NURBS). A UML description of the Boundary representation is shown in Fig. 2.

2.2 Cell Complex

A cell complex is a decomposition of the space into cells, where the interior of each cell can be obtained by continuously deforming a hyper-ball without its boundary and vice versa, the boundary of each cell is the union of lower-dimensional cells of the cell complex, and the topology of objects in the cell complex is defined from their intersections with all cells [4]. It can model one subdivision of the space. The topological relationships among the cells of the cell complex may be modeled using a second subdivision.

2.3 Quad-Edge Data Structure

The Quad-Edge data structure was introduced by Guibas and Stolfi Guibas and Stolfi (1985) as a primitive topological structure for the representation of any subdivision on a two-dimensional manifold (see p. 18 in [49]). The Quad-Edge data structure is the implementation of an edge algebra Guibas and Stolfi (1985) as shown in Fig. 3), which is the mathematical structure that defines the topology of any pair of dual subdivisions on a two-dimensional manifold Guibas and Stolfi (1985).

In three dimensions, dual subdivisions also permit us to understand the geometry of objects (primal subdivision) and how different solids are spatially related (dual subdivision, e.g. two rooms in a building are *adjacent*) as shown in Fig. 4. Arguably the most known use of the dual, which stores the topological relationships among 3D objects is to model navigational paths inside three-

---

[4] A subset of a cell complex is closed if, and only if, the complement of its intersection with the union of each cell and its boundary is a neighborhood.
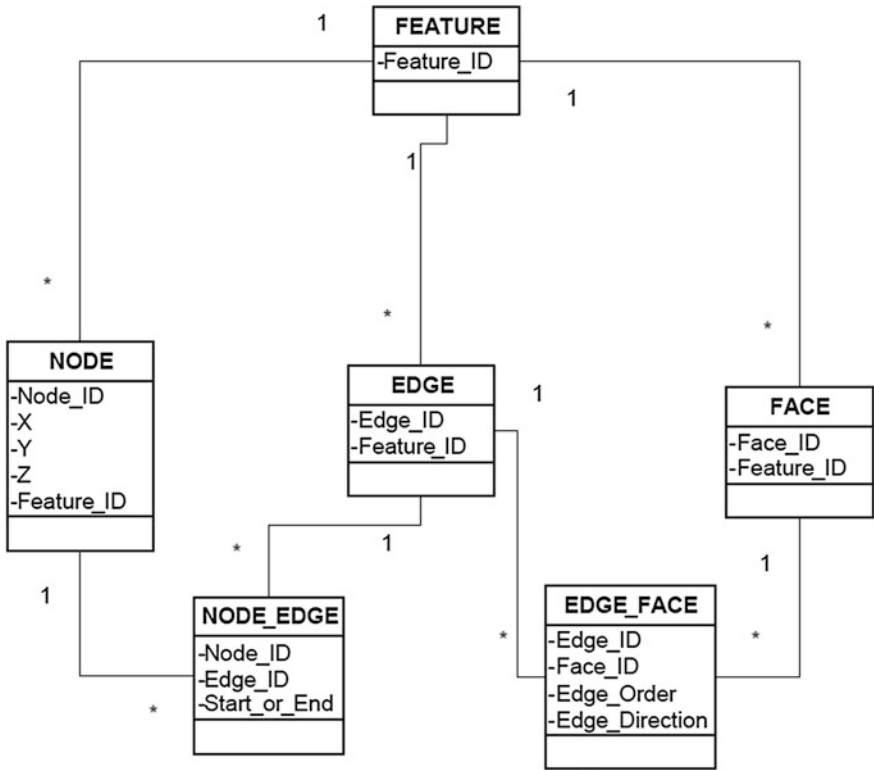
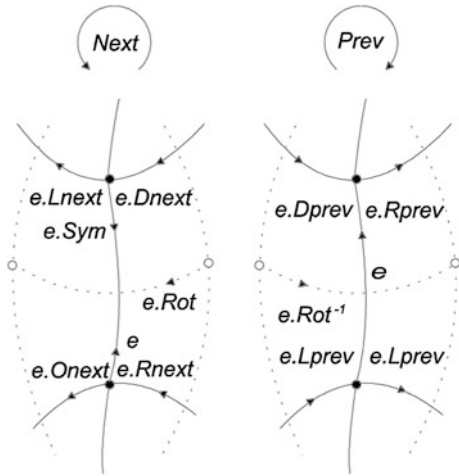**Fig. 2** The UML diagram of the boundary representation (taken from Ellul and Haklay (2009))

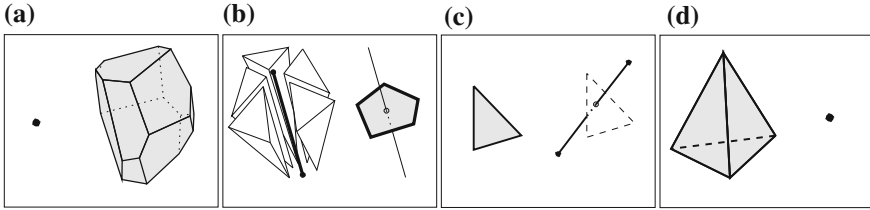**Fig. 3** Quad-edge data structure (from Guibas and Stolfi (1985))

Fig. 4 Duality in a 3D cell complex

dimensional buildings. However, there are other usages of the dual in spatial analysis for example finding the neighboring objects or buildings from any given object or analyzing the propagation of fire, floods, etc.

2.4 The Dual Half-Edge Data Structure

The Dual Half-Edge (DHE) structure, as proposed by Boguslawski et al. (Boguslawski et al. 2011; Boguslawski 2011), is a data structure that is able to represent a set of connected polyhedra forming a cell complex using a boundary representation (or B-rep). It does so by simultaneously storing both the primal and the dual graphs of the objects, in a similar manner as the Quad-Edge structure of Guibas and Stolfi (1985) in 2D.

As shown in Fig. 5a, with the DHE each polyhedron is represented independently with an edge-based structure (a *B-rep* model), and adjacent polyhedra are linked together by their shared faces, which are represented by Half-Edges joining 3-cells. These form a graph of connections in the dual of the original (primal) graph. Both the primal and the dual graphs are identical in terms of structure (i.e. their basic elements and connections). Figure 5b shows an idea of the relationships that are stored for each edge.

Since these graphs conform to Pointcaré's duality concept, the only cells that are needed to build a 3D model are the 0-cells (nodes) and 1-cells (edges); the nodes store the vertex coordinates, while the edges store the connections between the nodes. Meanwhile, the 2-cells (faces) and 3-cells (volumes) are only implicitly represented, but their attributes can be stored in their dual counterparts, the 1-cells and 0-cells in the dual graph.

However, an edge is not an atomic element in the DHE. Each edge consists of two Half-Edges, each of them being permanently connected with its corresponding Half-Edge in the dual. This pair, Half-Edge in the primal graph and Half-Edge in the dual one, is called the *dual Half-Edge*, and forms the atomic element in this model. Each Half-Edge is represented with five pointers which keep references to: an associated vertex (V in Fig. 5), the next edge around a shared vertex (N_V in Fig. 5), the next edge around a shared face (N_F in Fig. 5), the second Half-Edge of the edge (S in Fig. 5), and to the dual Half-Edge (D in Fig. 5).
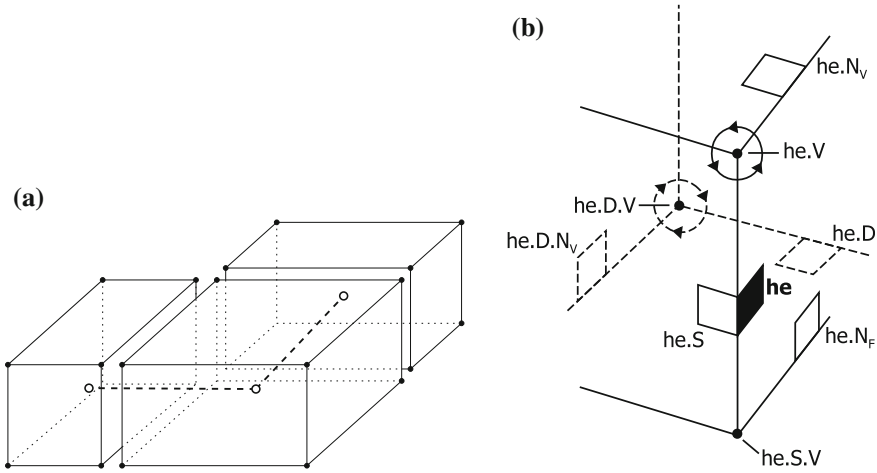
Fig. 5 The dual half-edge data structure in 3D. **a** The DHE models 3D subdivisions by representing the boundary of each polyhedron separately with a graph (edges are *black lines*), and two adjacent polyhedra are linked together by the dual graph (edges are *dashed lines*). **b** The DHE pointer based data structure; the primal graph (*solid lines*) is connected permanently with the dual graph (*dashed lines*); *he*-original Half- Edge; S, N_V, N_F, D, V - pointers.

These five pointers are necessary to represent complex models including non-manifold cases (when more than two cells are linked by a shared lower-dimensional cell. However, the number of pointers can be reduced by one if only cells linked by a shared face are taken into consideration. Additionally, a primal and dual Half-Edge pair can be merged and stored as a single record, since they are permanently connected (the number of pointers is reduced by one).

Using the data structure directly, without higher level construction operators would be extremely difficult ('manual' updating of pointers while edges are added to a model can easily cause many mistakes). Therefore, it is preferred to use the construction operators from Boguslawski (2011). They allow for model construction in an easy way, edge-by-edge, like in various CAD systems. Additionally, the dual graph is created automatically as the edges are added to the model and single cells are linked into a complex. These operators, used for modifications of the existing model, make only local changes in the primal and dual graph, and thus the whole dual graph does not need to be reconstructed after each modification.

During the construction process, the external cell, which encloses cells in a complex representing a modelled object, is automatically created. It can be considered as 'the rest of the world'. This external cell prevents topological inconsistencies at the boundary of the complex, where cells do not have an adjacent cell to connect to. Also, navigation can be implemented without testing if a boundary of the complex is approached.

Figure 6 shows one possible way to construct two cubes linked into one complex. It is based on CAD-like operators—Euler operators (Baumgart 1975,

Braid et al. 1980; Mäntylä 1988) and extended Euler operators (Masuda 1993). First, two separate cubes are created (see Fig. 6a). Then, they are linked by a shared face (see Fig. 6b). It is possible to define different sequences which results in the same model. It should be noted that the external cell and dual graph are present at each step of the process, but for the sake of clarity the external cell and dual graph are not shown. The final model consists of three cells: two internal cubes and one external cell (see Fig. 6c).

The DHE was originally designed for 3D models. However, a single polychoron (a 4D polyhedron) can be represented using the DHE without any modifications, except for the use of 4D coordinates. This is done by representing the polyhedra that lie on its boundary, in a similar manner as a 2D data structure is commonly used to represent a single polyhedron by storing the polygons in its boundary, cf. Baumgart (1975).

Lee and Zlatanova (2008) and Lee and Kwan (2005) extract from a 3D building a graph that can be used in case of emergency, and Bogualawski et al. (2011) and Bogualawski (2011) perform the same using a data structure, the *dual half-edge* (DHE), which simultaneously represents the building (the rooms and their boundaries) and the navigation graph. With the DHE, the construction and manipulation operations update both representations at the same time, permitting the simultaneous modelling and characterisation of buildings. There are several other examples of duality in GIS: the Delaunay triangulation and the Voronoi diagram are often used to model continuous phenomena, these two structures being dual to each other. Dakowicz and Gold (2003) use them for terrain modelling, Lee and Gahegan (2002) for interactive analysis, and Ledoux and Gold (2008) for three-dimensional fields in geosciences. In higher dimensions, we can also store the geometry and the topological relationships in a pair of dual subdivisions.

3 Geometric Topology

This section has been written from the excellent visual introduction book on algebraic topology and geometric topology Fomenko (1994). *Geometric topology* is the branch of mathematics that studies *topology* (i.e. all the properties that are invariant by continuous mappings) through some geometric objects called *manifolds* (topological spaces that near each point resemble Euclidean spaces) and their mappings and embeddings into each other. A central concept in geometric topology is the concept of *ramification* (the intuitive concept of several sheets joining together, further explained in next paragraph and illustrated by Fig. 7). An important topological concept is the *genus* of a topological object i.e., the number of handles that need to be added to a sphere, so that the result is *homeomorphic* (resembles) the given topological object, i.e., there is a one-to-one continuous mapping between them whose inverse mapping is also continuous. Another important topological concept is the *Euler-Poincaré characteristic*, which is defined as $\chi = k_0 - k_1 + k_2 - k_3 + \cdots$, where k_i denotes the number of cells of dimension i in the cell complex. However, the

(a)

(b)

(c)
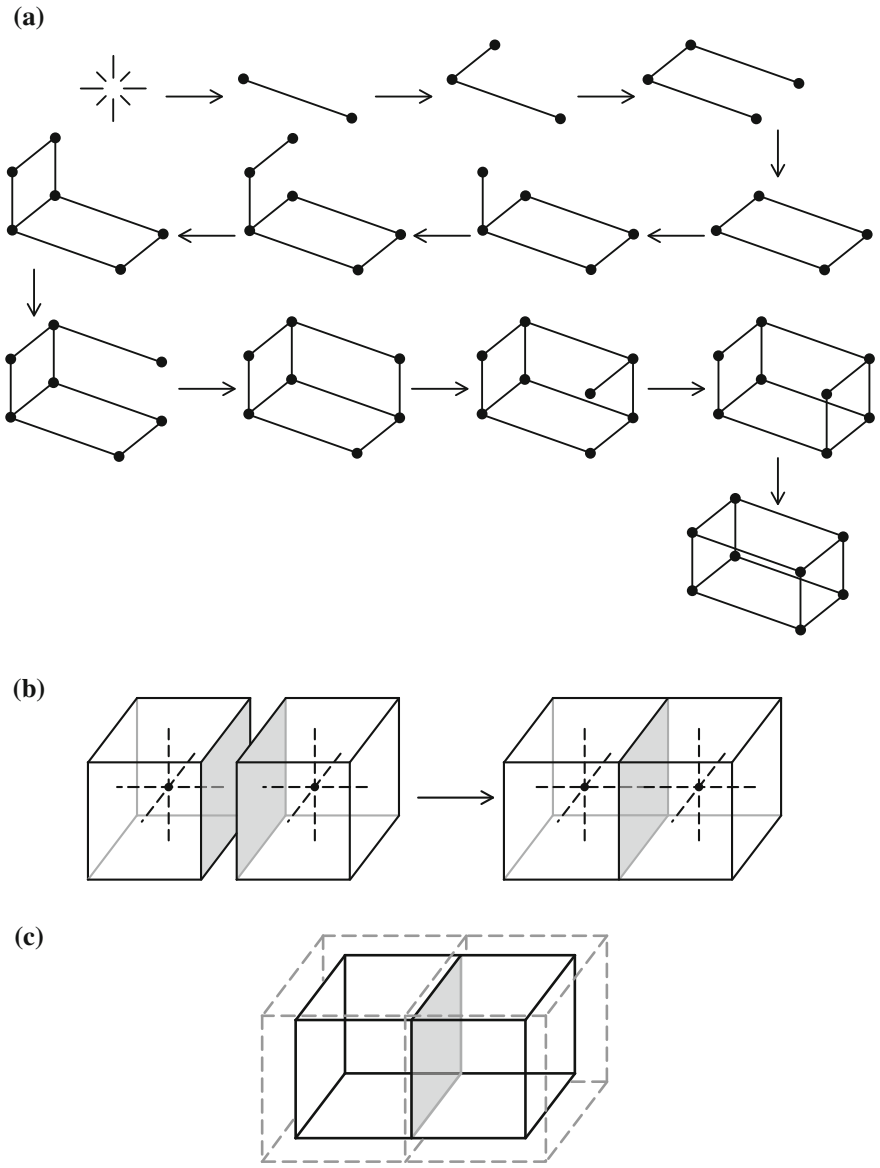
Fig. 6 Cell complex construction process. **a** A cube construction scenario. **b** Cubes share a common face (*grey*). Cells in the complex are connected using dual edges (*dotted lines*). **c** The resulting model consists of two internal (*solid lines*) and one external (*dotted grey lines*) cells

geometric concept of ramification is related to the topological concepts of genus and Euler-Poincaré characteristic through the *Riemann-Hurwitz formula*, also known as
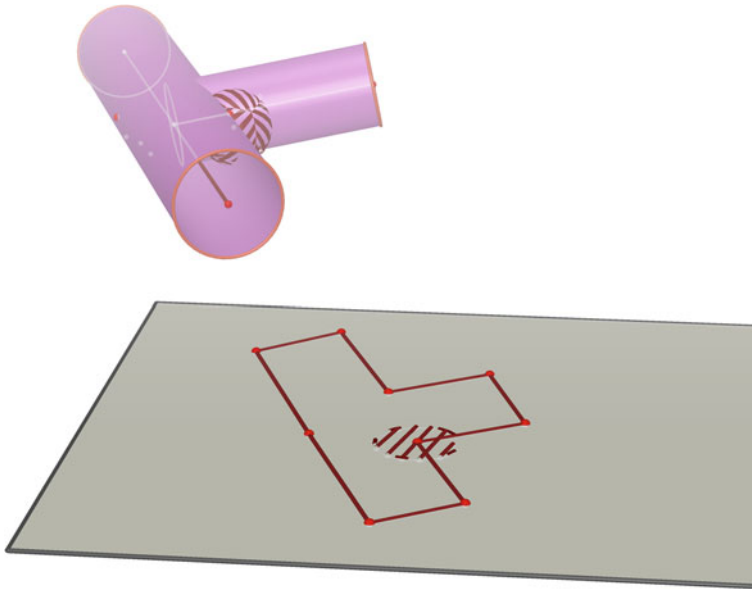
Fig. 7 The concept of ramification. Here the ramification points of the union of the two cylinders is the common intersection curve of these two cylinders. The neighborhood (hashed ball without its bounding sphere) of a ramification point of the union of two cylinders contains unramified points on two different sheets—the two cylinders without their boundaries and common intersection—, whose projection onto the plane are contained in a single neighborhood (hashed disk without its bounding circle) of the projection of the ramification point onto the plane. The degree of the covering map (projection in this case) is two, since each point on the neighborhood of the projection of the ramification point onto the plane has two antecedents by the covering map: one on each sheet, except at the ramification points, where the two sheets meet

the Hurwitz theorem in algebraic topology, which is a special case of the Riemann-Roch theorem in algebraic geometry.

Each point p of a geometric object X of dimension d has a neighborhood $V(p)$ which is *"evenly covered"* by *sheets* i.e., *disjoint arc-connected open sets* (where each point of these sheets has a neighborhood homeomorphic to a ball without its bounding sphere and it is possible to walk from any point to any other point of these sheets without leaving them, see Fig. 7). The minimum number of sheets (path-connected disjoint open sets) needed to cover X at p is referred to as the number of sheets N_p around p, and we say that the *covering* of the geometric object is N_p-sheeted around p, or the degree of the *covering map* (mapping the geometric object to a $d-1$ dimensional space like the projection onto the plane in Fig. 7) is N_p around p. Intuitively, a ramification point q is a point where several sheets meet together, i.e., the number of sheets is larger than one in all the points of the neighborhood of q except at q (where the sheets meet, see Fig. 7, where the ramification points are the points on the intersection of the two cylinders, the number of sheets at these points is one, while the number of sheets is two in their neighborhood

except themselves). The concept of *ramification index* e_p corresponds to the number of sheets that meet at a point p. Only finitely many points are ramification points. All other points (where there is only one sheet) have ramification index 1.

4 Generalizing the Quad-Arc Data Structure from 2D to 3D

The Quad-Arc data structure is a 2D data structure that modifies the Quad-Edge data structure Guibas and Stolfi (1985) in the following way. First, all points that belong to the same polygon are tagged with the polygon ID. Then, all the primal Quad-Edges that have the same polygon tag at the end-vertices of their dual Quad-Edge (polygon IDs) are grouped together into a single Quad-Arc, which is represented by a single arc composed of several straight line segments through intermediate vertices. The corresponding dual Quad-Arc is a straight Quad-Edge. This construction process can be easily generated to 3D or more generally to nD. The main difference between 2D and 3D is that in 3D, instead of considering polygon tags, we are considering volume tags. It is not only primal Quad-Edges that need to be grouped together if the end-vertices of their dual Quad-Edges have the same volume tag, but also these dual Quad-Edges (and possibly also the faces) of the dual subdivision.

5 The Dual Half-Arc Data Structure

The Dual Half-Arc data structure generalizes the Dual Half-Edge data structure by grouping together primal Half-Edges whose dual Half-Edges have the same volume tag at their end-vertices and these dual Half-Edges. The relational model corresponding to the Dual Half-Edge data structure is shown in Fig. 8, while the relational model corresponding to the Dual Half-Arc data structure is shown in Fig. 9.

This grouping of dual Half-Edges is done in the same way as the 3D Quad-arc data structure groups together the primal Quad-Edges whose dual Quad-Edges have the same volume tags at their end-vertices. One illustration of this grouping on the Dual Half-Edge data structure is provided in Figs. 10 and 11. Such an object is simple enough to show very easily the differences between the Dual Half-Edge, the Dual Half-Arc and the simplified Dual Half-Arc data structures. We could have shown a house, but the differences between these data structures would have been more difficult to visualize. Indeed, all the edges that correspond to ramifications (e.g. three or more walls that meet together) would remain in the Dual Half-Arc and in the simplified Dual Half-Arc data structure.

As explained in Sect. 3, a fundamental concept of geometric topology is the concept of ramification, i.e., the fact that several sheets (considered as disjoint path-connected open sets) meet at a point (or at a curve). In fact, we can model any
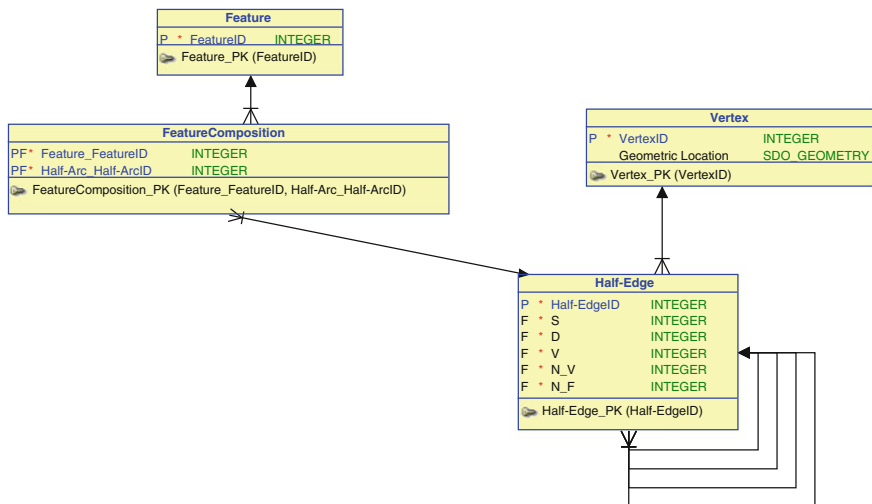
Fig. 8 The relational diagram of the dual half-edge data structure
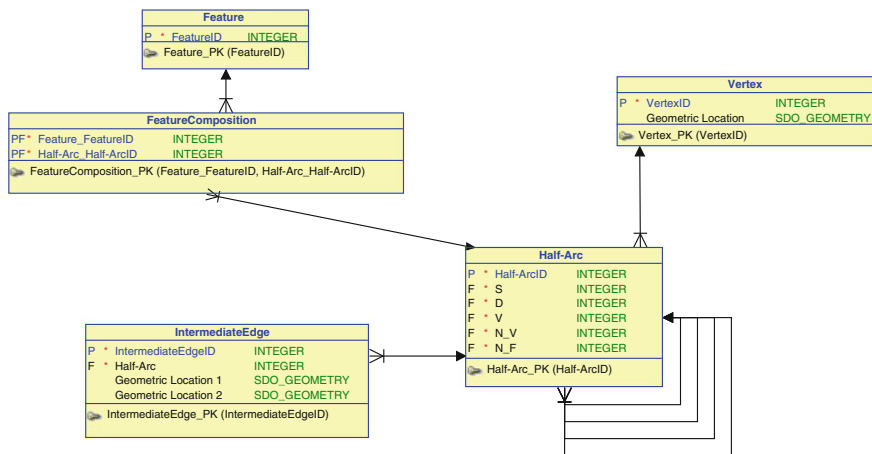
Fig. 9 The relational diagram of the dual half-arc data structure

geometric object by continuously deforming the primal subdivision of its Dual Half-Arc data structure to that geometric object. For example, we can model a cylinder as the glueing of two half-cylinders at their two end straight line segments. However, we can also consider the cylinder as the deformation of its development (a rectangle) to bend it continuously until its final shape and then, glueing the two end straight line segments. Then, we even need fewer Dual Half-Arcs, as shown in Fig. 12, which we call the simplified Dual Half-Arc data
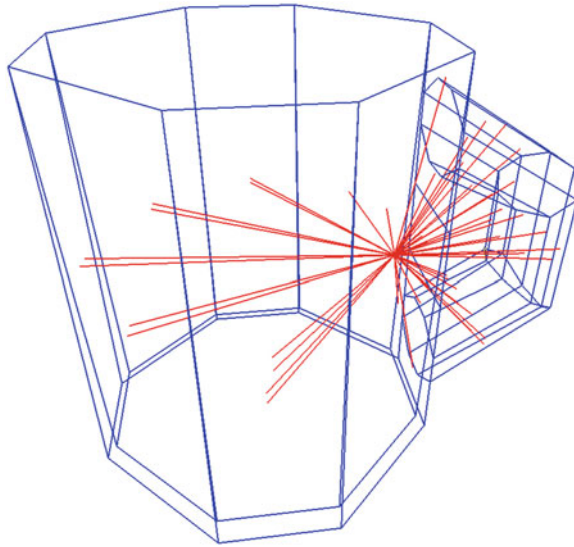
Fig. 10 A cup modeled with the dual half-edge data structure
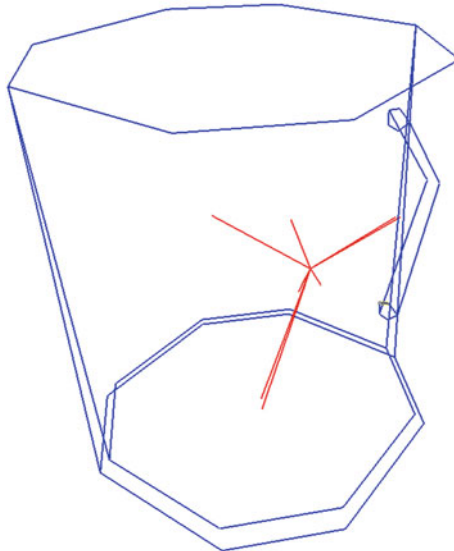
Fig. 11 A cup modeled with the dual half-arc data structure

structure. The main idea is that we can further group primal Half-Edges such as
end-vertices volume tags are the same if, and only if, these primal Half-Edges
correspond to edges of ramification index 1 and they are smooth edges.
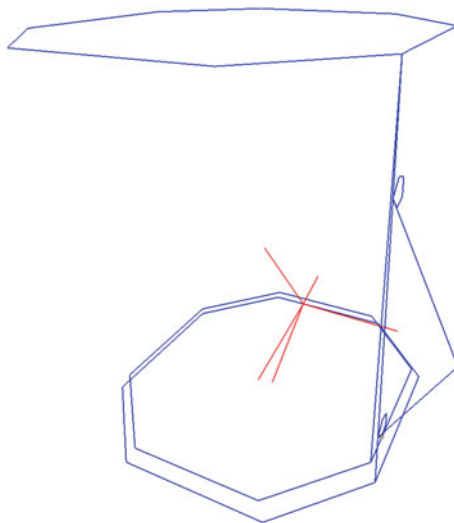
Fig. 12 A cup modeled with the simplified dual half-arc data structure

6 Discussion

In this chapter, we have generalized the Quad-Arc data structure from 2D to 3D and we have designed a novel 3D topological data structure called the Dual Half-Arc, that provides a synthesis between the newly generalized 3D Quad-Arc data structure and the Dual Half-Edge data structure. This is done by applying the idea of generalization of the newly generalized 3D Quad-Arc data structure using volume tags to the Dual Half-Edge data structure. The ultimate goal is to represent both the geometric (primal) subdivision of space induced by the geometric objects and the topological relationships among the geometric cells of the primal subdivision (dual subdivision) as a minimal (in the sense of set inclusion and number of cells of each dimension) geometrical/topological data structure. In our future work, we will prove the minimality of this data structure among the set of all boundary representations. The Dual Half-Arc data structure could have significant impact in GIS and spatial databases because it will induce more compact representations of the geometry and topology of geometric objects. This is crucial in applications, since most of the running time of any algorithm is lost in input/output operations (even with solid state disks). It is worth exploring potential future applications. Potential applications include emergency management (fires, earthquakes, tsunamis) with dynamic evacuation routes with changing building topology, mobile telecommunication networks modeling with addition of base stations, robotic injured evacuation, etc.

References

Baumgart BG (1975) A polyhedron representation for computer vision. In: Proceedings of the 19–22 May, 1975, national computer conference and exposition, pp 589–596

Boguslawski P (2011) Modelling and analysing 3d building interiors with the dual half-edge data structure. PhD thesis, University of Glamorgan

Boguslawski P, Gold CM, Ledoux H (2011) Modelling and analysing 3D buildings with a primal/dual data structure. ISPRS J Photogramm Remote Sens 66:188–197

Braid IC, Hillyard RC, Stroud IA (1980) Stepwise construction of polyhedra in geometric modelling. In: Brodlie KW (ed) Mathematical methods in computer graphics and design, Academic Press, pp 123–141

Dakowicz M, Gold CM (2003) Extracting meaningful slopes from terrain contours. Int J Comput Geometry Appl 13(4):339–357

Ellul C, Haklay M (2009) Using a b-rep structure to query 9-intersection topological relationships in 3d gis—reviewing the approach and improving performance. pp 127–151. http://www.scopus.com/inward/record.url?eid=2-s2.0-84879660700partnerID=40md5=890e5e0c556daba8b3e4ccda230106ce cited By (since 1996)2

Fomenko A (1994) Visual geometry and topology. Springer, New York. http://books.google.dk/books?id=47TvAAAAMAAJ

Gold C (1998) The quad-arc data structure. In: Poiker T, Chrisman N (eds) Proceedings of 8th international symposium on spatial data handling, pp 713–724

Gold CM (1991) Problems with handling spatial data—the Voronoi approach. CISM J 45(1):65–80

Guibas LJ, Stolfi J (1985) Primitives for the manipulation of general subdivisions and the computation of Voronoi diagrams. ACM Trans Graph 4(2):74–123

Ledoux H, Gold CM (2008) Modelling three-dimensional geoscientific fields with the Voronoi diagram and its dual. Int J Geogr Inf Sci 22(5):547–574

Lee I, Gahegan M (2002) Interactive analysis using Voronoi diagrams: algorithms to support dynamic update from a generic triangle-based data structure. Trans GIS 6(2):89–114

Lee J, Kwan MP (2005) A combinatorial data model for representing topological relations among 3D geographical features in micro-spatial environments. Int J Geogr Inf Sci 19(10):1039–1056

Lee J, Zlatanova S (2008) A 3D data model and topological analyses for emergency response in urban areas. In: Zlatanova S, Li J (eds) Geospatial information technology for emergency response. Taylor & Francis, New York, pp 143–168

Mäntylä M (1988) An introduction to solid modeling. Computer Science Press, New York

Masuda H (1993) Topological operators and boolean operations for complex-based nonmanifold geometric models. Comput Aided Des 25(2):119–129

Stroud I (2006) Boundary representation modelling techniques. Springer-Verlag New York Inc, Secaucus

Webster J (2003) Cell complexes, oriented matroids and digital geometry. Theoret Comput Sci 305(1–3):491–502, doi: 10.1016/S0304-3975(02)00712-0, URL http://dx.doi.org.globalproxy.cvt.dk/10.1016/S0304-3975(02)00712-0, Topology in computer science (Schloß Dagstuhl, 2000)

Earthquake Precursory Signals
from Satellite Imagery and Seismography:
A Review

Habibeh Valizadeh Alvan and Shattri Mansor

Abstract Earthquake prediction has been always an interesting, controversial subject among researchers. Scientists, data providers, geologists, geochemists, and remote sensing experts are working on new theories and data compositions to provide better understanding of earthquake related processes to present opportunities for detection short term precursory events. Satellite based data are now used for a wide variety of experimental earth studies. Several atmospheric and surface phenomena have been recognized as precursory events and efforts are being made to produce local prediction models which encompass all the regional, climatic, and geological setting of earthquake prone areas. The first step of a successful prediction would be producing thorough information about the geodynamics of the region. While long term prediction enable scientists to identify regions with expected future earthquakes, continuous monitoring of changes of known precursors may pave the way for establishing local warning systems. For this, in situ and satellite-based measurements should be compounded and co analyzed so that all seismic and non-seismic factors in a particular region are identified. This review is a quick look at the recent advances and problems in identifying earthquake precursors as well as new technologies for solving old problems of geologists such as mapping hidden faults.

Keywords Earthquake prediction · Phenomenon · Fault, remote sensing · Early warning

H. V. Alvan (✉) · S. Mansor
Civil Engineering Department, University Putra Malaysia, Serdang, Malaysia
e-mail: habibeh.valizadeh@mutiara.upm.edu.my

S. Mansor
e-mail: shattri@eng.upm.edu.my

1 Introduction

Earthquake is the trembling or shaking movement of the earth's surface. It occurs when energy stored within the earth, usually in the form of strain in rocks, suddenly releases. This energy is transmitted to the surface by seismic waves. Most earthquakes are minor tremors. Larger earthquakes usually begin with tremors, but rapidly take the form of one or more violent shocks, and end in vibrations of gradually diminishing force called aftershocks.

The emergence of high quality measurement devices from a decade ago had directed the courses of earth-related efforts towards providing better and more accurate knowledge of the mechanical and chemical ongoing in the earth during natural phenomena. Laboratory micro-scale experiments, powerful sensors, and advance imaging devices allow scientists to present detailed explanations of possible atomic and molecular interactions in materials. With the satellites research organizations that could send their sensors to high altitudes producing round-the-clock monitoring of the earth's surface and atmosphere in wide scales, there is long list of image and non-image datasets proposing a wide array of views from any part of our globe. In this climate, theoreticians are able to base their theories about the origins and mechanisms of natural events upon encompassing, more accurate inspections of what is going on under, on, and above the earth's surface.

During the past years, occurring numerous devastating earthquakes in different parts of the world that caused thousands of deaths and millions of dollars in property loss and impacts on strategic and scientific planning has stirred a lot of interest among researchers to work on the identification and detection of the earthquake precursory events to propose possible short-term prediction models that lead to mitigate damage from future earthquakes (Ryabinin et al. 2011). So far, they have identified some events that theoretically are expected to take place and practically are possible to detect before and during earthquakes. Studies on the surface and air temperature, surface latent heat flux, relative humidity, radon isotopes, ionosphere variations and some other precursors resulted in successful detection of extraordinary changes during several past oceanic and land earthquake instances and assumptions on the causes of these events observed during seismic activities (Wang and Shi 1984; Gorny et al. 1988; Nosov 1998; Freund and Ouzounov 2001; Tronin et al. 2002, 2004; Dey and Singh 2003a, b; Cervone et al. 2004, 2006; Pulinets 2004; Saraf and Choudhury 2003–2005a, b, c; Saraf et al. 2008; Choudhury et al. 2006; Parrot et al. 2006; Pulinets et al. 2006; Singh et al. 2006, Singh et al. 2007a, b, 2010; Qin et al. 2009; Kumar et al. 2009; Revathi et al. 2011; Alvan et al. 2012).

In this chapter we will look at heat based events on and above surface prior to and during main shakes (known as earthquake precursors) which can be monitored from space as well as the possibility of detecting warning foreshocks and movements of the earth's ground from seismograph.

2 Earthquake Prediction

The basic concept of the classical approach to earthquake prediction, which was suggested by Raid in 1910, is monitoring the places that have the previous records of this event (Revathi et al. 2011). Knowledge of the earthquake experiences, tectonic setting, and geological characteristics of an area help determining the locations and recurrence intervals of earthquakes (Nelson 2010). By studying the shake records of an area it will be possible to determine recurrence intervals of major earthquakes. In fact, long-term prediction methods suggest the occurrence of earthquakes soon or later but they do not give information about the location and time of an earthquake whose preparation stages have already begun. In contrast, monitoring surface and above surface phenomena during the earthquake preparation stage may provide clues to the location and time of an impending events.

Beside the anomalous events or processes that may precede an earthquake (precursory events) and might signal a coming earthquake, the energy built up in the earth's crust can cause swelling of rocks which result in ground uplift and tilting in active fault zones. This causes the formation of numerous small cracks and an unstable condition that may lead to small earthquakes before the main event (Nelson 2010). These foreshocks are considered as seismic precursory signals and usually appear less than 30 days before the main shake (Ihmle and Jordan 1994; Reasenberg 1999, Gavrilov et al. 2008; Ryabinin et al. 2011). Thus, significant ground deformations and the occurrence of successive small shakes in the vicinity of active faults may be signs for existence of seismic activities leading to a strong earthquake. However, short-term earthquake prediction through monitoring precursory events has always been difficult to obtain because earthquake related processes occur deep beneath the surface. Despite the array of precursors that are possible to monitor, successful short-term earthquake prediction has so far been difficult to obtain (Nelson 2010). In order to produce enough information for monitoring seismic activities along active fault zones large number of ground observation stations are necessary. But, satellite-based monitoring methods yield wider coverage, rich information and higher spatial and spectral resolutions. Instead of relying on a single precursor for earthquake prediction, different on-site and remotely-sensed data should be integrated to produce better and more comprehensive earthquake studies. There are several national and international space programs for monitoring earthquake precursory events (Ryabinin et al. 2011).

3 Earthquake Precursory Signals

3.1 Active Faults

Classical earthquake theories suggest that active faults are the generator of this event. Small shakes grow into main earthquakes while they are spreading along

these faults. The first stage of a successful short-time prediction would be a successful detection of active faults. However, the identification of an earthquake producing fault is not easy. In Japan, it took 14 years to survey 110 active faults but the next 6 major earthquakes (6.9–7.3) occurred along undetected ones. They suggested that the location and geometry of a source fault of a future earthquake can be inferred from fold structure. Other methods to get information about hidden faults are seismography and Radar imaging. Seismic data are used to detect faults with no ruptures on the earth's surface. Talebian et al. examined the 2005 Dahuiyeh earthquake sources (Talebian et al. 2006). They used seismic body waves, radar interferometry and field investigation to examine the source processes of the destructive earthquake. Using Landsat TM, ETM and SAR ERS-1 data and conducting long term monitoring of tectonic structures they identify linear features (active faults). Currently, researchers concentrate their efforts on identifying local and hidden faults and monitoring the precursory events along them. Infrared images are used to show thermal anomalies around fault zone for past earthquakes. Higher concentration of atmospheric water vapor along nearby active faults was reported 11 days before Wenchuan earthquake (Liu et al. 2007).

Scientists used Landsat TM, ETM and SAR ERS-1 data to successfully detect linear features on the earth's surface (faults) through visual interpretation (Zoran 2010). They reported that remote sensing multi-spectral images have great potentials in large scale active faults investigation. They declared fabulous result of their efforts in detection of invisible faults. They attributed the successfulness of remote sensing to its wide recording spectrum from visible to microwave. Nevertheless, those faults buried by soil layers may not be detected with satellite-based data.

Proper approach to identify the faults with no ruptures on the earth's surface or those which have been covered by soil is to perform geochemical surveys. In this method, sampling is carried away to record the amount of Radon gas in organized sampling networks or deep into the surface in certain points. By statistical analyses and re-sampling methods it will be possible to compare the resultant maps with fault maps and detect invisible faults deep enough to be a path to Radon reach the earth's surface.

3.2 Heat and Thermal Anomalies

The accumulated stress in the ground causes the generation of two phenomena; Heat and seismic waves. Heat is a direct result of the compression in underground rocks. Rocks are packed together to absorb some of the stress. In this level the underground water comes up causing higher resistance capability of the crustal and upper crustal part of the ground (Plastino et al. 2010). But, when the tolerance limit has passed the rocks break and micro-cracks form. This allows the water to come back filling the newly formed holes causing the loss of resistance of the whole system. It is when the ground is waiting for another pressure to rupture or move

along the already existing faults. During this process the friction between rocks and the release of gases caught inside rocks causes increase in temperature. The heat, water vapor and gas reach the Earth's surface and as a result the litho-atmospheric coupling starts. First, convective heat flux (hot water and gas) changes the temperature of the Earth's surface. Second, changes of the water level with usual temperature lead to alterations in soil moisture, and consequently the physical properties of the soil (Israel and Bjornsson 1966; King 1980; King et al. 1996; Immè et al. 2006; Giammanco et al. 2007; Giammanco and Bonfanti 2009). The difference in physical properties determines the different temperatures on the surface. Third is the greenhouse effect, when the optically active gases are escaped to the surface (Tronin et al. 2004).

The anomalies in heat and related phenomena occur in a vast area. Remote sensing techniques provide the opportunity of studying the consequences of seismic activities in large scales. However, other non-seismic factors like surface formation type and characteristics, seasonal changes, solar radiation, etc. may be affecting the temperature regime of an earthquake prone region. The heat generated by the chemical and physical processes inside the earth's ground may not be high enough to be distinguished from background noise. Nevertheless, the resultant phenomena like air humidity are found to be increased by the earthquake related energy release.

The idea that the thermal anomalies may be connected with seismic activity was put to application in Russia, China and Japan. In 1980, Russian researchers detected thermal anomalies prior to an earthquake in central Asia using satellite images. After that, thermal anomaly in surface temperature has been observed around 1–14 days before many strong earthquakes instances with abrupt change in the temperature value of the order of 3–7 °C or more and disappeared a few days after the main events (Gorny et al. 1988; Qiang et al. 1999; Tronin 2000; Tronin et al. 2002; Ouzounov and Freund 2004; Saraf and Choudhury 2005a, b, c; Choudhury et al. 2006; Genzano et al. 2007; Ma et al. 2008, 2010). Some remote sensing satellites can measure the radiations coming from the earth in thermal bands and provide useful information prior to earthquakes. Due to their suitable temporal and spatial resolutions, the thermal infrared bands of Advanced Very High Resolution Radiometer (AVHRR) and Moderate Resolution Imaging Spectroradiometer (MODIS) data can be used (Revathi et al. 2011).

Amount of water vapor in the atmosphere in a region is highly related to the speed of evaporation. Under stable conditions of water supply this factor is mainly proportional to the temperature. So changes in SLHF are controlled by variation in surface temperature, which is believed to be a precursory parameter during an earthquake. However topography, feature type, solar radiation, weather, seasonal changes and many non-shock factors can affect the temperature in a large area and some causes, such as human or construction activities may also influence on the temperature of a small area (Tronin 2000; Liu et al. 2007). Relationships between inland and oceanic seismic activities and anomalous changes in SLHF in different parts of the world have been registered by many researchers. Time series of SLHF have shown meaningful rises from a month to few days before the earthquake

events (Cervone et al. 2004, 2006; Dey et al. 2004; Singh et al. 2006; Alvan et al. 2012, 2013). SLHF data with resolution of 1.9° by 1.9° are available from the National Center for Environmental Prediction (NCEP–NCAR), reanalysis data of the IRI/LDEO Climate Data Library (http://iridl.ldeo.columbia.edu) which are generated by taken into consideration the measured values at various worldwide stations and also those retrieved from satellite data.

Among all gases emitted from rocks during the earthquake preparation stages, radon is the only gas which has radioactive isotopes under normal conditions. Its most stable isotope, ^{222}Rn, has a half-life of 3.8 days. Once the isotope Radon222 seeps out of rocks and its decay begins. This causes emission of α-particles from active tectonic faults. Emission of this positive ions results in ionization of the near-ground layer (Igarashi et al. 1995; Toutain and Baubron 1998; Omori et al. 2007; Inan et al. 2008; Ondoh 2009; Choubey et al. 2009; Kuo et al. 2010; Sac et al. 2011). The air ionization and emanation of some other gases like CO_2 leads to the changes in air temperature and humidity (Pulinets and Ouzounov 2011). But in fact, the origins and mechanisms leading to an expected higher air temperature in the seismic area is still a matter of debate among scientific theoreticians. In 2009, Freund et al. attributed this phenomenon to the local earthquake related electronic fields. They suggested that the ever increasing level of stress on rocks during the preparation stage of an earthquake causes the activation of highly mobile electronic charges in rocks and consequently air ionization. Then, a large number of atomic (ionic or covalent) bonds break increasing the crystal structure of the rocks. Finally, a chain of reactions result in an unbalanced charge distribution in underground material and the onset of strong local electric fields (Zoran 2010).

3.3 Seismography

The process of earthquake preparation does not end up with a single release of energy. In fact, much of the underground stress is released during small shakes before earthquakes. This low magnitude quakes which usually are not felt are called foreshocks (Console et al. 1993). Aftershocks are the signs of minor fracturing in compressed rocks which take place before main break in the earth's surface. They can start up to a year before a main event (Enescu et al. 2007). However, foreshocks do not necessarily occur before every earthquake. On the other hand, sometimes there is a chain of similar size earthquakes which occur one after the other without being followed by a strong main shake. These may limit the usefulness of foreshock monitoring in earthquake prediction.

On the whole, the appearance of seismic activities in seismic records is a subject of further analysis. Nowadays, with advances in seismograph technology we can get enough information about the origin and size of shakes in an earthquake prone area. Broadband, digital seismographs record the earth's movement in different directions which will allow for the identification of various stages of a quake, distance and direction, the extent and direction of effect, etc. In addition,

along with existing information about local faulting system of a particular area, these seismology investigations help in identifying hidden faults and release points of stress.

4 Conclusion

Among all surface and near surface phenomena and events which are supposed to be, theoretically or experimentally, related to the seismic activities during a major earthquake SLHF and temperature have been of most interest due to the capability of current remote sensing devices to record their variations. Other factors are either very hard to extract from satellite-based datasets or need costly and time-consuming in situ measurements on wide areas. These heat-based precursors are, somehow, considered as the underlying ones which may be supported by other clues such as changes in relative humidity or other factors for some case studies. The quality and precision of previous reports have always been a function of the recording facilities of data providers, data manipulation capabilities of data vendors, and types of the analyses used by researchers. Although, almost all researchers who worked on the topic of detection of the above-mentioned basic precursory events reported successful attempts, yet, most of them failed to perform accurate and encompassing spatio-temporal analyses which take into account the geological and geotechnical settings. In addition to assessing the condition in the epicentral region, one should bear in mind that, in most parts of the world, earthquakes are triggered by activities in the fault zones miles away from the epicenters. Statistical data of an epicenter could be of much importance, however, it will be more useful if the changing patterns of SLHF, surface and air temperature are mapped on wide scales and long time periods before and after a main event. On the other hand, Any research on this kind should be, more or less, complied with a chain of the events suggested by one of the available (micro or macro scale) geophysical or geochemical theories about the interactions take place during the gradual movements, compression, and decompression during the preparation stage of a major earthquake. This would need using all the possible ground or remote based information reflecting underground activities. Most of the theories on the underground changes in the earth insist on the movements which cause the generation and build-up of elastic strain in the crust. Seismograph stations, if dense enough and located at the immediate neighborhood, could be used to detect weak shakes prior to the main shakes which are not often reported by national or international bodies. The resultant shake maps may be used to determine the concurrency of ground movements and appearances of remotely sensible precursors, and also, for detection of possible local hidden or unmapped faults considering this fact that the partial releases of very energy that triggers the main event causes possible foreshocks weeks to days before the sensible shake.

References

Alvan HV, Azad FH, Omar HB (2012) Chlorophyll concentration and surface temperature changes associated with earthquakes. Nat Hazards 64(1):691–706

Alvan HV, Azad FH, Mansor SB (2013) Latent heat flux and air temperature anomalies along an active fault zone associated with recent Iran earthquakes. Adv Space Res 52(9):1678–1687

Cervone G, Kafatos M, Napoletani D, Singh RP (2004) Wavelet maxima curves of surface latent heat flux associated with two recent Greek earthquakes. Nat Hazards Earth Syst Sci 4:359–374

Cervone G, Maekawa S, Singh RP, Hayakawa M, Kafatos M, Shvets A (2006) Surface latent heat flux and nighttime LF anomalies prior to the Mw = 8.3 Tokachi-Oki earthquake. Nat Hazards Earth Syst Sci 6:109–114

Choubey VM, Kumar N, Arora BR (2009) Precursory signatures in the radon and geohydrological borehole data for M4.9 Kharsali earthquake of Garhwal Himalaya. Sci Total Environ 407:5877–5883

Choudhury S, Dasgupta S, Saraf AK, Panda S (2006) Remote sensing observations of pre-earthquake thermal anomalies in Iran. Int J Remote Sens 27(20):4381–4396

Console R, Murru M, Alessandrini B (1993) Foreshocks statistics and their possible relationship to earthquake prediction in the Italian region. Bull Seismol Soc Am 83:1248–1263

Dey S, Singh RP (2003a) Comparison of chlorophyll distribution in the Northeastern Arabian Sea and Southern Bay of Bengal using IRS-P4 ocean color monitor data. Remote Sens Environ 85:424–428

Dey S, Singh RP (2003b) Surface latent heat flux as an earthquake precursor. Nat Hazards Earth Syst Sci 3:749–755

Dey S, Sarkar S, Singh RP (2004) Anomalous changes in column water vapor after Gujarat earthquake. Adv Space Res 33:274–278

Enescu B, Mori J, Miyazawa M (2007) Quantifying early aftershock activity of the 2004 mid-Niigata Prefecture earthquake (Mw6.6). J Geophys Res 112:B04310. doi:10.1029/2006JB004629

Freund F, Ouzounov D (2001) Earth-atmospheric coupling prior to strong earthquakes analyzed by IR remote sensing data. AGU Fall Meet 82(47)

Freund FT, Kulahci IG, Cyr G, Ling J, Winnick M, Tregloan-Reed J, Freund MM (2009) Air ionization at rock surfaces and pre-earthquake signals. J Atmos Solar-Terr Phys 71:1824–1834

Gavrilov V, Bogomolov L, Morozova Y, Storcheus A (2008) Variations in GAE in a deep borehole and its correlation with seismicity. Ann Geophys 51:737–753. doi:10.4401/ag-3013

Genzano N, Aliano C, Filizzola C, Pergola N, Tramutoli VA (2007) Robust satellite technique for monitoring seismically active areas: the case of Bhuj-Gujarat earthquake. Tectonophysics 431:221–230

Giammanco S, Bonfanti P (2009) Cluster analysis of soil CO_2 data from Mt. Etna (Italy) reveals volcanic influences on temporal and spatial patterns of degassing. Bull Volcanol 71:201–218

Giammanco S, Sims KW, Neri M (2007) Measurements of 220Rn and 222Rn and CO2 emissions in soil and fumarole gases on Mt. Etnavolcano (Italy): implications for gas transport and shallow ground fracture. Geochem Geophys Geosyst 8:Q10001

Gorny VI, Salman AG, Tronin AA, Shilin BB (1988) Outgoing IR radiation of the Earth as an indicator of seismic activity. Proc Acad Sci USSR 301(1):67–69

Igarashi G, Saeki S, Takahata N, Sumikawa K, Tasaka S, Sasaki Y, Takahashi M, Sano Y (1995) Groundwater radon anomaly before the Kobe earthquake in Japan. Science 269(5220):60–61

Ihmle PF, Jordan TH (1994) Teleseismic search for slow precursors to large earthquakes. Science 266:1547–1551

Immè G, La Delfa S, Lo Nigro S, Morelli D, Patanè G (2006) Soil radon concentration and volcanic activity of Mt. Etna before and after the 2002 eruption. Radiat Meas 41:241–245

Inan S, Akgu T, Seyis C, Saatc R, Baykut S, Ergintav S, Bas M (2008) Geochemical monitoring in the Marmara region (NW Turkey): a search for precursors of seismic activity. J Geophys Res 113:B03401. doi:10.1029/2007JB005206

Israel H, Bjornsson S (1966) Radon (Rn-222) and thoron (Rn-220) in soil air over faults. Z Geophys 33:48–64

King CY (1980) Episodic radon changes in subsurface soil gas along active faults and possible relation to earthquakes. J Geophys Res 85:3065–3078

King CH, King BS, Evans WC (1996) Spatial radon anomalies on active faults in California. Appl Geochem 11:497–510

Kumar A, Singh S, Mahajan S, Bajwa BS, Kalia R, Dhar S (2009) Earthquake precursory studies in Kangra valley of North West Himalayas, India, with special emphasis on radon emission. Appl Radiat Isotopes 67:1904–1911. doi:10.1016/j.apradiso.2009.05.016

Kuo T, Su C, Chang C, Lin C, Cheng W, Liang H, Lewis C, Chiang C (2010) Application of recurrent radon precursors for forecasting large earthquakes (Mw > 6.0) near Antung, Taiwan. Radiat Meas 45:1049–1054

Liu SJ, Wu LX, Li JP et al (2007) Features and mechanisms of the satellite thermal infrared anomaly before Hengchun earthquake in Taiwan region. Sci Technol Rev 25(6)

Ma W, Zhao H, Li H (2008) Temperature changing process of the Hokkaido (Japan) earthquake on 25 September 2003. Nat Hazards Earth Syst Sci 8:985–989

Ma Y, Zhao Y, Liu S, Wu L (2010) Possible abnormal phenomenon of the atmospheric water vapor before Hengchun earthquake. In: Proceedings of electromagnetic research symposium China 2010, pp 109–113

Nelson SA (2010) Earthquake prediction and control. Natural Disasters, Tulane University Press

Nosov MA (1998) Ocean surface temperature anomalies from underwater earthquakes. Volcanol Seismol J 19(3):371–376

Omori Y, Yasuoka Y, Nagahama H, Kawada Y, Ishikawa T, Tokonami S, Shinogi M (2007) Anomalous radon emanation linked to pre-seismic electromagnetic phenomena. Nat Hazards Earth Syst Sci 7:629–635

Ondoh T (2009) Investigation of precursory phenomena in the ionosphere, atmosphere and groundwater before large earthquakes of M > 6.5. Adv Space Res 43:214–223

Ouzounov D, Freund F (2004) Mid-infrared emission prior to strong earthquakes analyzed by remote sensing data. Adv Space Res 33(3):268–273

Parrot M, Berthelier JJ, Lebreton JP, Sauvaud JA, Santolik O, Blecki J (2006) Examples of unusual ionospheric observations made by the DEMETER satellite over seismic regions. Phys Chem Earth 31(4–9):486–495

Plastino W, Povinec PP, De Luca G, Doglioni C, Nisi S, Ioannucci L, Balata M, Laubenstein M, Bella F, Coccia E (2010) Uranium groundwater anomalies and L'Aquila earthquake: 6th April 2009 (Italy). J Environ Radioact 101:45–50

Pulinets, S. (2004) Ionospheric precursors of earthquakes, recent advances in theory and practical application. TAO 15(3):413–435

Pulinets SA, Ouzounov D, Ciraolo L, Singh R, Cervone G, Leyva A, Dunajecka M, Karelin AV, Boyarchuk KA, Kotsarenko A (2006) Thermal, atmospheric and ionospheric anomalies around the time of the Colima M7.8 earthquake of 21 January 2003. Ann Geophys 24:835–849

Pulinets SA, Ouzounov D (2011) Atmosphere-ionosphere coupling (LAIC) model-an unified concept for earthquake precursors validation. J Asian Earth Sci 41:371–382

Qiang ZJ, Dian CG, Li L, Xu M, Ge F, Liu T, Zhao Y, Guo M (1999) Satellite thermal infrared brightness temperature anomaly image short-term and impending earthquake precursors. Sci China: D 42(3):313–324

Qin K, Guangment G, Wu L (2009) Surface latent heat flux anomalies preceding inland earthquakes in China. Earthq Sci 22:555–562

Revathi R, Brahmanandam PS, Raghavendra Vishnu T, Uma G (2011) Possible prediction of earthquakes by utilizing multi precursor parameters in association with ground and satellite-based remote sensing techniques. Int J Earth Sci Eng 4(6):978–981

Reasenberg PA (1999) Foreshock occurrence before large earthquakes. J Geophys Res 104:4755–4768

Ryabinin GV, Polyakov YS, Gavrilov VA, Timashev SF (2011) Earthquake precursors in the data for the Kamchatka peninsula. Cornel University Library

Sac MM, Harmansah C, Camgoz B, Sozbiler H (2011) Radon monitoring as the earthquake precursor in fault line in Western Turkey. Ekoloji 20(79):93–98

Saraf AK, Choudhury S (2003) Earthquakes and thermal anomalies. Geospatial Today 2(2):18–20

Saraf AK, Choudhury S (2005a) Thermal remote sensing technique in the study of pre-earthquake thermal anomalies. J Ind Geophys Union 9(3):197–207

Saraf AK, Choudhury S (2005b) NOAA-AVHRR detects thermal anomaly associated with 26 January, 2001 Bhuj earthquake, Gujarat, India. Int J Remote Sens 26(6):1065–1073

Saraf AK, Choudhury S (2005c) Satellite detects surface thermal anomalies associated with the Algerian earthquakes of May 2003. Int J Remote Sens 26(13):2705–2713

Saraf AK, Rawat V, Banerjee P, Choudhury S, Panda SK, Dasgupta S, Das JD (2008) Satellite detection of earthquake thermal precursors in Iran. Nat Hazard 47:119–135

Singh RP, Dey S, Bhoi S, Sun D, Cervone G, Kafatos M (2006) Anomalous increase of chlorophyll concentrations associated with earthquakes. Adv Space Res 37:671–680

Singh RP, Cervone G, Kafatos M, Prasad AK, Sahoo AK, Sun D, Tang DL, Yang R (2007a) Multi sensor studies of the Sumatra earthquakes and tsunami of 26 December, 2006. Int J Remote Sens 28(13–14):2885–2896

Singh RP, Cervone G, Singh VP, Kafatos M (2007b) Generic precursors to coastal earthquakes: inferences from Denali fault earthquake. Tectonophysics 431:231–240

Singh RP, Cervone G, Singh VP, Kafatos M (2010) Complementary nature of surface and atmospheric parameters associated with Haiti earthquake of 12 January 2010. Nat Hazards Earth Syst Sci 10:1299–1305

Talebian M, Biggs J, Bolourchi M, Copley M, Ghassemi A, Ghorashi M et al (2006) The Dahuiyeh (Zarand) earthquake of 2005 February 22 in central Iran: reactivation of an intermountain reverse fault. Geophys J Int 164, 137–148

Toutain JP, Baubron JC (1998) Gas geochemistry and seismotectonics: a review. Tectonophysics 304:1–27

Tronin AA (2000) Thermal IR satellite sensor data application for earthquake research in China. Int J Remote Sens 21(16):3169–3177

Tronin AA, Hayakawa M, Molchanov OA (2002) Thermal IR satellite data application for earthquake research in Japan and China. J Geodyn 33:519–534

Tronin AA, Biagi PF, Molchanov OA, Khatkevich YM, Gordeeev EI (2004) Temperature variations related to earthquakes from simultaneous observation at the ground stations and by satellites in Kamchatka area. Phys Chem Earth 29:501–506

Wang CY, Shi YL (1984) On the thermal structure of subduction complexes: a preliminary study. J Geophys Res 89(B9):7709–7718

Zoran M (2010) Earthquake precursors assessment in Vrancea area, Romania by satellite and geophysical in situ data. In: Proceedings of Fringe 2009 workshop, Frascati, Italy, ESA SP-677, March 2010

Hybrid 3D Segmentation Technique for 3D City Models

Khairul Hafiz Sharkawi and Alias Abdul Rahman

Abstract 3D city model is a virtual representation of a city or urban environment, where in GIS related context, represents existing cities in the world. Initially, they are used only as presentations that complement the results of 2D analyses and bear no analytical capabilities. The advancement in computer graphics technology has effectively sparked the effort towards realizing 3D GIS where the 3D models can be used directly in analyses rather than just purely visual enhancement. A lot of research has been conducted in an effort to provide analytical capabilities to the 3D models. Rapid developments in computer-related industries have led to cutting edge technologies that enable analyses to be conducted on the 3D models. The ability of 3D city models to represent real world objects more accurately have boosted its efficiency and usability in geospatial related analyses. Now, it has become the new trend in building and urban management while modelling 3D objects are getting easier with the emergence of user-friendly tools for 3D modelling available in the market. The Open Geospatial Consortium (OGC) has accepted City Geography Markup Language CityGML specifications as one of the international standards for representing and exchanging spatial data, making it easier to visualize, store and manage 3D city models data efficiently. CityGML represents the semantics, geometry, topology and appearance of 3D city models in five well-defined Level-of-Details (LoD), namely LoD0 to LoD4. However, complex building structures are making the 3D models unsuitable for analyses as it takes a lot of time to process large data. Thus, it is only logical to breakdown the complex building into manageable segments. Segmentation is basically a method to break down an object into simpler parts. This chapter introduces a hybrid 3D segmentation method based on semantic and geometric decomposition for 3D

K. H. Sharkawi (✉) · A. A. Rahman
3D GIS Research Group, Department of Geoinformation, Faculty of Geoinformation
and Real Estate, Universiti Teknologi Malaysia, 81310 Johor Bahru, Malaysia
e-mail: khafiz4@live.utm.my; hafiz.sharkawi@gmail.com

A. A. Rahman
e-mail: alias@utm.my

buildings in CityGML. The proposed method deals with segmentation of a 3D building based on its semantic value and surface characteristics, fitted by one of the predefined primitives. For future work, the segmentation method will be implemented as part of the change detection module that can detect any changes on the 3D buildings, store and retrieve semantic information of the changed structure.

Keywords 3D city models · 3D model segmentation · CityGML

1 Introduction

3D city model is a digital representation of a city or urban area that was previously generated only for visualization purposes to complement the results from 2D geospatial related analysis. The involvement of major industry players, private and government organizations as well as participation from the mass public has propelled the popularity and interests in 3D city modelling. Now, it has become the new trend in building and urban management while modelling 3D objects are getting easier with the emergence of user-friendly tools for 3D modelling available in the market. Currently, many countries around the world have been generating virtual 3D representation of their major cities. The growing interest in improving the usability of 3D city models has resulted in the development of various tools for analysis. Today, 3D city models are generated for various purposes such as for tourism, location-based services, disaster management and urban planning.

Over the years, there are quite a number of researches have been carried out to improve the usability of 3D city models in geospatial related analyses such as noise mapping (Kolbe 2009), pollution control, disaster management, navigational and network analysis.

The core entity in 3D city model is buildings since it is the entity that defines a city. However, other entities such as terrain, landscape, street furniture and vegetation also play important roles in representing the city as a whole. Since new developments, constructions and renovations are always happening all around the city, the buildings will change over time and their structures become more complex. However, complex building structures are actually a combination of several basic 3D primitives such as cubes, cuboids, spheres and cylinders. These combinations can be easily recognized by human brains naturally but computers do not have the same skill, hence the need for 3D segmentation for 3D city model objects. Segmentation is a method to breakdown a complex object into simpler parts and in 3D city models, each segmented parts usually represent a meaningful part of the building.

This chapter mainly focuses on the 3D segmentation technique for 3D city model objects (3D buildings) that can be deployed for several analyses in GIS such as change detection and automatic updating. In Sect. 2, this chapter will discuss about past researches related to CityGML and 3D city models, the building generation methods, and 3D segmentation on 3D buildings. Meanwhile, Sect. 3 will

discuss the segmentation technique for 3D city models which decomposed the model based on semantic and geometric values. The Sect. 4 will discuss the future work and conclusion that can be drawn from this chapter.

2 Related Works

2.1 3D City Models and CityGML

CityGML is a data model and an exchange format that represents 3D spatial data i.e. 3D city models, especially urban objects. According to Kolbe (2009), Groger and Plumer (2012), CityGML is in XML-based format and an application schema for the Geography Markup Language version 3.1.1 (GML3). The Open Geospatial Consortium (OGC) has accepted CityGML specifications as one of the international standards for representing and exchanging spatial data, along with GML3. CityGML represents the semantics, geometry, topology and appearance of 3D city models in five well-defined Level-of-Details (LoD), namely LoD0 to LoD4. The accuracy and structural complexity of the 3D objects increases with the LoD level where LoD0 is the simplest LoD (2.5D Digital Terrain Model (DTM)) while LoD4 is the most complex LoD (architectural details with interior structures). Kolbe (2009) discussed in detail the role of CityGML in exchanging and representing 3D city models, the aim of CityGML development, its modelling aspects, recent applications and its relation to other 3D standards such as IFC and KML.

Previously, 3D city models have been used mainly for visualization purposes but the rapid development in 3D city modelling has prompted some applications such as facilities management, building information model and simulations to utilize additional information about the city objects with standardized representations as suggested by Kolbe (2009). Meanwhile, Groger and Plumer (2012) elaborated on the current development in CityGML, its features being the interoperable semantic 3D city model and current researches that aim to enhance the format for geospatial purposes. They provided several key points that differentiate CityGML with other graphically-focused format such as KML and X3D. Kolbe (2009), Groger and Plumer (2012) also stated the importance of semantic information supported in CityGML which is crucial in geospatial applications. In explaining the semantic aspect supported in CityGML, Groger and Plumer (2012) had provided UML diagrams that shows hierarchical structures of the semantic information for every LoDs which emphasized that coherent semantical-geometrical modelling is a very important aspect in CityGML.

2.2 3D Buildings Generation

The emergence of better hardware and software in the computer-related industries makes it easier for the users to generate 3D buildings. Some researchers even

focused on developing an automated process for generating 3D city models Takase et al. (2003), Sugihara and Hayashi (2008) and (Steinhage et al. 2010). 3D building generation process is important in change detection and analysis since it will provide the input for the applications.

Isikdag and Zlatanova (2010) introduced an approach to draw and visualize simple geometric representation of 3D buildings directly in the Google Earth environment. Urban planning is known to be a complex and tedious process which involves many parties and joint decision making. They suggested that by introducing this approach, all parties involved can easily access and view the data, and get the better picture on the proposed structures and how it relates to the environment on the actual site rather than just looking at the architectural model while lacking on the information of the surrounding area.

Kim et al. (2008) presented a method to automatically generate Digital Building Models (DBM) with complex structures (parts with different slopes, sizes, and shapes) from LiDAR point clouds. The method consists of four steps. First, the ground/non-ground points are classified based on the visibility analysis among ground and non-ground points in a synthesized perspective view. Then, the non-ground points are analysed and used to generate hypotheses of building instances based on the point attributes and the spatial relationships among the points. Next, each building is segmented into a group of planar patches. The intermediate boundaries for segmented clusters are produced by using a modified convex hull algorithm. These boundaries are used as initial approximations of the planar surfaces comprising the building model of a given hypothesis. Finally, those initial boundaries are used to derive a refined set of boundaries, which are connected to produce a wireframe representing the DBM.

The research done by Kim et al. (2008) provide an interesting idea on how to automatically acquire a high quality 3D models with complex structures as an input for detecting and analysing the changes that occurs on 3D building especially for building management purposes.

2.3 3D Segmentation on 3D Buildings

3D model segmentation method has been used in various fields such as medical technology, computer vision and geospatial applications. However, it serves the same purpose which is to break down an object into simpler parts to be manipulated for different applications such as object analysis, feature extraction and classification, object recognition, model reconstruction and generalization. Although most of the segmentation method used in geospatial and building-related applications are based on 2D segmentation (Mian et al. 2006; Tolt et al. 2006; Miliaresis and Kokkas 2007; Sampath and Shan 2010; Cheng et al. 2010), there are some researches that dwelled into the 3D segmentation as presented by You et al. (2003), Hu et al. (2004), Thiemann and Sester (2004), Poupeau and Bonin (2006) and, Manferdini and Remondino (2010).
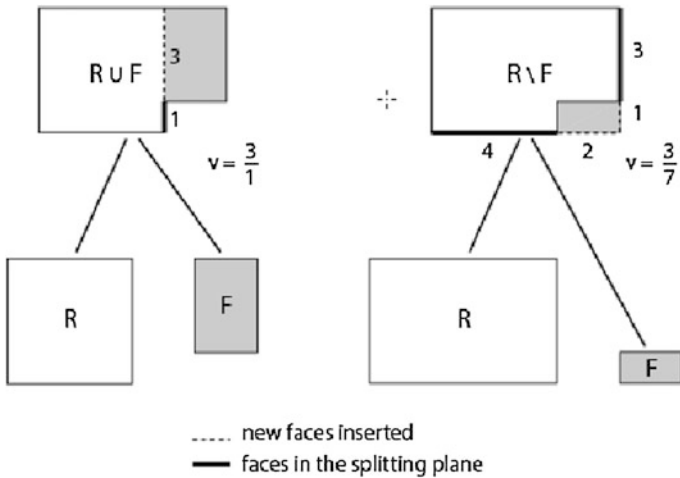
Fig. 1 Two different segmentations on the same geometry with different quality values (Thiemann and Sester 2004)

Thiemann and Sester (2004) presented a research on segmentation of 3D building for generalization that utilized an adaptation of algorithm by Ribelles et al. (2001). Ribelles proposed a segmentation process that will detect holes, bumps and notches on a 3D building model by segmenting the model with one or more planes of its boundary.

The same polyhedron can be segmented with different operations and combination of planes which resulted in many different features. Ribelles et al. (2001) determine the best feature by dividing the new area of the splitting face with the old area, where the smaller value indicate a better feature. Figure 1 shows two different segmentation on the same body where a protrusion (left) is detected with the quality value, v, of 3 while a complex hole (right) is detected with better quality value, v, of 3/7.

However, Thiemann and Sester (2004) considered the algorithm by Ribelles et al. (2001) employed a "brute force" method as it tries all split with all combinations of planes increases the complexity of the algorithm and running it with four or more splitting planes makes it extremely time consuming.

To counter the problems, Thiemann and Sester (2004) introduced an extension from the original algorithm based on the theory that reducing the number of Boolean operation will reduce the complexity of the algorithm and its processing time. They suggested that only one split-plane is used and only if it yields no result, then two or more split-planes will be used. In order to balance out the separation of bad protrusion features before the good complex hole, they also introduced a heuristics where only parts with value smaller than 1 are considered as valid. Figure 2 shows the segmentation on a building with 34 different split-planes.
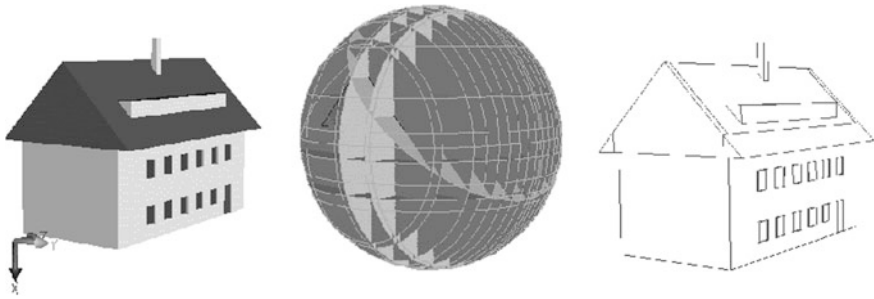
Fig. 2 Segmentation of a sample building with 34 split-planes (Thiemann and Sester 2004)

3 Segmenting 3D City Model Objects Based on Geometric-Semantic Decomposition

3.1 3D Segmentation Overview

Segmentation is basically a method to partition or break down an object into simpler parts for various objectives (object detection, analysis and management, texture mapping, etc.). Currently, 3D segmentation is heavily utilized in computer vision and medical technology. However, the development in 3D GIS has triggered the needs to use the tool for geospatial-related applications (You et al. 2003; Hu et al. 2004; Thiemann and Sester, 2004). Generally, there are two principal types of segmentation; surface-type and part-type (Agathos et al. 2007; and Shamir, 2008). The surface-type segmentation uses various primitives such as planes, cylinder and sphere as an approximation of the mesh to create distinct surface regions. On the other hand, the part-type segmentation creates volumetric parts by partitioning the mesh into meaningful or semantic components. Figure 3 shows the result for the part-type and surface-type segmentations.

3.1.1 Region Growing Segmentation

There are several different segmentation techniques introduced in different fields, but based on the survey made by Shamir (2008), the simplest segmentation technique is called the Region Growing Segmentation meanwhile a comparative study on segmentation techniques done by Attene et al. (2006) and several other research (Attene et al. 2006; You et al. 2003; Hu et al. 2004; Manferdini and Remondino 2010) shows that a suitable segmentation algorithm for manmade objects is segmentation based on primitives fitting or 3D volumetric approaches.

Region growing is also known as a local-greedy approach where it starts with a seed element, then, examines its neighbouring elements and grows a sub-mesh incrementally by determining whether the adjacent elements should be added to

Fig. 3 Results for part-type (*Left*) and surface-type (*Right*) segmentations (Shamir 2008)

the seed's cluster based on predefined criteria. Shamir (2008) has provided the pseudo codes for the region growing algorithm as follows:

```
Region Growing Algorithm:

Initialize a priority queue Q of elements
Loop until all elements are clustered
Choose a seed element and insert to Q
Create a cluster C from seed
Loop until Q is empty
Get the next element s from Q
If s can be clustered into C
Cluster s into C
Insert s neighbours to Q

Merge small clusters into neighbouring ones
```

The concept of region growing is illustrated in Fig. 4 from Agathos et al. (2007). Seed point A examines all its neighbouring elements and adding the qualified elements in its cluster based on predefined criteria.

3.2 3D Segmentation Based on Surface-Semantic Decomposition

The proposed segmentation technique attempts to introduce a hybrid; part-type (often known as semantic) and surface-type elements to the segmentation process so that the segmentation result will not only be based on fitting primitives, but also

Fig. 4 Seed point A grows by adding adjacent elements to its segmentation region (Agathos et al. 2007)
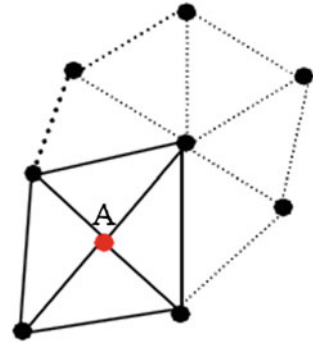
based on their semantic properties. This technique is able to segment a 3D model directly in vector data format, making the result have a higher accuracy than segmenting a raster data.

3.2.1 Semantic Segmentation

In order to preserve the semantic data during the segmentation process, first, the 3D building need to be segmented based on its semantic attributes. The semantic data can be provided together in the CityGML file of the 3D building. Figure 5 shows a CityGML file that contains semantic data of the building.

In this phase, geometries that represent the semantic data will be differentiated with each other, regardless the shapes they assembled. The segmented parts based on the semantic also known as parent geometries. The child geometries will be obtained using the segmentation technique based on the fitting primitives.

Even though the semantics are present in the CityGML structure, the proposed segmentation method will classify the Wall Surface according to their semantic information, recognized the objects as parent geometries and used it as a starting point for geometric segmentation. Furthermore, it will enable the proposed method to retain the semantic information of the child objects, which are inherited from the parent geometries. If the model is not a semantic model, the segmentation method will attempt to derive the semantic information based on user-predefined criteria for certain features (if any) such as roof before proceeding with the geometric segmentation. Figure 6 shows the result of the segmentation based on semantic-type.
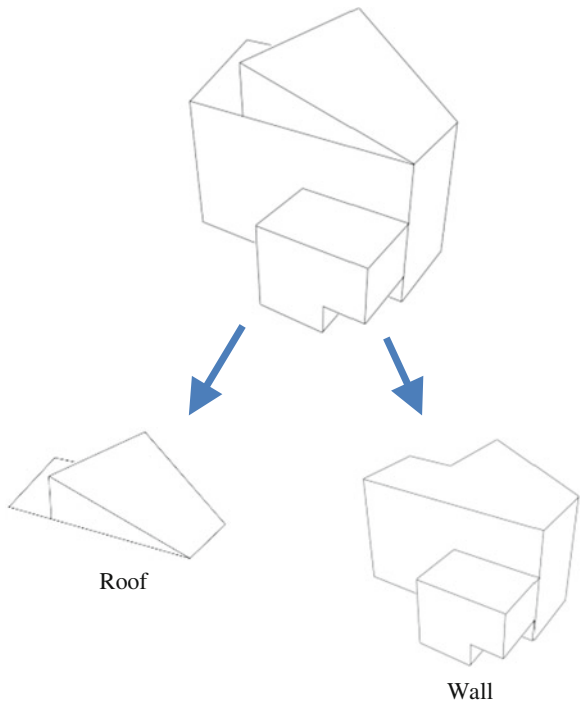
3.2.2 Geometric Segmentation

Since the model has been segmented based on its semantics, the geometric segmentation will start on each parent, instead of based on the whole model. Segmenting the parent geometries will allow complex shapes to be broken down to

```
<bldg:boundedBy>
  <bldg:WallSurface>
    <gml:name>Wall South</gml:name>
    <bldg:lod2MultiSurface>
      <gml:MultiSurface>
        <gml:surfaceMember>
          <gml:Polygon gml:id="GML_1d350a50-6acc-4d3c-8c28-326ca4305fd1">
            <gml:exterior>
              <gml:LinearRing>
                <gml:posList>458875.0 5438350.0 112.0 458885.0 5438350.0 112.0 458885.0 5438350.0 115.0 458875.0 5438350.0
                115.0 458875.0 5438350.0 112.0 </gml:posList>
              </gml:LinearRing>
            </gml:exterior>
          </gml:Polygon>
        </gml:surfaceMember>
      </gml:MultiSurface>
    </bldg:lod2MultiSurface>
  </bldg:WallSurface>
</bldg:boundedBy>
<bldg:boundedBy>
  <bldg:WallSurface>
    <gml:name>Wall North</gml:name>
    <bldg:lod2MultiSurface>
      <gml:MultiSurface>
        <gml:surfaceMember>
          <gml:Polygon gml:id="GML_d3909000-2f18-4472-8886-1c127ea67df1">
            ...
```

Fig. 5 Semantic attributes in CityGML file

Fig. 6 The result of the semantic-type segmentation
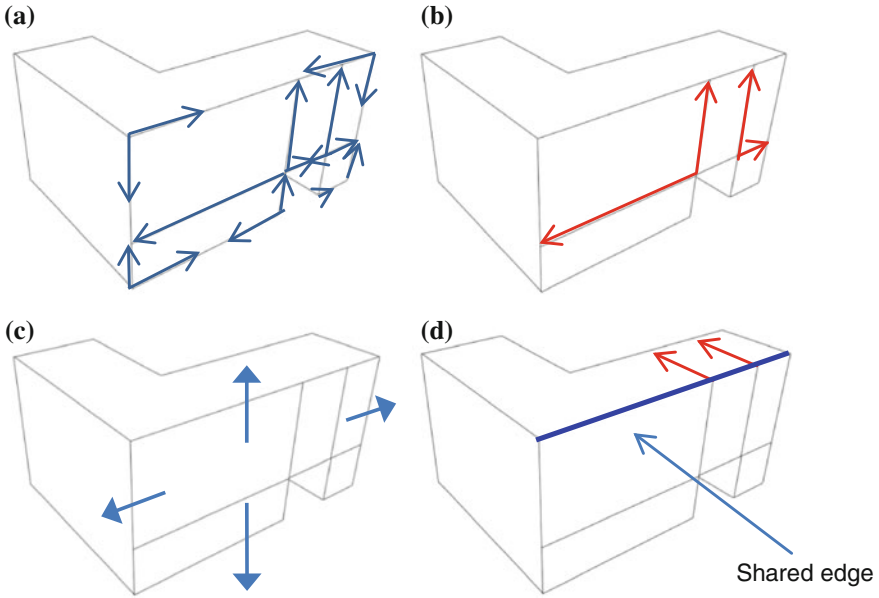

Roof

Wall

Fig. 7 The geometric segmentation process on each face

simpler parts, thus, making it easier to thoroughly analyse the segmented structures while the semantic data is still intact. The segmentation by fitting primitives will attempt to identify shapes from a small family of primitives such as cuboids and cylinders, in the complex shapes of the parent geometries.

The segmentation method will extract the boundary nodes and classify them according to their parent geometries and surface ID respectively. It means that every geometric faces in the parent geometries will be given a unique ID. Then, each node from every faces in the parent geometries will be tested against the predefined criteria and projected orthogonally to relevant boundary lines.

Then the process will move on to the connecting face that share a boundary with the previous face and the same process will be repeated but this time the newly accepted nodes will also be taken into account if it was projected on the common boundary. Figure 7 shows the selection of faces in the segmentation process.

This process will be done face by face until all faces have been visited. After visiting the last face, the segmentation will validate all projected nodes to ensure all accepted nodes have been projected on every eligible boundary. Figure 8 shows the result of the segmentation process.
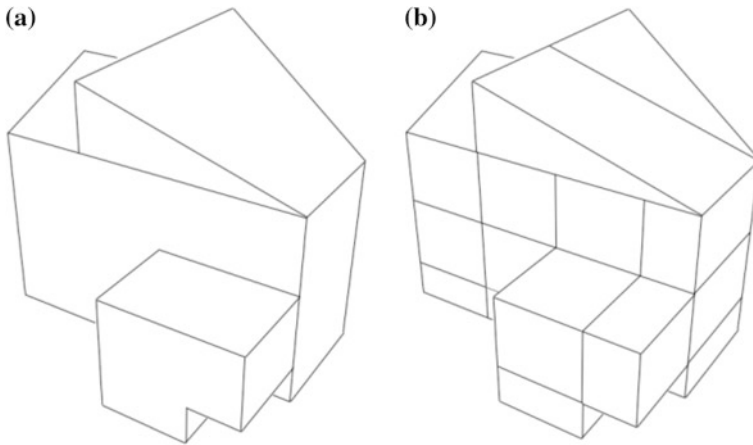
Fig. 8 The results of the segmentation process. **a** Original building. **b** Segmented model

4 Conclusions and Future Work

The popularity of 3D city models is evidently increasing. The rapid development of computer hardware and software has allowed the generation of 3D models to be done in various ways. A number of research works attempt to provide more analytical capabilities that can enhance the usability of 3D city models as a reliable 3D decision making tool for urban planners, local authorities and building managers. However, the lack of standardized guidelines for generating 3D city models has often resulted in 3D models with undefined parts. The proposed method described in this chapter should be able to breakdown complex building structure into simpler segments based on its semantic and geometric values. The segmentation technique will also enable users to define building parts and add specialized semantic information on the building parts in post-modelling stage. The results from the segmentation process can be used in other analyses such as change detection and automatic updating.

For future work, the segmentation technique will be implemented in 3D change detection module and visualized in 3D city model environment.

References

Agathos A, Pratikakis I, Perantonis S, Sapidis N, Azariadis P (2007) 3D Mesh segmentation methodologies for cad applications. Comput Aided Des Appl 4(6): 827–841

Attene M, Falcidieno B, Spagnuolo M (2006) Hierarchical mesh segmentation based on fitting primitives. Visual Comput 22(3):181–193

Cheng SC, Kuo CT, Wu DC (2010) A novel 3D mesh compression using mesh segmentation with multiple principal plane analysis. Pattern Recogn 43(1):267–279

Gröger G, Plümer L (2012) CityGML—Interoperable semantic 3D city models. Isprs J Photogrammetry Remote Sens 71:12–33

Hu J, You S, Neumann U, Park KK (2004) Building modeling from LiDAR and aerial imagery. In: Proceedings of ASPRS, May 2004

Isikdag U, Zlatanova S (2010) Interactive modelling of building in google earth: A 3D tool for urban planning. In: Neutens T, De Maeyer P (eds) Developments in 3D geo-information sciences, Springer, pp 52–70

Kim C, Habib A, Chang YC (2008) Automatic generation of digital building models for complex structures from lidar data. The International Archives of the Photogrammetry, Remote Sensing and Spatial Information Sciences. Vol. 37, Part B4. Beijing 2008

Kolbe TH (2009) Representing and exchanging 3D city models with CityGML. In: Jiyeong L, Zlatanova S (eds): Proceedings of the 3rd international workshop on 3D geo-information, Seoul, Korea. Lecture Notes in Geoinformation and Cartography, Springer 2009

Manferdini AM, Remondino F (2010) Reality-based 3D modeling, segmentation and web-based visualization. In: Ioannides M (ed) EuroMed 2010, LNCS 6436, 2010. © Springer Berlin, pp 110–124

Mian AS, Bennamoun M, Owens R (2006) Three-dimensional model-based object recognition and segmentation in cluttered scenes. IEEE Trans Pattern Anal Mach Intell 28(10):1584–1601

Miliaresis G, Kokkas N (2007) Segmentation and object-based classification for the extraction of the building class from Lidar Dems. Comput Geosci 33(8):1076–1087

Poupeau B Bonin O (2006) 3D analysis with high-level primitives: a crystallographic approach. In: Riedl A, Kainz W, Elmes GA (eds) Progress in spatial data handling. © Springer, Berlin, pp 599–616

Ribelles J, Heckbert P, Garland M, Stahovich T, Srivastava V. (2001) Finding and removing features from polyhedra. In: American association of mechanical engineers (ASME) Design automation conference, Pittsburgh PA, September 2001

Sampath A, Shan J (2010) Segmentation and reconstruction of polyhedral building roofs from aerial lidar point clouds. IEEE Trans Geosci Remote Sens 48(3):1554–1567

Shamir A (2008) A survey on mesh segmentation techniques. Comput Graph Forum 27(6):1539–1556

Steinhage V, Behley J, Meisel S, Cremers AB (2010) Automated Updating and Maintenance of 3D City Models. Core Spatial Database—Updating, Maintenance and Services. ISPRS Archive 38(Part 4-8-2-W9)

Sugihara K, Hayashi Y (2008) Automatic generation of 3D building models with multiple roofs. Tsinghua Sci Technol 13(S1):368–374

Takase Y, Sho N, Sone A, Shimiya K (2003). Automatic Generation of 3D city Models and Related Applications. International Archives of the Photogrammetry, Remote Sensing and Spatial Information Sciences, Vol. 34-5/W10. Tarasp, Switzerland, 27–28 Feb 2003

Thiemann F, Sester M (2004) Segmentation of buildings for 3D-generalisation. ICA workshop on generalisation and multiple representation, Leicester, 20–21 Aug 2004

Tolt G, Persson A, Landgard J, Soderman U (2006) Segmentation and classification of airborne laser scanner data for ground and building detection–Art. No. 62140c. Laser Radar Technol Appl XI 6214:C2140–C2140

You S, Hu J, Neumann U, Fox P (2003). Urban site modeling from LiDAR. In: 2nd international workshop on computer graphics and geometric modeling CGGM'2003, Montreal, Canada

A Javascript Decoder for CitySAC in 3D SDI Web Transaction

Siew Chengxi Bernad, Alias Abdul Rahman, Mohd Latif bin Zainal and Fuziah binti Abu Hanifah

Abstract Sharing of spatial data using internet is getting common as seen in various developments in Spatial Data Infrastructure (SDI). Spatial data sharing requires standardized file format for interoperability which could be seen in different working groups in Geography Mark-up Language (GML) and CityGML where different level of details (LOD) is described in CityGML for 3D city. In order to solve the large dataset problem that arises due to XML describ-able advantage used in CityGML, a schema-aware encoder (CitySAC) is invented and achieved better compression ratio and required lesser time, compared to the novel Lemper-Zipf-Markov (LZMA) algorithm. Since geometries and semantics data are required in data transaction over the web services especially for analysis, the use case of the proprietor schema-aware encoder is defined. The advantage of the decoder is the availability for code-on-demand. This chapter discusses brief introduction of the schema-aware development background as well as the related works; the development of javascript decoder to solve the interoperability issue in implementing CitySAC over the open web environment as well as the example application.

Keywords 3D SDI · Javascript · Decoder · XML · CityGML

S. C. Bernad (✉) · A. A. Rahman
3D GIS Research Lab, Faculty of Geoinformation Science and Real Estate,
Universiti Teknologi Malaysia (UTM), Johor Bahru, Malaysia
e-mail: cbsiew2@live.utm.my

A. A. Rahman
e-mail: alias@utm.my

M. L. b. Zainal · F. b. A. Hanifah
Malaysian Centre for Geospatial Data Infrastructure (MaCGDI), Ministry of Natural
Resources and Environment (NRE), Level 7 & 8, Wisma Sumber Asli, No. 25, Persiaran
Perdana, Presint 4, Putrajaya, Malaysia
e-mail: mohdlatif@macgdi.gov.my

F. b. A. Hanifah
e-mail: fuziah@macgdi.gov.my

1 Introduction

Implementation of SDIs using open standards are well discussed over the recent years, where in three-dimensions (3D) SDIs are developed using City Geography Mark-up Language (CityGML) (Kolbe et al. 2008) as back-end data transfer and implementing X3D in geometry portrayal layer. (Basanow et al. 2008). City models are especially important for presentation of business locations, urban development that is required by public and private sectors, such as providing the platform supporting from civic participation to decision-making and policy-formulation extent (Kolbe et al. 2008). The distinct feature of CityGML is that it is a schema based on XML standard carries geometries and semantics information in one format. XML is a popular W3C standard in data exchange and sharing usage in computing systems due to its readable and self-describing benefits. Considering the cost involved, transmitting 3D models in CityGML format is considered impractical. However, dealing with semantic data requirements in analysis over web services, compressing CityGML should be a step forward. Different work-arounds of compression tasks could be implemented, however in this chapter the schema-aware encoder (CitySAC) is used as a proprietor encoder and act as a compression component in the web services.

In this chapter, the development of schema-aware encoder for CityGML and its results compared with dictionary and arithmetic compression modules such as 7-zip, WinZIP, InfoSet, etc. are briefly discussed, then the following section discusses the development of javascript decoder and how the retrieval process could be done via code-on-demand in web application. The dataset that is used in this research is 3D Putrajaya city, managed by Malaysian Geospatial Data Infrastructure (MacGDI).

2 Background and Related Works

Various compression techniques have been discussed such as geometry compression by Deering (1995), Isenburg and Snoeyin (2000), Taubin et al. (1998) and Touma and Gotsman (1998), whereas connectivity compression could be subdivided into edge-based compression and vertex-based compression. Rossignac (1999) and Szymczak and Rossignac (1999) have discussed edge-based related techniques while Alliez (2001) and Touma and Gotsman (1998) have also discussed vertex-based techniques. Not a single algorithm could serve all scenarios as shown in the review by Peng et al. (2005). In Siew and Abdul Rahman (2013), a schema aware compressor is invented coupling with the LZMA compression module in the final stage. The development of the encoder is well discussed and could be implemented as a component in web services transaction. The main idea of the encoder is to allow "schema-awared" binary data transacted which could largely reduce file size up to 8 % of original size. As compression schemes are
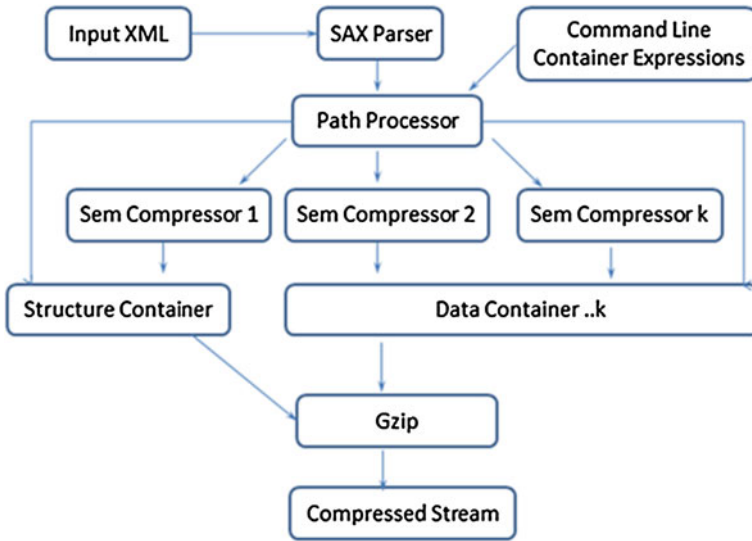
Fig. 1 XMill workflow (Liefke and Suciu 1999)

well discussed in Isenburg (2013), this encoder adapts lossless, non-progressive, streaming and random access behavior. On the other hand, some discussed techniques are targeted specifically for XML, such as Infoset dictionary method (Oracle 2005) and other general text compressors XMill (Liefke and Suciu 1999), XGrind (Tolani et al. 2002), XPRESS (Min et al. 2003), XComp (Li 2003), XCQ (Ng et al. 2006). However, none of them are suitable for solving the core problem in transmitting geometry and semantic data in a Document Object Model (DOM) form, which is embedded with equal importance for geometries and semantics information, e.g. CityGML. Some modifications are required for GIS 3D SDI use cases.

XMill (Liefke and Suciu 1999) implements split, group, and compress methodology and the GZip compression module placed at the last stage. Containers are prepared with structure domain and data domain, and each container is defined via default 8 MB window size. The workflow is shown in Fig. 1.

To improve XMill, XGrind (Tolani et al. 2002) improved with query ability onto compressed document, while a structure of document is left without encoding. While the improvisation able to solve the query limitation which is not available in previous compressor, XGrind only adapts DTD of XML but not XSD which was introduced later in common XML document. On the other hand, XPRESS (Min et al. 2003) introduced reverse arithmetic encoder which divides the elements and content path into floating [0.0–1.0] interval. This concept was being used in other common arithmetic encoders. In addition, this encoder does not encode data types or the value of the elements. In the scenario of XComp (Li 2003), it improves XMill by introducing more containers rather than structure containers, which are data-length container and dictionary container, while XCQ
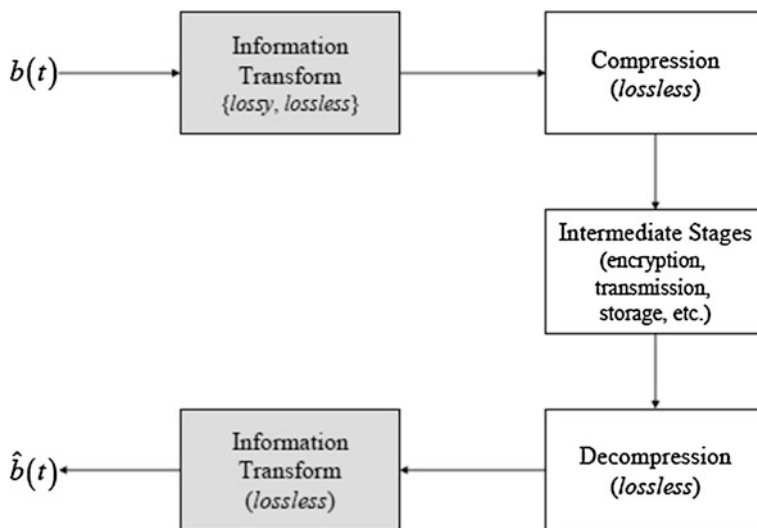
Fig. 2 The compression and decompression pipeline

(Ng et al. 2006) introduced indexing method via Pseudo-Depth-First strategy which builds a DTD tree. Fast Infoset (FI) uses ASN.1 (2005) notation which is currently the standard: ITU-T Rec. X.891 and ISO/IEC 24824-1.

Various SDI seen around the world, such as INSPIRE (Infrastructure for Spatial Information in the European Community), Digital China Geospatial Framework (DCGF) (Lia et al. 2008), National Land Information System (NLIS) in Poland (Gazdzicki and Linsenbarth 2004), etcshow the importance of spatial data sharing for various requirements. Sharing of data using a common file format such as GML is seen in various researches (Christensen et al. 2007) (Galip 2007). Extending 2-dimensional into 3-dimensional SDI initiatives are well discussed in Berlin-3D and Heidelberg-3D (Basanow et al. 2008), which uses CityGML and common data sharing format. Few other examples that use semantics and geometries in analysis are shown in, (Walenciak et al. 2009; Stollberg and Zipf 2007; Lanig and Zipf 2010). This chapter aims to discuss the methodology or workflow that involved in developing the decoder for the prebuilt schema aware encoder CitySAC (Siew and Abdul Rahman 2013) and how the web transaction could achieve interoperability while allowing binary data transaction within the web service using HTTP protocols.

3 City Schema-Aware Compressor

The flow of encoding pipeline follow stages discussed by Augeri (2001) (Fig. 2) showing the general stages on how information is transformed. b(t) denoted the source file symbol and the transformed output would be ^b(t).

Table 1 The compression ratio (near-lossless) with quantization option set to true

	Original (MB)	Deflate zip (MB)	Fast-Infoset (MB)	LZMA (MB)	Bzip2 (MB)	CitySAC + Deflate (MB)	CitySAC + LZMA (MB)
Commercial_ Building3C6.xml	0.836	0.086	0.469	0.073	0.079	0.072 (91.39 %)	0.056 (93.3 %)
National Audit.xml	8.594	0.948	4.132	0.696	0.869	0.723 (91.59 %)	0.561 (93.47 %)
Putrajaya_ Mosque.xml	10.928	1.56	4.81	0.992	1.226	0.98 (91.03 %)	0.782 (92.84 %)
Seri Gemilang Bride.xml	27.454	3.612	12.352	2.714	3.519	2.59 (90.57 %)	1.94 (92.93 %)

Table 2 The time consumption for different techniques with default setting (Using Stopwatch library)

Input \ Techniques	Deflate zip (sec)	Fast-Infoset (sec)	LZMA (sec)	Bzip2 (sec)	CitySAC + Deflate (sec)	CitySAC + LZMA (sec)
Commercial_Bulding_3C6.xml	0.2	0.5	0.3	0.1	0.3	0.4
National Audit.xml	3.8	3.6	4.5	1.2	1.6	1.9
Putrajaya_Mosque.xml	3.5	4.2	5.8	2.2	3.1	4.1
SeriGemilangBride.xml	9.8	11.5	15.2	4.5	10.5	11.2

Since CitySAC use dictionary encoding, all occurrences are indexed and stored. Furthermore, geometries are built in chunk of 65,000 face sets where each face represents a polygon in CityGML. The main idea of the encoder is to follow the XML original structure so query-able capability is retained and compressed content is retrievable. The encoder defines each representation as a symbol denoted in 16-bits.

The compression ratio is calculated with the following equation:

$$\mathrm{CR}_2 = \left(1 - \frac{\text{size of (compressed file)}}{\text{size of (original file)}}\right) \times 100\%$$

WinZip is used as the benchmark, and this encoder aims to perform better than direct 7-zip results in terms of timespan and compressed size and used 7-zip the final compression stage. It is worth mentioning that the encoder achieved a 35–50 % better compression rate compare to WinZip, and 20–30 % better compression rate compare to direct 7-zip (See Table 4). In near-lossless scheme, better compression ratio is achieved (see Tables 1, 2, 3). The environment for encoding is shown in Table 4.

Table 3 The improvement comparison between CitySAC and LZMA

Compressed document	LZMA (MB)	CitySAC + LZMA (MB)
Commercial_Building3C6	0.073	0.056 (23.29 %)
National Audit	0.696	0.561 (19.83 %)
Putrajaya_Mosque	0.992	0.782 (21.17 %)
Seri Gemilang Bride	2.714	1.94 (28.52 %)

Table 4 The encoding environment

Processor	Intel Core i7-3610 M 2.3Ghz
Memory	6 GB DDR3
Hard disk	1 TB HDD with 34.6 GB free space on C:
Operating system	Windows 7 Professional on DOT.NET Framework 4.5

4 The Javascript Decoder for CitySAC

Interoperability is one of the key requirements in web service utilizations and implementations. The fact that various realizations of web services and service-oriented architecture over the years are due to the sharing and standardization efforts by several working groups formulating a standard file format that allow seamless and ubiquitous data access and sharing. The large benefit of interoperability is undeniably important. By employing tightly-coupled encoder decoder architecture in web service, it could of course allow small data transfer which could highly reduce the bandwidth and time consumption. However, to accommodate the tightly-coupled encoder decoder requirements, a newly dedicated design for the infrastructure, or else a major modification of the existing architecture. This also requires consideration of platform dependency at client side.

For platform independent requirements, the options are less. In order to deploy the decoder with the client-side applications, the alternative to tightly-coupled decoder is to deploy a browser scripting decoder which runs at browser that is platform-independent. The browser scripting approach supports code-on-demand where script could be loaded at client side in order to decode retrieved data.

Decoder is built with a binary-reader.js (See jDataView) and lzma.js (See LZMA-JS) which are openly available. With these javascripts the decoder able to decode the binary data and information is retrieved via the modules that allow user to decode fully back to original CityGML file or query the XML tag on-the-fly.
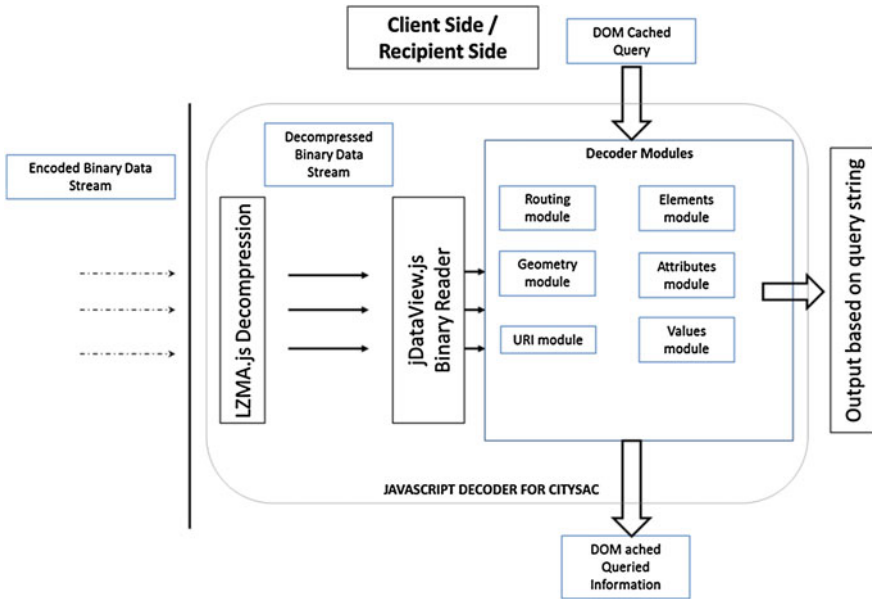
Fig. 3 The javascript decoder workflow in modules

Figure 3 shows the workflow for different modules in the decoder. The decoder shows how information could be retrieved by modules that are written in javascript.

The encoded binary stream is retrieved and will be decompressed by on demand lzma.js and decoded stream will be read by binary reader supported by jData-View.js. The reader will then populate the related information in different modules which later on parsed the output for client side applications. The default output of the decoder generates CityGML data. However, using customized modules such as routing module, specified data output could be generated such that only geometry array or URI identifier is cached. The cached could then be retrieved as a Document Object Model (DOM).

5 Implementation and Discussions

The implementation of the javascript decoder in browser script gains large benefits as user does not need to consider platform dependency in deploying the decoder for the encoded stream. This approach is a step forward to realize binary stream between client and server without platform-dependency at client side and allow small data size transactions. Though thin-client does not require CityGML as the

data input, however the decoder provides advantages for medium-client and thick-client usage, as well as within web services transactions.

The information retrieval procedures for decoder allow geometries array output from queried data; tag-search capability to decode content on-the-fly or even raw CityGML output. This gains flexibility for different client side applications. The current modules available are such as routing module, geometry module, URI module, element module, attribute module, and value module. Routing module searches and parses related information from all the other modules. Routing modules retrieved information and parses information in key value pair (KVP) formatting. Specified query could be adapted into the module to retrieve particular information without going through full decompression.

6 Concluding Remarks

In this chapter we discussed briefly the CitySAC encoder and how a decoder could be deployed considering platform-independent client side using existing javascript libraries and in-house developed decoder. The output of the decoded information is readable therefore interoperability is achieved on top of binary streamed data. We also demonstrated the workflow of the decoder and how user could retrieve information from the encoded data stream. In future, the encoder-decoder will apply in the use-case of city modelling for Putrajaya 3D Corporation, Malaysia via MaCGDI server. The applications will be extended into mobile devices where simple query from mobile devices that utilizes HTML5 will be executed and retrieved encoded information via this javascript decoder deployed in mobile devices.

References

Alliez P, Desburn M (2001) Valence-driven connectivity encoding for 3D meshes. In: Proceedings of the Eurographics '01
Augeri Christophe J, Mullins Barry E, Bulutonglu Dursun A, Baldwin Rusty O, Baird III Leemon C (2001) An analysis of XML compression efficiency. In: Proceedings of the workshop on experimental computer science (EXPCS), San Diego, CA, 13–14 June 2007. 978-1-59593-751-3/07/06
ASN.1: Fast infoset (2005) Series X: data networks, open system communications and security, ITU-T X.891, Telecommunication standardization sector of ITU
Basanow J, Pascal N, Neubauer S, Schilling A, Zipf A (2008) Towards 3D spatial data infrastructures (3D-SDI) based on open standards—experiences, results and future issues. In: Oosterom P et al (ed) Advances in 3D geoinformation systems (2008) Springer, Berlin, pp 65–86

Christensen AF, Lutz M, Ostlander N, Bernard L (2007) Designing service architectures for distributed geoprocessing. Trans GIS 11(6):799–817

Deering M (1995) Geometry compression. In: SIGGRAPH '95 proceedings of the 22nd annual conference on computer graphics and interactive techniques

Galip A (2007) Service oriented architecture for geographic information systems supporting real time data grids, Dissertation. Department of Computer Science, Indiana University

Gazdzicki J, Linsenbarth A (2004) 10th EC GI & GIS Workshop, ESDI State of the Art, Warsaw

Isenburg M, Snoeyin J (2000) Spirale reversi: reverse decoding of edgebreaker encoding. In: Proceeding of 12th Canadian conference on computational geometry

Isenburg M (2013) LAZzip: Lossless compression of LiDAR data. ASPRS J 79(2):209–217

Kolbe TH, Gerhard K, Nagel C, Stadler A (2008) 3D Geodatabase Berlin version 2.0.1a, Fachgebiet Methodik der Geoinformationstechnik der TU Berlin

Lanig S, Zipf A (2010) Proposal for a web processing services (WPS) application profile for 3D processing analysis. In: IEEE second international conference on advanced geographic information systems, applications, and services, pp 117–122. 978-0-7695-3951-5/10

Li W (2003) Xcomp: an XML compression tool. Diss. University of Waterloo, School of Computer Science

Lia P, Lan W, Xiao X (2008) Sdi in China:progress and issues. In: The international archives of the photogrammetry, remote sensing and spatial information sciences, vol XXXVII Part B4. Beijing

Liefke H, Suciu D (1999) XMill: an efficient compressor for XML data. http://sourceforge.net/projects/xmill. Accessed 05 May 2012

Min J, Park M, Chung C (2003) XPRESS: a queriable compression for XML Data. In: Proceedings of the 2003 ACM SIGMOD international conference on management of data

Ng W, Lam WY, Wood PT, Levene M (2006) XCQ: A queriable XML compression system. Knowl Inf Syst 10(4):421–452 (Springer-Verlag London Limited 2006)

Oracle Sun, Fast Infoset Documentation (2005). http://java.sun.com/developer/technicalArticles/xml/fastinfoset/. Accessed 01 March 2011

Peng J, Chang-Su Kim, Jay Kuo C.-C (2005) Technologies for 3D mesh compression: a survey. J Vis Commun Image R 16:688–733

Rossignac J (1999) Edgebreaker: connectivity compression for triangle meshes, GVU Technical report GIT-GVU-98-35

Siew CB, Alias AR (2013) A schema-aware encoder for putrajaya 3d, urban and regional data management. In: Proceedings of the urban data management society symposium 2013 (UDMS), pp 181–190

Stollberg B, Zipf A (2007) OGC web processing service interface for web service orchestration. Springer, Heidelberg

Szymczak A, Rossignac J (1999) Wrap and zip decompression of the connectivity of triangle meshes compressed with Edgebreaker. Comput Geom 14(1–3):119–135

Taubin G, Horn W, Lazarus F, Rossignac J (1998) Geometry coding and VRML. Proc IEEE 86(6):1228–1243

Tolani P, Harista J (2002) XGrind: a query-friendly XML compressor. In: International conference on data engineering (ICDE), pp 225–234

Touma C, Gotsman C (1998) Triangle mesh compression. Graphics interface 98 conference proceedings, pp 26–34

Walenciak G, Stollberg B, Neubauer S, Zipf A (2009) Extending spatial data infrastructures 3D by geoprocessing functionality—3D simulations in disaster management and environmental research. Advanced Geographic Information Systems & Web Services, 2009. GEOWS '09. International Conference on, 40(44): 1−7. doi:10.1109/GEOWS.2009.16

The Effects of Vegetation Growth on the Microclimate of Urban Area: A Case Study of Petaling District

Siti Nor Afzan Buyadi, Wan Mohd Naim Wan Mohd and Alamah Misni

Abstract It is well known that the surface temperature distribution in the urban area is significantly warmer than its surrounding suburban areas. This phenomenon is known as urban heat island (UHI). Vegetations play a vital role to mitigate the UHI effects especially in regulating high temperature in saturated urban area. This study attempts to assess the effect of vegetation growth on the surface temperature distribution of the surrounding areas. The area of study for this research is Petaling District (i.e. City of Shah Alam, Petaling Jaya and Subang Jaya), Selangor. To monitor the land use/land cover changes within the study areas, Landsat 5 TM images of 1991 and 2009 are used. The land use/land cover of the study area is classified into five major classes i.e. water bodies, high-dense trees, mix-vegetation, built-up area and open land. Based on the thermal band of Landsat 5 TM, the land surface temperature maps are derived. Mono-window algorithm is used to convert digital number to surface temperature. Results from this study have shown that there are significant land use changes within the study area. This study demonstrates that rapid urban growth significantly decreased the vegetated area, hence increased the surface radiant temperature. Although the conversion of green areas to residential and commercial areas significantly increases the land surface temperature (LST), matured trees help to mitigate the effects of UHI.

Keywords Normalized difference vegetation index (NDVI) · Land surface temperature (LST) · Urban heat island (UHI)

S. N. A. Buyadi · W. M. N. W. Mohd (✉) · A. Misni
Centre of Studies for Surveying Science and Geomatics, Faculty of Architecture, Planning and Surveying, Universiti Teknologi MARA, Shah Alam, Selangor, Malaysia
e-mail: wmn@salam.uitm.edu.my; wmnaim1960@gmail.com

1 Background

The urban heat island (UHI) phenomenon can be found in many major cities throughout the world. UHI occurs when air and surface temperatures are hotter than their rural surrounding (Gartland 2008). Rapid urbanization causes reduction of vegetated areas and increases the built-up surfaces. The built-up surfaces trap the incoming solar radiation during the day and then re-radiate it at night (Solecki et al. 2004). Several studies have been carried out to investigate the UHI impacts (Mallick and Rahman 2012; Choi et al. 2012; Yan et al. 2012; Omar 2009; Shahmohamadi et al. 2009). Thus, the seriousness of UHI phenomena cannot be denied and the mitigation strategy should be applied to combat the UHI effects at the macro and micro levels.

The Landsat 5 TM and Landsat 7 ETM+ are widely used to monitor the land use changes and derive land surface temperature of an area. Example on the use of these satellite images in Malaysia in UHI studies can be found in (Wan Mohd et al. 2004) and (Takeuchi et al. 2010). Previous studies clearly demonstrated that the implication of rapid urban growth is the decrease in vegetated areas, increased surface temperature and hence, modified urban microclimate. However, the vegetated area helps to keep the temperature of the surroundings lower than the developed area (Buyadi et al. 2013). Additionally, maturity of trees and vegetation is considered as a vital parameter to ensure lower temperature in an urban area through shadow and transpiration.

2 Study Area and Data Acquisition

The study area is located within the District of Petaling (i.e. City of Shah Alam, Petaling Jaya and Subang Jaya). These cities are selected due to rapid urban development activities. The climate of the cities is categorized as a hot and humid tropical climate which is warm and sunny, along with abundant rainfall, especially during the Northeast Monsoon seasons from October to March. Temperatures tend to remain constant with maximum values of between 31 and 33 °C, while the minimum between 22 and 23.5 °C. Relative humidity is around 72–78 %, and the annual rainfall is about 3300 mm. The geographical location of the study area is shown in Fig. 1. The data (i.e. temperature and water vapor content) of nearby weather station *(Subang Meteorological Station)* are obtained from the Malaysian Meteorological Department (MMD). The data obtained coincide with the time and date of the Landsat TM satellite pass. Landsat TM images dated 21st February 1991 and 21st January 2009 are used. For a more detailed study on the effects of vegetation on the surrounding areas, three study areas are selected i.e. Shah Alam Lake Garden, Kelana Jaya Recreational Park and Subang Ria Recreational Park located in Subang Jaya.
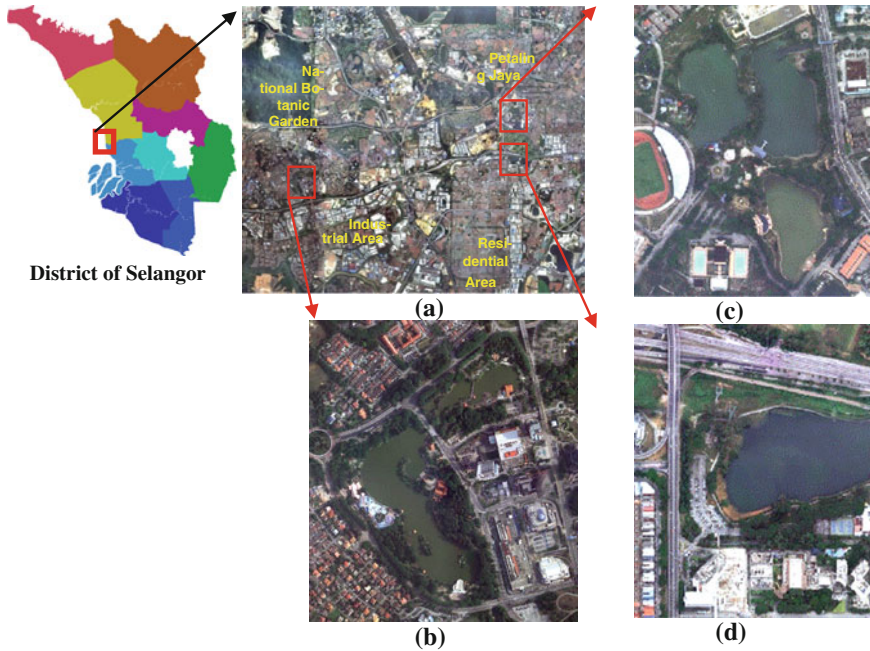
Fig. 1 Location of the study areas **a** part of Petaling District **b** Shah Alam Lake Garden, **c** Kelana Jaya Recreational Park and **d** Subang Ria Recreational Park. *Source* Google Map, 2013

3 Methodology

The methodology adopted for this study is given in the following sub-sections.

3.1 Generation of Land Use/Cover Map

Satellite images are used to generate the land use/land cover maps of two different dates. The Landsat 5 TM satellite images are acquired from the Malaysian Remote Sensing Agency (ARSM). The 18 year period is selected to ensure the maturity of vegetation growth within the study area. The process of generating land use maps was carried out in the ERDAS Imagine digital image processing software. The unsupervised classification method is used to generate land use/land cover maps. The percentages of land use/land cover changes are later calculated.

3.2 Land Surface Temperature (LST) Retrieval

The mono-window algorithm method as utilized by Qin et al. (2001) is used to generate the Land Surface Temperature (LST) map. The mono-window algorithm requires three parameters; emissivity, transmittance and effective mean atmospheric temperature (Sobrino et al. 2004). The atmospheric water vapour content and the near surface air temperature are used to calculate the air transmittance and effective mean atmospheric temperature (Liu and Zhang 2011). The third parameter is emissivity, which is calculated from the normalized difference vegetation index (NDVI). The mono-window algorithm is given as:

$$T_s = \{a(1 - C - D) + [b(1 - C - D) + C + D]T_i - DT_a\}/C \qquad (1)$$

where Ts is LST in Kelvin; $a = -67.355351$; $b = 0.458606$; ($C = T_i \times T_a$; where T_i = emissivity can be computed from NDVI); $D = (1 - T_a)[1 + (1 - T_i) \times T_a]$; Ti is the brightness temperature (K) and T_a is the effective mean atmospheric temperature.

3.3 Generation of Normalized Difference Vegetation Index Maps

GIS spatial analysis and zonal statistical analysis technique are used to visualize the vegetation fragmentation and surface temperature distribution. Equation 2 is used to calculate the NDVI of the study area. The proposed emissivity values from different NDVI range; i.e. NDVI < 0.2 (bare soil), 0.2 < NDVI < 0.5 (mixture of bare soil, vegetation and hard surfaces) and NDVI > 0.5 (fully vegetated) are 0.99, 0.98 and 0.98 respectively

$$NDVI = (NIR - R)/(NIR + R) \qquad (2)$$

where
   NIR—the pixel digital number (DN) of TM Band 4
   R—DN of TM Band 3

3.4 Spatial Analysis

The spatial analysis stage involves the generation of transaction profiles of the surface temperature and NDVI value across detailed studies area for the year 2009. The process of extracting profiles is carried out in the ArcGIS software.

4 Results and Analysis

The results of this study is presented in four main sub-sections i.e. land use/land cover maps, land surface temperature distribution, NDVI assessment and evaluation based on the vegetation growth within eighteen years and the transect profiles (for LST and NDVI) of the detailed study areas.

4.1 Land Use/Land Cover Changes

The land use/land cover maps for the two dates of part of the Petaling District are shown in Fig. 2. The total acreage of the study area is 16,904.547 hectares. The detail acreage of individual land cover of the study area is listed in Table 1. Over the period of 18 years, there is significant decrease in the high dense trees (i.e. forest and agricultural land) land cover category. The total area for the mixed vegetation category (i.e. crops, parks and bushes) and built-up areas (i.e. commercial, residential and administrative building) increased by 11.24 and 13.63 % respectively. The cleared land decreased due to its conversion to built-up areas. Although there is significant increase in built-up areas, the mixed-vegetation area also increased. This is due to more trees being planted to replace the lost of natural greenery within the study area.

4.2 Land Surface Temperature

The surface temperature distributions of 1991 and 2009 are shown in Fig. 3. The mean temperature for individual land use/land cover is summarized in Table 2. Based on Fig. 3 and Table 2, the lowest and highest radiant temperature for 1991 are 25.8 °C (in the high density tree area) and 33.1 °C (in the built-up area) respectively. Meanwhile, for 2009 the radiant temperatures range between 24.0 and 38.0 °C. The highest mean temperature is within the built-up area while the lowest is within water bodies. The implication of urban development by replacing natural vegetation (forest) to built-up surfaces such as concrete, stone, metal and asphalt clearly can increase the surface radiant temperature. Although there is significant increase in the built-up areas, the surface temperature is still relatively lower (refer to Fig. 3b). This could be due to the vegetation growth within the study area. In average, over eighteen years of development, regular matured trees, green parks, and other vegetation in urban area potentially can reduce urban temperature and the surrounding areas.
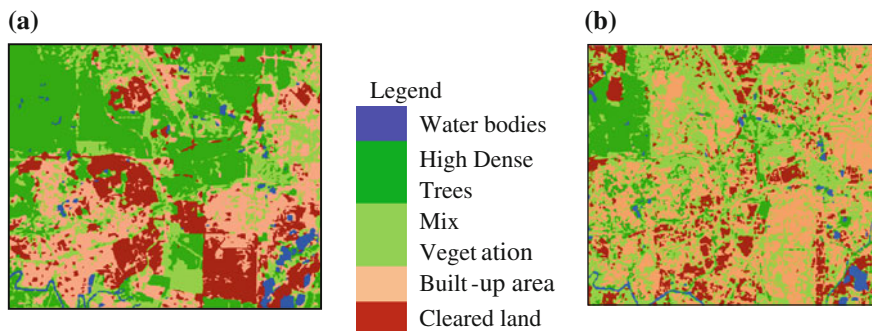
(a) **(b)**

Legend

■ Water bodies
■ High Dense Trees
■ Mix Veget ation
■ Built -up area
■ Cleared land

Fig. 2 Land use/Land cover maps of **a** 1991 and **b** 2009

Table 1 Land use/land cover coverage

Land use/land cover class	Area in hectare				Changes (%)
	1991	Percentage (%)	2009	Percentage (%)	
(1) Water bodies	464.554	2.75	317.827	1.88	−0.87
(2) High dense trees	5726.516	34.09	2807.432	16.61	−17.48
(3) Mix vegetation	3503.806	20.73	5403.899	31.97	+11.24
(4) Built-up area	4300.606	25.44	6608.361	39.09	+13.65
(5) Cleared land	2873.065	17.00	1767.028	10.45	−6.55
Total	16,904.547	100	16,904.547	100	

4.3 Analysis of Normalized Difference Vegetation Index

Figure 4a, b show the NDVI maps generated from the Landsat 5 TM imagery for the year 1991 and 2009. The increase in the vegetation growth coverage within the study area can clearly be seen. This could be due maturity of the trees grown within the built-up areas. As more trees and vegetation within the study area are getting matured, the NDVI value increase and hence lowering the LST (refer to Fig. 3).

The digital orthophoto of 2009 (refer to Fig. 5a) is used to visualize the urban growth of the detailed study area in Shah Alam Lake Garden. The lake garden area is surrounded by residential, high rise building, road and commercial areas. Figures 5b shows the NDVI maps of study area. Referring to Fig. 5b, lower NDVI values are clearly evident in water bodies and vegetated areas. Figure 5c shows the surface temperature pattern in detailed study area for the year 2009. It can clearly be seen that the surface temperature in much lower within the water bodies and vegetated areas (high NDVI value) as compared to the built-up areas (residential areas). As shown in Fig. 6a, Kelana Jaya area has been transformed to new urban area and is surrounded by industrial area, high rise building, sport facilities (i.e. stadium and sport centre), road and commercial building. The NDVI pattern and
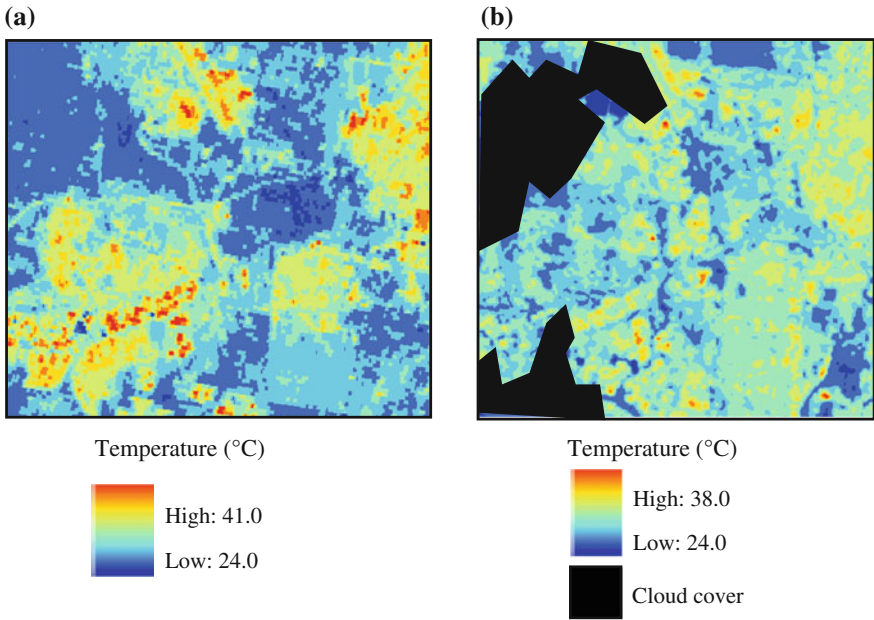
Fig. 3 Land surface temperature for **a** 1991 and **b** 2009

Table 2 LST distribution within different land use/land cover

Land use/land cover	1991 (Temperature °C)	2009 (Temperature °C)
Water	26.3	25.3
High dense tree	25.8	25.4
Mix vegetation	28.2	28.0
Built-up area	33.1	30.8
Cleared land	28.7	28.7

the surface temperature maps are shown in Fig. 6b, c respectively. Figure 7a–c show the orthophoto, NDVI pattern and surface temperature maps of Subang Ria Recreational Park. The surrounding areas consist of multiple land use (i.e. highway, high-rise building, private club and residential areas). Based on Figs. 6, 7 and 8, it is evident that the vegetation can help to reduce of the hard surface emissivity and lowering the solar exposure of the building envelope as well as cooling down the high temperature in built-up areas.
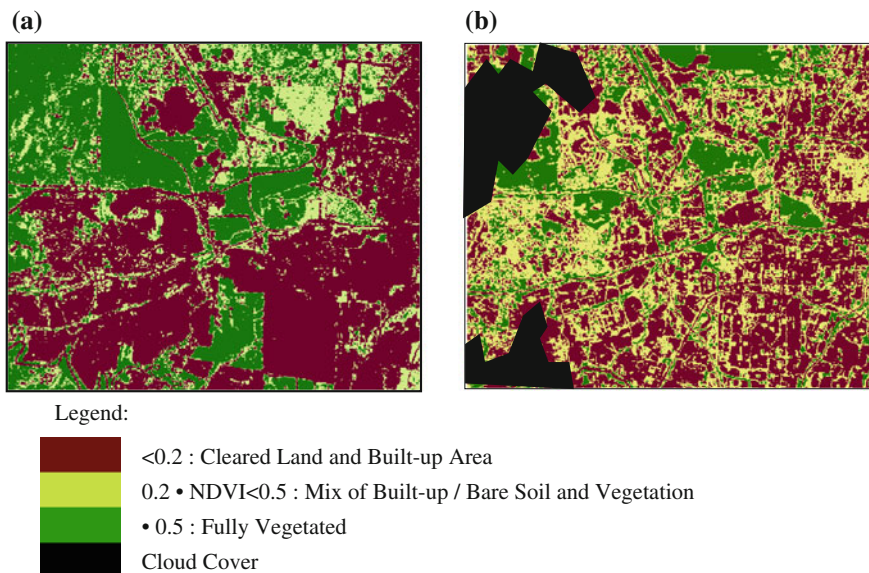
(a)   (b)

Legend:

 <0.2 : Cleared Land and Built-up Area

0.2 • NDVI<0.5 : Mix of Built-up / Bare Soil and Vegetation

• 0.5 : Fully Vegetated

Cloud Cover

Fig. 4 Vegetation growth in **a** 1991 and **b** 2009
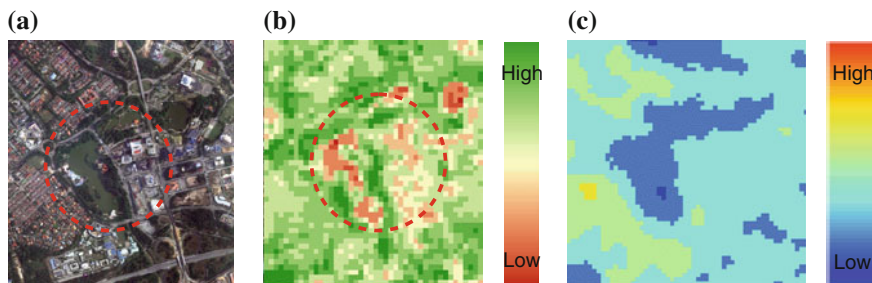
(a)   (b)   (c)

Fig. 5 **a** Orthophoto image, **b** NDVI map and **c** surface temperature of the detailed study area in Shah Alam

4.4 Transect Profile Between Surface Temperature and NDVI

As shown in Fig. 8a, the cross section profiles pass through residential area (Sect. 3), urban park (i.e.; water body, high density trees and vegetation) and administrative building. Figure 8b shows the NDVI value range from −0.2 to 0.28 and the surface temperature range from 25.5 °C in urban park area to 29.9 °C (max) in commercial area. The difference in the surface temperature between built-up areas and high density tree areas is more than 4 °C. As the profile line crossed over the grass area the temperature remain unchanged. It is clear that grass does not

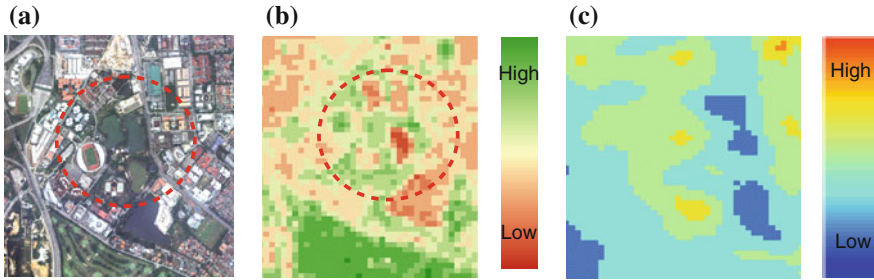**Fig. 6** **a** Orthophoto image, **b** NDVI map and **c** surface temperature map of the detailed study area in Kelana Jaya
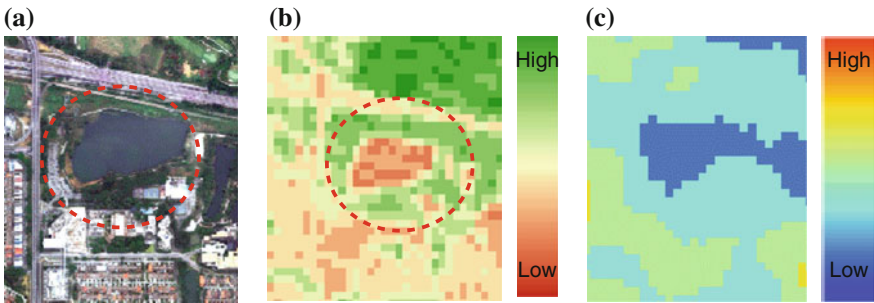

Fig. 7 **a** Orthophoto image, **b** NDVI maps and **c** surface temperature of the detailed study area in Subang Jaya
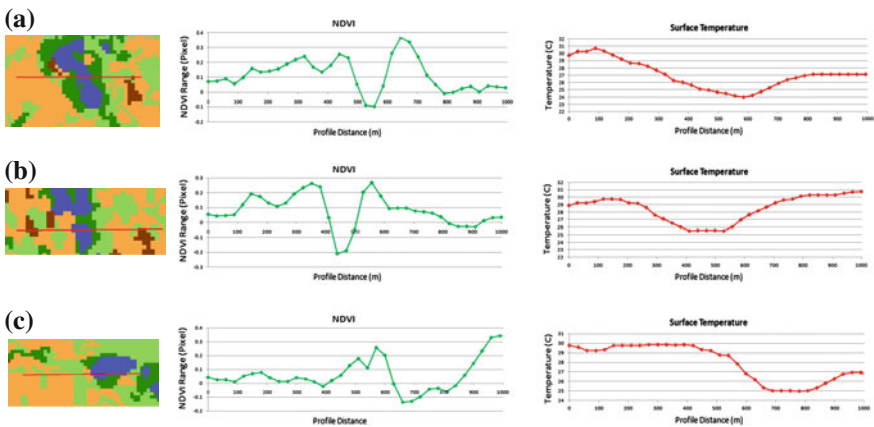

Fig. 8 Transection profile of surface temperature and NDVI for **a** Shah Alam Lake Garden (Residential-urban park-water-commercial area) **b** Kelana Jaya Park (Built-up (Stadium Kelana Jaya)-urban park (vegetation)-built-up (highway and industrial area)) and **c** Subang Ria Park in 2009 (Residential-vegetation (along road)-parking-water body-trees)

significantly reduce the surface temperature within the built-up area. Different tree type and density of vegetation could have different effects in reducing surface temperature in urban areas. The cross section profile at Subang Ria Recreational Park is shown in Fig. 8c. The transect line crossed different types of land use (i.e. residential, vegetation, built-up, urban park-water body and trees). It is clear that water body also could be another variable besides vegetation that can help lowering the surface radiant temperature of the surrounding area.

5 Conclusion and Recommendation

This initial study has shown that there have been a significant increase in the built-up areas within the District of Petaling over the period of 18 years. This has resulted in higher LST especially in the built-up areas as compared to the vegetated areas. Vegetation and water bodies have significant influence on the surrounding surface temperature. Although urbanization significantly increase the LST, the initiative taken by the Shah Alam City Council, Petaling Jaya City Council and Subang Jaya Municipal Council to plant more trees to help mitigate the UHI effects within the developed urban area. A comprehensive ground observation work is still required to validate the results obtained from satellite images.

References

Buyadi SNA, Wan Mohd WMN, Misni A (2013) The impact of land use changes on the surface temperature distribution of area surrounding the National Botanic Garden, Shah Alam. AMER international conference on quality of life

Choi H-A, Lee W-K, Byun W-H (2012) Determining the effect of green spaces on urban heat distribution using satellite imagery. Asian J Atmos Environ 6(2):127–135

Gartland L (2008) Heat islands: understanding and mitigating heat in urban areas, 1st edn. Earthscan, London

Liu L, Zhang Y (2011) Urban heat island analysis using the Landsat TM Data and ASTER data: a case study in Hong Kong. Remote Sens 3(7):1535–1552

Mallick J, Rahman A (2012) Impact of population density on the surface temperature and micro-climate of Delhi. Curr Sci 102(12)

Omar D (2009) Urban form and sustainability of a hot humid city of Kuala Lumpur. Eur J Soc Sci 8(2):353–359

Qin ZH, Karnieli A, Berliner P (2001) A Mono-window Algorithm for Retrieving Land Surface Temperature from Landsat TM Data and Its Application to the Israel-Egypt Border Region. Int J Remote Sens 22(18):3719−3746

Shahmohamadi P, Sairi A, Surat M (2009) Mitigating the urban heat island effect : some points without altering existing city planning. Eur J Sci Res 35(2):204–216

Sobrino JA, Jiménez-Muñoz JC, Paolini L, Jime JC (2004) Land surface temperature retrieval from LANDSAT TM 5. Remote Sens Environ 90(4):434–440

Solecki WD, Rosenzweig C, Pope G, Chopping M, Goldberg R (2004) Urban heat island and climate change: an assessment of interacting and possible adaptations in the camden. New Jersey Department of Environmental Protection, New Jersey Region

Takeuchi W, Hashim N, Thet KM (2010) Application of remote sensing and GIS for monitoring urban heat island in Kuala Lumpur metropolitan area. International symposium geoinformation

Wan Mohd WMN, Hashim S, Mohd Noor AM (2004) Integrating satellite remote sensing and GIS for analysing urban heat island. *Built Environ J* 1(2), p 34–44

Yan H, Wang X, Hao P, Dong L (2012) Study on the microclimatic characteristics and human comfort of park plant communities in summer. Procedia Environ Sci 13:755–765

Ushahidi and Sahana Eden Open-Source Platforms to Assist Disaster Relief: Geospatial Components and Capabilities

Khanh Ngo Duc, Tuong-Thuy Vu and Yifang Ban

Abstract In responses to recent large-scale disaster events, huge amount of ground information have been collected in addition to the synoptic views from satellite images. Different platforms have been in place to facilitate the collection and management of such critical location-based information from the crowd. This study investigated the current implementation of geospatial components and their capabilities in open-source platforms, particularly Ushahidi and Sahana Eden. Using the 2011 Christchurch earthquake data and following the four main functions of a geo-info system: Data input, Geospatial analysis, Data management, and Visualization, the performance of geospatial-components were evaluated by a group of users. The result showed that with rich visualization on interactive map both Sahana Eden and Ushahidi enable emergency managers to track the needs of disaster-affected people. While Ushahidi can only filter incidents records by time or category, geospatial data management of Sahana Eden is proven to be more powerful, allowing emergency managers input different geospatial data such as incidents, organizations, human resource, warehouses, hospitals, shelters, assets, and projects and visualizing all of these features on a map. It also helps to simplify the coordination among aids agencies. However, geospatial analysis is the limitation of both platforms. The findings recommended that data input with more variety of formats and more geospatial analysis functions should be added. Further research will expand to more case studies taking into account the requirements of disaster management practitioners and emergency responders.

K. N. Duc · Y. Ban
Department of Urban Planning and Environment, Royal Institute of Technology, Stockholm, Sweden

T.-T. Vu (✉)
School of Geography, University of Nottingham, Semenyih, Malaysia
e-mail: tuongthuy.vu@nottingham.edu.my

1 Introduction

In the last two decades, particularly from 2004 to 2011, most countries located on the Pacific Ring of Fire such as Japan, Philippines, Indonesia, New Zealand, and some Central American countries like Haiti have suffered severe damages as the consequences of tremendous earthquakes. A recent statistic by the United States Geological Survey (2012) showed that over 230,000 people were killed by the devastating 2004 Indian Ocean tsunami whereas the number of people killed and injured by the 2010 Haiti earthquake and the Mw 9.0 magnitude Japan earthquake were a quarter of million and nearly 20,000 people, respectively.

In the 1990s of the twentieth century, researchers and practitioners concerned with disaster management have engaged in a lengthy attempt to define fundamental concepts such as emergency, risk, hazard, disaster, and disaster management. According to Johnson (2000) an emergency is "a deviation from planned or expected behavior or a course of events that endangers or adversely affects people, property, or the environment". In another study, Gravley (2001) stated that disasters often result in great damage, loss, or destruction, so a disaster can also be defined as the onset of an extreme event causing profound damage or loss as perceived by the inflicted people. Furthermore, in the research titled *Disasters and Development*, Cuny (1983) concluded that disaster management deals with the set of complex decision-making issues related to prevention, control, and recovery from natural and human-made disasters. Disaster management, hence, involves lot of information collection, management, analysis and visualization, and especially all are location-based information.

Practical deployment has proved that the contribution of geoinformation technologies significantly improved the effectiveness in disaster management, especially during the post-disaster response to assist the disaster relief activities. Over a decade, under the coordination of International Charter on Space and Major Disasters and UN-SPIDER, satellite images have been acquired timely providing the unique information from the sky; especially to some hard-hit and inaccessible areas they are the only source of information (Stryker and Jones 2009; Vu and Ban 2010). Remote sensing imageries, however, cannot reveal truly the situations on the ground and up to the details of requirement. Advanced technologies today, fortunately, provided appropriate mechanism for collection and management of vast amount information contributed from the crowd formed by disaster practitioners, NGO teams, residences, etc. In recent large-scale disasters, we could observe the contribution of wiki, blogs, social networks, and collaborative mapping platforms in emergency responses (Heinzelman and Waters 2010; Vivacqua and Borges 2012; Kerle and Hoffman 2013; Vu 2013).

Advanced computer and IT technologies have brought GIS deployment from desktop to web-based platforms providing map, geospatial data and processing services and now cloud-based services. Desktop environment limits in local organisation and has to be handled by trained experts; data sharing and collaborative analysis, hence, are localised within an organisation. The web-based

platform helps to open widely the data sharing and accessibility, not yet provides a full data analysis mechanism on the web with past technologies. The emergence of web 2.0 technology enables the phenomenon of volunteer GIS (Goodchild 2007) introducing new terms as data mashup, crowdsourcing, and neogeography (Turner 2006) into GIS research, development and practices. Nowadays, map making has no longer the task of experts or mapping agencies but everyone, e.g. openstreet-map (www.openstreetmap.org) is a typical success of voluntary efforts in developing open-source world map data. Whistle benefits from frequently updated map and substantial crowd-sourced collected data is obvious, the uncertainty of its quality presented as a major issue for wider uses (Hudson-Smith et al. 2009; Goodchild and Glennon 2010). Disaster aftermath when authoritative data acquisition may be disrupted, the contribution of such crowd-sourced data is necessary to quickly grasp the real situation and provide efficiently relief effort to the devastated areas.

Sahana Eden and Ushahidi are the most two common open source crowd-sourcing platforms so far, built specifically to aid in crisis and disaster management and deployed in response to the 2004 Indian Ocean tsunami, the 2010 Haiti earthquake and the 2011 Tohoku earthquake and tsunami among other events. Ushahidi means "witness" in Swahili, and the first Ushahidi platform was released during Kenya's post-election violence in January 2008. It enables individuals and groups to collaborate in making live multi-media maps and use for all kinds of projects (Anahi 2011). The word "Sahana" means "relief" or "compassionate help" in Sinhala, one of the Sri Lanka languages. Sahana Software was initially innovated by the information technology (IT) community in Sri Lanka to help the country recover after the 2004 Indian Ocean earthquake and tsunami (Sahana Software Foundation 2011).

Based on Ushahidi and Sahana Eden platforms, disaster managers and emergency response practitioners can track users' reports on the map and timeline, know the needs of the affected victims and coordinate emergency agencies and aid resources. Nevertheless, some barriers and issues in technology deployment exist in relief planning efforts. In particular, an interactive map seems to be the only obvious geospatial component in existing systems. It would be very interesting to review the current implementation and evaluate the capability of geospatial components of these platforms. Some questions of our concerns: Are there other geospatial functions provided in the platform? How geospatial data are fed into platform? How are they managed? Are users comfortable with working on these platforms? We used the data available after the 2011 Christchurch earthquake to mimic the situation of post-disaster responses. The study area and data are described in Sect. 2 followed by methodology in Sect. 3. The review and evaluation outcomes are given in Sect. 4 prior to concluding remarks in Sect. 5.

2 Study Area and Data Description

Christchurch, the second-largest city of New Zealand and the gateway to the South Island, locates on the edge of the Canterbury Plains, extending to the Southern Alps. Since New Zealand situates on the tectonic plate boundary between the Pacific Plate and the Australia-India Plate, the country suffers regular devastating earthquakes. On the 22 February 2011, the 6.3-magnitude (on Richter scale) earthquake struck the city of Christchurch, New Zealand. The earthquake caused serious damage to buildings and residential houses, extensive liquefaction, significant rock falls in areas of the Port Hills as well as considerable disruption to road and rail networks, airport and port, electricity supplies and water and wastewater systems.

Christchurch City declared a state of local emergency on 22 February 2011 and an Emergency Operations Centre was activated in the City's Art Gallery to manage the response. The co-ordination of response activities in Christchurch, via the Canterbury Response Centre involves:

- The emergency services, including Urban Search and Rescue;
- Welfare agencies and services;
- Medical and health services;
- Lifeline utilities and restoration of services;
- Managing spontaneous volunteers.
- Management of the international dimension and offer of support.
- Management of logistic, in terms of procurement and distribution as well as co-ordination between the Christchurch Response Centre and the National Crisis Management Centre.
- Management of building safety evaluations.
- Management of building demolition and cordoned areas.

Based on real state of incidents and the response activities in the 2011 Christchurch earthquake, research data retrieved from ANZAA (2011) includes damaged or collapsed buildings, closure areas, closed or damaged roads, closed bridges, power failures, trapped people, broken waterspouts, hospitals, warehouses, shelters and welfare centers.

3 Methodology

The comparative review and evaluation of Sahana Eden and Ushahidi platforms was organized into three stages.

Installation: Sahana Eden and Ushahidi platforms were downloaded from the Sahana Software Foundation and Ushahidi main website and properly installed according to their requirements. For instance, Sahana Eden requires Python and/or Java Script programming language and database systems such as PostgreSQL

Table 1 Basic requirements for installing Ushahidi and Sahana Eden

Ushahidi	Sahana Eden
PHP version 5.2.3 or greater	Python and java script
MySQL version 5.0 or greater	MySQL, PostgreSQL, or SQLite
An HTTP server: e.g. Apache, lighttpd, microsoft internet information server, or nginx	Apache, other webservers like cherokee can be used.

whereas Ushahidi requires access to a web server that supports PHP language and a MySQL database. Basic requirements are listed in Table 1.

Data acquisition: Christchurch earthquake data was downloaded from ANZAA and imported into Sahana Eden and Ushahidi. Based on the capacity of each platform, the categories of earthquake data including destroyed and collapsed infrastructure, and hospitals and shelters data input to Sahana Eden may be different from that into Ushahidi platform. Data of *incidents*, *organizations*, *human resource*, *warehouses*, *hospitals*, *shelters*, *assets*, and *projects* were designed and imported to the Sahana Eden platform. Since Ushahidi is mainly designed to report incidents in emergency, there was only *incidents* data among other data selected to input into Ushahidi.

Evaluation and comparison: the comparison was based on five features: *Data input* (the type of data format imported to these platforms; the way data to be input to these platforms, online or directly imported), *Geospatial analysis* (e.g. buffer, overlay, etc.), *Data management* (e.g. search or query or filter desirable records of incidents), *Visualization* (Interactive map or static map), and *overall user's evaluation*.

4 Results and Discussion

A group of ten volunteers at Royal Institute of Technology (KTH) campus, Sweden was introduced to Ushahidi and Sahana Eden and experienced the platforms' performances with the 2011 Christchurch earthquake data. At the first glance, Ushahidi plays as a means for data collection and visualization, which also provides few simple data filtering capabilities for users to visually assess the information. On the other hand, Sahana Eden is a project management platform for relief and emergency response management; it provides a number of different modules such as organization registry, project tracking, human resource, inventory, asset, assessment, map and shelter management and those are customizable.

In our study, the following modules were designed: *incidents, organizations, human resource, warehouses, hospitals, shelters, assets,* and *projects.* Real incidents including short descriptions of incidents from raw data were added to *Incident* module. Each incident must be assigned accordingly to a specific category such as buildings collapsed, bridges closed, people trapped, or other items in

Fig. 1 Incident report

category list (Fig. 1). After being imported all data of incidents, organizations, human resource, warehouses, hospitals, shelters, assets, and projects will be presented on an interactive map with different icons (Fig. 2).

Likewise, after the incidents list was put into Ushahidi, the points were displayed according to their categories as shown in the list sorted in chronological order (Fig. 3). Figure 3 presents all of the incidents reports, which were submitted to Ushahidi and displayed on the homepage. Based on the Ushahidi platform, disaster managers and emergency response practitioners can track user's reports on the map and timeline.

Regarding *data input*, Ushahidi platform benefits disaster managers by multiple data streams. Ushahidi platform accepts gathering information via multiple data stream such as text messages, email, twitter, web-forms, smart-phone both Android and iOS. Sahana Eden (end-user version) platform limits its *data input* only from Ushahidi and Comma-Separated Value (CSV) format. In response to a large-scale devastating disaster, when a variety of formats such as ".kml", or ".shp" retrieved from field mapping, a direct import or conversion mechanism would significantly help responders and save time.

Creating a buffer around a selected incident within specific radius can be considered as a minor *geospatial analysis* function installed in Ushahidi (Fig. 4). To some extent, this function facilitates emergency response activities. For instance, if the distribution of incidents in an area within specific radius shown on
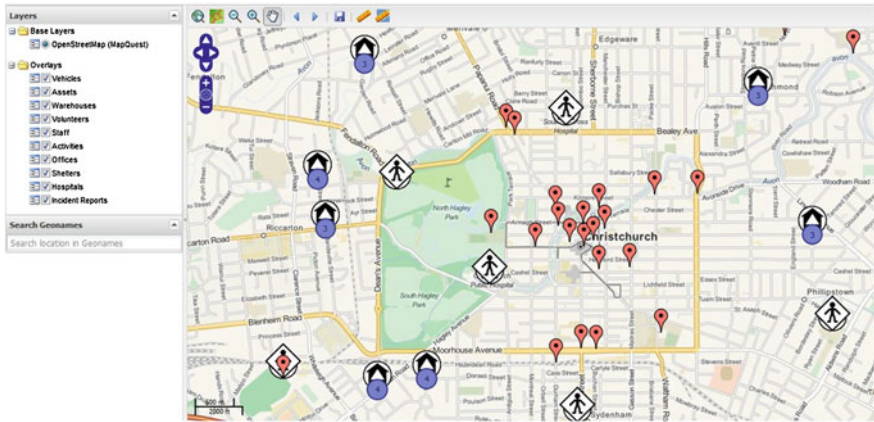
Fig. 2 The 2011 Christchurch earthquake response map using Sahana Eden
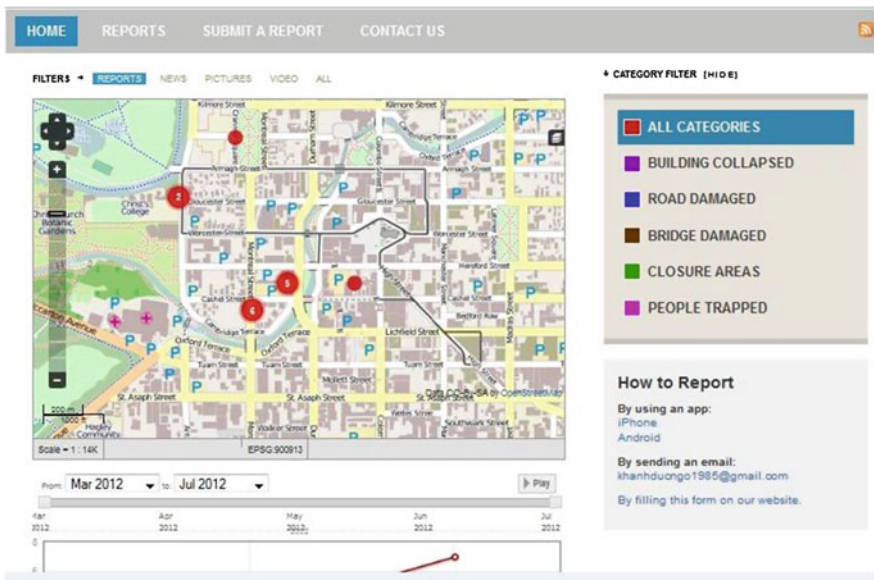
Fig. 3 Incident report on Ushahidi

the map was dense, the area could be unsafe for people's life and hence, a relief and evacuation plan needs to immediately be implemented.

Dynamic timeline and report filtering show *data management* capacity of Ushahidi. The timeline helps track users' reports on the map and over time, and data can be filtered by time and incidents can be visualized whenever and wherever, as it is tied to the map. The provision of the reported information mapping

Fig. 4 Report filtering based on buffer capability of Ushahidi

tools in Ushahidi presents rich *visualization* capacity, showing post-disaster incidents on the interactive map. Therefore, disaster responders could quickly realize the places that were in emergency.

Although the Ushahidi platform only supports minor geospatial analysis functions, to some extent, it is helpful for current disaster aid activities. There may be enough mobilization of disaster responders and volunteers in large-scale disaster events, search and rescue activities would have troubles in locating suffered people. Via Ushahidi platform, the affected people can tell where their locations are via messages or web-forms, so it can be considered as the bridge of delivering information between suffering people and aid organizations.

Sahana Eden aims at providing disaster managers with tools to minimize the negative effects from devastating disasters through tracking the needs of the affected people and coordinating emergency agencies and aid resources. In addition, the platform can enable disaster managers, emergency response practitioners, and communities around the world to access and share the needed information in

order to reduce casualty during pre-disaster preparedness and post-disaster response phase through free and open source software and open standards.

Powerful *data management* tools make Sahana Eden more outstanding than Ushahidi platform. In fact, Sahana Eden supports various modules such as organization registry, project tracking, human resource, inventory, asset, assessment, and shelter management and it enables staffs to query or filter any desirable records. Sahana Eden shows rich *visualization* capacities, providing an interactive map with fully fundamental functions to visualize features such as zoom in/out tools, layers options (enable/disable), and markers changes.

Nevertheless, there is a weakness that needs to be pointed out. Sahana Eden (end-user version) only shows incidents in term of points on the map. The matter under consideration is that an earthquake may cause damage to roads and railways, or a row of houses or a block of flats, which should be better represented as a polylines and/or polygon. However, Sahana Eden cannot display polygons and polyline on the map. When showing assets on the map, Sahana Eden only displays locations of warehouses or sites managing assets, the platform is unable to show the position of person assigned to use assets on the general map. Let's examine the following case: an incident I1, we immediately need an ambulance A1 which is assigned to a person working at incident I2 500 m away from location of I1. The map would only present three ambulances A2, A3, and A4 located in the warehouse about 10 km from incident I1 to the emergency response practitioners. Here, it should be better to show the incident assigned to a person on the map, which effectively helps in saving time in the short distance.

Lack of *geospatial analysis* capability found in Sahana Eden, which only provides a distance measurement tool. In fact, Sahana Eden could become a perfect platform in disaster management if some geospatial analysis components could be implemented in the platform and the users do not need for additional tools and software. Logistics planning is the most in need activity and hence obviously shortest path analysis will be a helpful tool. Knowing the shortest route to hospitals could save more lives when large-scale disasters strike and cause numerous seriously injured victims.

In most emergency responses, helicopters are mobilized in order to transport victims and provide aid. Hence, the shortest distance to specific features may be based on a straight-line path, as the crow flies. Nevertheless, once a large-scale catastrophe occurs and helicopters may be insufficient, ambulances and other vehicles might be used. In order to indicate the shortest route to specific features such as hospitals, welfare sites or camps, analysis of destroyed infrastructure is required and maps of damaged roads must be produced. As a whole, professional user's satisfaction may be at a high level if some spatial analysis could be implemented in Sahana Eden.

In developed countries, iPhone and Android applications used in Ushahidi platform are more common, so it is easier to cope with natural disasters at any time. However, it is really an obstacle and limitation in developing countries such as Vietnam, Bangladesh, Indonesia and the Philippines because these high-tech applications are uncommon and deficient in far-off areas in the countryside. Even

Table 2 Comparison of main functions between Ushahidi and Sahana Eden

	Ushahidi	Sahana Eden
Data input	Multiple data stream: text message, email, twitter, web-forms	Comma-separated value (CSV) format
Analysis	Medium level	Limited
Data management	Medium level with data filter by time and incidents	High level with various modules
Visualization	Interactive mapping	Interactive mapping
User's evaluation	Fairly satisfied	Satisfied

though text messages are designed as one of data collection methods in Ushahidi, such low-tech 2G phones and network infrastructures may be even not available in remote, low-developed disaster-affected areas. That deficiency may be considered as the barrier of high-tech deployment in disaster relief.

Users are fairly satisfied with Ushahidi. Based on user's evaluation of the Ushahidi platform, although Ushahidi could provide the precise location of incidents, it is said that in serious emergency situations (such as people trapped or injured), victims usually need fast response by calling emergency centers, and filling in the Ushahidi web-forms is not effective. In fact, calling emergency or sending messages to give short descriptions and the location of incidents is faster than turning on a computer or smart-phone to fill in the web-form which needs time to start up and log on, and depends on the internet connection. Users also highlighted that it may not be people's highest priority to report incidents to the Ushahidi platform during or immediately after disaster strike. In order to enable the system to work effectively, there should be programs building preparedness capacity for communities in general framework of disaster mitigation planning, e.g. in the case of the 2011 Japan earthquake, people reported through the internet via Facebook and Twitter. These systems provide only one aspect as important ground-truth information, and it cannot provide a complete picture of the damages. Therefore, such information needs to be integrated with other sources of information.

In general, based on the designing purpose, the data input capacity of Ushahidi platform is more diverse than the one of Sahana Eden while Sahana Eden shows more prominent capacity of data management in comparison to the Ushahidi platform. Although both platforms present rich visualization capacity, the limitation of geospatial analysis also exists in both of them (Table 2).

5 Conclusion

Sahana Eden and Ushahidi are the two most effective open source software platforms, designed specifically to aid in disaster management and achieved the great success in the 2004 Indian Ocean tsunami and the 2011 Japanese earthquake

responses. Open source platforms are the promising tools for disaster management but these platforms have not yet been fully developed for geospatial services. We found that limited geospatial analysis was provided in both platforms although other input, management and visualization capability were reasonably sufficient.

Ushahidi has been developed mainly for information collection, visualization and interactive mapping and those are well developed and utilized. The current roadmap for development is more towards facilitating the ease of uses and data mining. Integrating more GIS analysis functions seems not the priority (https://wiki.ushahidi.com/display/WIKI/Our+Products). With rich capability as a project management platform, Sahana Eden would be easily enhanced to be a suitable platform for relief planning and management by adding more geospatial analysis functions, one of which is the shortest route to a specific feature since logistic management is critical in post-disaster and emergency responses. In addition, Sahana Eden would be further improved its data input capability to accept more common spatial data format like shapefile. GIS research is highlighted as one of the future research directions of Sahana Eden (http://wiki.sahanafoundation.org/doku.php/research:future).

The growth of natural disaster in the last decade is alarming that in the near future the world would deal with more natural disasters with extreme intensity and at a large scale. Therefore, the role of geoinformation technologies should be efficiently strengthened, developed, and improved to overcome the current weaknesses in minimizing negative impacts and vulnerability resulted from natural disasters. Due to time-constraints, the current research only explored the performance of Ushahidi and Sahana Eden (end-user version) platforms with one specific earthquake case study. The comparison was carried out from only the perspective of geospatial analysts. Further researches will come up with more comprehensive investigations of geospatial capabilities of the platforms in different real case studies taking into account the requirements of disaster management practitioners and emergency responders.

References

Anahi A (2011) Ushahidi guide. http://community.ushahidi.com/uploads/documents/Ushahidi-Manual_4.pdf. Accessed 03 Feb 2012

Australian New Zealand American Association of Minnesota (ANZAA) (2011) Christchurch earthquake information resource. http://anzaa.com/2011/02/christchurch-earthquake-information-resources. Accessed 25 March 2012

Cuny FC (1983) Disasters and development. Oxford University Press, Oxford

Gravley D (2001) Risk, hazard, and disaster. http://homepages.uc.edu/~huffwd/Volcanic_HazardRisk/Gravley.pdf. Accessed 01 March 2012

Goodchild MF (2007) Citizens as sensors: the world of volunteered geography. GeoJournal 69:211–221

Goodchild MF, Glennon AJ (2010) Crowdsourcing geographic information for disaster response: a research frontier. Int J Digit Earth 1:1–11

Heinzelman J, Waters C (2010) Crowdsourcing crisis information in disaster-affected Haiti. USIP Special Report. (www.usip.org)

Hudson-Smith A, Batty M, Crooks A, Milton R (2009) Mapping for the masses: accessing web 2.0 through crowdsourcing. Soc Sci Comput Rev 27(4):524–538

Johnson R (2000) GIS technology for disasters and emergency management. http://www.geo.umass.edu/courses/geo250/disastermgmt.pdf. Accessed 01 March 2012

Kerle N, Hoffman RR (2013) Collaborative damage mapping for emergency response: the role of cognitive systems engineering. Nat Hazards Earth Syst Sci 13:97–113

Sahana Software Foundation (2011) Annual Report, http://wiki.sahanafoundation.org/lib/exe/fetch.php/foundation:ssf_2011_annual_report.pdf. Accessed 31 July 2012

Stryker T, Jones B (2009) Disaster response and the international charter program. Photogram Eng Remote Sens 75:1342–1344

Turner A (2006) Introduction to neogeography. O'Reilly Media, Sebastopol

United States Geological Survey (USGS) (2012) Historic world earthquake. http://earthquake.usgs.gov/earthquakes/world/historical.php. Accessed 16 April 2012

Vivacqua AS, Borges MRS (2012) Taking advantages of collective knowledge in emergency response systems. J Netw Comput Appl 35:189–198

Vu TT (2013) Geospatial technology uses in post-disaster response—the power of the crowd. Disaster Adv 6(4):1–3

Vu TT, Ban Y (2010) Context-based damage mapping from high-resolution optical satellite images. Int J Remote Sens 31(13):3411–3425

Combining Two Clustering Ideas for Typification of Ditches

Jing Tian, Wen-Yu Yang and Li-Jun Chen

Abstract Ditches are important components of hydrological ecosystem and play a critical role in capturing and removing the micro-organisms and pollutants from water body. The generalization of ditches supports the multi-scale analysis and modeling of hydrological and ecological environment that relate to ditches. This paper proposes and implements a new method that combines two clustering ideas for typification of ditches. This method groups the ditches based on the edge-cutting of the minimal spanning tree of ditches, and represents the ditches in each group based on K-means++ algorithm. This study also presents the validation of the method with the experimental data of Guangzhou city.

Keywords Map generalization · Typification · Ditches · Clustering

1 Introduction

Ditches are important components of hydrological ecosystem and have a great influence on capturing and removing the microorganisms and pollutants from water body (Dunn and Mackay 1996; Bennett and Moore 2005; Smith 2009). The cartographic generalization and multi-scale representation of ditches support the multi-scale analysis, as well as the modeling of hydrological and ecological environment. A simple selection algorithm is not enough to maintain the distribution pattern of ditches that are approximately parallel distributed (Sandro et al. 2011). Therefore, typification is needed to address this issue.

Typification is a generally accepted operator in the community of map generalization (Shea and McMaster 1989; Li 2007). It reduces the quantity of the objects

J. Tian · W.-Y. Yang (✉) · L.-J. Chen
School of Resource and Environment Science, Wuhan University, 129 Luoyu Road,
Wuhan 430079, China
e-mail: yewenyusheng@gmail.com

while preserving the distribution characteristics of the initial pattern. The majority of the existing researches focus on the building typification (Regnauld 2001; Sester 2005; Anders 2006; Burghardt and Cecconi 2007). Meanwhile, there are a few researches aiming at linear elements such as drainage system and ditches (Sandro et al. 2011; Zhang 2007). More works remains to be done to promote two operators, displacement and typification, which were found to be the most problematic operators during the generalization process (Foerster and Stoter 2008). Therefore, the study of typification is challenging and meaningful.

Typification usually consists of two steps. It should begin with the recognition of the pattern of those objects in groups that are subjected to typification, that is, classifying those objects or recognizing the specific alignment. For instance, the classification of the building set and the recognition of the arrangement pattern such as grid pattern (Anders 2006), linear pattern and curve pattern (Zhang et al. 2013). Thereafter, those objects would be represented. In detail, the new objects would replace the old ones while the initial characteristics, such as direction, arrangement, and density, are preserved. For example, when the initial building set is replaced by the new ones, the new direction should be determined according to the initial average direction.

Following the idea of typification, this paper proposes a method aiming to work on ditches that run approximately parallel to each other. This method combines two clustering ideas. One is ditch grouping according to the idea of division, and the other is considering density variation.

The rest of this chapter is structured as follows. Section 2 introduces the basic concepts and characteristics of ditches. Section 3 describes the method. Section 4 presents the experimental results and the shortcomings of the method. Conclusions are drawn in Sect. 5.

2 Characterization of Ditches

A ditch is a man made channel that is used to irrigate, conduct, and drain water (Sandro et al. 2011). It can be classified as a linear element if only considering its geometry. As shown in Fig. 1, some ditches run approximately parallel to each other (i.e. Fig. 1a), while some are not (i.e. Fig. 1b).

The structure and morphological characteristics of the artificial hydrographic net in irrigated area should be reflected correctly in the map compilation. They cannot be selected based solely on their length, whereas the monolithic construction should be taken into account. It is obvious that simply using the length of the ditches or practically choosing one out of two cannot meet the requirement of the cartographic generalization of those ditches in almost parallel distribution pattern. To address this issue, this paper proposes an approach to the typification for this particular case.

Fig. 1 Ditches of different distribution pattern. **a** almost parallel. **b** not parallel
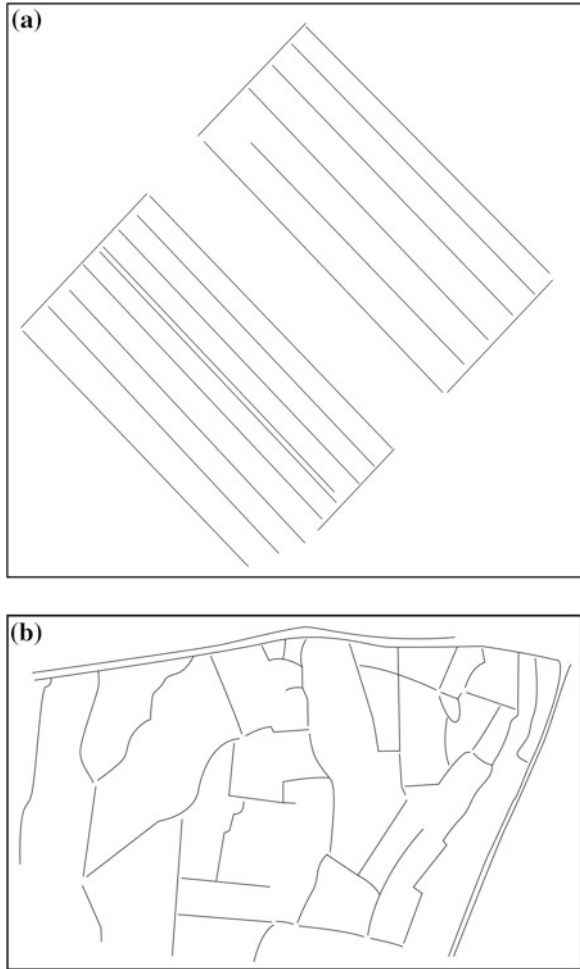
3 Typification Approach to Almost Parallel Ditches

As for the typification of almost parallel ditches, the ditches should be first divided into several groups, and then replacement of the old ditches with new ones should be carried out in each group. This paper proposes an approach with two steps. Firstly, the ditches are grouped based on the edge-cutting of the minimal spanning tree of ditches; Thereafter, the ditches in each group will be replaced by new ones based on K-means++ algorithm.

3.1 Ditch Grouping Based on the Edge-Cutting of Minimal Spanning Tree

Ditches that are subjected to be typification should be recognized before the typification process. This procedure identifies that which ditches should be considered as a whole. This study uses the edge-cutting of the minimal spanning tree for ditch grouping, the idea of which originates from Zahn (1971). This method has been widely applied to building grouping (Regnauld 2001; Zhang et al. 2013). The definition of the cognition distance between the objects is the key issue to implement this approach.

3.1.1 Definition of Cognition Distance of Ditches

Ditches run approximately parallel and adjacent to each other tend to be recognized within one group according to visual cognition. This paper combines the average distance (McMaster 1986), the angle difference and the overlapping relationship between two ditches to constitute the cognition distance between them, as shown in Eq. (1).

$$CognitionDistance = AverDistance * (\tan(4.5 * AngleDifference) + 1) \\ * (2 - OverlapDegree) \tag{1}$$

AverDistance is the average distance between two ditches, which is proportional to the *CognitionDistance*. The smaller *AverDistance*, the smaller *CognitionDistance*. As a result, they are more likely to be divided into the same group. The calculation of *AverDistance* can be written as:

$$AverDistance = 2Area_{AB} / (L_A + L_B) \tag{2}$$

where $Area_{AB}$ is the area of those polygons that consist of two ditches and their endpoints, L_A is the length of ditch A, and L_B is the length of Ditch B, as shown in Fig. 2a.

AngleDifference is denoted as the angle difference between two ditches. The smaller *AngleDifference*, the smaller *CognitionDistance*. Furthermore, ditches with smaller *AngleDifference* are more likely to be divided into one group. The calculation can be shown as:

$$AngleDifference = |Angle_A - Angle_B| \tag{3}$$

where $Angle_A$ is the angle of ditch A, $Angle_B$ is the angle of ditch B. Angledifference ranges from 0 to 10°.

OverlapDegree shows the overlapping relationship between two ditches. In contrast to *AverDistance*, *OverlapDegree* is inversely proportional to *CognitionDistance*, that is, the greater *OverlapDegree*, the smaller *CognitionDistance*. Thus, ditches with greater *OverlapDegree* are more likely to be divided into a group. The

Fig. 2 Illustration of
AverDistance and
OverlapDegree.
a AverDistance.
b OverlapDegree
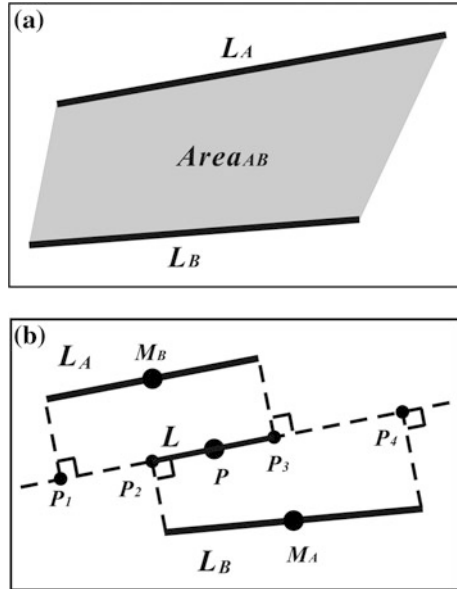
calculation of it which ranges from 0 to 1 is shown in Eq. (4). As illustrated in Fig. 2b, L_A is the length of the ditch A, L_B is the length of the ditch B, and L is the length of the overlap section.

$$OverlapDegree = 2L/\left(L_A + L_B\right) \tag{4}$$

After the definition of *CognitionDistance*, the minimal spanning tree of ditches can be created which is shown in Fig. 3. And Cognition distance between ditches is summarized in Table 1.

3.1.2 Edge-Cutting of the Minimal Spanning Tree

Edge-cutting of the minimal spanning tree is a process that removes the edges inconsistent with their neighboring edges. Those edges can be determined using the method (Sergios and Konstantinos 2009): All the edges that lie k or fewer steps away from the object edge e should be taken into consideration. Firstly, the mean and the standard deviation of their weights (refer to distance in this paper) are computed. If the weight of an edge were q times more than the standard deviation, it would be recognized as an inconsistent edge. More details can be found in (Zahn 1971). We found that two and four should be good values for the key parameters k and q. An example of the edge-cutting of the minimal spanning tree is displayed in Fig. 4.
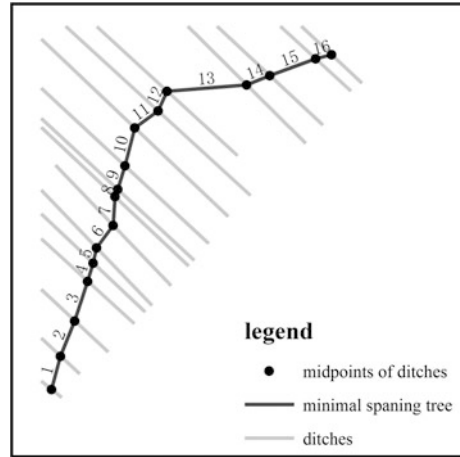
Fig. 3 Minimal spanning
tree of ditches

Table 1 Cognition distance between ditches

ID	AverDistance	AngleDiference	OverlapDegree	CognitionDistance
1	48.531	4.427	0.613	91.697
2	55.831	0.042	0.730	71.133
3	59.584	0.666	0.842	72.590
4	26.886	0.972	0.937	30.772
5	20.613	2.817	0.945	26.647
6	43.227	0.007	0.972	44.465
7	34.107	2.951	0.898	46.449
8	11.395	0.384	0.985	11.916
9	34.790	0.007	0.951	36.504
10	54.088	0.635	0.922	61.190
11	44.645	1.053	0.978	49.404
12	32.380	0.053	0.865	36.896
13	93.481	2.273	0.702	143.246
14	35.692	1.782	0.931	43.526
15	68.490	0.438	0.797	85.247
16	21.660	0.758	0.899	25.268

3.2 Ditch Representation Based on K-means++ Algorithm

After grouping the ditches, the next step would be representation. This step replaces the original clusters by a smaller number of objects. In the meantime, the distribution characteristics of the initial pattern need to be preserved. Thus, three questions need to be answered. How many ditches should be contained in the new group? How to represent the initial objects by new ones and how to evaluate the results?

legend

● midpoints of ditches

▬ consistent edges in minimal spanning tree
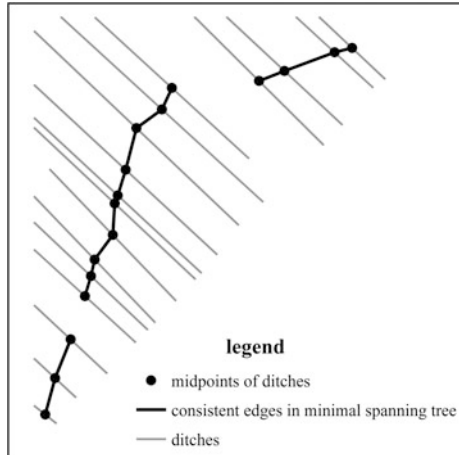
━ ditches

### 3.2.1 The Determination of the Number of Ditches

The number of ditches can be either determined with the radical law (Topfer and
Pillewizer 1966) or defined according to the facts, and it should be smaller than the
number of the initial ditches.

3.2.2 Representation

Representation is to replace the initial clusters with new ones that are simpler.
Meanwhile the original distribution pattern should be preserved. Moreover, the
density variation should be taken into account as well. Vector quantization is used
to maintain the density distribution. It works by dividing a large set of points
(vectors) into groups and each group is represented by its centroid point. The
density matching property of vector quantization is powerful. As for the spatial
point clusters, some algorithms such as K-means and self-organized maps express
this idea excellently. K-means++ algorithm is selected in this study, considering its
success in overcoming some of the problems associated with other ways of
defining initial cluster-centers for k-means clustering (Arthur and Vassilvitskii
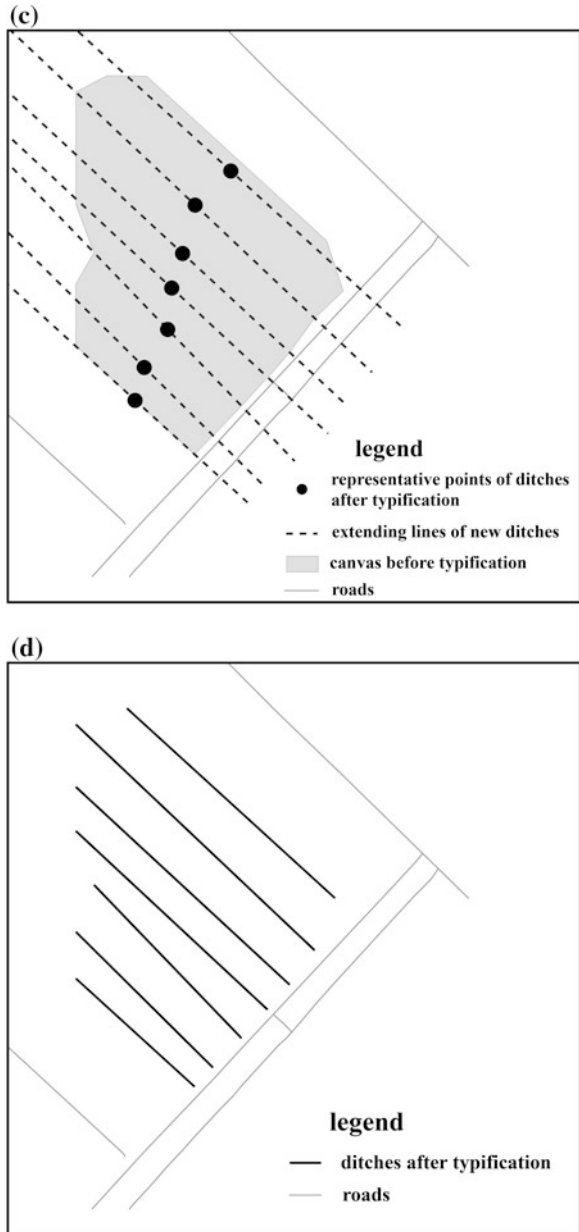2007; Shindler 2008).

Procedures of the representation are summarized as follows: ① Generate the
envelope of ditches, knows as canvas in (Sandro et al. 2011). As can be seen
shown in Fig. 5a, the canvas is a polygon around all the segments of each ditch
cluster, reflecting the distribution range of ditches. ② Take the midpoints of each
ditch and input the midpoints of each ditch and the number of ditches into the
K-means++ algorithm. As shown in Fig. 5b, the output would be the representative
points created by K-means++ algorithm. ③ Rebuild the new ditches according to
the average direction of the initial ditches, which extends lines from the

Fig. 5 Representation of
Ditches. **a** midpoints of the
ditch and the canvas. **b** the
output of K-means algorithm.
c extending lines of new
ditches. **d** final result
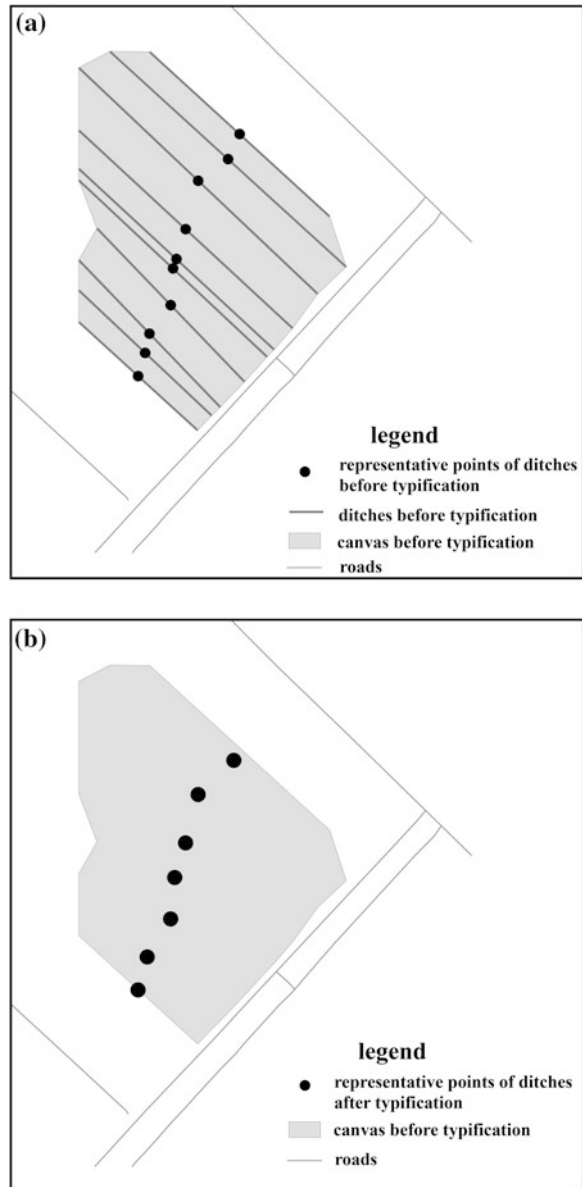
representative points in accordance with the average direction. And it should be
noted that the lines are extended to the side of the canvas, as can be seen from
Fig. 5c. The final result is showed in Fig. 5d.

Fig. 5 continued

(c)

legend

● representative points of ditches after typification

- - - extending lines of new ditches

canvas before typification

—— roads

(d)

legend

—— ditches after typification

—— roads

3.2.3 Evaluation of Results

Evaluation of generalization results has been recognized as the difficult part in map generalization. In our study, *Similarity* was used to carry out the evaluation. The basic idea of the *Similarity* is that a great overlap of ditch clusters before and after

Fig. 6 Evaluation of the result
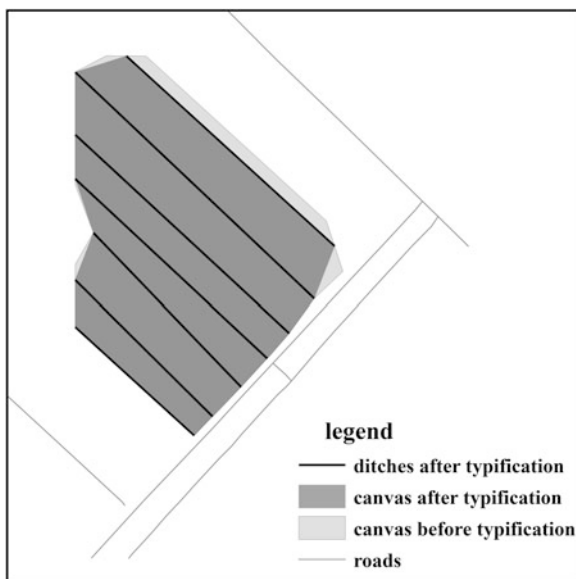
typification presents a good result. The calculation is shown in formula (5), where S is the area of the canvas of those initial ditches, while T is the area of the canvas of ditches that have been typified, $S \cap T$ is the area of the overlap of canvas of ditches before and after typification. It is worth noting that the S*imilarity* ranges from 0 to 1 in this study.

The evaluation of the result is shown in Fig. 6 for the case that is displayed in Fig. 5d. The value of *Similarity* is determined as 0.933. Presuming that there are n ditch clusters, the average *Similarity* would be the average value of that for the n ditch clusters.

4 Experiment

Part of the Guangzhou ditch data was selected to verify the method in this study. As can be seen from the areas that are marked in the red ovals in Fig. 7a, ditches at the upper location have an irregular parallel distribution pattern, while the lower group of ditches is more regular distributed. Therefore, the data is very suitable for the experiment. The experimental result is shown in Fig. 7b, where the average *Similarity* is 0.851. Therefore, the proposed approach preserves the distribution pattern effectively.

It should be mentioned that the approach has some shortcomings. (1) K-means++ algorithm in the representation step was selected with good performance but may not be the best in the initial seed selection. The uncertainty may be induced significantly by the selection of the initial seed methods. Practically, we

Fig. 7 Experimental data
and result. **a** source data.
b generalized data
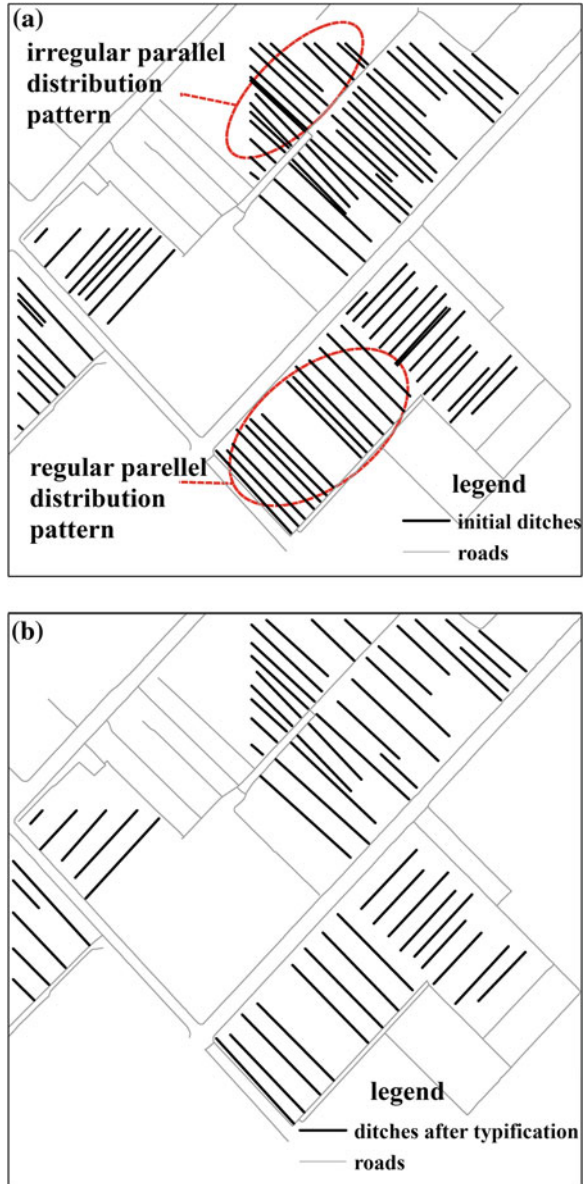
conducted 100 experiments and chose the result that had the greatest average *Similarity*. (2) Some factors were not taken into consideration in this study, such as canals and buildings, since they might conflict with the new ditches.

5 Conclusion

This paper presented a new approach to typification of ditches, which combined two clustering ideas, i.e., grouping according to the idea of division and considering the density variation. The original distribution pattern and the density variation of ditches were taken into account in representation, which made visualization of ditches after typification similar to the initial condition. Future work will focus on the conflict detection and coordination between the ditches and other objects.

References

Anders KH (2006) Grid typification. In: 12th international symposium on spatial data handling, progress in spatial data handling. Springer, Heidelberg, pp 633–642

Arthur D, Vassilvitskii S (2007) k-means++: the advantages of careful seeding. Proceedings of the 18th annual ACM-SIAM symposium on discrete algorithms 2007, pp 1027–1035

Bennett ER, Moore MT (2005) Vegetated agricultural drainage ditches for the mitigation of pyrethroid-associated runoff. Environ Toxicol Chem 24(9):2121–2127

Burghardt D, Cecconi A (2007) Mesh simplification for building typification. Int J Geogr Inf Sci 21(3–4):283–298

Dunn SM, Mackay R (1996) Modelling the hydrological impacts of open ditch drainage. J Hydrol 179(1–4):37–66

Foerster T, Stoter J (2008) Generalization operators for practice—a survey at national mapping agencies. In: Proceedings of the 11th ICA workshop on generalization and multiple representation, Montpellier

Li Z-l (2007) Digital map generalization at the age of enlightenment: a review of the first forty years. Cartograph J 44(1):80–93

McMaster R (1986) A statistical analysis of mathematical measures for linear simplification. Am Cartograph 13(2):103–116

Regnauld N (2001) Contextual building typification in automated map generalization. Algorithmica 30(2):312–333

Sandro S, Massimo R, Matteo Z (2011) Pattern recognition and typification of ditches. In: Ruas A(ed) Advances in cartography and giscience, Lecture Notes in Geoinformation and Cartography. Springer, Heidelberg, pp 425–437

Sergios T, Konstantinos K (2009) Pattern recognition, 4th edn. (ISBN 978-1-59749-272-0)

Sester M (2005) Optimization approaches for generalization and data abstraction. Int J Geogr Inf Sci 19(8–9):871–897

Shea KS, McMaster RB (1989) Cartographic generalization in a digital environment: when and how to generalize. In: Proceedings of Auto-carto 9, Baltimore, pp 56–67

Shindler M (2008) Approximation algorithm for the metric k-median problem. Masters thesis, Department of Computer Science, UCLA

Smith DR (2009) Assessment of in-stream phosphorus dynamics in agricultural drainage ditches. Sci Total Environ 407(12):3883–3889

Topfer F, Pillewizer W (1966) The principles of selection: a means of cartographic generalization. Cartograph J 3(1):10–16

Zahn CT (1971) Graph-theoretical methods for detecting and describing gestalt clusters. IEEE Trans Comput 20(1):68–86

Zhang Q-n (2007) Drainage typification based on dendritic decomposition. Cartograph J 44(4):321–328

Zhang X, Ai T-h, Stoter J, Kraak MJ, Molenaar M (2013) Building pattern recognition in topographic data: example on collinear and curvilinear alignments. Geoinformatica 17(1):1–33

Seasonal Sea Surface Circulation in the Northwest Region Off the Borneo Island Based on Nineteen Years Satellite Altimetry Data

Muhammad Faiz Pa'Suya, Kamaludin Mohd Omar, Benny N. Peter and Ami Hassan Md Din

Abstract Seasonal variation of sea surface circulation in the northwest coast of Borneo Island were illustrated using altimetry data provided by six missions of satellite altimetry for the period of nineteen years (1993–2011). The estimated sea level anomaly (SLA) from altimetry data using Radar Altimeter Database System (RADS) is consistent with the tide gauge measurement at Kota Kinabalu and Bintulu. The SLA is combined with the 1992–2002 Mean Dynamic Ocean Topography to determine the absolute dynamic topography. Assuming geostrophic balance, the geostrophic current is estimated from the absolute dynamic topography and mapped for four specific months which represent the monsoon seasons; August (Southwest Monsoon), December (Northeast Monsoon), April (inter-monsoon) and October (inter-monsoon). The pattern of estimated surface current is consistent with the Argos-tracked Drifting Buoy's track. In general, surface circulation in the central part of the southern region of South China Sea during April, October and December is cyclonic. Along the northwest coast of Borneo Island, the surface current is flowing north eastward during all months except in August, when the current is flowing northward. A few eddies have also been observed from the estimated surface current pattern.

Keywords Sea surface circulation · Monsoon · RADS · Borneo Island · Satellite altimetry

M. F. Pa'Suya (✉)
Faculty of Architecture Planning and Surveying, Department of Surveying Science and Geomatics, Universiti Teknologi Mara (Perlis), Arau, Perlis, Malaysia
e-mail: mhmdfaiz86@gmail.com

K. M. Omar · B. N. Peter · A. H. M. Din
GNSS and Geodynamic Research Group, Infocomm Research Aliance, Faculty of Geoinformation and Real Estate, Universiti Teknologi Malaysia, Johor Bahru, Malaysia
e-mail: kamaludin_omar2004@yahoo.com

B. N. Peter
e-mail: bennynpeter@gmail.com

A. H. M. Din
e-mail: amihassanmddin@gmail.com

1 Introduction

Borneo Island, the southern border of South China Sea (SCS) comprises of the East Malaysia (Sabah and Sarawak) and Brunei in the north western part and the Indonesia (Kalimantan) in the southern part. The island is surrounded by the South China Sea in the northwest, the Sulu Sea in the northeast, the Celebes Sea and Makassar Strait in the east, and the Java Sea in the south. The oil exploration and shipping industries in the northwest coast of Borneo Island have been growing rapidly and have played an important role in the development of the Malaysian economy. However, oil pollution of this region waters largely arises from vessel operation, tanker accidents, oil exploration and production activities, is one of the main problems affecting the marine coastal environments. Thus, to mitigate and control the oil pollution, an accurate knowledge of the ocean circulation is very essential.

Most of the previous investigations by Malaysian researchers focus on the Peninsular Malaysia water region (Saadon and Marghany 1996; Taira et al. 1996; Akhir 2011) whereas, northwest coast of Borneo Island is less studied. The information of surface currents of this region so far relies on early observational studies of Dale (1956), Wyrtki (1961), and Xu et al. (1982). They have pointed out that surface circulation in the region is greatly controlled by the monsoons. Generally, it is very hard to predict the exact monsoon timing, duration and severity of each season. According Malaysian Meteorological Department (MMD), the north-east monsoon (NE) usually dominates the Malaysian region in early November and ends in March. Meanwhile, the south-west monsoon (SW) usually established in the later half of May or early June and ends in September. Earlier studies by Wyrtki (1961) and Xu et al. (1982) have produced surface current chart based on the observation data. However, the sampling stations were too sparse to demonstrate in detail the surface circulation in the northwest coast of Borneo Island. Therefore, the main objective of this paper is to illustrate the surface circulation in the northwest coast of Borneo Island in detail using space based technology; satellite altimetry.

2 Data and Method

2.1 Altimeter Data

Nineteen years (1993–2011) of sea level anomaly (SLA) data from six satellite altimetry mission are used for this study. The altimeter data from six satellite missions: TOPEX, Jason-1&2, ERS-1&2 and ENVISAT are extracted and processed from January 1993 until June 2011 using Radar Altimeter Database System (RADS). The sea surface height observation from altimetry data have been corrected for orbital altitude, altimeter range corrected for instrument, sea state bias, ionospheric delay, dry and wet tropospheric corrections, solid earth and ocean

tides, ocean tide loading, pole tide, electromagnetic bias and inverse barometer correction.

Homogeneous and cross-calibrated sea surface height (SSH) data sets are required to merge multi-satellite altimeter missions. Thus, crossover adjustment has been performed for the integrated data processing for multi-satellite missions. In this study, only crossovers between ERS-class (ERS and ENVISAT) and TOPEX-class satellites (TOPEX, POSEIDON and JASON) has been considered and not those between themselves. Besides that, the area used for the crossover minimization is defined much larger than the study area to have sufficient crossover. ERS-class and TOPEX-class data are merged and gridded into $0.25 \times 0.25°$ latitude/longitude bins using Inverse Distance Weighting (IDW) Interpolation method. The gridding involved both temporal and spatial weighing. Then, the SLA data are smoothed using Gaussian filtering to filter out noise in the data. The summary of environmental corrections applied in altimeter data processing is shown in the Table 1.

2.2 Mean Dynamic Topography

The SLA derived from the RADS are combined with 1992–2002 Mean Dynamic Ocean Topography (Maximenko et al. 2009) to obtain absolute dynamic topography. This Mean Dynamic Ocean Topography model has been developed using joint data of satellite altimetry, near-surface drifters, National Centre for Environmental Prediction (NCEP) wind and Gravity Recovery and Climate Experiment (GRACE). More information about the MDT used in this study can be found at http://apdrc.soest.hawaii.edu/projects/DOT/.

2.3 Argos-Tracked Ocean Surface Drifters

Observational data of Argos-tracked ocean surface drifters are widely used to reveal basic features of surface current pattern in the surface and subsurface layers (Yang et al. 2002). The current measurement error by drifter is ~ 5 cm/s, and the locating error is ~ 1 km (Su et al. 2002). Thus, to evaluate the absolute geostrophic current pattern obtained in this study, it is compared with the tracks of a satellite-tracked drifting buoy ID 49696. The drifter data is provided by the Marine Environmental Data Services (MEDS) of Canada (http://www.meds-sdmm.dfo-mpo.gc.ca/isdm-gdsi/drib-bder/index-eng.htm).

Table 1 Summary of environmental correction

Correction/model	Editing (m)		Description
	Min	Max	
Orbit/gravity field			All satellites: EIGEN GL04C
			ERS: DGM-04/D-PAF
Dry troposphere	−2.4	−2.1	All satellites: Atmospheric pressure grids
Wet troposphere	−0.6	0.0	All satellites: Radiometer measurement
Ionosphere	−0.4	0.04	All satellites: Smoothed dual-freq,
			ERS/POSEIDON: NIC08
Dynamic atmosphere	−1.0	1.0	All satellites: MOG2D
Ocean tide	−5.0	5.0	All satellites: GOT4.7
Load tide	−0.5	0.5	All satellites: GOT4.7
Solid earth tide	−1.0	1.0	Appplied (Elastic response to tidal potential)
Pole tide	−0.1	0.1	Aplied (Tide produced by Polar Wobble)
Sea state bias	−1.0	1.0	All satellites: CLS non parametric
			ERS/POSEIDON: BM3/BM4 parametric
Reference	−1.0	1.0	DNS08 mean sea surface
Engineering flag			Applied
Applied reference frame biases (cm)			JASON-1:−4.8, ERS-1: +3.4, ERS-2: +7.3, ENVISAT: +5.2, JASON-2: +15.9, POSEIDON: −1.5, TOPEX: Reference frame

3 Estimation of Geostrophic Current

Satellite altimetry is one of the promising techniques to understand the ocean surface currents. The geostrophic currents are proportional to the slope of the topography, a quantity that can be measured by satellite altimeters if the geoid is known. Thus, after obtaining the gridded SLA fields as explained in Sect. 2.1 and assuming geostrophic balance, the geostrophic current is computed from the absolute dynamic topography using the following equation (Benny et al. 2008; Hwang and Chen 2000; Wahr et al. 2002;

$$\zeta = \text{SLA} + \text{MDT}$$

$$u = -\frac{g}{f}\frac{\partial \zeta}{\partial y} \quad v = \frac{g}{f}\frac{\partial \zeta}{\partial x}$$

$$f = 2\Omega \sin(\varphi)$$

where ζ is the absolute dynamic topography, u and v are the eastward and northward velocity components of sea surface geostrophic current, g is the local acceleration due to gravity, f is the Coriolis parameter with Ω being the earth rotational rate (7.292115×10^{-5}), φ is the latitude, and x and y are the local rectangular coordinates. Since the geostrophic balance is not valid near the equator where Coriolis force is almost zero, the surface geostrophic current is not estimated between 2°N and equator.
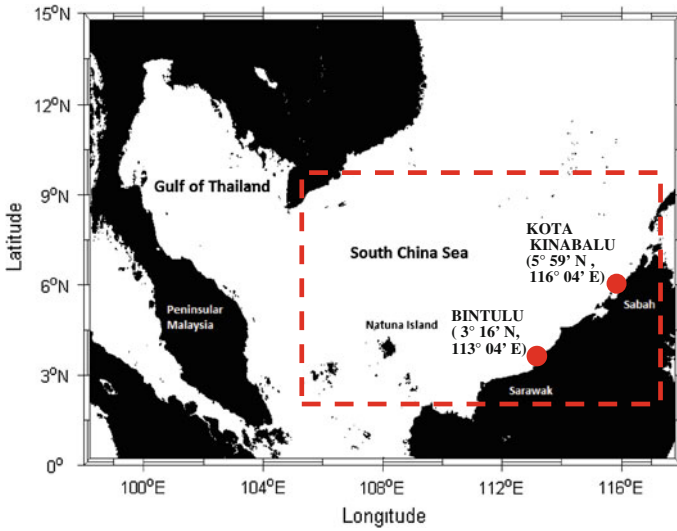
Fig. 1 Map of the study region and location of tide gauge stations (*red dots*)

4 Result

4.1 Comparison of SLA and Tide Gauge Data

In order to validate the SLA derived in this study, the monthly average SLA obtained from altimetry data through RADS are compared with tidal data from two tide gauge (TG) stations at the northwest coast of Borneo Island; Bintulu and Kota Kinabalu (Fig. 1) provided by Jabatan Ukur & Pemetaan Malaysia (JUPEM). For comparison, the monthly averaged SLA is interpolated onto the position of the TG stations using Inverse Distance Weighting (IDW) method. Figure 2 shows the plot of monthly sea level variation from altimeter and tide gauge station. Obviously, the tide gauge data are closely consistent with altimetry data that indicate good agreement between the in situ tide gauge and remotely observed altimetry data.

4.2 Comparison of Surface Current with Satellite-Tracked Drifting Buoy

The surface current derived from altimetry data compared with the track of satellite-tracked drifting buoy ID 49696 which is provided by the Marine Environmental Data Services (MEDS), Canada (http://www.meds-sdmm.dfo-mpo.gc.ca/isdm-gdsi/drib-bder/index-eng.htm). For comparison, the absolute geostrophic current are averaged in every 7 days corresponding to the period of drifter
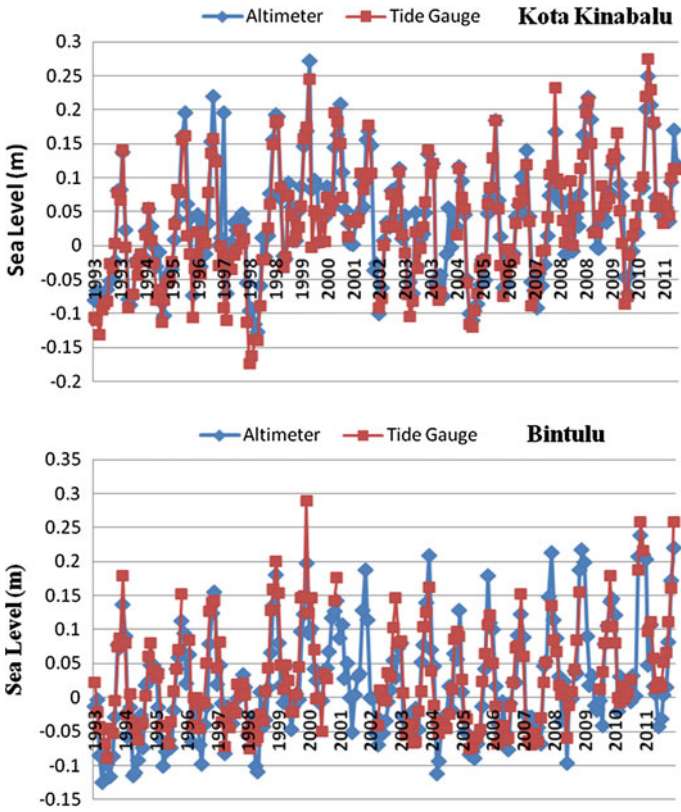
Fig. 2 Monthly sea level variation at **a** Kota Kinabalu **b** Bintulu from altimeter and tide gauge data

observation and mapped together with the track of the drifter. Figure 3 shows the complete track of drifter (red line) from 1st December 2005 to 2nd January 2006. Whereas, Fig. 4a–e shows the track of drifter 49696 for every seven days overlaid on the map of mean geostrophic current during the same period. Overall, the vortex rotation of drifter 49696 from the tracks is roughly consistent with the mean absolute geostrophic current pattern derived in this study. During the first and second week, the drifter 49696 which was released at 1.68°N 106.327°E on 30 November moved north eastward before it turned northward during the third week. Thus, the trail of the drifter is agreeing well with the pattern of mean geostrophic current. Interestingly, the drifter can be seen moving anti-clockwise in the fourth and fifth week, indicating the existence of cyclonic circulation. Surprisingly, the existence of vortex rotation illustrated by the track of drifter is well consistent with the cyclonic circulation revealed by the mean geostrophic current centred at (6.5°N 110°E). Based on the result, the surface flow fields derived from the altimetry data in this study are reliable and can be used to study mesoscale phenomena occurring in the surface layer.
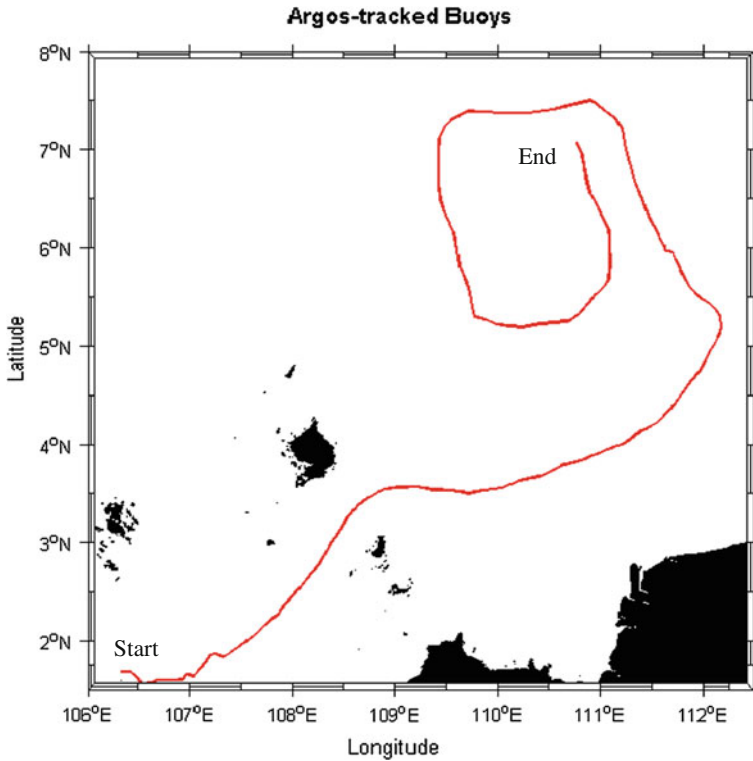
Fig. 3 Track of drifter 49596 (*red line*) from 1st December 2005 to 2nd January 2006

4.3 Analysis of Seasonal Surface Circulation

In order to understand the seasonal changes in surface circulation, geostrophic currents are computed from the long term averaged SLA (1993–2011) and plotted based on the monsoon season. The analysis is focused at four specific months April, August, October, and December. April and October represent the monsoon transition periods, while August and December represent the NE and SW monsoon, respectively. April is the transition period from the NE to SW monsoon system for the study region. General surface circulation in the central region of SSCS during April is cyclonic (Fig. 5a) and is consistent with Wyrtki (1961). Originating from Vietnam coastal area, the surface current flowing southward and part of the current turns eastward at around 3–6°N, reaches Natuna Island and west of Borneo Island as shown in Fig. 5a. Meanwhile, the northward flowing surface current from the Sarawak Coast branches into two at around 5°N. One branch flows northward and then turns eastward. The other branch turns north eastward and flows along the northwest coast of Boneo Island. A cyclonic eddy has found at around 6°N, 113°E and the prevalence of eddies in the region is also reported by
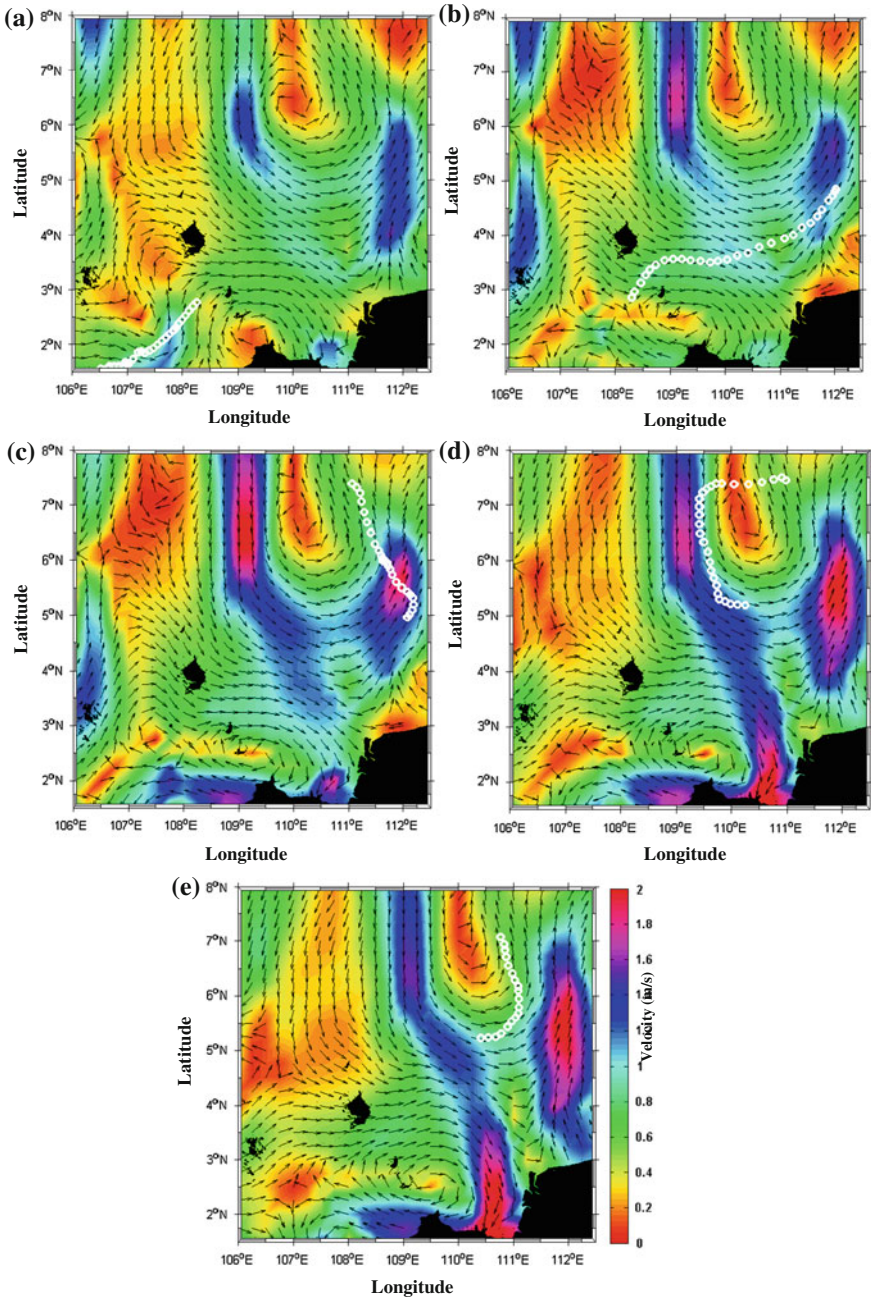
Fig. 4 The average geostrophic current from 1st December 2005 until 2 January 2006 for every seven days (**a–e**) with overlay of surface drifter trajectory (*white circles*). The *black arrow* and shaded colours represent the current direction and speed respectively
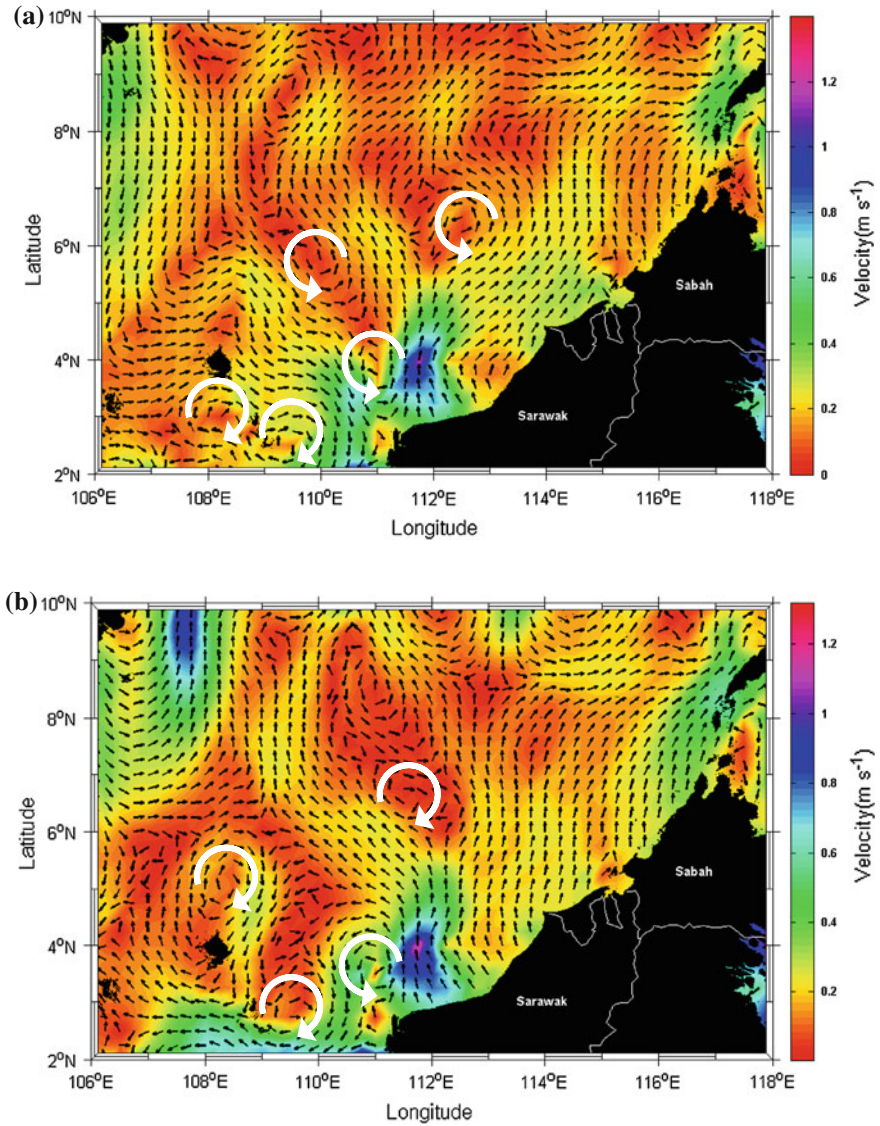
Fig. 5 Monthly average surface circulation from altimetry data (1993–2011) during (**a**) April and (**b**) August

Snidvongs (1999). Two anti-cyclonic eddies have formed in the south and southeast of Natuna Island centred at (3°N, 108°E) and (2.5°N, 109°E), respectively. Meanwhile, two cyclonic eddies are observed near the Sarawak coastal area and northeast of Natuna Island centred at (3°N, 111°E) and (6°N, 110°E), respectively.
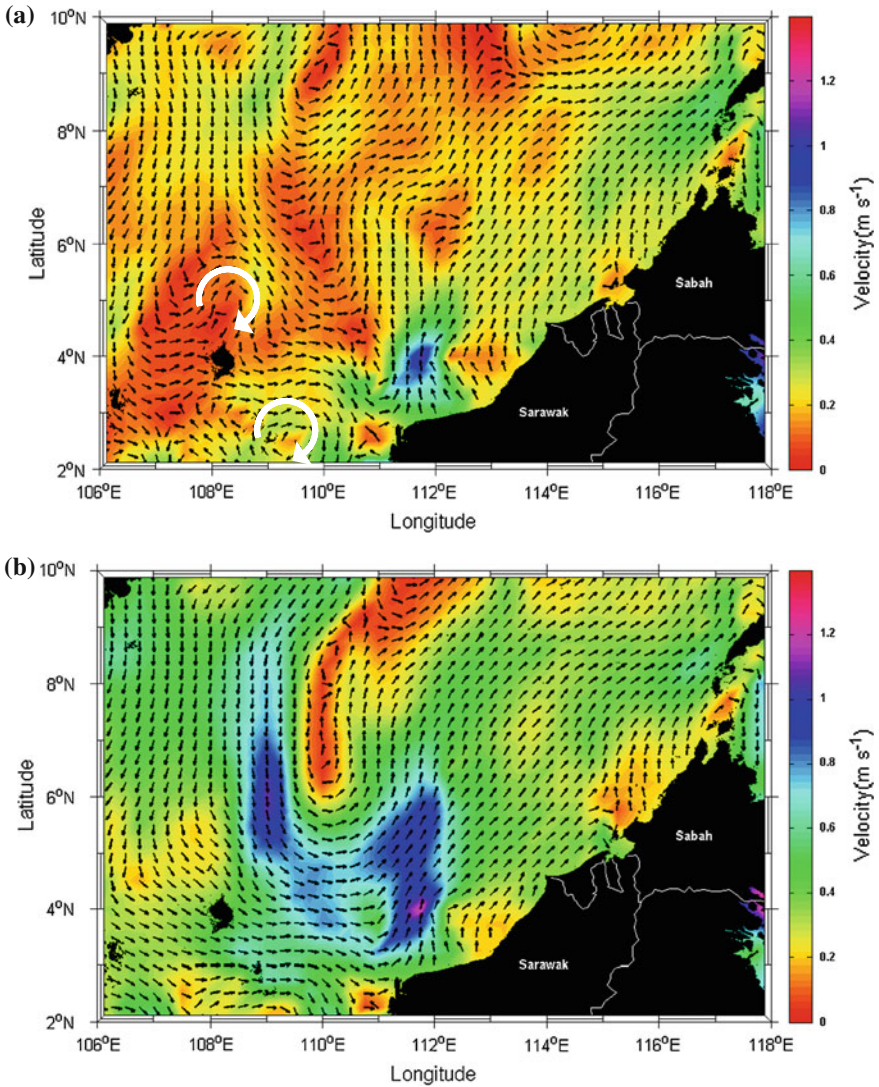
Fig. 6 Monthly average surface circulation from altimetry data (1993–2011) during (**a**) October and (**b**) December

In August, the general surface circulation is more complex compared to April especially in the offshore region (Fig. 5b). The surface current in the northwest coast of Borneo Island is flowing northward from the coast. An anti-cyclonic eddy has formed at around 6°N, 113°E. The anti-cyclonic eddy observed in the southeast of Natuna Island and near the Sarawak coastal area during April still found in August. Besides, a mesoscale anti-cyclonic eddy which is known as

Natuna eddy (Akhir 2012; Chu et al. 1998) is also observed north of Natuna Island centred at 5°N 108°E. The general surface circulation in October (Fig. 6a) is relatively weak compared to the first monsoon transition period (April). During this period, major part of the southward surface current is flowing from the Vietnam Coast towards Borneo Island and is also embedded with eddies and meanders. North eastward flow prevails along the coast of Borneo. The anti-cyclonic eddy observed in the north and southeast of Natuna Island which is formed during SW monsoon (August) is still visible. In December, the surface circulation has been strengthened (Fig. 6b). The southward flowing current from Vietnam coastal region turns direction to northwest along the Borneo coastal area. All eddies which observed during October totally disappeared during this season.

5 Conclusion

The present study derives the surface circulation off northwest Borneo Island using the satellite altimetry data. The SLA estimated from altimeter is consistent with the tide gauge measurements at Kota Kinabalu and Bintulu. The geostrophic current pattern derived by combining the SLA and 1992–2002 Mean Dynamic Ocean Topography well agree with the drifting buoy flow pattern. The general pattern of surface circulation in the central region of SSCS is cyclonic in April, October and December. Along the northwest coast of Borneo Island, the surface current is toward north eastward during April. While in August, the surface circulation is rather complex and the surface flow is northward near the Borneo Island. In October, the surface circulation is relatively weak in the region. By December, the circulation has again strengthened and strong southward surface current from the Vietnam Coast is clearly visible. The current is north eastward along the coast of Borneo Island during December.

Number of eddies and meandering patterns are found in seasonal surface circulation of the study region. A cyclonic eddy at around 61°N, 113°E is clearly identified. This eddy is weak in August and not visible during October and December. An anti-cyclonic eddy is found south of Natuna Island in April but diffused by August. Furthermore, a cyclonic and anti-cyclonic eddy found off the Sarawak and northeast of Natuna Island respectively during April and which are present in August and October but dispersed by December. A mesoscale anti-cyclonic eddy is found in the north of Natuna Island during August which sustains up to October.

References

Akhir MF (2011) Seasonal variation of South China Sea physical characteristics off the east coast of Peninsular Malaysia from 2002–2010 datasets. Int J Environ Sci 2(2):569–575

Akhir MF (2012) Surface circulation and temperature distribution of Southern South China Sea from global ocean model (OCCAM). Sains Malays 41(6):701–714

Benny NP, Ambe D, Imawaki S (2008) Eulerian mean sea surface velocity of the South Indian Ocean derived by combining satellite altimeter and drifter data. Report of Research Institute for Applied Mechanics, Kyushu University. No. 135(37–44)

Chu PC, Chen Y, Lu S (1998) Wind-driven South China Sea deep basin warm core/cool-core eddies. J Oceanogr 54:347–360

Dale WL (1956) Wind and drift currents in the South China Sea. Malays J Trop Geogr 8:1–31

Hwang C, Chen S (2000) Circulation and Eddies over the South China Sea derived from TOPEX/Poseidon altimetry. J Geophys Res 105(C10):23943–23965

Maximenko N, Niiler P, Rio M-H, Melnichenko O, Centurioni L, Chambers D, Zlonicki V, Galperin B (2009) Mean dynamic topography of the ocean derived from satellite and drifting buoy data using three different techniques. J Atmos Ocean Technol 26(9):1910–1919

Saadon MN, Marghany MM (1996) Surface circulation off Kuala Terengganu in the transitional period between the Northeast and Southwest Monsoons. Pertanika J Sci Technol 4(1):141–148

Snidvongs A (1999) Geostrophic current, divergence and convergence in the South China Sea, area II: Sabah, Sarawak and Brunei Darussalam. Proceedings of the second technical seminar o marine fishery resources survey in the South China Sea, area II: Sarawak, Sabah and Brunei Darussalam Water, 14–15 Dec 1998, Kuala Lumpur

Su JZ, Lu J, Hou YJ, Fang GH, Wei ZX, Yin BS (2002) Analysis of satellite- tracked drifting buoys in the South China Sea. Oceanol Limnol Sinica 33(2):121–127

Taira K, Saadon MN, Kitagawa S, Yanagi T (1996) Observation of temperature and velocity in the coastal water off Kuala Terengganu, Malaysia. J Oceanogr 52(2):251–257

Wyrtki, K. (1961). Scientific result of marine investigation of the South China Sea and Gulf of Thailand NAGA Report 2,195

Wahr JM, Jayne SR, Bryan FO (2002) A method of inferring changes in deep ocean currents from satellite measurements of time-variable gravity. J Geophys Res 107(C12):3218

Xu XZ, Qui Z, Chen HC (1982) The general description of the horizontal circulation in the South China Sea. Proceedings of the 1980 symposiums on Hydrometeorology of the Chinese Society of Oceanology and Limnology, Beijing, Science Press, pp 137–145

Yang H, Liu Q, Liu Z, Wang D, Liu X (2002) A general circulation model study of the dynamics of the upper ocean circulation of the South China Sea. J Geophys Res 107(C7):3085

Improvement in Accuracy Through Self-Calibration for Panoramic Scanner

Mohd Azwan Abbas, Halim Setan, Zulkepli Majid, Albert K. Chong, Derek D. Lichti and Khairulnizam M. Idris

Abstract Currently, three-dimensional (3D) information has become a necessity for many purposes especially for documentation, management and analysis. With the rapid and dense 3D data (point clouds) and considerably at high accuracy has made terrestrial laser scanner (TLS) widely used for these purposes. However, similar to other 3D instruments, TLS measurements also cannot escape from the occurrence of various systematic errors. Through self-calibration, the significant systematic errors consisted in TLS can be modelled and subsequently removed to improve the accuracy of the data. To prove that statement, this study has performed self-calibration for panoramic scanner (Faro Photon 120) at a laboratory with dimensions of 15.5 m × 9 m × 3 m. By employing optimal network configuration, all 138 well-distributed planar targets were measured from seven scanner positions to derive four calibration parameters. Statistical analysis (e.g. t test) has shown that only two parameters, the constant rangefinder offset error (9.3 mm) and the vertical circle index error (9.4″) were significant for the calibrated scanner. To ensure that self-calibration can improve the accuracy of TLS data, photogrammetric technique was utilised to establish 15 3D test points at the calibration field. These test points were used to graphically and statistically demonstrate the improvement in accuracy between raw data and calibrated data of Faro Photon 120 scanner.

Keywords Terrestrial laser scanner · Accuracy · Systematic errors · Self-calibration

M. A. Abbas (✉)
Universiti Teknologi MARA, Shah Alam, Malaysia
e-mail: mohdazwanabbas@yahoo.com

H. Setan · Z. Majid · K. M. Idris
Universiti Teknologi Malaysia, Johor Bahru, Malaysia

A. K. Chong
University of Southern Queensland, Toowoomba, Australia

D. D. Lichti
University of Calgary, Calgary, Canada

1 Introduction

According to Abdul and Halim (2001), there is a difference between precision and accuracy. Precision is defined as the closeness of the agreement between independent test results obtained compared to the mean value. Accuracy is defined as the closeness of the agreement between the result of a measurement and its true value. However, both precision and accuracy have an important role for the TLS measurements. As provided by Schulz (2007) in his study regarding typical applications for TLS with respect to the scanner precision (Fig. 1), the user needs to understand which scanner is the best-suited for a specific application according to scanner precision. The precision can be obtained by referring to manufacturer specification or by independent testing.

On the other hand Luhmann et al. (2006) have discussed the selection of measurement techniques which can determine the range of accuracy that can be achieved as illustrated in Fig. 2. In geomatic jargon, accuracy has become an important issue especially for applications that require high accuracy (e.g. millimetre level) information such as industrial measurement, deformation survey and reverse engineering.

Figure 2 shows several measurement techniques that are able to provide accuracy less than millimetre (e.g. interferometry and industrial metrology). Though the achievable accuracies are adequate the price of the instruments used are quite expensive. As mentioned in González-Jorge et al. (2012), the used of industrial metrology (e.g. coordinate measuring machines) is not suitable for economical investments, which led them to evaluate the others measurement techniques (e.g. photogrammetry and terrestrial laser scanning). Results from their study have indicated that both evaluated techniques are significant for industrial measurement.

With the speed and accuracy of TLS, this instrument can be widely used for many purposes including accurate 3D applications. For instance, TLS has been utilized by Bokhabrine and Seulin (2012) for 3D characterization of hot metallic shells during industrial forging. In the application, accurate measurements of dimensional, volume and shape are crucial for controlling and monitoring the forging process. For another example Timothy et al. (2010) implemented TLS measurement for tunnel deformation survey. Results obtained from their study have shown that accuracies achieved are within tolerance even in difficult field conditions for a railway tunnel. Delčev et al. (2012) have employed geodetic method for fuel tank inspection, which required measurement uncertainty of 1 mm. The capability of TLS to provide dense 3D data has made it applicable in this high accuracy application to minimizing the interpolation errors between points surveyed by others high precision geodetic methods.

Similar to other 3D spatial data capture instruments, the results obtained from TLS can be impaired by errors from different sources. These systematic errors
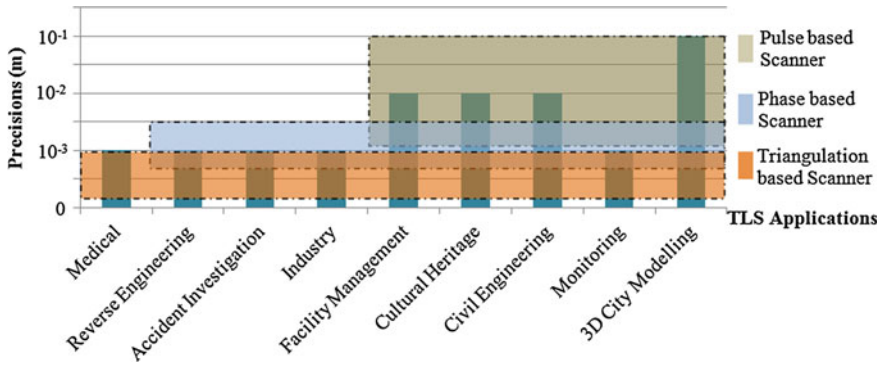
Fig. 1 Applications of scanner with respect to the measurement precision (Schulz 2007)
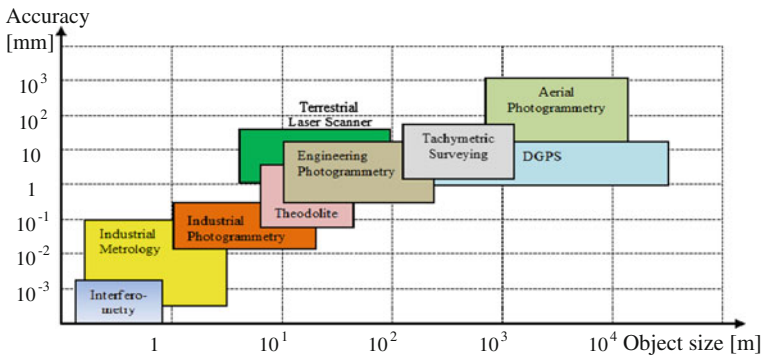

Fig. 2 Relationship between object size and accuracy for different measurement technique (Luhmann et al. 2006)

have to be investigated and modelled, and subsequently applied to the raw data, in order to improve the accuracy. There are two approaches available to investigate these errors, either separately (component calibration) or simultaneously (system calibration). Due to the difficulty to afford the requirements of special laboratories and tools to perform component calibration (Fig. 3), only academicians and manufacturers implement it. It is applicable to investigate systematic errors but most of the component calibration is used to identify the best-suited applications of the calibrated TLS and also to compare the performance of TLS from different manufacturers. In contrast, system calibration requires a room with appropriate targets to determine all significant systematic errors (see Fig. 11 under Sect. 5.2). As a result, system calibration can be considered as a more appropriate technique for investigation of systematic errors.
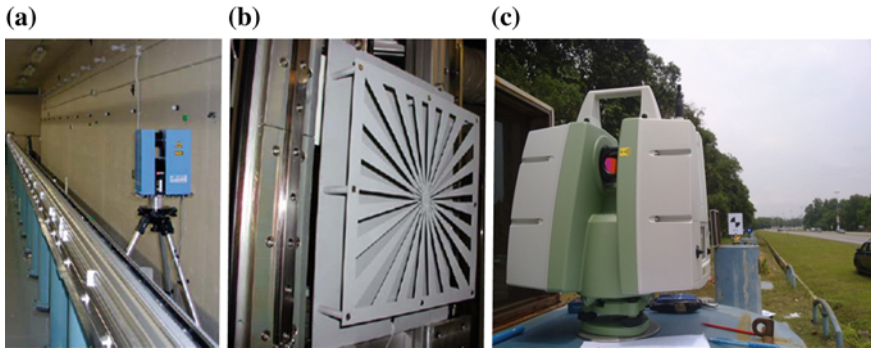
Fig. 3 Facilities and devices required for component calibration, calibration trackline (**a**), targets with slots (**b**) and calibration baseline (**c**) (Brian et al. 2004; Abbas et al. 2013)

In this study, investigation of systematic errors was carried out by using point-based self-calibration for the panoramic scanner (Faro Photon 120). Fifteen test points were established using photogrammetry technique at the calibration field and these points were used to evaluate the significant of self-calibration in improving the accuracy. These test points then were used as the benchmark to investigate the discrepancy obtained from TLS raw data and calibrated data, which afterward indicates the reliability of calibration procedure for improving the accuracy of TLS data.

2 Terrestrial Laser Scanner

Terrestrial laser scanner is a non-contact sensor, optics-based technology that collects three-dimensional (3D) data of object surface automatically and in a systematic pattern with a high data collecting rate. Compared to the traditional approaches for the 3D measurement, TLS can be considered as combination of photogrammetric and reflectorless total station. The scanning process within field of view is similar to taking an image and data provided are similar to total station (points in 3D coordinate system). Even though most of the commercial software gives 3D data in Cartesian coordinates system (X, Y, Z). TLS actually measures using spherical coordinates system (r, φ, θ) and has intensity value as an attribute (Fig. 4). Therefore, the raw observables in TLS are (1) range (r); (2) horizontal direction (φ); and (3) vertical angle (θ).

For further processing, especially for calibration purposes, 3D data in spherical coordinate is more useful. Thus, conversion between Cartesian (x, y, z) and spherical (range, horizontal direction and vertical angle) coordinates system can be expressed as follows:

Fig. 4 Data measured using terrestial laser scanner
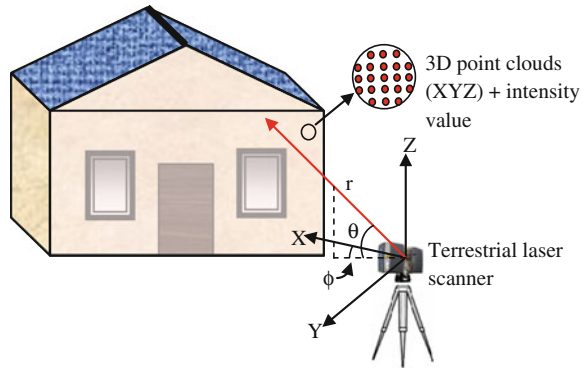
- Cartesian to spherical coordinates system.

$$\text{Range, } r = \sqrt{x^2 + y^2 + z^2}$$
$$\text{Horizontal direction, } \varphi = \tan^{-1}\left(\frac{x}{y}\right)$$
$$\text{Vertical angle, } \theta = \tan^{-1}\left(z\Big/\sqrt{x^2 + y^2}\right)$$

(1)

- Spherical to Cartesian coordinates system.

$$x = r \times \sin(\varphi) \times \cos(\theta)$$
$$y = r \times \cos(\varphi) \times \cos(\theta)$$
$$z = r \times \sin(\theta)$$

(2)

There are three types of beam deflection units used in TLS (1) Oscillating mirrors (Fig. 5a); (2) Rotating polygonal mirrors (Fig. 5b); and (3) Monogon (flat) rotating mirrors (Fig. 5c) which represents the field of view (FOV) of the TLS. According to Reshetyuk (2009), there are three classifications of TLS based on FOV (1) camera scanner (Fig. 5d); (2) hybrid scanner (Fig. 5e); and (3) panoramic scanner (Fig. 5c).

Camera scanner uses oscillating mirrors to deflect the laser beam about the horizontal and vertical axes of the scanner (Fig. 5a). The scanning head remains stationary during scanning process. It carries out the distance and angle measurement over a much more limited angular range and within a specific FOV (Fig. 5d). Hybrid scanner has the horizontal FOV of 360° and limited vertical FOV (Fig. 5e). This scanner employs the oscillating or rotating polygonal mirrors (Fig. 5b) to deflect the laser beam in vertical and horizontal axes. With aid of servomotor, hybrid scanner is capable of rotating by a small step around the vertical axis (horizontally). It works by scanning the vertical profile using the mirror, and this step is repeated around the vertical axis until the scanner rotates for 360°. Monogon mirror (Fig. 5c) used in panoramic scanner has improved the
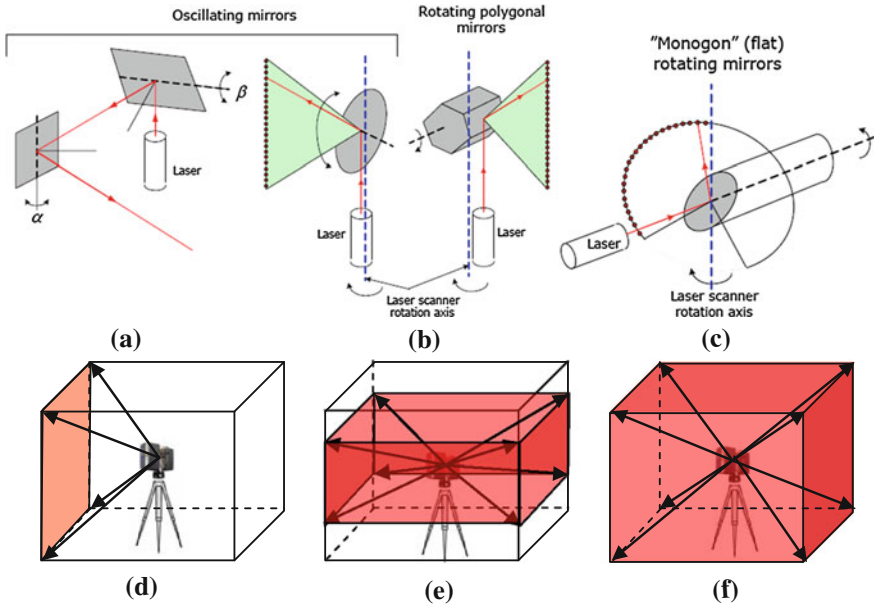
Fig. 5 *Top* Types of laser beam deflection units used in TLS. *Bottom* classification of TLS based on field of view (Reshetyuk 2009)

vertical FOV (Fig. 5f) compared to hybrid scanner. Using the same mechanism as hybrid scanner which is based on servomotor, this scanner is also capable of providing 360° horizontal FOV. These advantages (360° horizontal FOV and nearly the same for vertical FOV) has made panoramic scanner very useful for indoors scanning.

3 Geometric Model for Self-Calibration

Due to the limited knowledge regarding the inner functioning of modern terrestrial laser scanners, most researchers have made assumptions about a suitable error model for TLS based on errors involve in reflectorless total stations (Lichti 2007). Since the data measured by TLS are range, horizontal and vertical angle, the equations for each measurement are augmented with systematic error correction model as follows (Reshetyuk 2009):

$$\text{Range, } r = \sqrt{x^2 + y^2 + z^2} + \Delta r \tag{3}$$

$$\text{Horizontal direction, } \varphi = \tan^{-1}\left(\frac{x}{y}\right) + \Delta\varphi \tag{4}$$
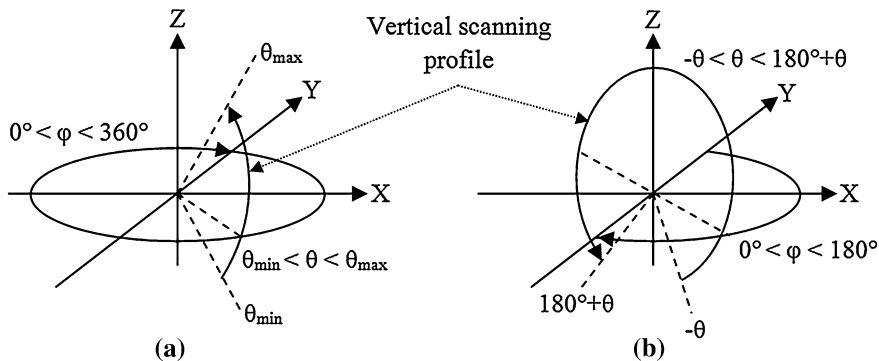
Fig. 6 Angular observation ranges for hybrid scanner (**a**) and panoramic scanner (**b**)

$$\text{Vertical angle, } \theta = \tan^{-1}\left(z \Big/ \sqrt{x^2 + y^2}\right) + \Delta\theta \tag{5}$$

where, Δr, $\Delta\varphi$ and $\Delta\theta$ are systematic error model for range, horizontal direction and vertical angle, respectively.

Since this study involved panoramic scanners (Faro Photon 120), the angular observations computed using Eqs. (4) and (5) must be modified. This is due to the scanning procedure applied by panoramic scanner, which rotates only through 180° to provide 360° information for horizontal and vertical angles as depicted in Fig. 6.

Based on Lichti (2010), the modified mathematical model for a panoramic scanner can be presented as follows:

$$\varphi = \tan^{-1}\left(\frac{x}{y}\right) - 180° \tag{6}$$

$$\theta = 180° - \tan^{-1}\left(z \Big/ \sqrt{x^2 + y^2}\right) \tag{7}$$

The modified models above Eqs. (6) and (7) are only applicable when the horizontal angle is more than 180° as shown in Fig. 6. Otherwise, Eqs. (4) and (5) can be used, which means that panoramic scanner has two equations for both angular observations.

In order to perform self-calibration bundle adjustment, the laser scanner observations have to be expressed as functions of the position and orientation of the laser scanner in a global coordinate system (Schneider 2009). Based on rigid-body transformation, for the jth target scanned from the ith scanner station, the equation is as follows:

$$
\begin{aligned}
x &= R_{11}(X_j - X_{Si}) + R_{21}(Y_j - Y_{Si}) + R_{31}(Z_j - Z_{Si}) \\
y &= R_{12}(X_j - X_{Si}) + R_{22}(Y_j - Y_{Si}) + R_{32}(Z_j - Z_{Si}) \\
z &= R_{13}(X_j - X_{Si}) + R_{23}(Y_j - Y_{Si}) + R_{33}(Z_j - Z_{Si})
\end{aligned}
\tag{8}
$$

where,

$[x \quad y \quad z]$ = Coordinates of the target in the scanner coordinate system
$_3R_3$ = Components of rotation matrix between the two coordinate systems for the ith scanner station
$[X_j \quad Y_j \quad Z_j]$ = Coordinates of the jth target in the global coordinate system
$[X_{Si} \quad Y_{Si} \quad Z_{Si}]$ = Coordinates of the ith scanner station in the global coordinate system.

4 Systematic Error Models

According to Lichti (2010), error models which are consisted in TLSs can be classified into two groups, either physical or empirical parameters. The first group can be considered as basic calibration parameters which have been derived from the total station systematic error models. This group includes the constant, cyclic, collimation, vertical circle index errors and others as described by Lichti and Licht (2006). The other group of error models may appear due to the geometric defects in construction or electrical cross-talk and may be system dependent. These are inferred from systematic trends visible in the residuals of a highly-redundant and geometrically strong, minimally-constrained least-square adjustment.

However, this study focuses on the most significant systematic error models which are categorised under physical parameters as follows:

- Systematic error model for range.

$$\Delta r = a_0 \tag{9}$$

- Systematic error model for horizontal direction.

$$\Delta \varphi = b_0 \sec \theta + b_1 \tan \theta \tag{10}$$

- Systematic error model for vertical angle.

$$\Delta \theta = c_0 \tag{11}$$

where,

a_0 = Constant rangefinder offset error.
b_0 = Collimation axis error.
b_1 = Trunnion axis error.
c_0 = Vertical circle index error.

Lichti et al. (2011) have mentioned that systematic error models for panoramic scanner can be recognised based on the trends in the residuals from a bundle
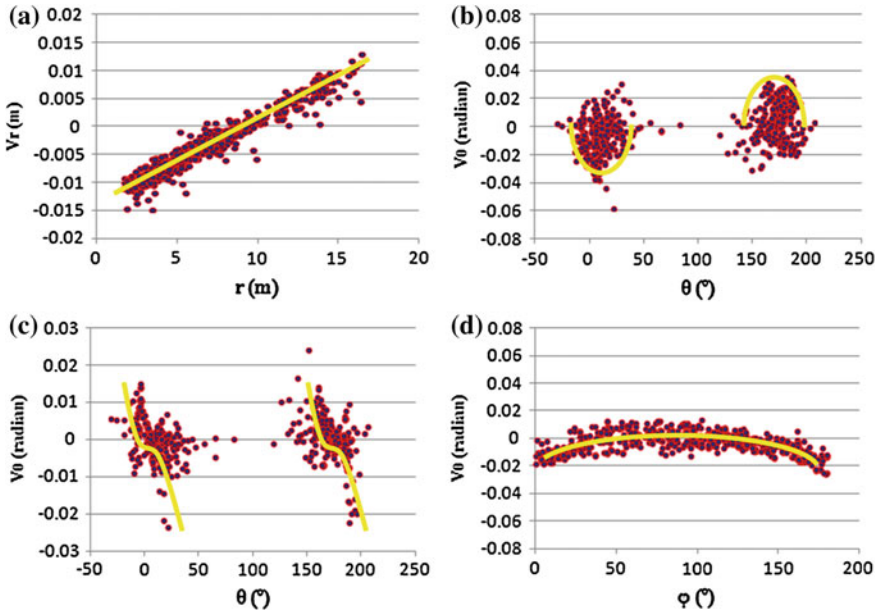
Fig. 7 Simulation residuals for panoramic scanner, constant rangefinder offset error (**a**), collimation axis error (**b**), trunnion axis error (**c**) and *vertical circle* index errors (**d**)

adjustment that excludes the relevant calibration parameters. Most of the cases, the trend of un-modelled systematic errors closely resembles the analytical form of the corresponding correction models. As depicted in Fig. 7, all systematic error models are identified by plotting a graph of adjusted observations against residuals. The graph of adjusted range against its residuals indicates a constant rangefinder offset error (a_0) if the trend seems like an inclining line (Fig. 7a). When residuals of horizontal observations against adjusted vertical angles shows the trend like secant function, which means that the scanner has collimation axis error (Fig. 7b). Trunnion axis error can be identified by having a trend like tangent function as shown in Fig. 7c. For vertical circle index error, by plotting graph of adjusted vertical angles against its residuals, this systematic error model considers exist when the trend looks like the big curve as depicted in Fig. 7d.

Nonetheless, it is quite difficult to identify these systematic errors based on residual pattern graph especially when the magnitudes of the errors are very small. As a result, this study has also implemented statistical tests to determine the significant of the parameter to the scanner observations. Known as t-test, the analysis is carried out using formula (Gopal 1999):

$$t = \frac{X}{\sigma_X} \tag{12}$$

where,

X = Parameter to be evaluated.
σ_X = Estimated standard deviation of parameter.

The hypothesis of the test is:

H_0: The parameter is not significant to the scanner observation.
H_A: The parameter is significant to the scanner observation.

The null hypothesis (H_0) is rejected if the calculated t value (Eq. 12) is higher than the critical t value (predicted from the t-distribution table based on the value of degree of freedom) with selected level of significant (confidence level 95 % equal to 0.05 of significant level). With the rejection of H_0, the test parameters is statistically significant (accept H_A).

5 Methodology

5.1 Preparation of Test Points

As illustrated in Fig. 2, industrial or close range photogrammetry can provide sub-millimetre accuracy. Thus, this measurement technique was used to establish 15 test points (Fig. 8) which subsequently were used to investigate the capability of a self-calibration to improve the quality of TLS data.

In order to perform photogrammetric measurement, digital camera Sony DSC F828 with pixel count 1920×1080 (8 megapixels) and 0.0027 mm pixel size was employed to capture the images of test points. As a routine procedure, the camera should be calibrated before it can be used for 3D measurement purposes. Figure 9 shows the calibration procedure carried out for digital camera Sony DSC F828 and the processing of the calibration parameters was made by using Photomodeler V5.0 software. Several scale bars were positioned at the measurement field (Fig. 9) for the purpose to set a scale value as well as to evaluate the accuracy of the calculated 3D coordinates of test points.

Fourteen independent vectors were generated from these test points to ensure that it can be used to evaluate the accuracy of TLS raw data and calibrated data (Fig. 10). By computing the discrepancies of the benchmark (vectors obtained from photogrammetry) and the vectors yielded from TLS raw data and calibrated data, then the accuracies of both TLS data can be statistically calculated. Afterward, those values were used to evaluate the significant of self-calibration thus improving the accuracy of TLS data.
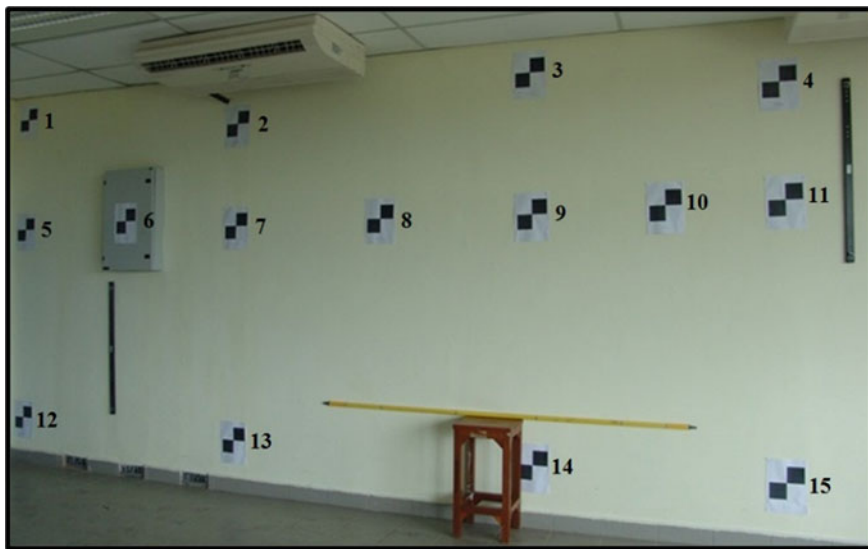
Fig. 8 Test points established at calibration field

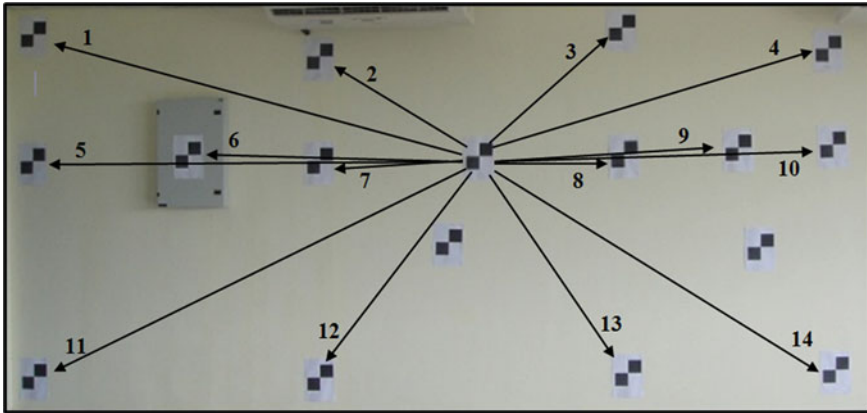**Fig. 9** Calibration of digital camera Sony DSC F828

Fig. 10 Fourteen independent vectors generated from test points

5.2 Self-Calibration of Panoramic Scanner (Faro Photon 120)

As shown in Fig. 11, a self-calibration has been performed over a dense 3D target field. There are 138 planar targets have been well-distributed on the four walls and the ceiling of the laboratory with dimensions 15.5 m (length) × 9 m (width) × 3 m (height).

Seven scan stations were established to capture the targets coordinates. As shown in Fig. 12, five scan stations were located at each corner and centre of the room. The other two were positioned close to the two corners and the scanner orientation were manually rotated 90° from scanner orientation at the same corner. In all cases the height of the scanner was midway between the floor and the ceiling.

In this experiment, the scan resolution was set to the 1/4 setting which is equivalent to the medium resolution. Higher resolution scans were not captured due to the longer time required to complete the scanning. Furthermore, medium resolution was sufficient for Faro scene V4.8 software to extract all targets except for those which have high incidence angle. After completing the scanning process, a bundle adjustment was performed with precision setting based on the accuracy of the scanner, which are 2 mm for distance and 30″ for both angles measurement.
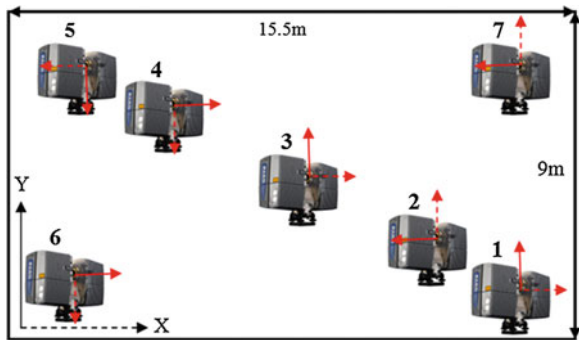
5.3 Evaluation of Calibrated Data

With the aid of residual graphs and statistical analysis, the significant calibration parameters can be determined. Having these significant parameters, that information then was applied to the raw data in order to remove the systematic errors which finally yield the calibrated data. By subtracting true value of vectors with

Fig. 11 Self-calibration for the Faro Photon 120 scanner

Fig. 12 Scanner locations during self-calibration

the vectors produced from both TLS raw and calibrated data, the accuracies can be calculated and statistically analysed. Results obtained were graphically and statistically presented to evaluate the significance of self-calibration for the TLS measurement.

6 Results and Analyses

Using a calibrated digital camera Sony DSC F828 and Photomodeler V5.0 software, 15 accurate test points were successfully captured. Results obtained have indicated that the average precision for all test points are below than 1 mm and root mean square (RMS) of residuals are less than 0.5 pixel. Size for each pixel is equal to 0.0027 mm, which means that maximum RMS residuals, is only 0.0014 mm. To finalise the accuracy achieved for all test points, comparison have

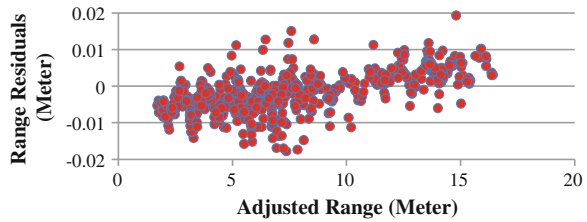**Fig. 13** Range residuals as a function of adjusted range for the adjustment without calibration parameters

Fig. 14 *Horizontal angle* residuals as a function of adjusted *vertical angles* for the adjustment without calibration parameters
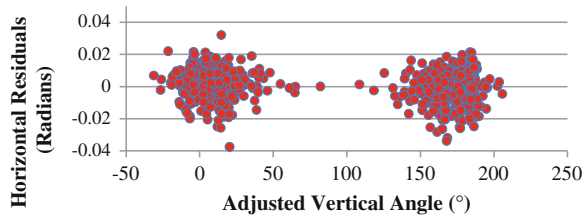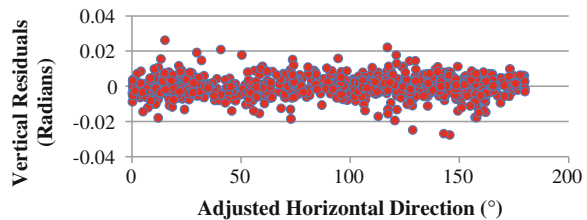

Fig. 15 *Vertical angle* residuals as a function of adjusted *horizontal angles* for the adjustment without calibration parameters

been made between true and measured values of scale bar. The scale bar analysis has indicated that test points produce via photogrammetry technique have 0.06 mm accuracy which is appropriate to be considered as true values in this study.

In contrast with the hybrid scanner, the residual patterns from a panoramic scanner bundle adjustment can be used to detect the systematic error trends. As a result, other than statistical analysis, residual patterns are also used in this analysis. After performing the bundle adjustment process without any calibration parameters, residual patterns were plotted as a function of the adjusted observations as shown in Figs. 13, 14 and 15.

Based on the sample of residual patterns shown in Fig. 7, all significant systematic errors have been investigated. There are no indications of systematic errors existed for horizontal direction and vertical angle measurements (Figs. 13 and 14, respectively). Nevertheless, a trend like incline line has depicted in the residual graph of range measurement, which indicates the existence of rangefinder offset error. According to the results obtained in Table 1, magnitude of errors for horizontal direction (e.g. b_0 and b_1) and vertical angle (e.g. c_0) are very small. This has become the main reason for no indications of errors can be identified in the previous plotted residual graphs (Figs. 13 and 14).

Table 1 Calibration parameters and their standard deviation

Calibration parameters	Values (mm/″)
$a_0 \pm \sigma_{a_0}$	9.3 ± 0.2
$b_0 \pm \sigma_{b_0}$	-1.1 ± 2.1
$b_1 \pm \sigma_{b_1}$	2.9 ± 8.0
$c_0 \pm \sigma_{c_0}$	9.4 ± 2.8

Table 2 RMS of residuals from the adjustments without and with calibration parameters

Observable	RMS (without)	RMS (with)
Range (mm)	5.6	4.0
Horizontal direction (″)	41.0	37.1
Vertical angle (″)	24.0	22.4

Table 3 Significant test for calibration parameters

	Calculated 't'	Significant test
Number of scanner stations		7
Degree of freedom		1925
Critical value for 't' (95 %)		1.645
Calibration parameters	*Calculated 't'*	*Significant test*
Constant rangefinder offset error (a_0)	46.5	Significant
Collimation axis error (b_0)	0.524	Not significant
Trunnion axis error (b_1)	0.363	Not significant
Vertical circle index error (c_0)	3.357	Significant

Further analysis has been carried out by running the bundle adjustment again with calibration parameters. Table 2 presents the RMS of residuals for each observable group for the cases without and with the self-calibration. The results obtained have indicated the improvement in precision up to 29 %.

In order to have a concrete solution regarding the significance of the estimated systematic error model, statistical tests were performed. All calibration parameters were tested to investigate their significant. Using 95 % confidence level, the results of the test are shown in Table 3.

Results in Table 3 shows that null hypothesis was rejected for parameter of constant rangefinder offset (a_0), and vertical circle index (c_0) errors. This indicates that those parameters are significant. For the collimation axis (b_0) and trunnion axis (b_1) errors, the null hypothesis has been accepted. In this study, only the significant errors were applied to the raw data to ensure the improvement in accuracy for the calibrated data.

By applying significant systematic errors to the raw data (test points), values of new 14 vectors were calculated from raw and calibrated data. These values then were subtracted from the true values (obtained from photogrammetry measurement technique). Presented graphically in Fig. 16, the results show an accuracy
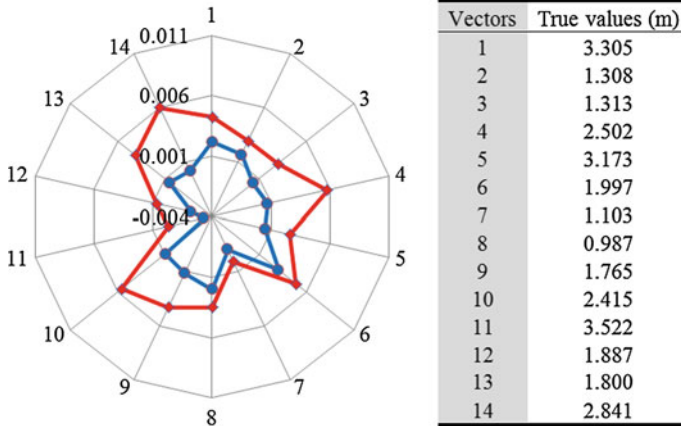
Vectors	True values (m)
1	3.305
2	1.308
3	1.313
4	2.502
5	3.173
6	1.997
7	1.103
8	0.987
9	1.765
10	2.415
11	3.522
12	1.887
13	1.800
14	2.841

Fig. 16 *Left* accuracies comparison for raw (*red*) and calibrated data (*blue*). *Right* true lengths for each vector provide by photogrammetry technique

improvement of the calibrated data of around 2 mm compared to raw data accuracy which is 4 mm. With 50 % improvement in accuracy, this study has mathematically proved the reliability of self-calibration to enhance the quality of TLS measurements.

7 Conclusions

This study has employed a dense 3D target field (138 well-distributed targets observed from seven scanner stations) to carried out a self-calibration of the panoramic scanner (Faro Photon 120). The adjustment results have been evaluated through residual graphs and statistical analysis procedures. Due to the magnitude of calculated calibration parameters are very small, the plotted residual graphs does not indicate any existence of errors except for constant rangefinder offset error. However, significant tests were performed and the results have shown that two (a_0 and c_0) of four calibration parameters are significant. To investigate the reliability of self-calibration, comparison has been made between RMS of residuals for adjustment with and without calibration parameters. The results have showed the ability of self-calibration with improvement in precision up to 29 %. For accuracy assessment purpose, 14 vectors (from 15 test points) were established using photogrammetry technique. These vectors (consider as benchmark) then were used to computed the discrepancies (or accuracies) of vectors obtained from TLS raw data and calibrated data. Based on the results, the improvement in accuracy from raw to calibrated data was graphically and statistically presented. With 50 % improvement in accuracy, self-calibration was mathematically proven as significant procedure to enhance the quality of TLS data.

References

Abbas MA, Halim S, Zulkepli M, Albert KC, Khairulnizam MI, Anuar A (2013) Calibration and accuracy assessment of leica ScanStation C10 terrestrial laser scanner. development in multidimensional spatial data models. Lecture Notes in geoinformation and cartography (LNG&C). Springer, Berlin, pp 33–47

Abdul WI, Halim S (2001) Pelarasan Ukur. Dewan Bahasa dan Pustaka, Kuala Lumpur

Bokhabrine Y, Seulin R (2012) 3D characterization of hot metallic shells during industrial forging. Mach Vis Appl 23:417–425

Brian F, Catherine LC, Robert R (2004) Investigation on laser scanners. IWAA2004, CERN, Geneva

Delčev S, Ogrizović V, Gučević J (2012) Geodetic method of the fuel tank form inspection. Measurement 45:2376–2381

González-Jorge H, Riveiro B, Arias P, Armesto J (2012) Photogrammetry and laser scanner technology applied to length measurements in car testing laboratories. Measurement 45:354–363

Gopal KK (1999) 100 statistical test. SAGE Publications Ltd, Thousand Oaks

Lichti DD (2007) Error modelling, calibration and analysis of an AM-CW terrestrial laser scanner system. ISPRS J Photogram Remote Sens 61(2007):307–324

Lichti DD (2010) A review of geometric models and self-calibration methods for terrestrial laser scanner. Bol. Ciênc. Geod. sec. Artigos, Curitiba (2010) 3–19

Lichti DD, Licht MG (2006) Experiences with terrestrial laser scanner modelling and accuracy assessment. IAPRS Vol XXXVI, Part 5, Dresden

Lichti DD, Chow J, Lahamy H (2011) Parameter de-correlation and model-identification in hybrid-style terrestrial laser scanner self-calibration. ISPRS J Photogram Remote Sens 66(2011):317–326

Luhmann T, Robson S, Kyle S, Harley I (2006) Close photogrammetry: principles, methods and applications. Whittles Publishing, Dunbeath Mains Cottages, Dunbeath, Scotland, UK, p 4

Reshetyuk Y (2009) Self-calibration and direct georeferencing in terrestrial laser scanning. Doctoral Thesis in Infrastructure, Royal Institute of Technology (KTH), Stockholm

Schneider D (2009) Calibration of riegl LMS-Z420i based on a multi-station adjustment and a geometric model with additional parameters. In: The international archives of the photogrammetry, remote sensing spatial information science, vol 38 (Part 3/W8), pp 177–182

Schulz T (2007) Calibration of terrestrial laser scanner for engineering geodesy. A dissertation submitted for the degree of Doctor of sciences. Technical University of Berlin, Berlin

Timothy N, Alain DW, Lander B, Bart DW, Leen C, Marijke DR, Cornelis S, Denis C, Hans DB (2010) High resolution terrestrial laser scanning for tunnel deformation measurements. FIG Congress 2010. Facing the Challenges-Building the Capacity, Sydney

Determination of Tidal Datum for Delineation of Littoral Zone for Marine Cadastre in Malaysia

Rasheila Rahibulsadri, Abdullah Hisam Omar, Ashraf Abdullah, Wan Muhammad Aizzat Wan Azhar, Hasan Jamil, Teng Chee Hua, Chan Keat Lim and Tan Ah Bah

Abstract The rapid development of coastal areas in Malaysia for economic generation activities and public interests has triggered the need for a new system of marine administration. Marine cadastre is the key in managing a complex marine administration that covers horizontal and vertical components. A tidal datum is a standard elevation defined by a certain phase of the tide. Tidal datum is also the basis for establishing privately owned land, state owned land, territorial sea, exclusive economic zone, and high seas boundaries. This chapter reviews some concepts and issues pertaining to the delineation of the tidal line for marine cadastre in Malaysia. This study analyzed the use of Lowest Astronomical Tide (LAT) as reference datum in marine cadastre. Localized hydrodynamic approach was used for generating the tidal model due to suitability and availability of global tidal model. Tide datasets acquired from Department of Survey and Mapping Malaysia (DSMM) has been processed using tidal analysis software for computing the LAT as the reference datum for marine cadastre. Output from the tidal data observed are tidal analysis can be made on sea levels, chart datum, types of tide

R. Rahibulsadri (✉) · A. H. Omar · W. M. A. W. Azhar
Department of Geoinformation, Faculty of Geoinformation and Real Estate, Universiti Teknologi Malaysia (UTM), 81310 Johor Bahru, Johor, Malaysia
e-mail: cikbelle@gmail.com

A. H. Omar
e-mail: abdullahhisam@utm.my

W. M. A. W. Azhar
e-mail: aizzatazhar@yahoo.com

A. Abdullah
Department of Surveying Science and Geomatic, Faculty of Architecture, Planning and Surveying, Universiti Teknologi Mara (Perlis), 02600 Arau, Perlis, Malaysia
e-mail: ashraf@perlis.uitm.edu.my

H. Jamil · T. C. Hua · C. K. Lim · T. A. Bah
Department of Survey and Mapping Malaysia (DSMM), Wisma JUPEM, Jalan Semarak 50578 Kuala Lumpur, Malaysia
e-mail: hasan@jupem.gov.my

and tidal constituents. This chapter aims to produce the tidal lines and littoral zone for use in marine cadastre procedures and practices. Based on the analysis, it can be concluded that the LAT is consistent and can potentially be used for marine cadastre reference level in order to improve the effectiveness of implementing the marine cadastre.

1 Introduction

The littoral zone is the region that lies between the lines of high tide and low tide. The physical location of the coastline is commonly referred to as the line of intersection between a specified tidal datum and the terrain. The exact tidal datum used for this purpose will lead to a different realization of the coastline (Quadros and Collier 2008b). Marine cadastre is an administration system with a 3D marine parcel administration controlled by legal and systematic technical arrangement of marine parcel right, restriction and responsibility elements for marine space activities covering marine natural resources, marine industry, tourism and national sea park, and wild life conservation (Ashraf et al. 2013).

Mean Sea Level (MSL) is normally used as a reference level for various land development applications while a low water level is applied as the reference level. The vertical datum used as a reference level in the marine environment is called chart datum. A chart datum is usually related to the mean of low ocean surfaces, such as Mean Lower Low Water Spring (MLLWS), Mean Lower Low Water (MLLW), Mean Low Water (MLW), Low Water (LW), Mean Low Water Spring (MLWS) or Lowest Astronomical Tide (LAT) and not all countries in the world is using the same level as chart datum for their marine administration.

Malaysia is a federal state with marine jurisdiction and management responsibility split between the states and the federal government. Following the Emergency (Essential Powers) Ordinance, No. 7 1969, now loosened and replaced by Territorial Water Act 2012, territorial water shall be constructed as a reference to such part of the sea that is adjacent to control the coast there of not exceeding three nautical miles measured from low water mark. In this situation, the states control up to three nautical miles from low water mark whilst the federal government has jurisdiction and management responsibility from the said three nautical miles limit to the outer edge of the EEZ and continental shelf. Through this specific jurisdiction by United Nations Convention on the Law of the Sea (UNCLOS), Malaysia enacted numerous acts related to the sea zone (Ashraf et al. 2011). According to Malaysia National Land Code, the limit of Land Cadastre administration is referred to the level of Highest Astronomical Tide (HAT). This description will create an uncertainty of jurisdiction of space between HAT and to the shoreline.

Based on the above mentioned acts, the determination of LAT as the reference level for marine cadastre is crucial. This study is an attempt to present the tidal

Table 1 Definition of International Hydrographic Organization (IHO) tidal datum (International Hydrographic Bureau 2010)

Level	Definition
LAT (HAT)	LAT (HAT) is defined as the lowest (highest) tide level which can be predicted to occur under average meteorological conditions and under any combination of astronomical conditions. It is recommended that LAT and HAT be calculated either over a minimum period of 19 years using harmonic constants derived from a minimum of 1 years observations or by other proven methods known to give reliable results. Tide levels should, if possible, reflect the estimated error values obtained during the determination of these levels

datum analysis and the use of Lowest Astronomical Tide (LAT) and Highest Astronomical Tide (HAT) to generate a littoral zone for marine cadastre.

The objective of this chapter is to present some fundamental principles that can be applied to produce the tidal line and analyze the consistency of LAT to use as a reference level in marine cadastre. In this chapter, we propose a computational technique of tidal datum to obtain the water level value based on LAT. In order to delineate the littoral zone, several of datasets have been identified to derive the tidal line.

2 Tidal Datum

Tides are the periodic vertical movement of water on the Earth's surface. It is also defined as the periodic variation in the surface level of the oceans and of bays, gulfs, inlets, and estuaries, caused by gravitational forces of the moon and sun. It also can be defined as the rise and fall of sea level. The measurement of the tide is called tide observation and the equipment used for the observation is called tide stations. Tide gauge is the device that we use to measure the changes in sea level.

A tidal datum is a standard elevation defined by a certain phase of the tide. Tidal datum is used as a reference level for measuring local water levels and should not be extended into areas having differing oceanographic characteristics without substantial measurements. The definition of tidal datum for Lowest Astronomical Tide and Highest Astronomical Tide is given in Table 1.

IHO resolves that Lowest Astronomical Tide (LAT) shall be adopted as chart datum where tides have an appreciable effect on the water level. A tidal datum is essentially the average of all the water elevations (high, low or mean) over an 18.6 year period. This eliminates most meteorological effects on water level. It is defined more simplistically as averaged stages of the tide such as MSL, MHW and MLLW. Tidal datum elevations vary significantly with geographic distance especially in shallow water. They are used as references to measure local water levels and should not be extended into areas having differing oceanographic
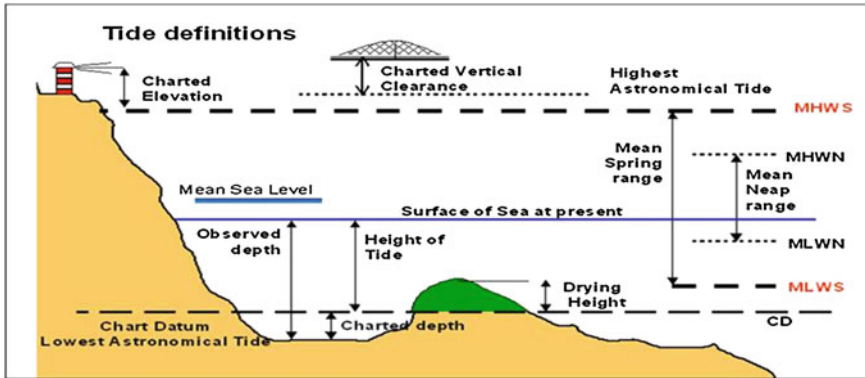
Fig. 1 Tide definitions that show the illustration of the terminology of tidal heights (Tide Definitions 2011)

characteristics without substantiating measurements. In order that they may be recovered when needed such as datum are referenced to bench mark (FIG 2006).

Lowest Astronomical Tide (LAT) is the lowest level of sea water where the sea water never gets lower than this LAT value. LAT is determined by tide prediction procedure using 18.6 years tide data. Chart datum has been rather more broadly defined as the level below which no predicted tide shall fall by more than 0.1 m. However, the Royal Malaysian Navy has chosen the lowest astronomical tide level (LAT) as the chart datum in producing their tide table prediction and also production of nautical charts in Malaysia. Figure 1 shows the tidal datum and its relation to the coastline.

3 Tidal Datum Determination for Marine Cadastre Commencement

Tides data from 12 Department of Survey and Mapping, Malaysia (DSMM) tide gauge stations have been acquired to assist the determination of tidal datum as shown in Fig. 2. Tides data period was started from the year 1993 to 2012. The computation of tidal datum is carried out using Total Tides Station (TOTIS) tidal analysis software. The software is able to compute the tidal datum based on the number of tidal constituents in relation to the number of months. The computation of tidal datum will focus on the study area Langkawi. The type of tides in Langkawi is semi-diurnal, consisting of two high tides and two low tides of nearly equal level of the lunar day.

The computation of water level value is based on LAT. The number of constituents will reflect the result. The analysis will cover the following periods: 15 days, 1 month, 3 months, 6 months, 1 year, every 5 years and 18.6 years. Table 2 tabulates the tide analysis period for 2012.
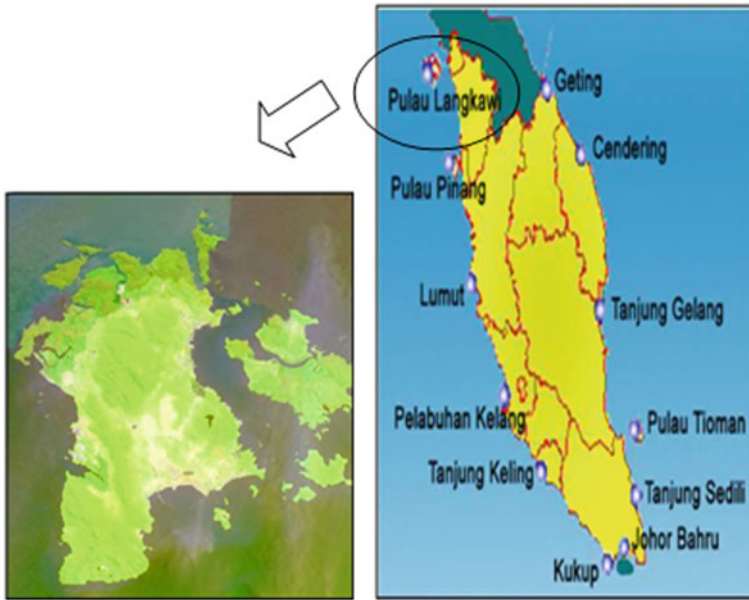
Fig. 2 Tide gauge stations location in Peninsular Malaysia

Day of analysis	Date
15 Days	1 Jan–15 Jan 2012
1 Month	1 Jan–31 Jan 2012
3 Months	1 Jan–31 Mar 2012
6 Months	1 Jan–30 June 2012
1 Year	1 Jan–31 Dec 2012

Table 2 Day of analysis from the year 2012

Table 3 and Fig. 3 show the tidal datum for Langkawi. Each type of water level is increasing apparently with long period of observation. The value of tidal datum is based on zero value of LAT.

Analysis of tidal datum for every 5 years is also based on zero value of LAT. (Tables 4 and 5).

Figure 4 show the stability of water level values for every 5 years period.

The water level value of 18.6 years observation has been computed from 15 Dec 1992 to 21 Jun 2011. Water level in harmonic analysis report (Table 6) for 18.6 years shows that LAT (Zo) is equal to 1.792 m. This indicates that with longer tide dataset, the tidal datum value is stable and can be accepted as reference level (Fig. 4). Table 7 shows the constituents value of M2, S2, N2, K2, K1, O1, P1 and Q1 for 18.6 years observation in Langkawi Island. Normally long tidal records are needed to determine amplitude and phase for a larger number of constituent with high accuracy.

Table 3 Tidal datum value for Langkawi

	15 Days (m)	1 Month (m)	3 Months (m)	6 Months (m)	1 Year (m)
HAT	2.991	3.335	3.506	3.570	3.542
MHWS	2.760	2.950	3.078	3.068	3.047
MHWN	1.909	2.048	2.042	2.191	2.151
MSL	1.555	1.692	1.761	1.823	1.790
MLWN	1.201	1.337	1.481	1.456	1.429
MLWS	0.350	0.435	0.445	0.579	0.533
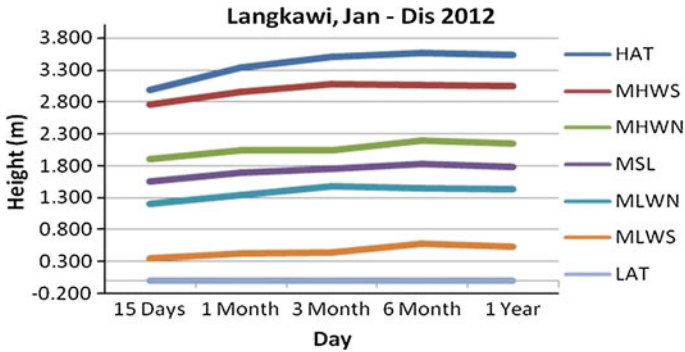
Fig. 3 The graph of water level values from year 2012

Table 4 Every 5 years of analysis

Year of analysis	Year
5 Years	1993–1997
5 Years	1998–2002
5 Years	2003–2007
5 Years	2008–2012

Table 5 Value of water levels (m)

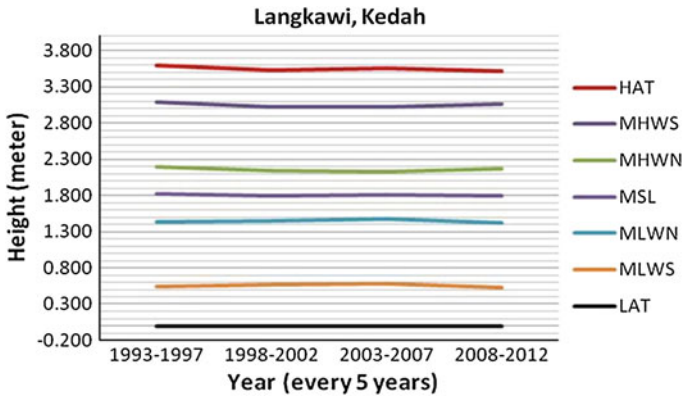|	1993–1997 (m)	1998–2002 (m)	2003–2007 (m)	2008–2012 (m)
HAT	3.591	3.535	3.556	3.512
MHWS	3.095	3.024	3.026	3.067
MHWN	2.202	2.137	2.131	2.175
MSL	1.820	1.795	1.805	1.799
MLWN	1.438	1.453	1.479	1.424
MLWS	0.545	0.565	0.584	0.532

Fig. 4 Water level values based on stability for every 5 years (1993–2012)

Table 6 Water level values for 18.6 years of observation for LAT system

LAT	MLWS	MLWN	MSL	MHWN	MHWS	HAT
0.000	0.560	1.451	1.792	2.134	3.025	3.510

Table 7 Constituents value of M2, S2, N2, K2, K1, O1, P1, Q1 for 18.6 years observation

	Amplitude	Phase
M2	0.786985	359.349945
S2	0.445315	36.221198
N2	0.144344	353.303280
K2	0.124387	50.304571
K1	0.167017	1.768064
O1	0.050599	294.273881
P1	0.050425	354.727930
Q1	0.008412	236.493450

4 Modeling of Tidal Datum

There are a number of tidal lines in littoral zone. In order to delineate the littoral zone, the location of the tidal line needs to be defined clearly. Tidal line describes the line of intersection between a specified tidal datum and the foreshore terrain (Quadros and Collier 2008a). The tidal datum calculated from the hydrodynamic model and it involves the computation of the harmonic constituents. The harmonic constituents from tide observation can be derived using Total Tide Solution (TOTIS) software.

The model of LAT surfaces has been discussed and derived using various strategies. LAT will be modelled relative to a geoid, after which the ellipsoid heights of LAT will be obtained by adding geoid heights to the model LAT values.

Modelling LAT relative to a geoid is realized by referencing the hydrodynamic model to the chosen geoid. (Slobbe et al. 2012). Terrain Irregular Network (TIN) and Digital Elevation Model (DEM) are needed to view the 3D model of seabed profile. The set of constituents used to derive the observed LAT values is that set for which the root means square (RMS) of the differences between the observe water levels and the reconstructed astronomical tide is lowest. The tidal lines can be derived from the integration of various datasets as follows:

- Topography data
- Bathymetry data (multi-beam sonar)
- Seabed topography data
- Tide data
- Light Detection and Ranging (LIDAR)
- High Resolution Satellite Image.

There are two methods in creating tidal model. The first method is by interpolating the tide height between tide gauges. This method only works well along open coastlines. It suffers major limitations in complex foreshore like bays, islands and rivers. So in this case, the second method is introduced. This method is localized a hydrodynamic model. Hydrodynamic model represent the movement of water and solving governing equations for oceanic movement. This hydrodynamic model has been derived using bathymetry data to get the depth and ocean tidal constants observed by tide gauges as the boundary conditions. The examples of global tidal model are FES2004, GOT4.8 and ORI96. The final data or result of tidal model contains the constituents and the constituents will separate by phase and amplitude. The amplitude and phase contain the longitude, latitude and the value of the respective constituents. Figures 5 and 6 show the phase and amplitude of the S2 constituent from the model Ori96.

5 Delineating the Littoral Zone

Quadros and Collier (2008a) summarized the steps to delineate the littoral zone. The littoral zone contains a number of tidal lines. A tidal line is used to describe the Intersection between a specified tidal datum and foreshore terrain. The step of delineating the zone is by computing the line of HAT and LAT using both bathymetric and topographic DEMs. The HAT line is derived from bathymetric data and the line of LAT is derived from bathymetric data and tidal lines. Figure 7 shows that the shoreline was present by many of sources and the data have been overlay. The different of grid of the data, so the two line of data have been analyzed for the intersection of the data. It is the digitizing data from Spot5 satellite image and bathymetric data. Figure 8 shows the zero elevation from line
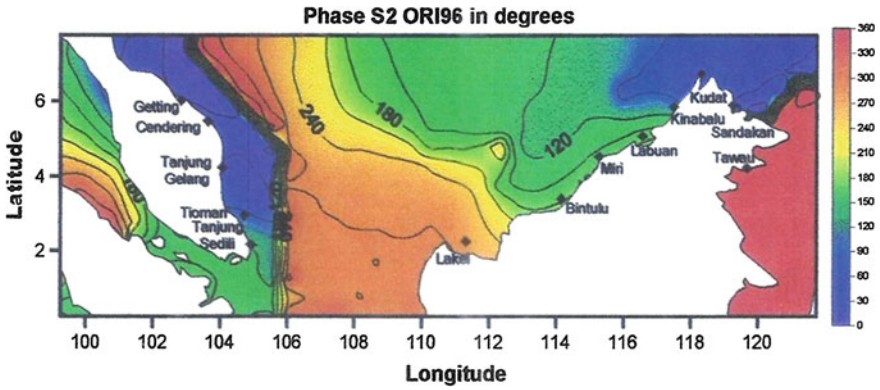
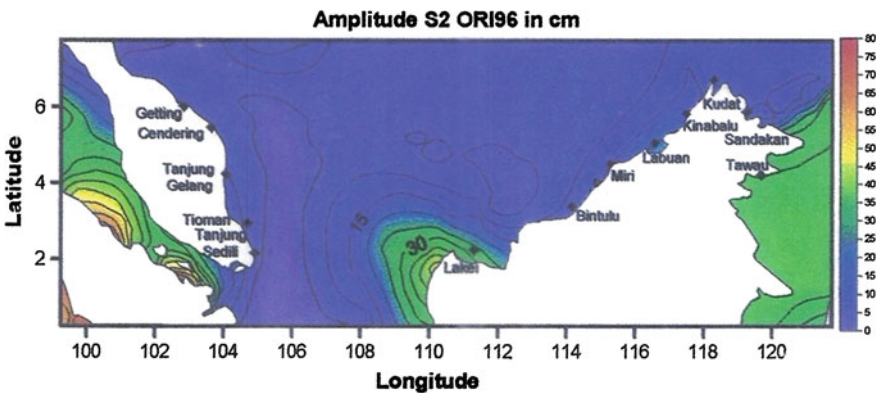**Fig. 5** Phase of the S2 constituent from the model Ori96 (Vella 2000)

Fig. 6 Amplitude of the S2 constituent from model Ori96 (Vella 2000)

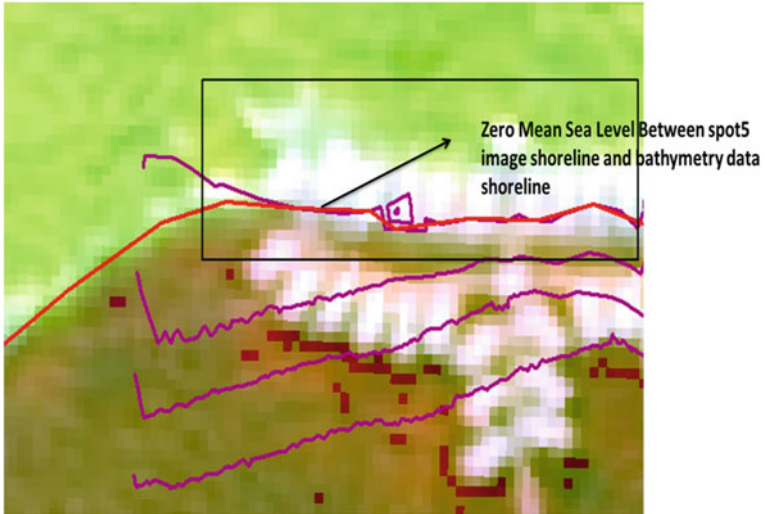**Fig. 7** Shoreline from all sources of data

Fig. 8 Zero elevation from line bathymetry and Spot5 maps
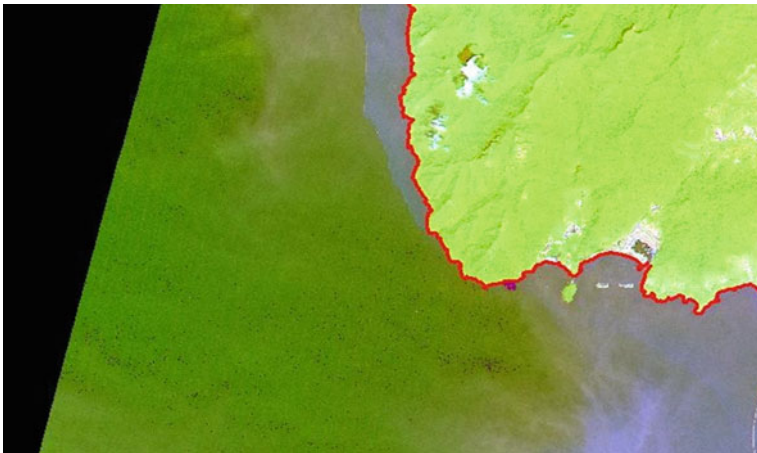

Fig. 9 Shoreline model part of Pulau Langkawi

bathymetry and Spot5 maps while Fig. 9 shows the shoreline model part of Pulau Langkawi. Figure 10 shows the littoral boundaries (LAT and HAT) as defined by bathymetric and topographic LIDAR.
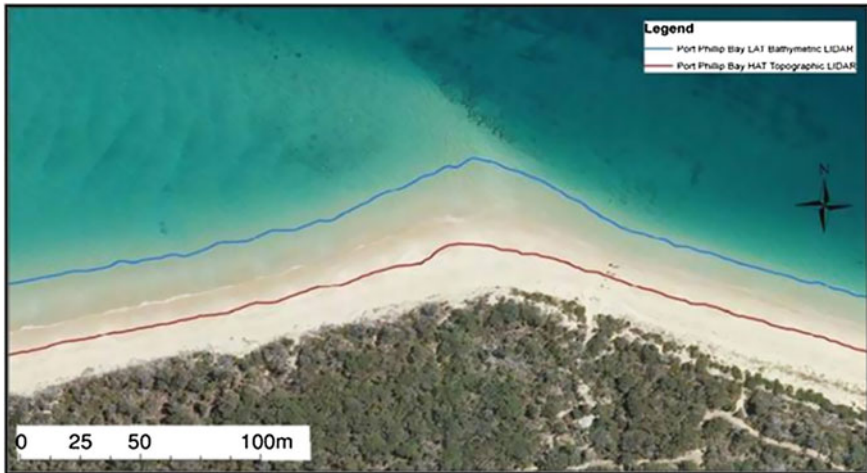
Fig. 10 Littoral boundaries (LAT and HAT) as defined by bathymetric and topographic LIDAR (Quadros and Collier 2008a)

6 Conclusion

A tidal datum is a standard water level defined by a particular phase of the tide. Tidal datum is used as a reference level for measuring local water levels and should not be extended into areas having differing oceanographic characteristics without substantial measurements. A number of techniques and datasets are available to delineate the littoral zone. The bathymetric and topographic data are used to define the terrain model. Meanwhile, the tides observation data are used to derive the tidal model and tidal line.

Based on the analysis of tidal datum that has been conducted, it shows that is a great potential to use LAT as reference level for marine cadastre. This will benefit the realization of marine cadastre in Malaysia due the availability of commencement point for parcel right. However, to develop the homogenous datum for land and sea, there is a need to develop a model for defining the relationship between different vertical reference surfaces. Large scale map of LAT tidal line and littoral zone for Malaysia is important towards the realization of marine cadastre in Malaysia.

References

Ashraf A, Zakaria MA, Abdullah OH (2011) Marine cadastre: issue on marine institutional governance in langkawi island as study case. International symposium and exhibition on geoinformation (ISG 2011)

Ashraf A, Zakaria MA, Jamil T (2013) Marine cadastre issue and conceptual for impementation in Malaysia. Jurnal Intelek 8(1), UiTM Perlis

FIG Guide on the Development of a Vertical Reference Surface for Hydrography (2006) International federation of surveyors (FIG), Guide no. 37

International Hydrographic Bureau (2010) Resolutions of the international hydrographic organization, Publication M-3 2nd edn

Quadros ND, Collier PA (2008a) Delineating the littoral zone using topographic and bathymetric. Lidar, ablos conference, 16–17 October 2008

Quadros ND, Collier PA (2008b) A new approach to delineating the littoral zone for an Australian marine cadstre. J Coastal Res. 24(3):780–789

Slobbe DC, Verlaan M, Klees R, Gerritsen H (2012) Lowest astronomical tide in the north sea derived from a vertically referenced shallow water model, and an assessment of its suggested sense of safety. Mar Geodesy 36(1):31–71

Tide Definitions (2011) http://www.skysailtraining.co.uk/tide_definitions_causes.htm. Accessed 21 May 2013

Vella MNJP (2000) The development of tide models for the shallow water area using satellite altimetry. a Malaysian case study. masters thesis, Universiti Teknologi Malaysia

The Improved Conceptual Design of Web-based GIS Residential Property Marketing Information System

Siti Aekbal Salleh, Wan Mohd Naim Wan Mohd and Eran Sadek Said Md Sadek

Abstract This chapter attempts to show the conceptual design a Web-based GIS Residential Property Marketing Information System (WGRPMIS). This system is intended to be integrated with the virtual GIS technology enabling the consumer to virtually explore the potential property based upon the multi criteria selection through assisted geo-processing query. The proposed system is built using Adobe Flex on ArcGIS Server framework to enable geo-processing and geometric network capabilities. Through the pilot system, the success of 3D and virtual reality integration was revealed. Due to limitations of the query functions and 3D feature complexity taking its toll on the system's performance, an improved geo-processing scheme is presented in this paper and the conceptual design of this system is revised. The improved query function which includes road network and accessibility were taken into consideration in solving buffer and radius query is developed. The revised conceptual design will further be used in designing the simplified 3D visualization viewer to the Virtual panoramic display.

Keywords GIS · Property · Virtual GIS

1 Background

> … the strongest tangible benefit noted by many users of GIS for land and property management was the ability to visualise relationships between property and the surrounding geography by mapping land and property assets… the strongest intangible benefit was the data audit and cleaning… (Wyatt and Ralphs, 2003)

S. A. Salleh (✉) · W. M. N. W. Mohd · E. S. S. M. Sadek
Centre for Surveying Science and Geomatics, Faculty of Architecture Planning and Surveying, Universiti Teknologi MARA, Shah Alam, Selangor, Malaysia
e-mail: aekbal@salam.uitm.edu.my

Table 1 Online Marketing Technological Dependencies (Ranchhod et al. 2001)

	Searching, browsing, capabilities	Posting, hosting, presentation capabilities	Communication capabilities	Transaction, security, and monitoring capabilities
Marketing research	Highly dependence			
Advertising, branding		Highly dependence		
Customer relations, public relations			Highly dependence	
Selling and distribution				Highly dependence

Decades ago property information such as location-based data were recorded and displayed on thousands of maps. Computer technology converts this information into digital format and shares it virtually on the web. However, the capability of current property marketing system has been stagnant as textual information, graphic images of property and location maps which have led to some spatial properties such as topographic conditions, neighbouring built environment and the property physical properties remain hidden.

GIS technology transpired to cater for the growing need of spatial data handling. With the emergence of current GIS technology such as enabling 3D visualization and analyses, GIS web server and cloud computing, compiling GIS functions through web-based sharing services is made possible. A matrix that can illustrate the relationship and dependency between marketing activities and technology which shows several issues that need to be tackled during the development of online information system is identified and reported (Ranchhod et al. 2001) (Table 1).

The introduction of GIS technology in property management information system has enabled users to handle large spatial data and improve the system efficiency (Qian 2013). GIS technology is typically implemented in property management when the property management system is designed to support geographical information (Ralphs and Wyatt 2003). Evidence and justification of insufficiencies in the existing information systems to handle spatial information were identified by several authors (Jitka and Renata 2006; Zlatanova and Tempfli 2000; Louwsma et al. 2006).

As technology has improved rapidly, many potential modernizations in the aspect of system display and communication can be found. The main improvement criteria that are most valuable for information system are virtual reality (VR), 3D visualization, 3D GIS and web-enable. VR GIS is a combination of VR technology and GIS where VR plays the role as the main interface and interaction method (Faust 1995). VR technology has been widely used in tourism (Guttentag 2010) and urban and regional planning (Ma et al. 2008; Ma et al. 2010). Integrating GIS, virtual reality and web-based applications increased the system complexity. Thus,

several constraints involving class definition, relationship, attributes and the implementation of such integration should be formed systematically (Louwsma et al. 2006).

2 The Pilot WGRPMIS

The pilot system was designed and developed based on user requirement study and direct semi-structured interview with the potential users of the system (i.e. consumers, real estate agents and property developer) (Salleh et al. 2008). The pilot system however is designed on a desktop platform and has not yet been integrated with web enabling functions. The schematic representation of the pilot system is illustrated in Fig. 1.

The search engine embedded in the pilot system is programmed using Visual Basic, and it has some limitation especially with regards to its networks and geo-processing query results. Figure 2 shows the results of radius and buffer query where, the geometric network dataset properties were found missing. Distance from one to another location should not be accessed purely according to radius and buffer from selected location but also the range of network distance and accessibility through road.

The 3D visualization and virtual reality integration come after the selection of the potential residential property is finalized. Hence, the virtual reality files are pre-recorded and linked from the property attribute table. The initial design of the system was to integrate 3D GIS with this system. One main constraint is whenever the system is compiled, and within the testing environment, the loading of 3D GIS features required more time to execute. Thus, this function is reconsidered and a more simplified alternative is investigated. Figure 3 shows the result of interior 3D representation of the tested property.

2.1 Rationale of Improvement

This paper seeks to address the gaps and limitations found in the pilot system developed by the authors (Salleh et al. 2008). The improved system include the query search engine by integrating geo-processing and geometric network analyst capabilities, simplified 3D visualization functions to reduce processing memory required to load the level of details (LODs) through virtual panoramic display and finally to allow online access. The revised system is not intended to generate high accuracy 3D model of the property, but a reasonable representation of the physical state of the house and the floor plan design is sufficient. In the earlier pilot system, loading the LODs requires more time than the user have anticipated. This is documented in testing the pilot system. The setback is not only the loading time but also the completeness of the 3D facade and texture is not as desirable. This limitation
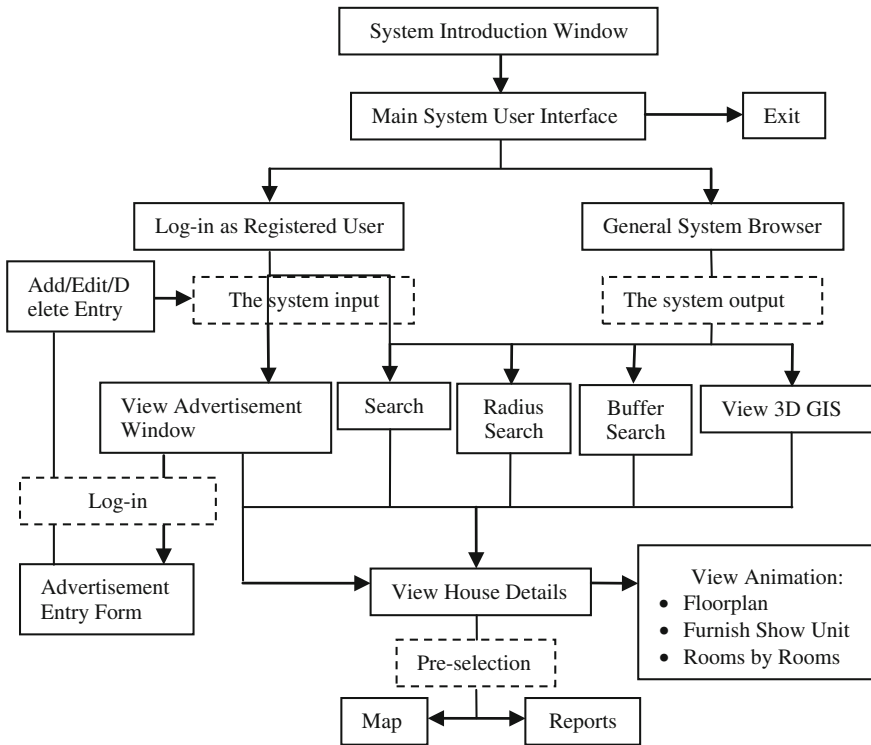
Fig. 1 The schematic representation of pilot system user interface (Salleh et al. 2008)

and issue was reported in previous studies (Louwsma et al. 2006; Salleh et al. 2008; Zlatanova and Prosperi 2005). The edge reduction as compared to traditional 3D surface model can significantly reduce the use of memory and computational time while offering a reasonable visualization quality (Lin et al. 2008). As such, the proposed system will be adopting the panoramic VR method to visualize the 3D environment of the selected residential property. The new system is designed to facilitate the consumers to make a decision on the most adequate matching criteria according to their specification. Consumers will be able to explore the potential housing property online without being present at the property location. With that, the improvement of this system functionality and performance is necessary.

3 The Revised Conceptual Design of WRGPMIS

The revised system is built on the framework of ArcGIS Server. To enable it to be used via web, ArcGIS Viewer for flex is employed. Currently, a number of applications have been built by employing ArcGIS internet mapping server (Wang

Fig. 2 Radius and buffer query results of the pilot system (Salleh et al. 2008)

et al. 2011; Mingyu 2008; Guang-rui 2007). This Graphical User Interface (GUI) is designed using Adobe Flex which enables the system to be viewed online either on windows, androids and iOS devices. The conceptual design of the revised system is illustrated in Fig. 4.
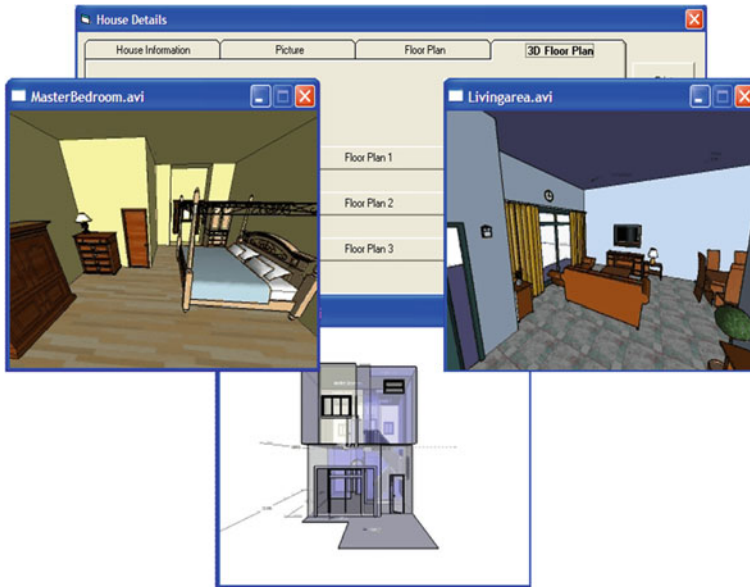
Fig. 3 3D function of the pilot system (Salleh et al. 2008)

3.1 Improvising Geo-Processing and Geometric Network Functions

The Geo-processing service engine is built on the ArcGIS Server and Adobe Flex viewer for its user interface. To ensure the success of this function, the following data are essential:

1. Street network (topologically correct), stored in Geometric Network—Polyline
2. Points of Interest data—Point
3. Property data—Polygon.

The new process requires three inputs from users relating to the type of property, the range of price and also the distance to Points of Interest (POI). The POI will represent the preferences of nearest facilities to the respective property such as school, mosque, bank, clinic or departmental store. In response to this function, topological correction and generation of geometric network data for the system function is crucial, and of essence to the success of this function. The Geo-processing Service comprises the following activities:

1. User selects a POI
2. Create a Buffer layer of the POI based on the user specified Distance
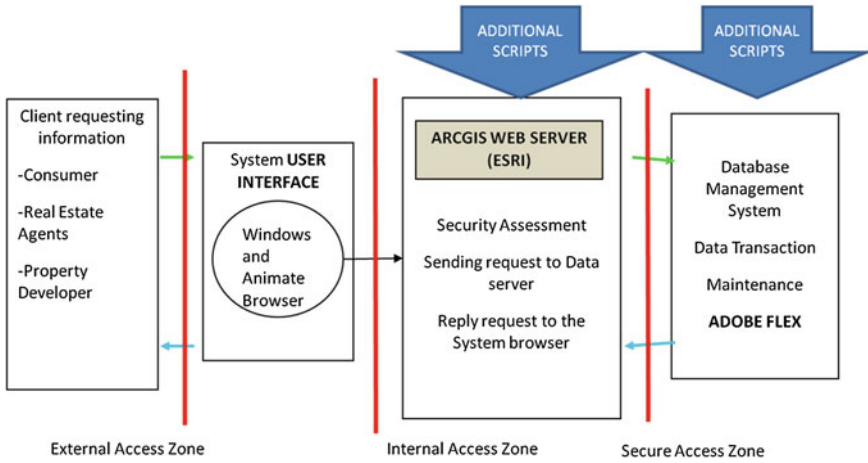3. Intersect buffer layer with the property polygon layer

Fig. 4 The conceptual design of WGRPMIS

4. Select from the selected property polygon, with the query statement formed using the user's input variables (Property Type and Price Range)
5. Create layer from the new selection
6. Calculate the route distance from the property to the user selected POI using network analysis
7. If more than one property is found, iterate the process in no. 6
8. Display results.

The POI selection exhibited the highest requirement of potential property criteria in which the system should allow interactive selection or query by attribute. This is crucial as presented in the matrix of online marketing technological dependencies (refer to Table 1). In real estate business, POI is not only important to market the property but an essential element to determine the property price. This determinant has been recognised ages ago, indicating location and price has been equally important in the property buying decision making (Chin and Foong 2006; Kuşan et al. 2010). In summary, the property belonging services, facilities and accessibility are the factors affecting house prices and further influenced by the macro-economic variables, spatial differences, characteristics of community structure, and environmental amenities (Kuşan et al. 2010; Kim and Park 2005).

The improvements made to the design and the function scripts are illustrated in Fig. 5.

Figures 6, 7 and 8 show the results of integrated geo-processing and geometry network functions. The results indicate significant differences as compared to the radius and buffer search functions in the pilot system.
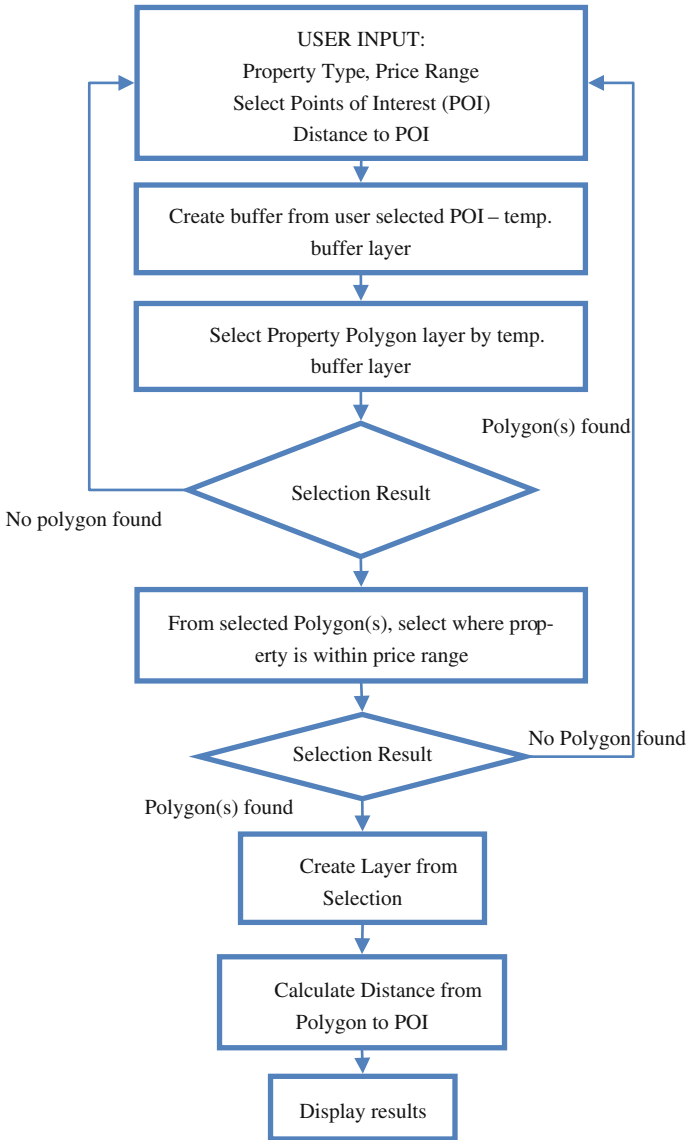
Fig. 5 The schematic process of Geo-processing and Geometric network query functions

3.2 Improvising 3D Visualization Functions

The 3D GIS visualization function in the pilot system is switched into the photographic panoramic display to replace heavy 3D visualization format. Other 3D visualization techniques will also be tested in the revised system. The proposed
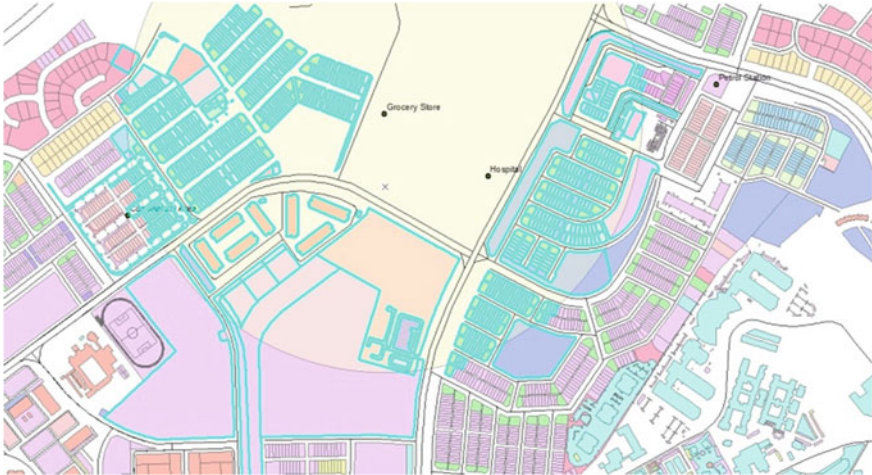
Fig. 6 Properties selection based on buffer of the POI

Fig. 7 A property selected based on the price range, within the buffer area

improvement of this function is expected to reduce the processing memory that delay the 3D texture rendering that demotes the use of this function. Figure 9 viewed the sample of photographic panoramic display of the revised system that is linked to the GIS polygon layer (land lot) attribute.
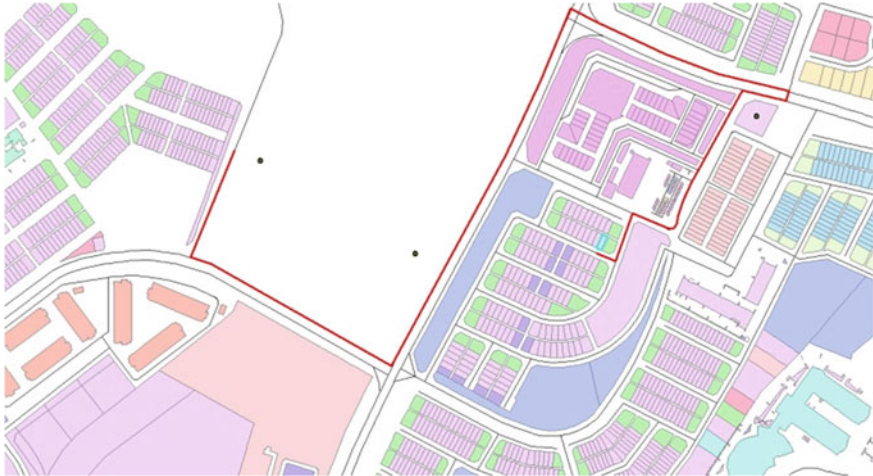
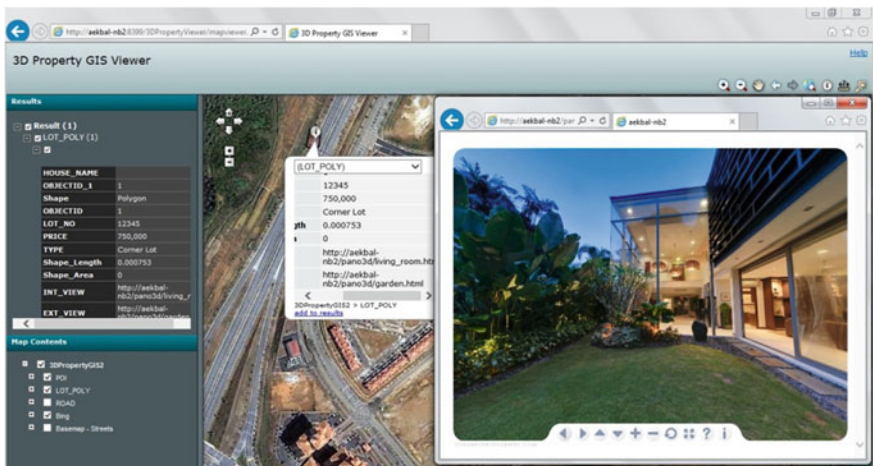**Fig. 8** Route from the POI to the selected property

Fig. 9 Panoramic VR window

4 Conclusion

This paper presents the improvised conceptual design and two major setbacks of the pilot system are mainly the physical complexity of the level of details (LODs) and inadequate functions for geo-processing and network query. Thus, alternative way of presenting 3D features through virtual panoramic display is used to simplify and reduce the used of processing memory that demotes the use of this system. The utilization of panoramic VR significantly improved the computational

time and memory space while still able to provide reasonably good 3D visualization representation. Additional drawback of the pilot system is the 3D texture and facade of the 3D surface model was not completely uploaded to the system viewer. Thus, simplifying of the 3D model is recommended and as a result 3D panoramic VR was employed in the revised system. Buffer and radius functions of the pilot system have been a sole geo-processing query that employed the most simplified rules of buffer and radius search. As accessibility and mobility of potential property to the nearest facilities or POI influenced the selling transaction, the improved buffer query was integrated with specific topological rules and geometric network data. These improvements allow users to query buffer and radius of selected property not by simply looking at the spatial location but also the route accessibility and connectivity. As such, the query result can also provide distance and road connectivity information. The new schematic function for geo-processing and geometric network query demands for shifting the independent system to ArcGIS Server with Adobe Flex viewer to enhance the GUI. These modifications have improved the traditional radius and buffer results and will potentially improve the 3D visualization functions.

References

Chin HC, Foong KW (2006) Influence of school accessibility on housing values. J urban Plan Dev 132(3):120–129

Faust NL (1995) The virtual reality of GIS. Environ Plann B 22:257

Guang-rui Z (2007) The development of estate management information system based on WebGIS. Sci Surveying Mapp 1:056

Guttentag DA (2010) Virtual reality: applications and implications for tourism. Tour Manag 31(5):637–651

Jitka K, Renata M (2006) Some problems connected to utilization of internet geographic information systems. In Proceedings of the 6th WSEAS international conference on multimedia, internet & video technologies, World scientific and engineering academy and society (WSEAS)

Kim K, Park J (2005) Segmentation of the housing market and its determinants: Seoul and its neighbouring new towns in Korea. Aust Geogr 36(2):221–232

Kuşan H, Aytekin O, Özdemir İ (2010) The use of fuzzy logic in predicting house selling price. Expert Syst Appl 37(3):1808–1813

Lin T-T, Hsiung Y-K, Hong G-L, Chang H-K, Lu FM (2008) Development of a virtual reality GIS using stereo vision. Comput Electron Agric 63(1):38–48

Louwsma J, Zlatanova S, van Oosterom R (2006) Specifying and implementing constraints in GIS—with examples from a geo-virtual reality system. GeoInformatica 10(4):531–550

Ma C, Chen G, Han Y, Qi Y, Chen Y (2008) VR-GIS: an integrated platform of VR navigation and GIS analysis for city/region simulation. In Proceedings of the 7th ACM SIGGRAPH international conference on virtual-reality continuum and its applications in industry, ACM, 2008

Ma C et al (2010) An integrated VR–GIS navigation platform for city/region simulation. Comput Anim Virtual Worlds 21(5):499–507

Mingyu Z (2008) Design and Implementation of Property Management WebGIS based on ArcIMS. Comput Dev Appl 4:021

Qian R (2013) The application of GIS in the real estate management system. In: Proceedings of the 2012 international conference of modern computer science and applications, Springer

Ralphs MP, Wyatt P (2003) GIS in land and property management. Taylor & Francis, London

Ranchhod A, Tinson J, Zhou F (2001) Factors influencing marketing performance on the web. Internet Marketing Research: Theory and Practice, p. 61

Salleh SA, Wan Mohd WMN, Nawawi AH, Md Sadek ESS (2008) The integration of 3D GIS and virtual technology in the design and development of residential property marketing information system (grpmis). computer and information. Science 1(4):37

Wang J-H, Zhu J, Fan Q-J, Lu J-L (2011) Web virtual campus research based on arcgis server and arcglobe. Geomatics Spat Inf Technol 2:012

Zlatanova S, Prosperi D (2005) Large-scale 3D data integration: challenges and opportunities. CRC Press, Baco Raton

Zlatanova S, Tempfli K (2000) Modelling for 3D GIS: Spatial analysis and visualisation through the web. In: International archives of photogrammetry and remote sensing, 2000, vol 33(B4/3; Part 4), pp 1257–1264